

Lecture Notes in Mechanical Engineering

Magd Abdel Wahab *Editor*


# Proceedings of the 4th International Conference on Numerical Modelling in Engineering

Volume 2: Numerical modelling in  
Mechanical and Materials Engineering,  
NME 2021, 24-25 August, Ghent  
University, Belgium

 Springer


# Lecture Notes in Mechanical Engineering

## Series Editors

Francisco Cavas-Martínez , Departamento de Estructuras, Universidad Politécnica de Cartagena, Cartagena, Murcia, Spain

Fakher Chaari, National School of Engineers, University of Sfax, Sfax, Tunisia

Francesca di Mare, Institute of Energy Technology, Ruhr-Universität Bochum, Bochum, Nordrhein-Westfalen, Germany

Francesco Gherardini , Dipartimento di Ingegneria “Enzo Ferrari”, Università di Modena e Reggio Emilia, Modena, Italy

Mohamed Haddar, National School of Engineers of Sfax (ENIS), Sfax, Tunisia

Vitalii Ivanov, Department of Manufacturing Engineering, Machines and Tools, Sumy State University, Sumy, Ukraine

Young W. Kwon, Department of Manufacturing Engineering and Aerospace Engineering, Graduate School of Engineering and Applied Science, Monterey, CA, USA

Justyna Trojanowska, Poznan University of Technology, Poznan, Poland

**Lecture Notes in Mechanical Engineering (LNME)** publishes the latest developments in Mechanical Engineering—quickly, informally and with high quality. Original research reported in proceedings and post-proceedings represents the core of LNME. Volumes published in LNME embrace all aspects, subfields and new challenges of mechanical engineering. Topics in the series include:

- Engineering Design
- Machinery and Machine Elements
- Mechanical Structures and Stress Analysis
- Automotive Engineering
- Engine Technology
- Aerospace Technology and Astronautics
- Nanotechnology and Microengineering
- Control, Robotics, Mechatronics
- MEMS
- Theoretical and Applied Mechanics
- Dynamical Systems, Control
- Fluid Mechanics
- Engineering Thermodynamics, Heat and Mass Transfer
- Manufacturing
- Precision Engineering, Instrumentation, Measurement
- Materials Engineering
- Tribology and Surface Technology

To submit a proposal or request further information, please contact the Springer Editor of your location:

**China:** Ms. Ella Zhang at [ella.zhang@springer.com](mailto:ella.zhang@springer.com)

**India:** Priya Vyas at [priya.vyas@springer.com](mailto:priya.vyas@springer.com)

**Rest of Asia, Australia, New Zealand:** Swati Meherishi at [swati.meherishi@springer.com](mailto:swati.meherishi@springer.com)

**All other countries:** Dr. Leontina Di Cecco at [Leontina.dicecco@springer.com](mailto:Leontina.dicecco@springer.com)

To submit a proposal for a monograph, please check our Springer Tracts in Mechanical Engineering at <https://link.springer.com/bookseries/11693> or contact [Leontina.dicecco@springer.com](mailto:Leontina.dicecco@springer.com)

**Indexed by SCOPUS. All books published in the series are submitted for consideration in Web of Science.**

More information about this series at <https://link.springer.com/bookseries/11236>

Magd Abdel Wahab  
Editor

# Proceedings of the 4th International Conference on Numerical Modelling in Engineering

Volume 2: Numerical modelling  
in Mechanical and Materials Engineering,  
NME 2021, 24-25 August, Ghent University,  
Belgium

 Springer

*Editor*

Magd Abdel Wahab  
Faculty of Engineering and Architecture  
Ghent University - Laboratory Soete  
Zwijnaarde, Belgium

ISSN 2195-4356

ISSN 2195-4364 (electronic)

Lecture Notes in Mechanical Engineering

ISBN 978-981-16-8805-8

ISBN 978-981-16-8806-5 (eBook)

<https://doi.org/10.1007/978-981-16-8806-5>

© The Editor(s) (if applicable) and The Author(s), under exclusive license to Springer Nature Singapore Pte Ltd. 2022

This work is subject to copyright. All rights are solely and exclusively licensed by the Publisher, whether the whole or part of the material is concerned, specifically the rights of translation, reprinting, reuse of illustrations, recitation, broadcasting, reproduction on microfilms or in any other physical way, and transmission or information storage and retrieval, electronic adaptation, computer software, or by similar or dissimilar methodology now known or hereafter developed.

The use of general descriptive names, registered names, trademarks, service marks, etc. in this publication does not imply, even in the absence of a specific statement, that such names are exempt from the relevant protective laws and regulations and therefore free for general use.

The publisher, the authors and the editors are safe to assume that the advice and information in this book are believed to be true and accurate at the date of publication. Neither the publisher nor the authors or the editors give a warranty, expressed or implied, with respect to the material contained herein or for any errors or omissions that may have been made. The publisher remains neutral with regard to jurisdictional claims in published maps and institutional affiliations.

This Springer imprint is published by the registered company Springer Nature Singapore Pte Ltd.

The registered company address is: 152 Beach Road, #21-01/04 Gateway East, Singapore 189721, Singapore

# Organising Committee

## Chairman

Prof. dr. ir. Magd Abdel Wahab, Laboratory Soete, Ghent University, Belgium

## International Scientific Committee

Prof. D. Ribeiro, School of Engineering, Polytechnic of Porto (ISEP-IPP), Portugal

Prof. J. Santos, University of Madeira, Portugal

Prof. J. Toribio, University of Salamanca, Spain

Prof. B. B. Zhang, Glasgow Caledonian University, UK

Prof. V. Silberschmidt, Loughborough University, UK

Prof. T. Rabczuk, Bauhaus University Weimar, Germany

Prof. L. Vanegas Useche, Universidad Tecnológica de Pereira, Colombia

Prof. N. S. Mahjoub, Institut Préparatoire aux Etudes d'Ingénieurs de Monastir, Tunisia

Prof. A. Cheknane, Amar Telidji University of Laghouat, Algeria

Prof. E. N. Farsangi, Kerman Graduate University of Advanced Technology (KGUT), Iran

Prof. N. A. Noda, Kyushu Institute of Technology, Japan  
Prof. K. Oda, Oita University, Japan

Prof. S. Abdullah, Universiti Kebangsaan Malaysia, Malaysia

Prof. C. Zhou, Nanjing University of Aeronautics and Astronautics, China

Prof. B. Bhusan Das, National Institute of Technology Karnataka, India

Prof. R. V. Prakash, Indian Institute of Technology, India

Prof. H. N. Xuan, Hutech University, Vietnam

Prof. Giuseppe Carbone, University of Calabria, Italy

Prof. Fadi Hage Chehade, Lebanese University, Lebanon

Prof. Sohail Nadeem, Quaid-i-Azam University, Pakistan

Dr. A. San-Blas, Miguel Hernández University of Elche, Spain  
Dr. G. Minafo, University of Palermo, Italy  
Dr. A. Caggiano, Technische Universität Darmstadt, Germany  
Dr. S. Khatir, Ghent University, Belgium  
Dr. T. Yue, Ghent University, Belgium  
Dr. A. Rudawska, Lublin University of Technology, Poland  
Dr. L. V. Tran, Sejong University, South Korea  
Dr. X. Zhuang, Leibniz Universität Hannover, Germany  
Dr. I. Hilmy, International Islamic University Malaysia, Malaysia  
Dr. C. Wang, Liaocheng University, China  
Dr. M. Mirrashid, Semnan University, Iran  
Prof. A. G. Correia, University of Minho, Portugal  
Dr. M. Wang, Los Alamos National Laboratory, USA  
Dr. Filippo Genco, Adolfo Ibáñez University, USA  
Dr. Denis Benasciutti, University of Ferrara, Italy  
Dr. Y. L. Zhou to Xi'an Jiaotong University, China

# Preface

This volume contains the proceedings of the 4th International Conference on Numerical Modelling in Engineering: Volume 2: Numerical modelling in Mechanical and Materials Engineering. Numerical Modelling in Engineering NME 2021 is the 4th NME conference and is held Online via MS Teams, during the period 24–25 August, 2021. Previous NME conferences were celebrated in Ghent, Belgium (2018), Beijing, China (2019) and Online (2020).

The overall objective of the conference is to bring together international scientists and engineers in academia and industry in fields related to advanced numerical techniques, such as FEM, BEM, IGA and their applications to a wide range of engineering disciplines. The conference covers industrial engineering applications of numerical simulations to Civil Engineering, Aerospace Engineering, Materials Engineering, Mechanical Engineering, Biomedical Engineering, etc. The presentations of NME 2018 are divided into 2 main sessions, namely (1) Civil Engineering and (2) Mechanical and Materials Engineering. This volume is concerned with the applications to Mechanical and Materials Engineering.

The organising committee is grateful to keynote speaker, Professor Yaroslav D. Sergeev, University of Calabria, Rende, Italy and Lobachevsky State University, Nizhni Novgorod, Russia, for his keynote speech entitled ‘Computations with numerical infinities and infinitesimals’.

Special thanks go to members of the Scientific Committee of NME 2021 for reviewing the articles published in this volume and for judging their scientific merits. Based on the comments of reviewers and the scientific merits of the submitted manuscripts, the articles were accepted for publication in the conference proceedings and for presentation at the conference venue. The accepted papers are of a very high scientific quality and contribute to advancement of knowledge in all research topics relevant to NME conference.



Finally, the organising committee would like to thank all authors, who have contributed to this volume and to those who have presented their research work at the conference in MS Teams.

Zwijnaarde, Belgium

Professor Magd Abdel Wahab  
Chairman of NME 2021

# Contents

<b>Dynamic Analysis of 3D Solid Structure Using a Consecutive-Interpolation Over Polyhedral Element Mesh</b> .....	1
Hau Nguyen-Ngoc, H. Nguyen-Xuan, and Magd Abdel Wahab	
<b>Study of Forced Vibrations of a Two-Layer Plate Under Harmonic Load</b> .....	9
Vitaly N. Paimushin, Vyacheslav A. Firsov, Victor M. Shishkin, and Ruslan K. Gazizullin	
<b>Peterson Charts for Functionally Graded Rotating Hollow Disks with an Eccentric Hole</b> .....	25
M. Cais, D. Casagrande, and H. M. A. Abdalla	
<b>Use of the Chebyshev Collocation Method for Vibration Analysis of Carbon-Nanotube Reinforced Composite Beams with Elastic Boundary Conditions</b> .....	35
Desmond Adair and Martin Jaeger	
<b>Analytical, Numerical and Experimental Analysis of the Creep Behaviour of Polyethylene Polymers</b> .....	49
A. Mostafa, D. G. S. Sanchez, N. Sirach, R. V. Padilla, and H. Alsanat	
<b>Numerical Investigation of Lithium Battery Using Heat Pipes in Electric Vehicles</b> .....	81
Zhao Liu, Jin Zhao, Chao Wang, Yangjun Qin, and Hang Zhang	
<b>Modeling the Intercooling of a Multi-stage Compression in Gas Turbines Using Absorption Chiller</b> .....	101
Kirolos A. Amin, Mohamed ElHelw, and Osama A. Elsamni	

<b>On the Design and Performance Analysis of Deadlock Controller for Automated Manufacturing Systems with Unreliable Resources</b> . . . . .	121
Mohammad Ashraful Karim Chowdhury, M. Krid, Ahnaf Akif, and A. Mostafa	
<b>The Device to Simulate Movement of Teeth Jaw</b> . . . . .	141
Ho Thi Thuy Duong, Tran Nam Cuong, Nguyen Thu Khoa, Nguyen Tran Kim Hoang, and Nguyen Tuong Long	
<b>The Plane Problem of Poroelasticity for a Semi-plane</b> . . . . .	151
Natalya Vaysfeld and Zinaida Zhuravlova	
<b>Crack Propagations in Functionally Graded Material Using a Phase-Field NURBS-Based Finite Element Approach</b> . . . . .	159
Khuong D. Nguyen, H. Nguyen-Xuan, and Magd Abdel Wahab	
<b>Superfluid Core Cooling Influence in the Braking Index of Young Pulsars</b> . . . . .	177
Carlos Frajuca and Fabio da Silva Bortoli	
<b>Simulation of a 2D Large Transformation Elastoplasticity Problem Using the ANM</b> . . . . .	185
Chafik El Kihal, Omar Askour, Youssef Belaasilia, Abdellah Hamdaoui, Bouazza Braikat, Noureddine Damil, and Michel Potier-Ferry	
<b>Modeling the Interface Between User Skin and Wearable Equipment, a Case Study</b> . . . . .	195
M. Filomena Teodoro	
<b>Reinforcement Learning to Refine FEM Meshes for Acoustic Problems</b> . . . . .	209
Mathieu Gaborit, Gwénaél Gabard, and Olivier Dazel	

# Dynamic Analysis of 3D Solid Structure Using a Consecutive-Interpolation Over Polyhedral Element Mesh



Hau Nguyen-Ngoc, H. Nguyen-Xuan, and Magd Abdel Wahab

**Abstract** In this study, we investigate the dynamic performance of the three-dimensional solid structures by using the latest development of a consecutive-interpolation scheme. The structure is discretized into finitely arbitrary polyhedral elements. The bounded faces of an element can be non-planar. The interpolation scheme is constructed through two main steps. The first step uses the piecewise linear shape functions, which are also formulated for arbitrary polyhedral elements. The second step is formulated based on the fact of continuity of the nodal strains, which could only be satisfied by post-processing in the conventionally polyhedral finite element method (PFEM). The natural frequencies of the solid structures are analysed by a dynamic problem. The efficiency of the method is approved by comparing the obtained solutions to those of the conventional finite element method (FEM) using tetrahedral elements and PFEM, which are two methods effectively implemented for complex solids.

**Keywords** Consecutive-interpolation scheme · Dynamic problem · Natural frequencies · Arbitrary polyhedral elements · Complex solids

---

H. Nguyen-Ngoc (✉) · M. Abdel Wahab  
Department of Electrical Energy, Metals, Mechanical Constructions and Systems, Faculty of Engineering and Architecture, Ghent University, Ghent, Belgium  
e-mail: [Hau.nguyennngoc@ugent.be](mailto:Hau.nguyennngoc@ugent.be); [nnhau@dut.udn.vn](mailto:nnhau@dut.udn.vn)

H. Nguyen-Ngoc  
University of Science and Technology, The University of Danang, Da Nang, Vietnam

H. Nguyen-Xuan  
CIRTECH Institute, Ho Chi Minh City University of Technology (HUTECH), Ho Chi Minh City, Vietnam  
e-mail: [ngx.hung@hutech.edu.vn](mailto:ngx.hung@hutech.edu.vn)

## 1 Introduction

Polyhedral shape is a 3D geometry that is favourite by nature and can be seen around us, such as turtle shells, honeycomb, pineapple, crystals, etc. In the framework of computational analysis, the polytopes were firstly applied in FEM in 1970s when the interpolation schemes over polygonal domains were developed. Wachspress [1] was a pioneering scientist presented linear interpolation formulation over elements with more than four vertices based on element geometry and rational functions, which were solved by using special technique. These interpolation functions are well-known as Wachspress shape functions. This is the first step to change from traditional FEM using tetrahedral or hexahedral elements to the use of a more general mesh of polyhedral elements. The polygonal/polyhedral finite element method provides a great potential in modelling problems of polycrystalline materials [2], intermediate elements to connect different meshes sharing a same boundary [3], cell base material design [4]. Additionally, the pFEM is also applied to the problems of topology optimization [5], plates [6] or fluid flows [7].

In the earlier development of the polygonal/polyhedral finite element method, the interpolation scheme was firstly proposed for convex 2D polygons with arbitrary number of vertices [1]. Thereafter, more general polygonal elements, which possess irregular (concave) shapes, were taken into account to increase the flexibility of the polygonal finite mesh [8]. In the three-dimensional problems, the simplest polyhedral interpolants were presented for convex polyhedron bounded by triangular faces [9]. Whereas, the polyhedral elements with arbitrary number of vertices and edges, and the facets which can be non-planar, are the latest arbitrary elements [10, 11].

The consecutive interpolation (CI) scheme was firstly developed for two-dimensional mechanics problems discretized into linear triangular elements [12], in which the nodal displacement unknowns are approximated through two steps. Firstly, the interpolation scheme is assumed to be similar to conventional FEM. Whereas, the problem domain is discretized into 4-node triangular elements and the conventional finite formulations were formulated based on linear shape functions of triangles. It should be noted that only the shape functions and its derivatives were constructed. Secondly, the consecutive shape functions with high-order polynomials were re-formulated based on the average nodal derivatives. Due to the process of formulating the consecutive shape functions, it can be named as a twice-interpolation finite element method. The adjacent nodes of interest element are considered for interpolating the objective variables, which are displacements, strains and stresses, in the CI scheme. Thus, it will increase the smoothness of the obtained solutions. After that, the method was implemented in different element types. For example, the 2D elasticity problems meshed into quadrilateral elements were presented by Bui et al. [13]. For 3D problems, tetrahedral and hexahedral elements can be found in the studies of Nguyen et al. [14, 15].

In this study, the consecutive interpolation scheme over 3D arbitrary star-convex polyhedral elements based on piecewise linear shape functions [16] is implemented

in the analysis of dynamic problems of solid structures. Then, the efficiency of the method will be further investigated.

## 2 Formulations of Consecutive Interpolation Over Arbitrary Star-Convex Polyhedron (CIPFEM)

Let us consider a three-dimensional domain  $\Omega$  with a boundary  $\Gamma = \Gamma_t \cup \Gamma_u$  and  $\Gamma_t \cap \Gamma_u = \emptyset$ . Whereas, the bounded domain  $\Omega$  is divided into a set of  $n$  finite non-overlapping arbitrary polyhedral elements,  $\Omega \approx \Omega^h = \bigcup_1^n \Omega_e$ . The consecutive shape functions and their derivatives based on PFEM at a point of interest  $\mathbf{x}$  are explicitly formulated as follows:

$$N_s(\mathbf{x}) = \sum_{i=1}^{n_e} \left( \varnothing_i(\mathbf{x})L_s^i + \varnothing_{ix}(\mathbf{x})\bar{\bar{L}}_{s,x}^i + \varnothing_{iy}(\mathbf{x})\bar{\bar{L}}_{s,y}^i + \varnothing_{iz}(\mathbf{x})\bar{\bar{L}}_{s,z}^i \right) \quad (1)$$

$$\nabla N_s(\mathbf{x}) = \sum_{i=1}^{n_e} \left( \nabla \varnothing_i(\mathbf{x})L_s^i + \nabla \varnothing_{ix}(\mathbf{x})\bar{\bar{L}}_{s,x}^i + \nabla \varnothing_{iy}(\mathbf{x})\bar{\bar{L}}_{s,y}^i + \nabla \varnothing_{iz}(\mathbf{x})\bar{\bar{L}}_{s,z}^i \right) \quad (2)$$

where  $\varnothing_i(\mathbf{x})$ ,  $\varnothing_{ix}(\mathbf{x})$ ,  $\varnothing_{iy}(\mathbf{x})$  and  $\varnothing_{iz}(\mathbf{x})$  are the auxiliary functions formulated as:

$$\varnothing_i = N_i + N_i^2(\Sigma_1 - N_i) - N_i(\Sigma_2 - N_i^2); i \in \{1, \dots, n_e\} \quad (3)$$

$$\varnothing_{ix} = \sum_{j=1, j \neq i}^{n_e} (x_j - x_i)[N_j N_i^2 + 0.5 N_i N_j(\Sigma_1 - N_i - N_j)]; i \in \{1, \dots, n_e\} \quad (4)$$

where  $x_i$  and  $x_j$  are the  $x$ -coordinate of nodes  $i$  and  $j$  of element containing point of interest  $\mathbf{x}$ , respectively. The formulations of  $\varnothing_{iy}$  and  $\varnothing_{iz}$  are similar to the Eq. (4), in which the  $x$ -coordinates are replaced by  $y$ - and  $z$ -coordinates instead.  $N_i$  is the piecewise linear shape functions (PFEM) of node  $\mathbf{v}_i$  at point of interest  $\mathbf{x}$ .

$\bar{\bar{L}}_{s,x}^i$ ,  $\bar{\bar{L}}_{s,y}^i$  and  $\bar{\bar{L}}_{s,z}^i$  are the average derivatives of each vertex  $\mathbf{v}_s$  based on the  $s$ -node support region  $R_i$ , which is the collection of all polyhedral element connecting to vertex  $\mathbf{v}_i$ , as follows:

$$\bar{\bar{L}}_s^i = \sum_{e \in R_i} W_e \nabla \bar{L}_s^{i[e]} \quad (5)$$

$$\text{and } \nabla \bar{L}_j^{i[s]} = \sum_{s \in S_i} W_k \nabla L_j^{i[s]} \quad (6)$$

with  $S_i$  is the collection of all sub-tetrahedra connecting to vertex  $\mathbf{v}_i$  of interest element.  $W_k$  and  $W_e$  are the weight functions given as

$$W_k = \frac{V_k}{\sum_{\tilde{k} \in S_i} V_{\tilde{k}}}, \text{ with } k \in S_i \text{ and } W_e = \frac{V_e}{\sum_{\tilde{e} \in S_i} V_{\tilde{e}}}, \text{ with } e \in R_i \quad (7)$$

where  $V_k$  and  $V_e$  are the volume of each sub-domain in  $S_i$  and volume of element in  $R_i$ , respectively.  $\mathbf{L} = \mathbf{N}$  is the PFEM shape functions.

The natural frequency of the solid structure is determined based on the equation

$$\mathbf{K}\mathbf{d} + \mathbf{M}\ddot{\mathbf{d}} = 0 \quad (8)$$

where  $\mathbf{d}$  and  $\ddot{\mathbf{d}}$  are the displacement and acceleration fields, respectively.

$\mathbf{K}$  and  $\mathbf{M}$  are the stiffness matrix and mass matrix of the problem's domains formulating by using CI shape functions as follows

$$\mathbf{K} = \mathbf{K}_{ij} = \begin{bmatrix} \int_{\Omega} \mathbf{B}_1^T \mathbf{D} \mathbf{B}_1 d\Omega & \int_{\Omega} \mathbf{B}_1^T \mathbf{D} \mathbf{B}_2 d\Omega & \dots & \int_{\Omega} \mathbf{B}_1^T \mathbf{D} \mathbf{B}_n d\Omega \\ \int_{\Omega} \mathbf{B}_2^T \mathbf{D} \mathbf{B}_1 d\Omega & \int_{\Omega} \mathbf{B}_2^T \mathbf{D} \mathbf{B}_2 d\Omega & \dots & \int_{\Omega} \mathbf{B}_2^T \mathbf{D} \mathbf{B}_n d\Omega \\ \vdots & \vdots & \ddots & \vdots \\ \int_{\Omega} \mathbf{B}_n^T \mathbf{D} \mathbf{B}_1 d\Omega & \int_{\Omega} \mathbf{B}_n^T \mathbf{D} \mathbf{B}_2 d\Omega & \dots & \int_{\Omega} \mathbf{B}_n^T \mathbf{D} \mathbf{B}_n d\Omega \end{bmatrix} \quad (9)$$

$$\text{and } \mathbf{M} = \mathbf{M}_{ij} = \begin{bmatrix} \int_{\Omega} \mathbf{N}_1^T \rho \mathbf{N}_1 d\Omega & \int_{\Omega} \mathbf{N}_1^T \rho \mathbf{N}_2 d\Omega & \dots & \int_{\Omega} \mathbf{N}_1^T \rho \mathbf{N}_n d\Omega \\ \int_{\Omega} \mathbf{N}_2^T \rho \mathbf{N}_1 d\Omega & \int_{\Omega} \mathbf{N}_2^T \rho \mathbf{N}_2 d\Omega & \dots & \int_{\Omega} \mathbf{N}_2^T \rho \mathbf{N}_n d\Omega \\ \vdots & \vdots & \ddots & \vdots \\ \int_{\Omega} \mathbf{N}_n^T \rho \mathbf{N}_1 d\Omega & \int_{\Omega} \mathbf{N}_n^T \rho \mathbf{N}_2 d\Omega & \dots & \int_{\Omega} \mathbf{N}_n^T \rho \mathbf{N}_n d\Omega \end{bmatrix} \quad (10)$$

with  $\mathbf{B}$  is the transformation matrix and  $\mathbf{N}$  is the matrix of CI shape functions.

### 3 Numerical Analysis

The dynamic analysis of the CIPFEM is performed for an experimental complex cantilever step-beam. The first three natural frequencies of the beam are predicted by present method and, then, they are compared to those of PFEM [11, 17], T4, ANSYS, empirical data [18] and CT4. The coding is performed on the MATLAB program. The dimensions of the cantilever step-beam are 463.55 mm in length and 3.175 mm in width. The beam is made of aluminium with Young's modulus  $E = 60.6$  GPa, density  $\rho = 2664$  kg/m<sup>3</sup> and Poisson's ratio  $\nu = 0.3$ .

Various mesh types are used, which are shown in Fig. 1. Whereas, tetrahedral elements are used for T4 and CT4 methods. Structured and unstructured polyhedral

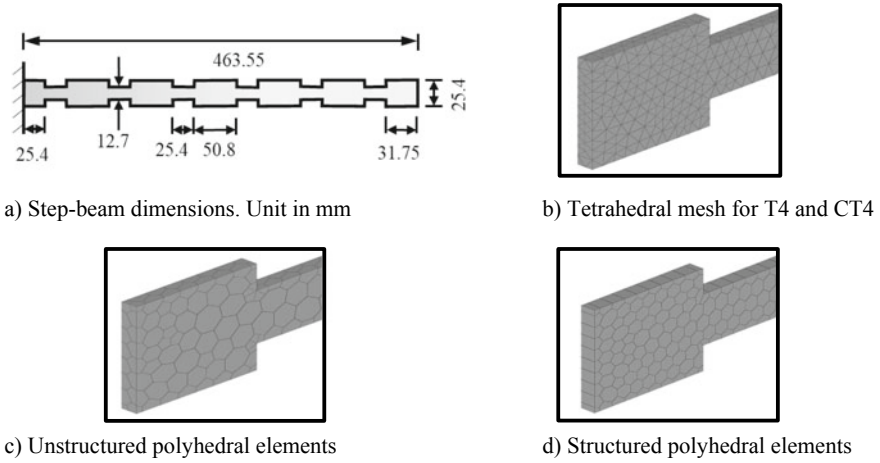


**Fig. 1** Illustrations of step-beam and meshes used for numerical analysis

elements are for PFEM and CIPFEM. Table 1 presents the meshes used for numerical investigation, in which  $h$  (mm) is the average element size of the mesh. In the table, the solutions of mode 1 natural frequency obtained by numerical approaches are compared to that of empirical results. As it can be observed that the errors in percentage of the first mode frequency predicted by present CIPFEM for the coarsest mesh are respectively 7.5 and 1.5% corresponding to structured and unstructured polyhedral meshes, respectively. While CT4 produces 22.1% error, and for predictions of PFEM and T4, those values are orderly 35.9, 45.4 and 89.9%. In the second mesh, those errors of CIPFEM frequency reduce to 0.5 and 0.0%. The data shows that the predictions of CIPFEM in terms of mode 1 natural frequency of the complex step-beam are converged with a very coarse mesh, which is superior to CT4 that reaches convergence at the third mesh. Additionally, the results obtained by CIPFEM are far more accurate than conventional PFEM and T4 due to the higher order of CI shape

**Table 1** Details of mesh resolutions and errors in percentage of mode 1 natural frequency of results obtained by numerical approaches compared to empirical results

Structured polyhedral mesh		CIPFEM-S	Unstructured polyhedral mesh		CIPFEM-U	Tetrahedral mesh		CT4
No. of Ele.	$h$	$f$ (Hz)	No. of Ele.	$h$	$f$ (Hz)	No. of Ele.	$h$	$f$ (Hz)
1396	4.8	11.4	1876	4.8	10.8	5793	4.7	13.0
2920	3.8	10.6	3317	3.5	10.6	13,966	3.5	11.5
7500	2.8	10.5	7961	2.7	10.5	25,052	2.8	10.7
13,989	2.2	10.5	12,768	2.2	10.5	43,347	2.3	10.6

\* The empirical frequency of mode 1 is  $f_1 = 10.63$  Hz



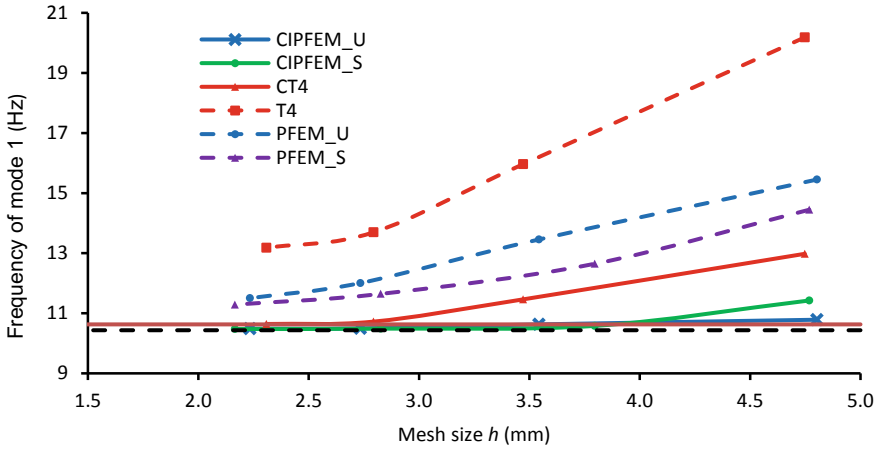


**Fig. 2** Convergence graph of the first natural frequency using various numerical approaches

functions. Figure 2 illustrates the data of first mode frequency in Table 1, which shows the convergence trend with respect to element size  $h$ . Herein, the visible comparison of the obtained mode 1 frequency is carried out for various numerical methods. As it can be seen that, the results of CIPFEM for structured mesh are similar to those of unstructured mesh, which shows the present CIPFEM is not sensitive to the distortion of the mesh and it can work well for various mesh types as long as the elements are star-convex. As expected, after convergence, the frequencies of CIPFEM are reaching the reference ones, which are the solution of ANSYS. There is a small gap (1.8%) between ANSYS and experimental results because the real beam cannot be exactly numerically modelled. There is always an error due to constructing activity, non-homogeneity of material, etc. The second meshes of all the studied cases are used for further investigation of the natural frequencies of the first three modes, which are shown in Table 2. The table also shows the differences in percentage between values of corresponding methods and experimental data. As it can be seen, 0.8% is the maximum deviation of CIPFEM's results, while that difference of CT4 is 8.2%.

Shortly, in this numerical example, the natural frequencies of the first 3 modes of an experimental step-beam are used to evaluate the present CIPFEM. It can be concluded that the CIPFEM can be used effectively to predict the natural frequencies

**Table 2** Comparison of natural frequencies between experimental data, CIPFEM and CT4

Mode	Exp	CIPFEM_S		CIPFEM_U		CT4	
	$f$ (Hz)	$f$ (Hz)	Error (%)	$f$ (Hz)	Error (%)	$f$ (Hz)	Error (%)
$m_{1l}$	10.6	10.6	0.5	10.6	0.0	11.5	7.8
$m_{2l}$	66.8	66.5	0.4	66.7	0.0	72.2	8.2
$m_{1b}$	49.4	50.0	1.2	49.8	0.8	50.3	1.8

of dynamic problems. The solutions of CIPFEM reach the exact values with very coarse mesh compared to CT4, PFEM and T4. Additionally, the method can be applied for various element types as long as they are arbitrary star-convex polyhedral elements, which include 4-node tetrahedral elements.

## 4 Conclusion

This article presents the implementation of CIPFEM in dynamic analysis of three-dimensional solid structures. The MATLAB program is used to compile the studied method. The empirical natural frequencies of a cantilever step-beam were used to evaluate those values approximated by CIPFEM. Some conclusions are derived as following:

- With the same mesh size, the CIPFEM gives more accurate results than CT4, PFEM and conventional FEM using linear tetrahedral elements (T4). Therefore, the CIPFEM can be used effectively for dynamic problems of three-dimensional solid structures.
- The CIPFEM can be applied for various element types, which is a great advantage for complex structures meshing into arbitrary star-convex elements.

**Acknowledgements** The authors acknowledge the financial support of VLIR-UOS TEAM Project, VLIRUOS2017-2021 – 75900, funded by the Flemish Government.



## References

1. Wachspress EL (1975) A rational finite element basis. Academic Press, New York
2. Ghosh S, Moorthy S (2004) Three dimensional Voronoi cell finite element model for microstructures with ellipsoidal heterogeneties. *Comput Mech* 34(6):510–531
3. Dohrmann CR, Key SW, Heinstejn MW (2000) A method for connecting dissimilar finite element meshes in three dimensions. *Int J Numer Meth Eng* 48(5):655–678
4. Diaz AR, Bénard A (2003) Designing materials with prescribed elastic properties using polygonal cells. *Int J Numer Meth Eng* 57(3):301–314
5. Talischi C, Paulino GH, Pereira A, Menezes IFM (2012) PolyMesher: a general-purpose mesh generator for polygonal elements written in Matlab. *Struct Multidiscip Optim* 45(3):309–328
6. Nguyen-Xuan H (2017) A polygonal finite element method for plate analysis. *Comput Struct* 188:45–62
7. Pereira A, Talischi C, Paulino GH, Menezes IFM, Carvalho MS (2016) Fluid flow topology optimization in PolyTop: stability and computational implementation. *Struct Multidiscip Optim* 54(5):1345–1364

8. Tiwary A, Hu C, Ghosh S (2007) Numerical conformal mapping method based Voronoi cell finite element model for analyzing microstructures with irregular heterogeneities. *Finite Elem Anal Des* 43:504–520
9. Floater MS, Kós G, Reimers M (2005) Mean value coordinates in 3D. *Comput Aided Geom Des* 22:623–631
10. Bishop JE (2014) A displacement-based finite element formulation for general polyhedra using harmonic shape functions. *Int J Numer Meth Eng* 97(1):1–31
11. Nguyen-Ngoc H, Phung-Van P, Dang B-L, Nguyen-Xuan H, Abdel Wahab M (2019) Static and dynamic analyses of three-dimensional hollow concrete block revetments using polyhedral finite element method. *Appl Ocean Res* 88:15–28
12. Zheng C, Wu SC, Tang XH, Zhang JH (2010) A novel twice-interpolation finite element method for solid mechanics problems. *Acta Mech Sin/Lixue Xuebao* 26(2):265–278
13. Bui TQ, Vo DQ, Zhang C, Nguyen DD (2014) A consecutive-interpolation quadrilateral element (CQ4): Formulation and applications. *Finite Elem Anal Des* 84:14–31
14. Nguyen MN, Bui TQ, Truong TT, Trinh NA, Singh IV, Yu T, Doan DH (2016) Enhanced nodal gradient 3D consecutive-interpolation tetrahedral element (CTH4) for heat transfer analysis. *Int J Heat Mass Transf* 103:14–27
15. Nguyen MN, Bui TQ, Truong TT, Tanaka S, Hirose S (2017) Numerical analysis of 3-D solids and composite structures by an enhanced 8-node hexahedral element. *Finite Elem Anal Des* 131:1–16
16. Nguyen-Ngoc H, Nguyen CK, Nguyen DK, Nguyen-Xuan H, Abdel-Wahab M (2021) A consecutive-interpolation polyhedral finite element method for solid structures. *Int J Numer Methods Eng*
17. Nguyen-Ngoc H, Nguyen-Xuan H, Abdel-Wahab M (2020) A numerical investigation on the use of pervious concrete for seawall structures. *Ocean Eng* 198:106954
18. Jaworski JW, Dowell EH (2008) Free vibration of a cantilevered beam with multiple steps: comparison of several theoretical methods with experiment. *J Sound Vib* 312(4–5):713–725

# Study of Forced Vibrations of a Two-Layer Plate Under Harmonic Load



Vitaly N. Paimushin, Vyacheslav A. Firsov, Victor M. Shishkin,  
and Ruslan K. Gazizullin

**Abstract** We propose a technique for the numerical study of the dynamic response under forced harmonic vibrations of a rectangular two-layer plate consisting of a main rigid layer and a low-rigid damping layer. The material of the rigid layer is considered to be isotropic and perfectly elastic. The dynamic deformation of the damping layer material is described by linear physical equations of a viscoelastic solid, which represent a generalization of the Kelvin-Voigt hypothesis for the case of a complex stress state. It is believed that a plate with a damping layer deforms according to the classical Kirchhoff-Love hypotheses. A rectangular two-layer finite element with twenty degrees of freedom has been developed to model the inertial, stiffness and damping properties of the plate layers. A system of differential motion equations of a finite element model of the plate under harmonic load is obtained. A solution of the resulting system is sought in the form of decomposition of nodal displacement vector of the finite-element model according to eigenforms, which leads to a system of equations of a significantly smaller order relative to the vector of modal coordinates of the plate. Numerical experiments were carried out to determine the dynamic response of a rectangular hingedly supported two-layer plate under the action of a surface harmonic load with a frequency varying from zero to 200 Hz for the cases with and without taking into account the damping properties of the viscoelastic layer material. The plate was divided into 144 elements (12 elements

---

V. N. Paimushin (✉) · V. A. Firsov · R. K. Gazizullin  
Kazan National Research Technical University named after A. N. Tupolev – KAI, Kazan, Russia  
e-mail: [vpajmushin@mail.ru](mailto:vpajmushin@mail.ru)

V. A. Firsov  
e-mail: [vafirsov\\_49@mail.ru](mailto:vafirsov_49@mail.ru)

R. K. Gazizullin  
e-mail: [gazizullin.rk@yandex.ru](mailto:gazizullin.rk@yandex.ru)

V. N. Paimushin  
Kazan (Volga region) Federal University, Kazan, Russia

V. M. Shishkin  
Vyatka State University, Kirov, Russia  
e-mail: [tism1@rambler.ru](mailto:tism1@rambler.ru)

in the direction of each side). It is shown that taking into account of the damping properties significantly limits the vibration amplitudes and dynamic stress of the plate only under vibrations in the resonance zone. At the same time, far from this zone the damping properties of the material can be practically ignored. It is noted that in the case of the uniform harmonic pressure applied over the whole area of the plate, the resonance oscillations are excited only at those frequencies which correspond to the eigenforms with an odd number of half-waves in the direction of each side of the plate. To determine the lower part of the spectrum of eigenforms and frequencies the subspace iteration method has been used.

## 1 Introduction

Modern thin-walled structures have a rather dense spectrum of natural frequencies and can operate under a wide frequency range of disturbing forces. This fact complicates the use of traditional methods of detuning from resonance and application of various kinds of damping devices. This is especially true for aircraft designs, where the use of such methods and devices is practically excluded. Hence, the ability of the structure itself to damp dangerous resonant vibrations, preventing the occurrence of significant displacements and overloads, becomes crucial. However, it should be noted that the majority of structural materials (such as metals, alloys and composites) along with their high strength and stiffness have a very low damping capacity [1]. Moreover, for many structures the main cause of energy dissipation under resonance is friction in the joints of their individual elements (structural damping), which is a difficult to predict factor. Therefore, in order to increase the damping parameters and to reduce the dynamic stress of thin-walled structures, their elements are often made as a two-layer structures which consist in thickness of a rigid durable layer and a relatively low-rigid coating with high damping properties. Such elements as a way to reduce overloads are currently widespread in aircraft shipbuilding, automotive and civil construction [2]. Various elastomers, mastics and polymeric compounds are used as damping coatings.

The aim of this work is a numerical study of the forced vibrations of a rectangular plate with a viscoelastic damping layer under a harmonic load varying over a wide frequency range (including resonance) based on the finite element method. This study makes it possible to evaluate the effect of the damping properties of the viscoelastic layer on the dynamic stress of the plate over the entire range of specified frequencies.

## 2 Rectangular Finite Element with Viscoelastic Damping Coating

The element consists of two layers (Fig. 1): a rigid isotropic layer 1 and a low-rigid damping layer 2 (Fig. 1a). The element is under the action of a surface dynamic load  $q(x, y, t)$ . Since the viscoelastic damping layer is low-rigid, it can be assumed that

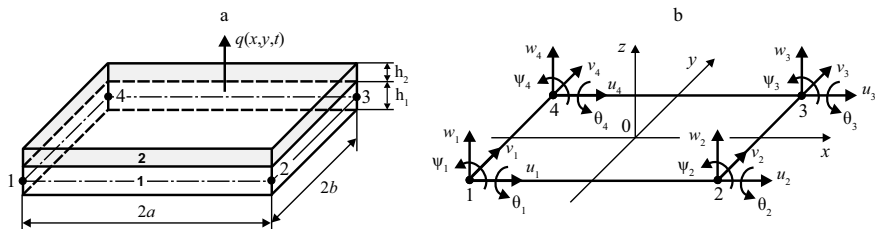


Fig. 1 Rectangular finite element of a two-layer plate

the element is deformed according to the classical Kirchhoff–Love hypotheses. The nodes of the element are located on the middle surface of layer 1. Each node  $i$  ( $i = 1, 2, 3, 4$ ) has five degrees of freedom (Fig. 1b): deflection  $w_i$ ; displacements  $u_i, v_i$  in the plane  $Oxy$  and angles  $\theta_i, \psi_i$  of rotation about the axes  $Ox, Oy$ , respectively.

Let us introduce vectors

$$\mathbf{u} = \begin{Bmatrix} u_1 \\ u_2 \\ u_3 \\ u_4 \end{Bmatrix}, \quad \mathbf{v} = \begin{Bmatrix} v_1 \\ v_2 \\ v_3 \\ v_4 \end{Bmatrix}, \quad \mathbf{w} = \begin{Bmatrix} w_1 \\ w_2 \\ w_3 \\ w_4 \end{Bmatrix}, \quad \boldsymbol{\theta} = \begin{Bmatrix} \theta_1 \\ \theta_2 \\ \theta_3 \\ \theta_4 \end{Bmatrix}, \quad \boldsymbol{\psi} = \begin{Bmatrix} \psi_1 \\ \psi_2 \\ \psi_3 \\ \psi_4 \end{Bmatrix}.$$

The displacements  $u, v$  of an arbitrary point of the middle surface of an element are represented by the expressions

$$u = \mathbf{S}\mathbf{u}, \quad v = \mathbf{S}\mathbf{v}, \quad (1)$$

where  $\mathbf{S}$  is the row matrix of basis functions  $H_i$  ( $i = 1, 2, 3, 4$ ) depending on the dimensionless coordinates  $\xi = x/a$  and  $\eta = y/b$  of the element:

$$H_1 = (1 - \xi)(1 - \eta)/4; \quad H_2 = (1 + \xi)(1 - \eta)/4; \\ H_3 = (1 + \xi)(1 + \eta)/4; \quad H_4 = (1 - \xi)(1 + \eta)/4.$$

Dependencies (1) can be represented as a single matrix expression

$$\begin{Bmatrix} u \\ v \end{Bmatrix} = \mathbf{H}\mathbf{r}_\alpha, \quad (2)$$

where

$$\mathbf{H} = \begin{bmatrix} H_1 & 0 & H_2 & 0 & H_3 & 0 & H_4 & 0 \\ 0 & H_1 & 0 & H_2 & 0 & H_3 & 0 & H_4 \end{bmatrix}; \quad \mathbf{r}_\alpha = \{u_1 \ v_1 \ u_2 \ v_2 \ u_3 \ v_3 \ u_4 \ v_4\}.$$

To reproduce the bending state of the plate, we define the deflection  $w$  in the form

$$\begin{aligned} w &= \mathbf{f}^T \mathbf{c}, \\ \mathbf{f} &= \{1 \ x \ y \ x^2 \ y^2 \ xy \ x^2y \ xy^2 \ x^3 \ y^3 \ x^3y \ xy^3\}, \\ \mathbf{c} &= \{c_0 \ c_1 \ c_2 \ c_3 \ c_4 \ c_5 \ c_6 \ c_7 \ c_8 \ c_9 \ c_{10} \ c_{11}\}. \end{aligned} \quad (3)$$

According to the accepted hypotheses, the angles of rotation of the plate cross sections with  $x$  and  $y$  coordinates are defined by expressions

$$\theta = \frac{\partial w}{\partial y} = \frac{\partial \mathbf{f}^T}{\partial y} \mathbf{c}, \quad \psi = \frac{\partial w}{\partial x} = \frac{\partial \mathbf{f}^T}{\partial x} \mathbf{c}. \quad (4)$$

Element nodes have coordinates  $x_1 = -a$ ,  $y_1 = -b$ ,  $x_2 = a$ ,  $y_2 = -b$ ,  $x_3 = a$ ,  $y_3 = b$ ,  $x_4 = -a$ ,  $y_4 = b$ . Substituting these coordinates into expressions (3) and (4), we obtain a system of twelve linear algebraic equations

$$\mathbf{A} \mathbf{c} = \mathbf{r}_\beta \quad (5)$$

with a matrix  $\mathbf{A}$  depending on the coordinates of the element's nodes and the right-hand side  $\mathbf{r}_\beta = \{w_1 \ \psi_1 \ \theta_1 \ w_2 \ \psi_2 \ \theta_2 \ w_3 \ \psi_3 \ \theta_3 \ w_4 \ \psi_4 \ \theta_4\}$ . After finding the vector  $\mathbf{c}$  from system (5) and its substitution in approximation (3), we come to the expression

$$w = \mathbf{f}^T \mathbf{A}^{-1} \mathbf{r}_\beta,$$

From here, we can find the basis functions that determine the relationship between the deflection  $w$  and the components of the finite element vector  $\mathbf{r}_\beta$ :

$$N_j = \mathbf{f}^T \mathbf{A}_j \quad (j = 1, 2, \dots, 12).$$

Here  $\mathbf{A}_j$  are the  $j$ -th columns of the matrix  $\mathbf{A}^{-1}$ , which is inverse to the matrix  $\mathbf{A}$ .

However, it should be noted that the procedure for analytical inversion of the matrix  $\mathbf{A}$  using traditional (manual) technologies is practically unrealistic. The solution to the problem can be found in the application of symbolic calculation mode of the mathematical package MATLAB [3], which makes it possible to quickly find the functions  $N_j$ :

$$\begin{aligned}
N_1 &= (2 - 3\xi - 3\eta + 4\xi\eta + \xi^3 + \eta^3 - \xi^3\eta - \xi\eta^3)/8, \\
N_2 &= a(1 - \xi - \eta - \xi^2 + \xi\eta + \xi^2\eta + \xi^3 - \xi^3\eta)/8, \\
N_3 &= b(1 - \xi - \eta - \eta^2 + \xi\eta + \xi\eta^2 + \eta^3 - \xi\eta^3)/8, \\
N_4 &= (2 + 3\xi - 3\eta - 4\xi\eta - \xi^3 + \eta^3 + \xi^3\eta + \xi\eta^3)/8, \\
N_5 &= a(-1 - \xi + \eta + \xi^2 + \xi\eta - \xi^2\eta + \xi^3 - \xi^3\eta)/8, \\
N_6 &= b(1 + \xi - \eta - \eta^2 - \xi\eta - \xi\eta^2 + \eta^3 + \xi\eta^3)/8, \\
N_7 &= (2 + 3\xi + 3\eta + 4\xi\eta - \xi^3 - \eta^3 - \xi^3\eta - \xi\eta^3)/8, \\
N_8 &= a(-1 - \xi - \eta + \xi^2 - \xi\eta + \xi^2\eta + \xi^3 + \xi^3\eta)/8, \\
N_9 &= b(-1 - \xi - \eta + \eta^2 - \xi\eta + \xi\eta^2 + \eta^3 + \xi\eta^3)/8, \\
N_{10} &= (2 - 3\xi + 3\eta - 4\xi\eta + \xi^3 - \eta^3 + \xi^3\eta + \xi\eta^3)/8, \\
N_{11} &= a(1 - \xi + \eta - \xi^2 - \xi\eta - \xi^2\eta + \xi^3 + \xi^3\eta)/8, \\
N_{12} &= b(-1 + \xi - \eta + \eta^2 + \xi\eta - \xi\eta^2 + \eta^3 - \xi\eta^3)/8
\end{aligned}$$

Having functions  $N_j$ , the deflection  $w$  can be represented as

$$w = \mathbf{N}\mathbf{r}_\beta = [N_1|N_2|\dots|N_{12}]\mathbf{r}_\beta \quad (6)$$

According to the Kirchhoff–Love hypotheses, it can be assumed that each layer of the plate is in a plane stress state with normal stresses  $\sigma_x$ ,  $\sigma_y$  and shear stress  $\tau_{xy}$ . These stresses correspond to linear strain  $\varepsilon_x$ ,  $\varepsilon_y$  and shear angle  $\gamma_{xy}$  determined by geometric relationships

$$\begin{aligned}
\varepsilon_x &= \frac{\partial}{\partial x} \left( u - z \frac{\partial w}{\partial x} \right) = \frac{\partial u}{\partial x} - z \frac{\partial^2 w}{\partial x^2}, \quad \varepsilon_y = \frac{\partial}{\partial y} \left( v - z \frac{\partial w}{\partial y} \right) = \frac{\partial v}{\partial y} - z \frac{\partial^2 w}{\partial y^2}, \\
\gamma_{xy} &= \frac{\partial}{\partial x} \left( v - z \frac{\partial w}{\partial y} \right) + \frac{\partial}{\partial y} \left( u - z \frac{\partial w}{\partial x} \right) = \frac{\partial v}{\partial x} + \frac{\partial u}{\partial y} - 2z \frac{\partial^2 w}{\partial x \partial y}.
\end{aligned}$$

The  $z$  coordinate for layer 1 varies within the limits  $-h_1/2 \leq z \leq h_1/2$ , for layer 2 within the limits  $h_1/2 \leq z \leq h_1/2 + h_2$ . It is convenient to write the presented dependencies in dimensionless coordinates  $\xi$  and  $\eta$  of the element:

$$\begin{aligned}
\varepsilon_x &= \frac{1}{a} \frac{\partial u}{\partial \xi} - z \frac{1}{a^2} \frac{\partial^2 w}{\partial \xi^2}; \quad \varepsilon_y = \frac{1}{b} \frac{\partial v}{\partial \eta} - z \frac{1}{b^2} \frac{\partial^2 w}{\partial \eta^2}; \\
\gamma_{xy} &= \frac{1}{a} \frac{\partial v}{\partial \xi} + \frac{1}{b} \frac{\partial u}{\partial \eta} - \frac{2z}{ab} \frac{\partial^2 w}{\partial \xi \partial \eta}.
\end{aligned} \quad (7)$$

Let us introduce the vector  $\boldsymbol{\varepsilon} = \{\varepsilon_x \ \varepsilon_y \ \gamma_{xy}\}$  and differentiating operators

$$\mathbf{A}_\alpha^T = \left[ \begin{array}{c|c|c} \frac{1}{a} \frac{\partial}{\partial \xi} & 0 & \frac{1}{b} \frac{\partial}{\partial \eta} \\ \hline 0 & \frac{1}{b} \frac{\partial}{\partial \eta} & \frac{1}{a} \frac{\partial}{\partial \xi} \end{array} \right], \quad \mathbf{A}_\beta^T = \left[ \begin{array}{c|c|c} \frac{1}{a^2} \frac{\partial^2}{\partial \xi^2} & \frac{1}{b^2} \frac{\partial^2}{\partial \eta^2} & \frac{2}{ab} \frac{\partial^2}{\partial \xi \partial \eta} \end{array} \right].$$



Then dependences (7) can be represented as a single matrix expression

$$\boldsymbol{\varepsilon} = \mathbf{A}_\alpha \begin{Bmatrix} u \\ v \end{Bmatrix} - z \mathbf{A}_\beta w. \quad (8)$$

Substituting then representations (8) and (2) into (6), we obtain the connection between strains and nodal displacements of the finite element:

$$\boldsymbol{\varepsilon} = \mathbf{A}_\alpha \mathbf{H} \mathbf{r}_\alpha - z \mathbf{A}_\beta \mathbf{N} \mathbf{r}_\beta.$$

The resulting expression can be represented as

$$\boldsymbol{\varepsilon} = \mathbf{B}_\alpha \mathbf{r}_\alpha - z \mathbf{B}_\beta \mathbf{r}_\beta, \quad (9)$$

where

$$\mathbf{B}_\alpha = \mathbf{A}_\alpha \mathbf{H} = [\mathbf{B}_{\alpha,1} | \mathbf{B}_{\alpha,2} | \mathbf{B}_{\alpha,3} | \mathbf{B}_{\alpha,4}], \quad \mathbf{B}_\beta = \mathbf{A}_\beta \mathbf{N} = [\mathbf{B}_{\beta,1} | \mathbf{B}_{\beta,2} | \dots | \mathbf{B}_{\beta,12}].$$

Blocks  $\mathbf{B}_{\alpha,i}$  ( $i = 1, 2, 3, 4$ ) and  $\mathbf{B}_{\beta,j}$  ( $j = 1, 2, \dots, 12$ ) are defined by expressions

$$\mathbf{B}_{\alpha,i}^T = \begin{bmatrix} \frac{1}{a} \frac{\partial H_i}{\partial \xi} & 0 & \frac{1}{b} \frac{\partial H_i}{\partial \eta} \\ 0 & \frac{1}{b} \frac{\partial H_i}{\partial \eta} & \frac{1}{a} \frac{\partial H_i}{\partial \xi} \end{bmatrix}, \quad \mathbf{B}_{\beta,j}^T = \begin{bmatrix} \frac{1}{a^2} \frac{\partial^2 N_j}{\partial \xi^2} & \frac{1}{b^2} \frac{\partial^2 N_j}{\partial \eta^2} & \frac{2}{ab} \frac{\partial^2 N_j}{\partial x_i \partial \eta} \end{bmatrix}. \quad (10)$$

The material of the rigid and damping layers of the plate is considered as isotropic. To take into account the material elastic and damping properties, linear physical dependences can be used

$$\boldsymbol{\sigma}_k = \mathbf{D}_k \boldsymbol{\varepsilon} + \mathbf{D}_{g,k} \dot{\boldsymbol{\varepsilon}}. \quad (11)$$

These dependences represent a generalization of the Kelvin–Voigt model [4, 5] for the case of the material complex stress state. Here  $\boldsymbol{\sigma}_k = \{\sigma_x \ \sigma_y \ \tau_{xy}\}_k$  ( $k = 1, 2$ ) are stresses  $k$ -th layer of the plate;  $\mathbf{D}_k$ ,  $\mathbf{D}_{g,k}$  are the stiffness matrix and the damping matrix of the material of this layer, respectively. For an isotropic viscoelastic material in a plane stressed state, the matrices  $\mathbf{D}_k$  and  $\mathbf{D}_{g,k}$  will be of the following form [6]:

$$\mathbf{D}_k = \begin{bmatrix} E_k/(1 - \nu_k^2) & E_k \nu_k/(1 - \nu_k^2) & 0 \\ E_k \nu_k/(1 - \nu_k^2) & E_k/(1 - \nu_k^2) & 0 \\ 0 & 0 & G_k \end{bmatrix};$$

$$\mathbf{D}_{g,k} = \frac{1}{\pi \omega} \begin{bmatrix} E_k \delta_{\varepsilon,k}/(1 - \nu_k^2) & E_k \delta_{\varepsilon,k} \nu_k/(1 - \nu_k^2) & 0 \\ E_k \delta_{\varepsilon,k} \nu_k/(1 - \nu_k^2) & E_k \delta_{\varepsilon,k}/(1 - \nu_k^2) & 0 \\ 0 & 0 & \delta_{\gamma,k} G_k \end{bmatrix}.$$

Here  $E_k$ ,  $G_k$ ,  $\delta_{\varepsilon,k}$ ,  $\delta_{\gamma,k}$  are elastic moduli and logarithmic decrements of vibrations of the layers' material under tension-compression and shear;  $\nu_k$  are Poisson's ratios;  $\omega$  is

the circular frequency of material deformation. Taking into account (9), dependences (11) are obtained as follows:

$$\boldsymbol{\sigma}_k = \mathbf{D}_k(\mathbf{B}_\alpha \mathbf{r}_\alpha - z \mathbf{B}_\beta \mathbf{r}_\beta) + \mathbf{D}_{g,k}(\mathbf{B}_\alpha \dot{\mathbf{r}}_\alpha - z \mathbf{B}_\beta \dot{\mathbf{r}}_\beta). \quad (12)$$

The first summand in (12) represents the elastic part of the stresses, which linearly depends on the nodal displacements  $\mathbf{r}_\alpha$  and  $\mathbf{r}_\beta$  of the element, the second summand is the inelastic part arising from the damping properties of the material and linearly depending on the nodal velocities  $\dot{\mathbf{r}}_\alpha$  and  $\dot{\mathbf{r}}_\beta$ .

Let us write down the virtual work of the elastic part of the stresses in the rigid layer of the plate on the virtual strain  $\delta \boldsymbol{\varepsilon}$  of this layer:

$$\delta A_1 = - \int_{-h_1/2}^{h_1/2} \int_{-a}^a \int_{-b}^b \delta \boldsymbol{\varepsilon}^T \mathbf{D}_1 (\mathbf{B}_\alpha \mathbf{r}_\alpha - z \mathbf{B}_\beta \mathbf{r}_\beta) dx dy dz.$$

Substituting here relation (9), we obtain

$$\delta A_1 = - \int_{-h_1/2}^{h_1/2} \int_{-a}^a \int_{-b}^b (\delta \mathbf{r}_\alpha^T \mathbf{B}_\alpha^T - z \delta \mathbf{r}_\beta^T \mathbf{B}_\beta^T) \mathbf{D}_1 (\mathbf{B}_\alpha \mathbf{r}_\alpha - z \mathbf{B}_\beta \mathbf{r}_\beta) dx dy dz.$$

After integration over the  $z$  coordinate, the last expression takes the form

$$\delta A_1 = -h_1 \delta \mathbf{r}_\alpha^T \int_{-a}^a \int_{-b}^b \mathbf{B}_\alpha^T \mathbf{D}_1 \mathbf{B}_\alpha dx dy \mathbf{r}_\alpha - \frac{h_1^3}{12} \delta \mathbf{r}_\beta^T \int_{-a}^a \int_{-b}^b \mathbf{B}_\beta^T \mathbf{D}_1 \mathbf{B}_\beta dx dy \mathbf{r}_\beta. \quad (13)$$

Let us introduce a vector  $\mathbf{r}^{(e)} = \{\mathbf{r}_\alpha \ \mathbf{r}_\beta\}$  containing all nodal displacements of the finite element. Taking into account this vector, expression (13) can be reduced to the form

$$\delta A_1 = -\delta(\mathbf{r}^{(e)})^T \mathbf{K}_1 \mathbf{r}^{(e)}$$

where  $\mathbf{K}_1$  is the block-diagonal matrix representing the contribution of layer 1 to the stiffness matrix of the finite element:

$$\mathbf{K}_1 = \left[ \begin{array}{c|c} \mathbf{K}_{\alpha\alpha,1} & \mathbf{0} \\ \hline \mathbf{0} & \mathbf{K}_{\beta\beta,1} \end{array} \right].$$

Blocks  $\mathbf{K}_{\alpha\alpha,1}$  and  $\mathbf{K}_{\beta\beta,1}$  defined by expressions

$$\mathbf{K}_{\alpha\alpha,1} = h_1 \int_{-a}^a \int_{-b}^b \mathbf{B}_\alpha^T \mathbf{D}_1 \mathbf{B}_\alpha dx dy = h_1 ab \int_{-1}^1 \int_{-1}^1 \mathbf{B}_\alpha^T \mathbf{D}_1 \mathbf{B}_\alpha d\xi d\eta, \quad (14)$$

$$\mathbf{K}_{\beta\beta,1} = \frac{h_1^3}{12} \int_{-a}^a \int_{-b}^b \mathbf{B}_\beta^T \mathbf{D}_1 \mathbf{B}_\beta dx dy = \frac{h_1^3}{12} ab \int_{-1}^1 \int_{-1}^1 \mathbf{B}_\beta^T \mathbf{D}_1 \mathbf{B}_\beta d\xi d\eta. \quad (15)$$

From expressions (10) it follows that the product  $\mathbf{B}_\alpha^T \mathbf{D}_1 \mathbf{B}_\alpha$  quadratically depends on the dimensionless coordinates  $\xi$  and  $\eta$  of the element. In this case, the Gaussian formula [7] with two points in each coordinate direction can be used to calculate the integral in (14) accurately.

$$\int_{-1}^1 \int_{-1}^1 \mathbf{B}_\alpha^T \mathbf{D}_1 \mathbf{B}_\alpha d\xi d\eta = \sum_{m=1}^2 \sum_{n=1}^2 \mathbf{B}_\alpha^T(\xi_m, \eta_n) \mathbf{D}_1 \mathbf{B}_\alpha(\xi_m, \eta_n) Q_m P_n, \quad (16)$$

where  $\xi_1 = \eta_1 = -0.57735$  and  $\xi_2 = \eta_2 = 0.57735$  are coordinates of Gaussian points;  $Q_1 = Q_2 = P_1 = P_2 = 1$  are weight factors. In the product  $\mathbf{B}_\beta^T \mathbf{D}_1 \mathbf{B}_\beta$ , the largest sum of the degrees of coordinates  $\xi$  and  $\eta$ , as again follows from (10), is equal to four. Therefore, to accurately calculate the integral in (15), it is necessary to take the Gaussian quadrature with three points along each of the element coordinates  $\xi$  and  $\eta$ :

$$\int_{-1}^1 \int_{-1}^1 \mathbf{B}_\beta^T \mathbf{D}_1 \mathbf{B}_\beta d\xi d\eta = \sum_{m=1}^3 \sum_{n=1}^3 \mathbf{B}_\beta^T(\xi_m, \eta_n) \mathbf{D}_1 \mathbf{B}_\beta(\xi_m, \eta_n) Q_m P_n, \quad (17)$$

$\xi_1 = \eta_1 = -0.77460$ ;  $\xi_2 = \eta_2 = 0$ ;  $\xi_3 = \eta_3 = 0.77460$ ;  $Q_2 = P_2 = 0.88888$ ;  $Q_1 = Q_3 = P_1 = P_3 = 0.55555$ .

Similarly, the contribution to the stiffness matrix of the element of the second (damping) layer is obtained:

$$\mathbf{K}_2 = \begin{bmatrix} \mathbf{K}_{\alpha\alpha,2} & \mathbf{K}_{\alpha\beta,2} \\ \mathbf{K}_{\alpha\beta,2}^T & \mathbf{K}_{\beta\beta,2} \end{bmatrix};$$

$$\mathbf{K}_{\alpha\alpha,2} = h_2 ab \int_{-1}^1 \int_{-1}^1 \mathbf{B}_\alpha^T \mathbf{D}_2 \mathbf{B}_\alpha d\xi d\eta; \quad (18)$$

$$\mathbf{K}_{\alpha\beta,2} = -\frac{1}{2} h_2^2 \left( \frac{h_1}{h_2} + 1 \right) ab \int_{-1}^1 \int_{-1}^1 \mathbf{B}_\alpha^T \mathbf{D}_2 \mathbf{B}_\beta d\xi d\eta; \quad (19)$$

$$\mathbf{K}_{\beta\beta,2} = \frac{h_2^3}{12} \left( 3 \frac{h_1^2}{h_2^2} + 6 \frac{h_1}{h_2} + 4 \right) ab \int_{-1}^1 \int_{-1}^1 \mathbf{B}_\beta^T \mathbf{D}_2 \mathbf{B}_\beta d\xi d\eta. \quad (20)$$

The integrals in expressions (18) and (19) are found at the same Gaussian points and weight factors as in formula (16). The integral in (20) is calculated by formula (17) with the replacement of the matrix  $\mathbf{D}_1$  in it by the matrix  $\mathbf{D}_2$ . The complete stiffness matrix of a finite element is obtained by summing the contributions of the rigid and damping layers:

$$\mathbf{K}^{(e)} = \left[ \begin{array}{c|c} \mathbf{K}_{\alpha\alpha,1} & \mathbf{0} \\ \hline \mathbf{0} & \mathbf{K}_{\beta\beta,1} \end{array} \right] + \left[ \begin{array}{c|c} \mathbf{K}_{\alpha\alpha,2} & \mathbf{K}_{\alpha\beta,2} \\ \hline \mathbf{K}_{\alpha\beta,2}^T & \mathbf{K}_{\beta\beta,2} \end{array} \right].$$

In a similar form one can write down a finite element damping matrix:

$$\mathbf{C}^{(e)} = \left[ \begin{array}{c|c} \mathbf{C}_{\alpha\alpha,1} & \mathbf{0} \\ \hline \mathbf{0} & \mathbf{C}_{\beta\beta,1} \end{array} \right] + \left[ \begin{array}{c|c} \mathbf{C}_{\alpha\alpha,2} & \mathbf{C}_{\alpha\beta,2} \\ \hline \mathbf{C}_{\alpha\beta,2}^T & \mathbf{C}_{\beta\beta,2} \end{array} \right].$$

The matrix  $\mathbf{C}^{(e)}$  blocks are found according to the same formulas as the corresponding matrix  $\mathbf{K}^{(e)}$  blocks with the replacement of stiffness matrices  $\mathbf{D}_k$  ( $k = 1, 2$ ) in them by damping matrices  $\mathbf{D}_{g,k}$ .

Let us proceed to the construction of the finite element mass matrix  $\mathbf{M}^{(e)}$ . Building this matrix, we can consider that the volume forces of inertia are caused only by accelerations  $\ddot{w}$  in the direction of the  $Oz$  axis of the element. Let us write down virtual work of these forces on virtual displacements  $\delta w$  of the element:

$$\delta A = -h\rho \int_{-a}^a \int_{-b}^b \delta w \ddot{w} dx dy. \quad (21)$$

Here  $h = h_1 + h_2$  and  $\rho = (\rho_1 h_1 + \rho_2 h_2)/h$  are the thickness and average density of the element, respectively. To represent the displacements  $w$  when determining the inertial forces, we can take a bilinear approximation similar to representations (1):  $w = \mathbf{S}\mathbf{w}$ . Substituting this approximation into (21), we obtain

$$\delta A = -h\rho \delta \mathbf{w}^T \int_{-a}^a \int_{-b}^b \mathbf{S}^T \mathbf{S} dx dy \ddot{\mathbf{w}}.$$

The last expression can be represented as

$$\delta A = -\delta \mathbf{w}^T \mathbf{M}_w^{(e)} \ddot{\mathbf{w}},$$

where

$$\mathbf{M}_w^{(e)} = h\rho \int_{-a}^a \int_{-b}^b \mathbf{S}^T \mathbf{S} dx dy = h\rho ab \int_{-1}^1 \int_{-1}^1 \mathbf{S}^T \mathbf{S} d\xi d\eta.$$

The integral in the resulting expression is calculated using the Gauss formula with two points in each coordinate direction:

$$\int_{-1}^1 \int_{-1}^1 \mathbf{S}^T \mathbf{S} d\xi d\eta = \sum_{m=1}^2 \sum_{n=1}^2 \mathbf{S}^T(\xi_m, \eta_n) \mathbf{S}(\xi_m, \eta_n) Q_m P_n. \quad (22)$$

It should be noted that the resulting matrix  $\mathbf{M}_w^{(e)}$  is constructed with respect to the nodal displacements  $w_i$  ( $i = 1, 2, 3, 4$ ) of the finite element and has dimensions of  $4 \times 4$ , and the total mass matrix  $\mathbf{M}^{(e)}$  of the element should have dimensions of  $20 \times 20$  (in accordance with the number of nodal displacements in vector). To form the necessary matrix we can use the following procedure

$$\mathbf{M}^{(e)} = \mathbf{L}^T \mathbf{M}_w^{(e)} \mathbf{L},$$

where  $\mathbf{L}$  is control matrix of  $4 \times 20$  size consisting of ones and zeros.

It remains to form the vector of external nodal forces (load vector) of the finite element, which can be obtained from the expression for the virtual work of the surface load  $q(x, y, t)$ :

$$\delta A = \int_{-a}^a \int_{-b}^b \delta w q(x, y, t) dx dy. \quad (23)$$

We represent the surface load and deflection  $w$  in the form

$$q(x, y, t) = \mathbf{S} \mathbf{q}(t), \quad w = \mathbf{S} \mathbf{w}.$$

Here  $\mathbf{q}(t)$  is the vector of  $q(x, y, t)$  values at the nodes of the finite element. Substituting these representations into expression (23), we obtain

$$\delta A = \delta \mathbf{w} \int_{-a}^a \int_{-b}^b \mathbf{S}^T \mathbf{S} dx dy \mathbf{q}(t).$$

Hence, the components of external nodal forces in the direction of displacements  $w_i$  of the element are obtained

$$\mathbf{P}_w^{(e)}(t) = \int_{-a}^a \int_{-b}^b \mathbf{S}^T \mathbf{S} dx dy \mathbf{q}(t) = ab \int_{-1}^1 \int_{-1}^1 \mathbf{S}^T \mathbf{S} d\xi d\eta \mathbf{q}(t).$$

The integral in the last expression is calculated by formula (22). To form the load vector of the finite element relative to the nodal displacements  $\mathbf{r}^{(e)}$ , one can use the previous control matrix  $\mathbf{L}$ :

$$\mathbf{P}^{(e)}(t) = \mathbf{L}^T \mathbf{P}_w^{(e)}(t).$$

### 3 Formation of the System of Resolving Equations

To obtain motion equations of a finite element, we use the Lagrange equations of the second kind, taking its nodal displacements  $\mathbf{r}^{(e)}$  as generalized coordinates:

$$\frac{d}{dt} \left( \frac{\partial T^{(e)}}{\partial \dot{\mathbf{r}}^{(e)}} \right) - \frac{\partial T^{(e)}}{\partial \mathbf{r}^{(e)}} = \mathbf{Q}^{(e)}. \quad (24)$$

Here,  $T^{(e)}$  and  $\mathbf{Q}^{(e)}$  are the kinetic energy and the vector of generalized forces, respectively, which take into account the elastic, damping and external nodal forces of the finite element.

The expression for  $T^{(e)}$  can be represented as a homogeneous quadratic form of the element's nodal velocities  $\dot{\mathbf{r}}^{(e)}$ :

$$T^{(e)} = 0.5 (\dot{\mathbf{r}}^{(e)})^T \mathbf{M}^{(e)} \dot{\mathbf{r}}^{(e)}.$$

This gives

$$\frac{d}{dt} \left( \frac{\partial T^{(e)}}{\partial \dot{\mathbf{r}}^{(e)}} \right) = \frac{d}{dt} (\mathbf{M}^{(e)} \dot{\mathbf{r}}^{(e)}) = \mathbf{M}^{(e)} \ddot{\mathbf{r}}^{(e)}, \quad \frac{\partial T^{(e)}}{\partial \mathbf{r}^{(e)}} = 0. \quad (25)$$

The vector  $\mathbf{Q}^{(e)}$  in Eq. (24) can be determined using the expression

$$\mathbf{Q}^{(e)} = - \frac{\partial U^{(e)}}{\partial \mathbf{r}^{(e)}} - \frac{\partial \Phi^{(e)}}{\partial \dot{\mathbf{r}}^{(e)}} + \mathbf{P}^{(e)}(t), \quad (26)$$

where,  $U^{(e)}$ ,  $\Phi^{(e)}$  are the potential deformation energy of the finite element and the Rayleigh dissipative function, represented in the form of the corresponding quadratic forms

$$U^{(e)} = 0.5 (\mathbf{r}^{(e)})^T \mathbf{K}^{(e)} \mathbf{r}^{(e)}, \quad \Phi^{(e)} = 0.5 (\dot{\mathbf{r}}^{(e)})^T \mathbf{C}^{(e)} \dot{\mathbf{r}}^{(e)}.$$

Taking this into account, expression (26) takes the form

$$\mathbf{Q}^{(e)} = -\mathbf{K}^{(e)} \mathbf{r}^{(e)} - \mathbf{C}^{(e)} \dot{\mathbf{r}}^{(e)} + \mathbf{P}^{(e)}(t). \quad (27)$$

After substituting (27) and (25) into (24) we obtain the system of differential motion equations of a finite element

$$\mathbf{M}^{(e)} \ddot{\mathbf{r}}^{(e)} + \mathbf{C}^{(e)} \dot{\mathbf{r}}^{(e)} + \mathbf{K}^{(e)} \mathbf{r}^{(e)} = \mathbf{P}^{(e)}(t). \quad (28)$$

Combining Eq.(28) for all finite elements by the method of direct stiffness [8, 9], we obtain the equations of motion for the finite element model of the plate

$$\mathbf{M}\ddot{\mathbf{r}} + \mathbf{C}\dot{\mathbf{r}} + \mathbf{K}\mathbf{r} = \mathbf{P}(t). \quad (29)$$

Here  $\mathbf{M}$ ,  $\mathbf{C}$ ,  $\mathbf{M}$ ,  $\mathbf{r}$ ,  $\mathbf{P}(t)$  are the mass matrix, damping matrix, stiffness matrix, vector of nodal displacements and vector of external nodal forces of the marked model, respectively.

To solve system (29), we use the expansion of the vector  $\mathbf{r}$  in terms of eigenforms of vibrations:  $\mathbf{r} = \mathbf{F}\mathbf{s}(t)$ , where  $\mathbf{F}$  is a rectangular matrix, the columns of which are the  $m$  lowest eigenforms,  $\mathbf{s}(t)$  is the column of generalized coordinates. Substituting this expansion into (29) and then using the procedure of the Bubnov-Galerkin method, we arrive at a system of differential equations for the vector  $\mathbf{s}(t)$ :

$$\begin{aligned} \mathbf{M}_F \ddot{\mathbf{s}} + \mathbf{C}_F \dot{\mathbf{s}} + \mathbf{K}_F \mathbf{s} &= \mathbf{Q}(t), \\ \mathbf{M}_F &= \mathbf{F}^T \mathbf{M} \mathbf{F}, \quad \mathbf{C}_F = \mathbf{F}^T \mathbf{C} \mathbf{F}, \quad \mathbf{K}_F = \mathbf{F}^T \mathbf{K} \mathbf{F}, \quad \mathbf{Q}(t) = \mathbf{F}^T \mathbf{P}(t). \end{aligned} \quad (30)$$

In the case of harmonic load, the vector  $\mathbf{Q}(t)$  can be represented in the form  $\mathbf{Q}(t) = \mathbf{Q}_0 e^{ipt}$ , where  $\mathbf{Q}_0 = \mathbf{F}^T \mathbf{P}_0$ ;  $i$  is an imaginary unit;  $p$  is the circular frequency of the load change;  $\mathbf{P}_0$  is the amplitude vector of the external nodal forces of the plate. System (30) in this case takes the form

$$\mathbf{M}_F \ddot{\mathbf{s}} + \mathbf{C}_F \dot{\mathbf{s}} + \mathbf{K}_F \mathbf{s} = \mathbf{Q}_0 e^{ipt}. \quad (31)$$

The solution to system (31) will be sought in the form

$$\mathbf{s}(t) = \mathbf{diag}[e^{i(pt-\phi)}] \mathbf{s}_0. \quad (32)$$

Here  $\mathbf{diag}[e^{i(pt-\phi)}]$  is a diagonal matrix with elements  $e^{i(pt-\phi_k)}$ ;  $\phi_k$  is phase shift of the vector components  $\mathbf{s}_0$  relative to the corresponding vector components  $\mathbf{Q}_0$ . After substituting (32) into system (31) and canceling the common factor  $e^{ipt}$ , we arrive at the system of linear algebraic equations

$$\left[ \begin{array}{c|c} \mathbf{K}_F - p^2 \mathbf{M}_F & p \mathbf{C}_F \\ \hline p \mathbf{C}_F & -\mathbf{K}_F + p^2 \mathbf{M}_F \end{array} \right] \begin{Bmatrix} \mathbf{s}_a \\ \mathbf{s}_b \end{Bmatrix} = \begin{Bmatrix} \mathbf{Q}_0 \\ 0 \end{Bmatrix}. \quad (33)$$

Vectors  $\mathbf{s}_a$  and  $\mathbf{s}_b$  consist of components

$$s_{a,k} = s_{0,k} \cos \phi_k, \quad s_{b,k} = s_{0,k} \sin \phi_k.$$

This gives the vector  $\mathbf{s}_0$  elements and the tangents of the angles  $\phi_k$ :

$$s_{0,k} = \sqrt{s_{a,k}^2 + s_{b,k}^2}; \quad \operatorname{tg} \phi_k = s_{b,k} / s_{a,k}.$$

To clarify the  $\phi_k$  influence on the dynamic response of the plate, let us consider the case  $\phi_k = 0$ . To implement such a case, the equalities  $s_{a,k} = r_{0,k}$ ,  $s_{b,k} = 0$  must be satisfied. System (33) in this case takes the form

$$\left[ \begin{array}{c|c} \mathbf{K}_F - p^2 \mathbf{M}_F & p \mathbf{C}_F \\ \hline p \mathbf{C}_F & -\mathbf{K}_F + p^2 \mathbf{M}_F \end{array} \right] \begin{Bmatrix} \mathbf{s}_0 \\ 0 \end{Bmatrix} = \begin{Bmatrix} \mathbf{Q}_0 \\ 0 \end{Bmatrix}. \quad (34)$$

This gives two independent systems of equations:

$$(\mathbf{K}_F - p^2 \mathbf{M}_F) \mathbf{s}_0 = \mathbf{Q}_0, \quad (35)$$

$$p \mathbf{C}_F \mathbf{s}_0 = 0. \quad (36)$$

System (35) gives a vector  $\mathbf{s}_0$  in the absence of damping and far from resonance. System (36) at  $\mathbf{s}_0 \neq 0$  can be realized only under static loading ( $p = 0$ ) or under the condition  $\mathbf{C}_F = 0$ .

The same result can be obtained using substitution (32) in the case  $\phi_k = 0$ . System (31) in this case takes the form

$$(-p^2 \mathbf{M}_F + ip \mathbf{C}_F + \mathbf{K}_F) \mathbf{s}_0 = \mathbf{Q}_0, \quad (37)$$

Equating the real and imaginary terms on the left and right sides of system (37), we arrive at the previous systems of equations

$$(\mathbf{K}_F - p^2 \mathbf{M}_F) \mathbf{s}_0 = \mathbf{Q}_0, \quad p \mathbf{C}_F \mathbf{s}_0 = 0.$$

## 4 Numerical Experiments

Let us consider rectangular two-layer plate with dimensions  $480 \times 560$  mm which is hinged at all edges and consists of rigid and viscoelastic layers. It is assumed that the plate is under the action of a surface load  $q(t) = q_0 e^{ipt}$  with amplitude  $q_0 = 95$  N/m<sup>2</sup> and frequency  $p = 2\pi f$  at  $f = [0; 200]$  Hz. The rigid layer material is D16AT aluminum alloy, the material of the viscoelastic layer is technical rubber. Hard layer thickness is 1 mm, rubber layer thickness is 3.6 mm. Characteristics of alloy D16AT are following: Young's modulus  $E = 7.2 \cdot 10^{10}$  N/m<sup>2</sup>; shear modulus  $G = 2.77 \cdot 10^{10}$  N/m<sup>2</sup>; Poisson's ratio  $\nu = 0.3$ ; logarithmic decrements of vibrations in tension-compression and shear  $\delta_\varepsilon = \delta_\gamma = 0.005$ ; density  $\rho = 2700$  kg/m<sup>3</sup>. Rubber characteristics are the following:  $E = 5.3 \cdot 10^6$  N/m<sup>2</sup>;  $G = 2 \cdot 10^6$  N/m<sup>2</sup>;  $\nu = 0.49$ ;  $\delta_\varepsilon = 1.23$ ;  $\delta_\gamma = 1.1$ ;  $\rho = 1345$  kg/m<sup>3</sup>. The plate was divided into 144 finite elements (12 elements in the direction of each side). To determine the nodal displacements in the expansion  $\mathbf{r} = \mathbf{F} \mathbf{s}(t)$ , 12 lower eigenforms were taken into account.

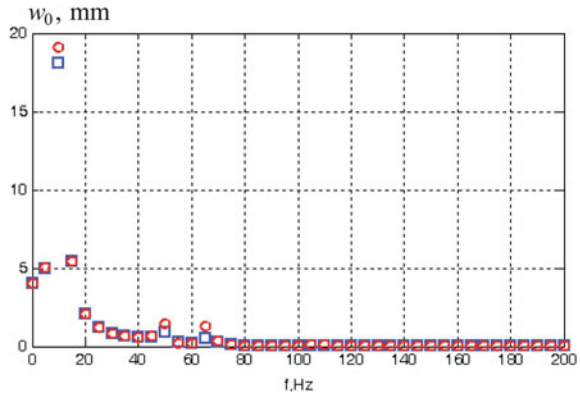
Table 1 shows 12 natural frequencies of vibrations found from a system of homogeneous equations  $(\mathbf{K} - \omega^2 \mathbf{M}) \mathbf{F} = 0$  by the method of iterations in a subspace [10, 11]. In order to reduce the amount of necessary calculations, the symmetry and strip structure of the matrices  $\mathbf{K}$  and  $\mathbf{M}$  were taken into account.



**Table 1** Natural frequencies of plate vibrations

$j$	$f_j$ , Hz	$j$	$f_j$ , Hz
1	11.2816	7	72.1762
2	25.9891	8	81.2843
3	31.2542	9	89.8884
4	46.1702	10	107.8782
5	51.6157	11	111.0019
6	66.0542	12	116.0356

**Fig. 2** Deflection amplitudes  $w_0$  of the plate center: squares denote the dependence with damping, circles denote the dependence without damping



The results in Fig. 2 shows the deflection amplitudes  $w_0$  of the plate center depending on the frequency  $p$ , found by solving system (34) (with damping taken into account) and by system (35) (without damping). Figures 3, 4 and 5 demonstrate the amplitudes of normal stresses  $\sigma_{x,0}$  and  $\sigma_{y,0}$  on the bottom surface in the center of the plate and the amplitudes of shear stresses  $\tau_{xy,0}$  in the corner of the plate, depending on the frequency  $f = p/(2\pi)$  of forced vibrations, found on the basis of the previous systems of equations.

Analyzing the results from Figs. 2, 3, 4 and 5, one can see a noticeable difference between the results of calculations for the plate with and without damping only in the neighborhood of the resonance frequencies. Meanwhile, far from resonance the results are practically the same in both cases. It is interesting to note that from the surface load  $q(t) = q_0 e^{ipt}$  applied over the entire area of the plate, resonant oscillations are excited only at those frequencies that correspond to eigenforms with an odd number of half-waves in the direction of each side of the plate. This corresponds to the classical concepts of the forms of resonant vibrations of a hingedly supported plate under the action of a load  $q(t) = q_0 e^{ipt}$  constant over the area. Of the twelve natural frequencies found such frequencies are  $f_1, f_5, f_6$  and  $f_{10}$ .

**Fig. 3** Amplitudes of normal stresses  $\sigma_{x,0}$  on the bottom surface in the center of the plate: squares denote the dependence with damping, circles denote the dependence without damping

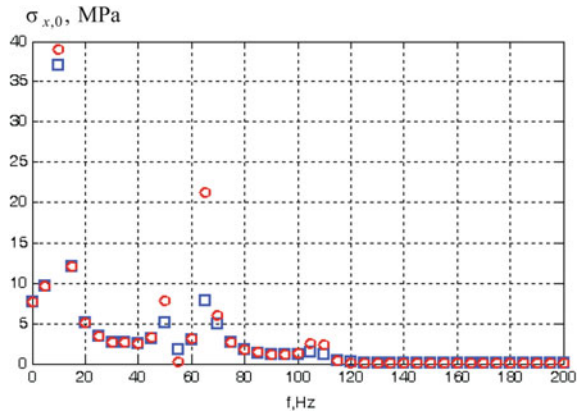


**Fig. 4** Amplitudes of normal stresses  $\sigma_{y,0}$  on the bottom surface in the center of the plate: squares denote the dependence with damping, circles denote the dependence without damping

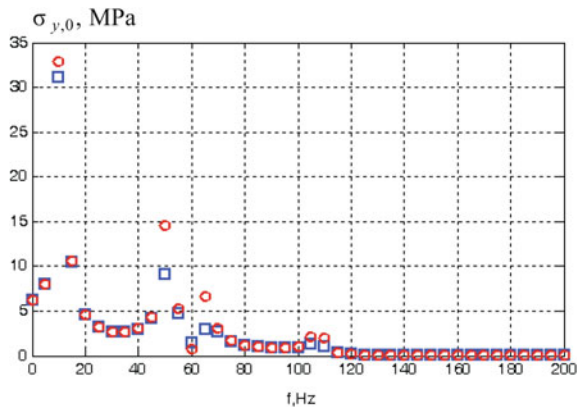
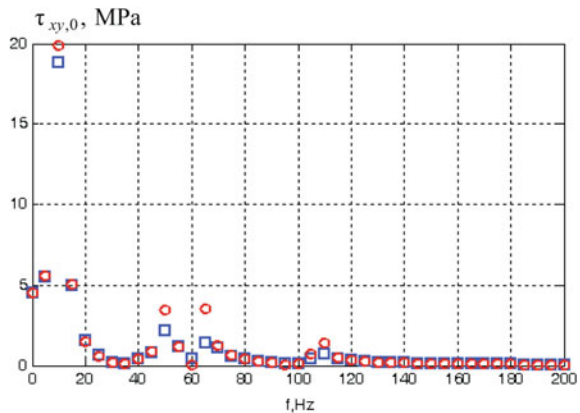


**Fig. 5** Amplitudes of shear stresses  $\tau_{xy,0}$  on the bottom surface in the corner of the plate: squares denote the dependence with damping, circles denote the dependence without damping



**Acknowledgements** This paper has been supported by the Russian Science Foundation (Project No. 19–19–00058) (Sects. 1, 2) and by the Kazan Federal University Strategic Academic Leadership Program (“PRIORITY-2030”) (Sects. 3, 4).

## References

1. Pisarenko GS, Yakovlev AP, Matveev VV (1971) Vibropogloshchayushchie svoystva konstrukcionnykh materialov: Spravochnik [Vibration-damping properties of structural materials: Handbook]. Naukova Dumka, Kiev [in Russian]
2. Zelenev YuV, Kirilin AA, Slobodnik EB, Talitskiy EN (1984) Vibrozashchita radioelektronnoj apparatury polimernymi kompaundami [Vibration protection of electronic equipment with polymer compounds]. Radio i svyaz, Moscow [in Russian]
3. Mathews JH, Fink KD (1999) Numerical methods using MATLAB. Prentice Hall, Upper Saddle River
4. Postnikov VS (1969) Vnutrennee trenie v metallah [Internal friction in metals]. Metallurgy, Moscow [in Russian]
5. Khilchevsky VV, Dubenets VG (1977) Rasseyanie energii pri kolebaniyah tonkostennykh elementov konstrukcij [Energy dissipation during vibrations of thin-walled structural elements]. Vishcha school, Kiev [in Russian]
6. Paimushin VN, Firsov VA, Shishkin VM (2020) Numerical modeling of resonant vibrations of an elongate plate with an integral damping coating. *Mech Compos Mater* 56(2):149–168
7. Zienkiewicz OC, Morgan K (1983) Finite elements and approximation. Wiley, New York
8. Postnov VA, Kharkhurim IYa (1974) Metod konechnykh elementov v raschetah sudovykh konstrukcij [Finite element method in ship structure calculations]. Sudostroenie, Leningrad [in Russian]
9. Obraztsov IF, Saveliev LM, Khazanov KhS (1985) Metod konechnykh elementov v zadachah stroitel'noj mekhaniki letatel'nykh apparatov [The finite element method in the problems of structural mechanics of aircraft]. Vysshaya shkola [in Russian]
10. Bathe KJ, Wilson EL (1976) Numerical methods in finite element analysis. Prentice Hall, Englewood Cliffs, N.J
11. Paimushin VN, Shishkin VM (2015) Modeling the elastic and damping properties of the multilayered torsion bar-blade structure of rotors of light helicopters of the new generation 2. Finite-element approximation of blades and a model of coupling of the torsion bar with the blades. *Mech Compos Mater* 51(6):771–788

# Peterson Charts for Functionally Graded Rotating Hollow Disks with an Eccentric Hole



M. Cais, D. Casagrande, and H. M. A. Abdalla

**Abstract** It is well known that fractures in elastic bodies initiate at locations of stress concentrations, which could arise due to geometrical discontinuities. While there are several works available in the literature about fracture mechanics studies for homogeneous bodies (both experimental and analytical), only a few studies analyzed the effects of geometrical discontinuities in bodies made of nonhomogeneous materials. The present study aims to fill this gap analyzing the effect of a circular eccentric hole in functionally graded hollow disks subject to centrifugal body forces. The material is assumed to be linearly elastic and isotropic, while its properties radially vary in a prescribed law. The effect of the non-homogeneity on two suitably defined stress concentration factors is numerically forecast by means of finite element method. Graphical charts are then provided to assess critical stresses and thoroughly discussed. Comments on the location of the eccentric hole such that stress concentrations attain their minimum are finally addressed.

**Keywords** Functionally graded materials · Stress concentration · Hollow disks · Eccentric hole · Peterson charts · Finite element analysis

## 1 Introduction

Functionally graded materials (FGMs) are multiphase materials with spatially varying properties tailored to satisfy specific requirements encountered in engineering applications. From continuum mechanics viewpoint, they are nonhomogeneous

---

M. Cais (✉) · D. Casagrande · H. M. A. Abdalla  
Polytechnic Department of Engineering and Architecture, University of Udine, Via delle Scienze  
206, 33100 Udine, Italy  
e-mail: [cais.mauro@spes.uniud.it](mailto:cais.mauro@spes.uniud.it)

D. Casagrande  
e-mail: [daniele.casagrande@uniud.it](mailto:daniele.casagrande@uniud.it)

H. M. A. Abdalla  
e-mail: [abdalla.hma@spes.uniud.it](mailto:abdalla.hma@spes.uniud.it)

materials whose compositions and volume fractions of the constituents are gradually varied, thus giving a microstructure in the material with continuously graded properties. So far, there is a very large number of researches available in theoretical analysis, numerical simulations, and experimental observations [1]. Works reporting the analysis of functionally graded beams [2], plates [3], and other various structures have been increasing in time. In particular, several attempts have been made dealing with axisymmetric structures such as tubes [4], rotating disks [5] and vessels [6], and their optimum response to an actual environment has been considered in both analytical [7, 8] and numerical forms by means of commercial softwares [9], gradient-based methods [10] and meta-heuristic algorithms [11].

Parallel to these researches, nevertheless, in comparison with Peterson's treatises for homogeneous structures [12, 13], a little progress has been made concerning the interaction of the flow of the stress in FGMs with functional geometrical discontinuities such as re-entrant corners, grooves, holes, notches, fillets, etc. Such stress raisers are accounted for by the so-called stress concentration factors (SCFs), suitably defined taking into account the analyzed component, boundary and load conditions and the nature of the discontinuities. In fact, most of the literature assessing SCFs in FGMs principally concerns plates subject to uni- or bi-axial load with a central hole or an edge crack, e.g., [14–18], whereas studies dealing with geometrical discontinuities in axisymmetric bodies, to the extent of the authors' knowledge, have not been addressed yet.

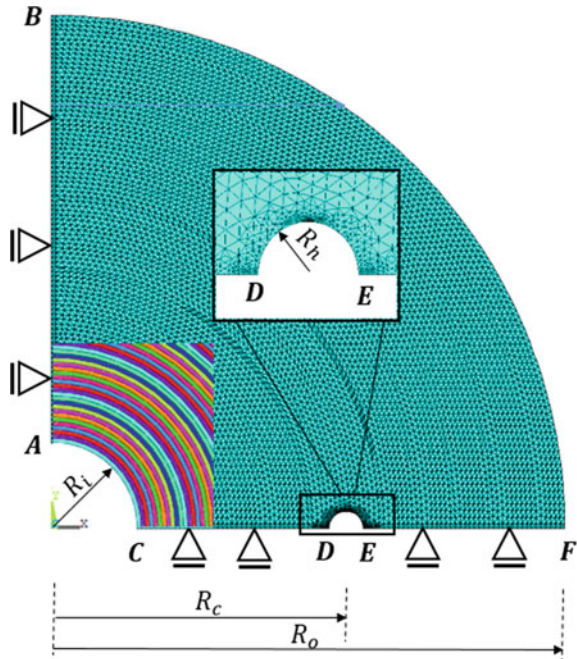
In the present article, a preliminary study on the effect of a circular eccentric hole in functionally graded hollow disks subject to centrifugal body forces is addressed. As the intuition suggests, the SCF achieves its high value as the eccentric hole approaches either the inner or the outer radius where the maximum hoop stress occurs at the innermost or outermost point of the eccentric hole, respectively, and therefore there will be an optimal location of the eccentric hole such that SCFs attain their minimum values. Accordingly, the SCFs have been defined as the ratio of these peak stresses to a reference stress taken to be the hoop stress at a radial distance corresponding to the center of the hole in a zone where no interruption to the flow of the stress is encountered, e.g., circumferentially distant. Such stress raisers are forecast by means of a two-dimensional (2D) Finite Element (FE) model, whose validity is firstly examined within a discontinuity-free rotating disk with a specific class of material gradation functions. In particular, it is assumed that no interactions exist between the two constituent's phases and both Young's modulus and density radial distributions are supposed to vary according to widely accepted power-law functions, so that closed form expressions are derivable and consequently a comparison with the proposed FE model is made. Consequently, an eccentric circular hole is introduced and SCFs are numerically forecast for different radial positions as well as hole sizes.

## 2 Description of the FE Model

In this Section, the 2D FE model is briefly described. Figure 1 shows a schematic view of such model, whose inner and outer radii are denoted by  $R_i$  and  $R_o$ , respectively. Only the quarter of the disk is modeled for symmetrical issues. An eccentric circular hole of radius  $R_h$  and at distance  $R_c$  from the origin is introduced, whose center lies on the X-axis. Such geometrical discontinuity introduces an interruption of the flow of the stress, giving rise to a concentration of the stress field in this region.

A natural and straightforward attempt to best mimic the nonhomogeneity of the disk is to partition it into many radial layers and consider each layer as isotropic and homogeneous and having the same material properties. Adjacent layers therefore present different properties such that the resulting piecewise constant variation approximates the prescribed material property distributions. Given the distributions of mechanical and physical properties, ad-hoc routines have been written to assign elements associated with each layer their properties and to numerically assess the stress field when subject to a constant angular velocity  $\omega$  around the Z-axis. It is worth noting that displacement constraint must be applied in a way that the simplified model in Fig. 1 reproduces the behavior of the entire disk. To this purpose, while horizontal displacements for nodes laying on the line  $AB$  and vertical displacements

**Fig. 1** Description of the simplified FE model, definitions of  $R_i$ ,  $R_o$ ,  $R_c$  and  $R_h$  and mesh detail in the vicinity of the eccentric hole



for nodes laying on lines  $CD$  and  $EF$  have been identically set to zero, the semi-circumference  $DE$  has not been constrained, where a finer mesh compared to the rest of the model has been employed to better simulate the stress concentration.

### 3 Validity of the Model

In this Section, the validity of the proposed FE model is addressed. Hence, closed form expressions of the stress field are necessarily needed. The stress response of discontinuity-free disks has been analytically treated under many load scenarios when Poisson's ratio is constant and Young's modulus obeys a power law dependence on the radial coordinate (see e.g., [10, 19–21]):

$$E(r) = \widehat{E} \left( \frac{r}{R_i} \right)^n, \quad (1)$$

where  $\widehat{E}$  is the Young's modulus of the material at the inner surface and  $n$  is the *grading index*, offering therefore a direct opportunity to be compared with FE numerical results on the line  $AB$ , and hence a straightforward key to compute reference (or nominal) stresses for the SCFs.

Assuming no interactions between phases, both Young's modulus and the density may be modeled by Voigt's rule of mixture [22], leading to the following density distribution:

$$\rho(r) = \frac{E_c \rho_m - E_m \rho_c}{E_c - E_m} + \frac{\widehat{E}(\rho_c - \rho_m)}{E_c - E_m} \left( \frac{r}{R_i} \right)^n \quad (2)$$

and the following lower and upper bounds for the grading index:

$$\frac{\ln(E_m/\widehat{E})}{\ln(R_o/R_i)} \leq n \leq \frac{\ln(E_c/\widehat{E})}{\ln(R_o/R_i)}. \quad (3)$$

Subscripts  $m$  and  $c$  in Eqs. (2) and (3) refer to the metal and ceramic components, respectively.

Following the analysis reported in [10], the radial stress is determined by solving the boundary value problem:

$$\begin{cases} r^2 \sigma_r'' + [3 - r(\ln E)'] r \sigma_r' + \widehat{\nu} r (\ln E)' \sigma_r = \rho \omega^2 r^2 [r (\ln E)' - r (\ln \rho)' - \widehat{\nu}], \\ \sigma_r(R_i) = \sigma_r(R_o) = 0, \end{cases} \quad (4)$$

where  $\widehat{\nu} = \nu - 1 < 0$ ,  $\tilde{\nu} = 3 + \nu > 0$  and a prime  $(.)'$  denotes the first derivative with respect to the radial coordinate. For the sake of simple notation, the dependence on  $r$  has been omitted in Eq. (4). Closed form solutions for both stresses are reported in the Appendix.

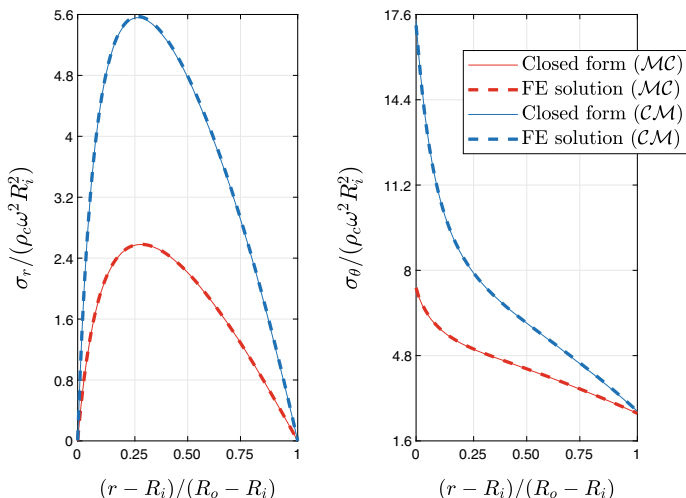


**Fig. 2** Normalized radial and hoop stress distribution throughout the radius in  $MC$  ad  $CM$  functionally graded hollow disks. FE solutions are extracted along the line  $AB$

Figure 2 shows analytical and FE solutions normalized stresses along the line  $AB$  for  $R_o/R_i = 6$  and associated with the two possible graded scenarios  $MC$  and  $CM$ , which are the functionally graded disks with  $\hat{E} = E_m$  and  $\hat{E} = E_c$ , respectively. The selected materials are Alumina ( $E_c = 390$  GPa,  $\rho_c = 3.9 \times 10^{-9}$  t/mm<sup>3</sup>) and Steel ( $E_m = 210$  GPa,  $\rho_m = 7.8 \times 10^{-9}$  t/mm<sup>3</sup>), while  $\nu = 0.3$ . It is worth to highlight how closed form solutions and numerical simulations are in agreement, ensuring the validity of the FE simplified model. Moreover, radial and hoop stresses arising in the  $MC$  disk are considerably less than those exhibited by the  $CM$  one if subject to the same  $\omega$ .

## 4 Numerical Evaluation of SCFs

In this Section, the numerical forecast of the stress localization due to the presence of the eccentric hole is addressed. From the nature of the applied load, infinitesimal elements of the disk are stressed more circumferentially than radially. As mentioned in the Introduction, the SCF, denoted herein by  $K$  similarly to engineering textbooks, e.g., [23], is defined as the ratio of the peak stress and a reference stress. This latter depends on the problem at hand. Here, it has been chosen to be the hoop stress on the line  $AB$  at a radial coordinate corresponding to the center of the eccentric hole,  $R_c$ . This choice is convenient to suitably enhance peculiar aspects dealing with the optimal radial location of the hole, reported below.

As far as the hoop stress is concerned, from the nature of the geometrical aspect of the considered disk, the peak stress corresponds to either the innermost or outermost



points of the eccentric hole (points  $D$  and  $E$ , respectively, Fig. 1), depending on its radial location. Similar to [24], two stress concentration factors can be therefore defined as follows

$$K_i = \frac{(\sigma_\theta)_D}{\sigma_\theta(R_c)}, \quad K_e = \frac{(\sigma_\theta)_E}{\sigma_\theta(R_c)}. \quad (5)$$

To broaden the analysis to include arbitrary constituents, a parameter accounting for base materials bulk properties is needed. Let  $(\eta := E_o/E_i, \delta := \rho_o/\rho_i)$  be this parameter, where subscripts  $i$  and  $o$  refer to the inner and outer borders, respectively. At this preliminary stage, only base materials with Young's moduli and densities with  $\eta = 2.0$  and  $\rho = 0.5$  are considered. Note that this is almost the case of Steel-Alumina  $\mathcal{MC}$  functionally graded structures as well as whenever  $E_o = 2E_i$  and  $\rho_o = \rho_i/2$ . The reversed scenario is also considered, namely the  $\mathcal{CM}$  structure with  $E_o = E_i/2$  and  $\rho_o = 2\rho_i$ .

Numerical values for the stress concentration factors  $K_i$  and  $K_e$  as  $R_c$  increases are shown in Fig. 3a, b, respectively, for the two graded structures for  $R_o/R_i = 5$  and for two instances of the radius of the eccentric hole  $R_h$ . Both figures show that there exists an optimal location of the eccentric hole, namely when  $K_i$  and  $K_e$  attain their minimum values. Unlike  $K_i$ , it is observed that the behavior of  $K_e$  for both graded structures is marginally influenced by  $R_h$  far from the outer border, where  $K_e$  considerably increases as  $R_h$  increases. Moreover, the localization of the flow of the stress is likely more accentuated in the  $\mathcal{MC}$  structure with respect to  $\mathcal{CM}$ . A similar comment holds for  $K_i$ , unless  $R_c$  approaches the inner border.

Finally, a comment on the optimal location of the eccentric hole for different instances of  $R_o/R_i$  and  $R_h$  is addressed. For brevity, this interest is investigated only for  $\mathcal{MC}$  graded structures, where stresses due to centrifugal body forces, as previously illustrated in Fig. 2, are remarkably lower than those arising in  $\mathcal{CM}$  ones.

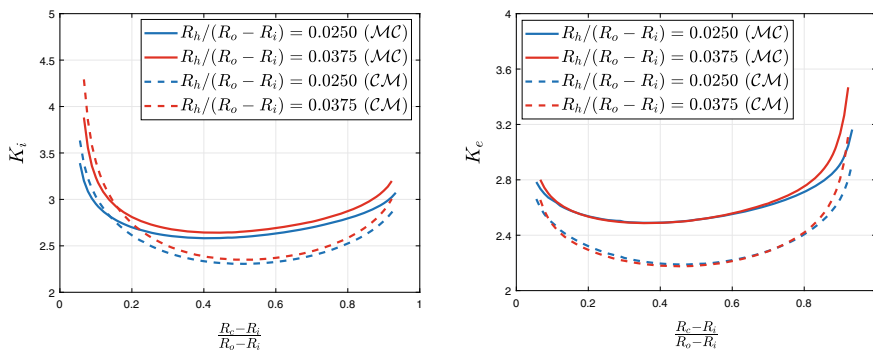


**Fig. 3** FE results for stress concentration factors at the **a** innermost and **b** outermost points with  $R_o/R_i = 5$ . Solid and dashed lines correspond to  $\mathcal{MC}$  ( $\eta, \delta$ ) and  $\mathcal{CM}$  ( $1/\eta, 1/\delta$ ), respectively, namely interchanging base materials at inner and outer surfaces

**Table 1** Optimal location of the eccentric hole for  $\mathcal{MC}$  structures for different instances of  $R_h$  and  $R_o/R_i$

$\frac{R_h}{R_o - R_i}$	$\frac{R_o}{R_i} = 3$	$\frac{R_o}{R_i} = 4$	$\frac{R_o}{R_i} = 5$
0.0250	0.500	0.453	0.411
0.0375	0.511	0.466	0.444

Accordingly, Table 1 lists optimal values of  $\frac{R_o - R_i}{R_o - R_i}$ , which shows that the concentration of hoop stress at the innermost point attains its minimum for radial positions almost close to  $(R_o - R_i)/2$ , independently from the dimension of the eccentric hole.

## 5 Conclusions

In this article, a preliminary study on the effect of an eccentric hole on the interruption of the flow of the hoop stress in functionally graded hollow disks is numerically forecast by means of finite element method. Two stress concentration factors corresponding to the innermost and outermost points of the hole have been suitably defined and Peterson charts have been provided for a specific case of functionally graded disks whose properties obey a widely accepted gradation law. Charts have been commented and the influence of the dimension of the hole has been addressed. In particular, it is found that both concentration factors attain a minimum value for a specific radial location of the eccentric hole, which has been listed in a tabular form for different aspect ratios of the disk and different radii of the eccentric hole.

## Appendix

The radial and hoop stresses are given by

$$\sigma_r(r) = Ar^{m_1} + Br^{m_2} + C_1r^2 + C_2r^{n+2}$$

and

$$\begin{aligned} \sigma_\theta(r) = & A(1 + m_1)r^{m_1} + B(1 + m_2)r^{m_2} + C_1 \left( \frac{1 + 3\nu - n\nu}{\tilde{\nu} - n} \right) r^2 \\ & + C_2 \left( \frac{17 + 6n + 2n\nu + 3\nu}{\tilde{\nu}} \right) r^{n+2}, \end{aligned}$$

respectively, where  $m_{1,2} = \frac{n - 2 \pm \sqrt{n^2 - 2nv + 4}}{2}$ ,

$$C_1 = \frac{(n - \tilde{\nu})(E_c \rho_m - E_m \rho_c) \omega^2}{(8 + nv - 3n)(E_c - E_m)},$$

$$C_2 = \frac{\tilde{\nu}(\rho_m - \rho_c) \omega^2 \widehat{E}}{(8 + nv - 3n)(E_c - E_m) R_i^n},$$

$$A = C_1 R_i^{2-m_1} \left[ \frac{(R_o/R_i)^2 - (R_o/R_i)^{m_2}}{(R_o/R_i)^{m_2} - (R_o/R_i)^{m_1}} \right] + C_2 R_i^{n+2-m_1} \left[ \frac{(R_o/R_i)^{n+2} - (R_o/R_i)^{m_2}}{(R_o/R_i)^{m_2} - (R_o/R_i)^{m_1}} \right],$$

$$B = C_1 R_i^{2-m_2} \left[ \frac{(R_o/R_i)^2 - (R_o/R_i)^{m_1}}{(R_o/R_i)^{m_1} - (R_o/R_i)^{m_2}} \right] + C_2 R_i^{n+2-m_2} \left[ \frac{(R_o/R_i)^{n+2} - (R_o/R_i)^{m_1}}{(R_o/R_i)^{m_1} - (R_o/R_i)^{m_2}} \right].$$

## References

1. Nikbakht S, Kamarian S, Shakeri M (2019) A review on optimization of composite structures. Part II: functionally graded materials. *Compos Struct* 214:83–102
2. Chu P, Li XF, Wu JX, Lee KY (2015) Two-dimensional elasticity solution of elastic strips and beams made of functionally graded materials under tension and bending. *Acta Mech* 226:2235–2253
3. Reddy JN, Cheng ZQ (2001) Three-dimensional thermomechanical deformations of functionally graded rectangular plates. *Euro J Mech: A/Solids* 20:841–860
4. Liew KM, Kitipornchai S, Zhang XZ, Lim CW (2003) Analysis of the thermal stress behavior of functionally graded hollow circular cylinders. *Int J Solids Struct* 40:2355–2380
5. Kordekheili S, Naghdabadi R (2007) Thermoelastic analysis of a functionally graded rotating disk. *Compos Struct* 79:508–516
6. Li XF, Peng XL, Kang YA (2009) Pressurized hollow spherical vessels with arbitrary radial nonhomogeneity. *AIAA* 47:2262–2265
7. Abdalla HMA, Casagrande D (2021) An intrinsic material tailoring approach for functionally graded axisymmetric hollow bodies under plane elasticity. *J Elast* 144:15–32
8. Abdalla HMA, Casagrande D, De Bona F (2020) A dynamic programming setting for functionally graded thick-walled cylinders. *Materials* 13(18):3988
9. Wang ZW, Zhang Q, Xia LZ, Wu JT, Liu PQ (2015) Stress analysis and parameter optimization of an FGM pressure vessel subjected to thermo-mechanical loadings. *Proc Eng* 130:374–389
10. Abdalla HMA, Casagrande D, Moro L (2020) Thermo-mechanical analysis and optimization of functionally graded rotating disks. *J Strain Anal Eng* 55(5–6):159–171
11. Khorsand M, Tang Y (2018) Design functionally graded rotating disks under thermoelastic loads: weight optimization. *Int J Press Vessels Piping* 161:33–40
12. Peterson RE (1953) *Stress concentration design factors*. Wiley
13. Peterson RE (1974) *Stress concentration factors*. Wiley
14. Jin ZH, Batra RC (1996) Some basic fracture mechanics concepts in functionally graded materials. *J Mech Phys Solids* 44(8):1221–1235
15. Kubair D, Bhanu-Chandar B (2008) Stress concentration factor due to a circular hole in functionally graded panels under uniaxial tension. *Int J Mech Sci* 50(4):732–742
16. Mohammadi M, Dryden JR, Jiang LY (2011) Stress concentration around a hole in a radially inhomogeneous plate. *Int J Solids Struct* 48(3–4):483–491
17. Sbulrati R (2013) Stress concentration factor due to a functionally graded ring around a hole in an isotropic plate. *Int J Solids Struct* 50:3649–3658
18. Nie GJ, Zhong Z, Batra RC (2018) Material tailoring for reducing stress concentration factor at a circular hole in a functionally graded material (FGM) panel. *Compos Struct* 205:49–57
19. Erslan AN, Akis T (2006) On the plane strain and plane stress solutions of functionally graded rotating solid shaft and solid disk problems. *Acta Mech* 181:43–63

20. You LH, You XY, Zhang JJ (2007) On rotating circular disks with varying material properties. *Z Angew Math Phys* 58:1068–1084
21. Zenkour AM (2009) Stress distribution in rotating composite structures of functionally graded solid disks. *J Mater Process Technol* 209:3511–3517
22. Miyamoto Y, Kaysser WA, Rabin BH, Kawasaki A, Ford RG (1999) Functionally graded materials. Design, processing and applications. Kluwer Academic, London
23. Pilkey DW (1997) Peterson's stress concentration factors. Wiley, New York
24. Ang HE, Tan CL (1988) Stress concentrations at holes in thin rotating disks. *J Strain Anal Eng* 23(4):223–225

# Use of the Chebyshev Collocation Method for Vibration Analysis of Carbon-Nanotube Reinforced Composite Beams with Elastic Boundary Conditions



Desmond Adair and Martin Jaeger

**Abstract** An investigation of the vibration behaviour of carbon-nanotube reinforced composite beams utilizing both traditional and non-traditional boundary conditions is carried out. The Timoshenko formulation is chosen so as to include the effects of deformation of shear and rotary inertia and to obtain the coupled equations of motion which govern vibration of the beam. The Chebyshev collocation method is employed to solve the governing equations to determine the frequencies of the beams with different boundary conditions and compressive loading imposed. Correctness and dependability of the Chebyshev collocation method are validated by comparison with previous results found in the literature for the traditional boundary conditions. Calculations will also be presented for non-traditional (elastic) boundary conditions for different parameters.

**Keywords** Chebyshev collocation · Timoshenko · Mechanical vibration · Carbon-nanotube · Composite

## 1 Introduction

A most promising reinforcement material for use when building multifunctional composites to produce high strength structures are carbon nanotubes otherwise known as CNTs. This is because of their excellent mechanical, thermal and physical characteristics. More conventional composite materials, for example glass fibre reinforced polymers, as used extensively in the production of aerospace structures, wind turbines, sailing boats, etc., are generally manufactured from high volume fillers, which can lead to problems like de-bonding between fibre and the polymer matrix interface. This type of problem can be alleviated using CNTs where, when small

---

D. Adair (✉)  
Nazarbayev University, Nur-Sultan 010000, Republic of Kazakhstan  
e-mail: [dadair@nu.edu.kz](mailto:dadair@nu.edu.kz)

M. Jaeger  
Australian College of Kuwait, 13015 Safat, Kuwait

amounts of CNTs are added to the polymeric matrices, significant improvements in strength and the mechanical properties of the given polymeric composite most often result [1].

The coupled equations of motion which govern carbon nanotube reinforced composite (CNTRC) beam behavior can be solved by an efficient method called the Chebyshev collocation (CCM). Here Chebyshev functions in the form of polynomials are utilized when solving integral–differential equations with sufficient correctness and dependability, and, with a fast convergence rate [2–5]. A number of papers on the modelling of carbon nanotube reinforced composite beams have been recently published. For example, a comprehensive review paper [6] and methods of calculation ranging from using the Ritz method [7] to finite-element modelling [8].

When dealing with realistic applications, damaged or inadequate boundary conditions may also be simulated using translational and/or rotational springs. In this investigation, the CCM is applied to investigate the displacement characteristics of CNTRC beams with different traditional and non-traditional boundary conditions specified by a combination of the coefficients of the two types of springs.

## 2 Carbon Nanotube Reinforced Composite Beams (CNTRCs)

A CNTRC beam can be prepared by including single-walled carbon nanotubes (SWCNTs) within an isotropic polymeric matrix. Here, the beam’s length is  $l$ , and thickness is  $h$ , and, elastic boundary conditions, compactly described by translation and rotation springs are used, as shown on Fig. 1a. Various patterns of carbon-nanotube reinforcement across the sections can be used as illustrated on Fig. 1b.

The properties of a CNTRC beam are usually calculated by the use of the mixture rule to give the effective Young’s and shear moduli

$$E_{11} = \eta_1 V_s E_{11}^s + V_p E^p \tag{1}$$

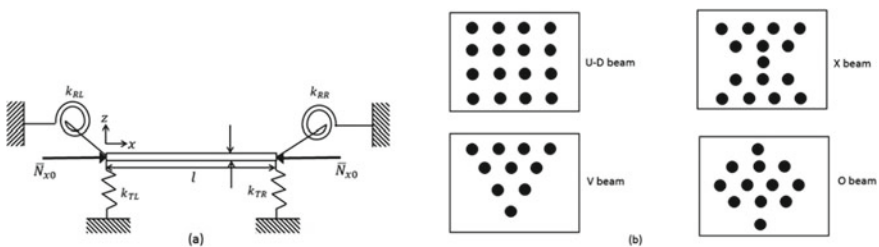


**Fig. 1** **a** The CNTRC beam showing the elastic-elastic boundary conditions. **b** Patterns of cross-section reinforcement

$$\frac{\eta_2}{E_{22}} = \frac{V_s}{E_{22}^s} + \frac{V_p}{E_p} \quad (2)$$

$$\frac{\eta_3}{G_{12}} = \frac{V_s}{G_{12}^s} + \frac{V_p}{G^p} \quad (3)$$

Here,  $E_{11}^s$ ,  $E_{22}^s$  and  $G_{12}^s$  are defined as the Young's and moduli and shear modulus of the single-walled carbon nanotubes, respectively, while,  $E^p$  and  $G^p$  are the equivalent for the polymeric matrix. The volume fractions,  $V_s$  and  $V_p$  for the carbon nanotube and polymer matrix, respectively, combine as

$$V_s + V_p = 1 \quad (4)$$

The size-dependent material properties of the single-walled carbon nanotubes are considered by introducing the CNT efficiency parameters,  $\eta_i$  ( $i = 1, 2, 3$ ) and are determined by matching the elastic moduli of the CNTRCs estimated by molecular dynamics modelling with the results calculated using the mixture rule. From this the, Poisson's ratio ( $\nu$ ) and mass density ( $\rho$ ) of the beams are

$$\nu = V_s \nu^s + V_p \nu^p \quad (5)$$

$$\rho = V_s \rho^s + V_p \rho^p \quad (6)$$

where,  $\nu^s$ ,  $\nu^p$  and  $\rho^s$ ,  $\rho^p$  are respectively the Poisson ratios and densities of the single-walled carbon nanotubes and polymeric matrix. For the different patterns of reinforcement over the cross-sections, mathematical functions are used as described below [9, 10]

$$\text{U-Dbeam} : V_s = V_s^* \quad (7a)$$

$$\text{O beam} : V_s = 2 \left( 1 - 2 \frac{|z|}{h} \right) V_s^* \quad (7b)$$

$$\text{X beam} : V_s = 4 \frac{|z|}{h} V_s^* \quad (7c)$$

$$\text{V beam} : V_s = \left( 1 + \frac{2z}{h} \right) V_s^* \quad (7d)$$

Here,  $V_s^*$  is the CNTs' volume fraction and this can be found from [9, 10]

$$V_s^* = \frac{W_s}{W_s + (\rho^s / \rho^m)(1 - W_s)} \quad (8)$$

Here,  $W_s$  is the CNTs' mass fraction.

### 3 Displacement Governing Equations

The Timoshenko beam formulation is selected here, so as to include rotary inertia and shear deformation. For a given beam, the displacement at a specific point in relation to the  $x$  and  $z$  axes can be given by  $u(x, z, t)$  and  $w(x, z, t)$  respectively where

$$u(x, z, t) = u_0(x, t) + z\varphi(x, t), w(x, z, t) = w_0(x, t) \quad (9)$$

Here,  $u_0(x, t)$  and  $w_0(x, t)$  are the local point displacements at the centre plane ( $z = 0$ ),  $\varphi$  is beam cross-section rotation, and  $t$  is time. Based on the displacement field described by Eq. (9), the normal strain ( $\varepsilon_{xx}$ ) and shear strain ( $\gamma_{xz}$ ) can be expressed

$$\varepsilon_{xx} = \frac{\partial u_0}{\partial x} + z \frac{\partial \varphi}{\partial x}, \gamma_{xz} = \frac{\partial w_0}{\partial x} \gamma \quad (10)$$

Based on the elastic constitutive law, the normal and shear stresses take the form

$$\sigma_{xx} = \frac{E_{11}(z)}{1 - \nu(z)^2} \varepsilon_{xx}, \tau_{xz} = \frac{E_{11}(z)}{2[1 + \nu(z)]} \gamma_{xz} \quad (11)$$

The governing equations, from Hamilton's principle, which also account for axial and rotary inertia for vibration and buckling analyses are

$$\frac{\partial N_x}{\partial x} = I_0 \frac{\partial^2 u_0}{\partial t^2} + I_1 \frac{\partial^2 \varphi}{\partial t^2} \quad (12)$$

$$\frac{\partial Q_x}{\partial x} - \bar{N}_{x0} \frac{\partial^2 w_0}{\partial x^2} = I_0 \frac{\partial^2 w_0}{\partial t^2} \quad (13)$$

$$\frac{\partial M_x}{\partial x} - Q_x = I_1 \frac{\partial^2 u_0}{\partial t^2} + I_2 \frac{\partial^2 \varphi}{\partial t^2} \quad (14)$$

In the above the stress resultants are  $N_x$ ,  $M_x$  and  $Q_x$  are

$$N_x = A_{11} \frac{\partial u_0}{\partial x} + B_{11} \frac{\partial \varphi}{\partial x} \quad (15)$$

$$M_x = B_{11} \frac{\partial u_0}{\partial x} + D_{11} \frac{\partial \varphi}{\partial x} \quad (16)$$



$$Q_x = K_s A_{55} \left( \frac{\partial u_0}{\partial x} + \varphi \right) \quad (17)$$

In these equations the shear correction factor is  $K_s = 5/6$  and  $A_{11}$ ,  $B_{11}$ ,  $D_{11}$  and  $A_{55}$  are the components of stiffness obtained from.

$$[A_{11}, B_{11}, D_{11}] = \int_{-h/2}^{h/2} \frac{E_{11}(z)}{1 - \nu(z)^2} [1, z, z^2] dz, \quad A_{55} = \int_{-h/2}^{h/2} \frac{E_{11}(z)}{2[1 + \nu(z)]} dz \quad (18)$$

The components of moment of inertia are

$$[I_0, I_1, I_2] = \int_{-h/2}^{h/2} \rho(z) [1, z, z^2] dz \quad (19)$$

To solve the governing equations (Eqs. 12–14), with the E-E boundary conditions shown on Fig. 1a, expressions for the boundary conditions are.

For  $x = 0$ ,

$$u_0 = 0, \quad Q_x + k_{TL} w_0 = 0, \quad M_x + k_{RL} \varphi = 0 \quad (20a)$$

For  $x = l$ ,

$$u_0 = 0, \quad Q_x - k_{TR} w_0 = 0, \quad M_x - k_{RR} \psi = 0 \quad (20b)$$

Here,  $k_{TL}$ ,  $k_{RL}$ ,  $k_{TR}$ ,  $k_{RR}$  are the translational and rotational spring constants. The quantities are now non-dimensionalized

$$\begin{aligned} X &= \frac{x}{l}, \quad (\tilde{u}, \tilde{w}) = \frac{(u_0, w_0)}{h}, \quad \eta = \frac{l}{h}, \quad N_{x0} = \frac{\tilde{N}_{x0}}{A_{110}} \\ (a_{11}, a_{55}, b_{11}, d_{11}) &= \left( \frac{A_{11}}{A_{110}}, \frac{A_{55}}{A_{110}}, \frac{B_{11}}{A_{110}h}, \frac{D_{11}}{A_{110}h^2} \right) \\ (\bar{a}_{11}, \bar{a}_{55}, \bar{b}_{11}, \bar{d}_{11}) &= \left( \frac{A_{11}h^2}{D_{110}}, \frac{A_{55}h^2}{D_{110}}, \frac{B_{11}h}{D_{110}}, \frac{D_{11}}{D_{110}} \right) \\ \tau &= \frac{t}{L} \sqrt{\frac{A_{110}}{I_{00}}}, \quad (\bar{I}_0, \bar{I}_1, \bar{I}_2) = \left( \frac{I_0}{I_{00}}, \frac{I_1}{I_{00}h}, \frac{I_2}{I_{00}h^2} \right) \\ \Phi &= \frac{A_{110}h^2}{D_{110}}, \quad \omega = \Omega l \sqrt{\frac{I_{00}}{A_{110}}} \end{aligned}$$

$$\beta_{TL} = \frac{k_{TL}L}{A_{110}}, \beta_{TR} = \frac{k_{TR}L}{A_{110}}, \beta_{RL} = \frac{k_{RL}L}{D_{110}}, \beta_{RR} = \frac{k_{RR}L}{D_{110}} \quad (21)$$

On using these dimensionless quantities, a dimensionless form of the governing equations of motion are now

$$a_{11} \frac{\partial^2 \tilde{U}}{\partial X^2} + b_{11} \frac{\partial^2 \varphi}{\partial X^2} = \tilde{I}_0 \frac{\partial^2 \tilde{U}}{\partial \tau^2} + \tilde{I}_1 \frac{\partial^2 \varphi}{\partial \tau^2} \quad (22)$$

$$K_s a_{55} \left( \frac{\partial^2 \tilde{W}}{\partial X^2} + \eta \frac{\partial \varphi}{\partial X} \right) - N_{x0} \frac{\partial^2 \tilde{W}}{\partial X^2} = \tilde{I}_0 \frac{\partial^2 \tilde{W}}{\partial \tau^2} \quad (23)$$

$$\bar{b}_{11} \frac{\partial^2 \tilde{U}}{\partial X^2} + \bar{d}_{11} \frac{\partial^2 \varphi}{\partial X^2} - K_s \bar{a}_{55} \eta \left( \frac{\partial \tilde{W}}{\partial X} + \eta \varphi \right) = \Phi \left( \bar{I}_1 \frac{\partial^2 \tilde{U}}{\partial \tau^2} + \bar{I}_2 \frac{\partial^2 \varphi}{\partial \tau^2} \right) \quad (24)$$

The boundary conditions in dimensionless form become

$$\text{For } X = 0, \tilde{U} = 0$$

$$K_s a_{55} \frac{\partial \tilde{W}}{\partial X} + K_s a_{55} \eta \varphi + \beta_{TL} \tilde{W} = 0 \quad (25)$$

$$K_s a_{55} \frac{\partial \tilde{W}}{\partial X} + K_s a_{55} \eta \varphi + \beta_{TR} \tilde{W} = 0$$

$$\text{For } X = 1 : \tilde{U} = 0$$

$$K_s a_{55} \frac{\partial \tilde{W}}{\partial X} + K_s a_{55} \eta \psi - \beta_{TR} \tilde{W} = 0 \quad (26)$$

$$\bar{b}_{11} \frac{\partial \tilde{U}}{\partial X} + \bar{d}_{11} \frac{\partial \psi}{\partial X} - \beta_{RR} \psi = 0$$

## 4 The Chebyshev Collocation Method

Displacement problems involving CNTRC beams with various boundary conditions can be modelled using the Chebyshev collocation method (CCM) [11]. The technique is based on the Gauss–Chebyshev–Lobatto method which constructs an interpolation grid in the interval  $[-1, 1]$ , specifically

$$x_j = \cos\left(\frac{j\pi}{N}\right), j = 0, 1, 2, 3, \dots, N \quad (27)$$

A differentiation Chebyshev matrix,  $D_N$ , of dimensions  $(N + 1)$  by  $(N + 1)$  is created from the grid points by using Lagrange polynomials of degree  $N$  at each of the points by the differentiation of the polynomials, and then assessing the result at each of the points [11]. The elements of the matrix,  $D_N$ , are

$$(D_N)_{00} = \frac{2N^2 + 1}{6}, (D_N)_{NN} = -\frac{2N^2 + 1}{6} \quad (28a)$$

$$(D_N)_{jj} = \frac{-x_j}{2(1 - x_j^2)}, j = 1, 2, 3, \dots, N - 1 \quad (28b)$$

$$(D_N)_{ij} = \frac{c_j(-1)^{i+j}}{c_j(x_i - x_j)}, i \neq j, i, j = 0, 1, 2, \dots, N \quad (28c)$$

Here

$$c_i = \begin{cases} 2, & i = 0 \text{ or } N \\ 1, & \text{otherwise} \end{cases} \quad (29)$$

A change in the range of the independent variables for both the governing equations and boundary conditions (Eqs. 22–26) is needed from  $X \in [0, 1]$  to  $\zeta \in [-1, 1]$  by the use of the relationship  $\zeta = (2X - 1)$ ,  $\in [-1, 1]$ . Also, for the separation of temporal and spatial terms the following is used

$$\tilde{U}(X, \tau) = U(X)e^{i\omega\tau} \quad (30a)$$

$$\tilde{W}(X, \tau) = W(X)e^{i\omega\tau} \quad (30b)$$

$$\varphi(X, \tau) = \psi(X)e^{i\omega\tau} \quad (30c)$$

Here  $\omega$  is the dimensionless natural frequency. On substituting the displacement functions and changing the range, Eqs. (22–26) can be rewritten as

$$4a_{11} \frac{\partial^2 U}{\partial \zeta^2} + 4b_{11} \frac{\partial^2 \psi}{\partial \zeta^2} = -\bar{I}_0 \omega^2 U - \bar{I}_1 \omega^2 \psi \quad (31)$$

$$K_s a_{55} \left( 4 \frac{\partial^2 W}{\partial \zeta^2} + 2\eta \frac{\partial \psi}{\partial \zeta} \right) - 4N_{x0} \frac{\partial^2 W}{\partial \zeta^2} = -\bar{I}_0 \omega^2 W \quad (32)$$

$$K_s a_{55} \left( 4 \frac{\partial^2 W}{\partial \zeta^2} + 2\eta \frac{\partial \psi}{\partial \zeta} \right) - 4N_{x0} \frac{\partial^2 W}{\partial \zeta^2} = -\bar{I}_0 \omega^2 W \quad (33)$$

At  $\zeta = -1 : U = 0$

$$2K_s a_{55} \frac{\partial W}{\partial \zeta} + K_s a_{55} \eta \psi + \beta_{TL} W = 0 \quad (34)$$

$$2\bar{b}_{11} \frac{\partial U}{\partial \zeta} + 2\bar{d}_{11} \frac{\partial \psi}{\partial \zeta} + \beta_{RL} \psi = 0$$

At  $\zeta = 1 : U = 0$

$$2K_s a_{55} \frac{\partial W}{\partial \zeta} + K_s a_{55} \eta \phi - \beta_{TR} W = 0 \quad (35)$$

$$2\bar{b}_{11} \frac{\partial U}{\partial \zeta} + 2\bar{d}_{11} \frac{\partial \phi}{\partial \zeta} - \beta_{RR} \phi = 0$$

To solve vibration problems with the Chebyshev collocation method, the left-hand sides of Eqs. (31–33) can be written, using the Chebyshev differentiation matrix [11]

$$EM1 = 4a_{11}([1 \ 0 \ 0] \otimes D_2) + 4b_{11}([0 \ 0 \ 1] \otimes D_2) \quad (36)$$

$$EM2 = K_s(4([0 \ 1 \ 0] \otimes D_2) + 2\eta([0 \ 0 \ 1] \otimes D_1)) - 4N_{x0}([0 \ 1 \ 0] \otimes D_2) \quad (37)$$

$$EM3 = 4\bar{b}_{11}([1 \ 0 \ 0] \otimes D_2) + 4\bar{d}_{11}([0 \ 0 \ 1] \otimes D_2) - K_s \eta \bar{a}_{55}(2([0 \ 1 \ 0] \otimes D_1) + \eta([0 \ 0 \ 1] \otimes I)) \quad (38)$$

Here  $\otimes$  is the Kronecker product and sizes of  $EM1$ ,  $EM2$  and  $EM3$  are  $(N + 1) \times 3(N + 1)$ . Here  $N$  is the number of Chebyshev points. Stacking these matrices together gives an overall matrix of size  $3(N + 1) \times 3(N + 1)$

$$EM = \begin{bmatrix} EM1 \\ EM2 \\ EM3 \end{bmatrix} [\delta]^T \quad (39)$$

Here  $[\delta]^T$  is the displacement vector given as

$$[\delta]^T = [U_1 \ U_2 \ \dots \ U_{N+1} \ W_1 \ W_2 \ \dots \ W_{N+1} \ \psi_1 \ \psi_2 \ \dots \ \psi_{N+1}]^T \quad (40)$$

At each end of the beams the displacements are  $U_1 \ W_1 \ \psi_1 \ U_{N+1} \ W_{N+1} \ \psi_{N+1}$  and so a displacement vector can now be written as

$$[\delta]^T = [W_1 \ \psi_1 \ U_{N+1} \ W_{N+1} \ \psi_{N+1} \ U_2 \ U_3 \ \dots \ U_N \ W_2 \ W_3 \ \dots \ W_N \ \psi_2 \ \psi_3 \ \dots \ \psi_N]^T \quad (41)$$

For the boundary conditions of Eqs. (34, 35), at  $\zeta = -1$

$$([00] \otimes [100 \dots \dots 0])[\delta]^T = 0([00] \otimes [100 \dots \dots 0])[\delta]^T = 0 \quad (42)$$

$$2K_s a_{55}([010] \otimes [D_1(1, :)])[\delta]^T + K_s a_{55} \eta([001] \otimes [100 \dots \dots 0])[\delta]^T + \beta_{TL}([010] \otimes [100 \dots \dots 0])[\delta]^T = 0 \quad (43)$$

$$2\bar{b}_{11}([100] \otimes [D_1(1, :)])[\delta]^T + 2\bar{d}_{11}([001] \otimes [D_1(1, :)])[\delta]^T \quad (44)$$

and for  $\zeta = 1$

$$([100] \otimes [000 \dots \dots 1])[\delta]^T = 0 \quad (45)$$

$$2K_s a_{55}([010] \otimes [D_1(N+1, :)])[\delta]^T + K_s a_{55} \eta([001] \otimes [000 \dots \dots 1])[\delta]^T + K_s a_{55} \eta([001] \otimes [000 \dots \dots 1])[\delta]^T \quad (46)$$

$$2\bar{b}_{11}([100] \otimes [D_1(N+1, :)])[\delta]^T + 2\bar{d}_{11}([001] \otimes [D_1(N+1, :)])[\delta]^T - \beta_{RR}([001] \otimes [000 \dots \dots 1])[\delta]^T = 0 \quad (47)$$

A system of algebraic equations can now be formed on application of the boundary equations

$$\begin{bmatrix} [S_{bb}] & [S_{bd}] \\ [S_{db}] & [S_{dd}] \end{bmatrix} \begin{Bmatrix} [\delta_b] \\ [\delta_d] \end{Bmatrix} = \omega^2 \begin{bmatrix} [0] & [0] \\ [0] & [M_{dd}] \end{bmatrix} \begin{Bmatrix} [\delta_b] \\ [\delta_d] \end{Bmatrix} \quad (48)$$

Here,  $b, d$  are subscripts which refer to the points used to write the algorithm of the boundary conditions and the equations of motion, respectively. Here  $S_{bb}$  and  $S_{bd}$  have sizes of  $6 \times 6$  and  $6 \times (3(N+1) - 6)$ , respectively. The size of  $S_{db}$  is  $(3(N+1) - 6) \times 6$  and the size of  $S_{dd}$  is  $(3(N+1) - 6) \times (3(N+1) - 6)$ .  $M_{dd}$  is the inertia matrix with a size the same as  $S_{dd}$  and can be written as

$$M_{dd} = - \begin{bmatrix} \bar{I}_0[I] & 0[I] & \bar{I}_1[I] \\ 0[I] & \bar{I}_0[I] & 0[I] \\ \Phi \bar{I}_1[I] & 0[I] & \Phi \bar{I}_2[I] \end{bmatrix} \quad (49)$$

Here  $[I]$  is the identity matrix of size  $(N-1) \times (N-1)$ .

The free frequency results can be solved by setting  $N_{x0} = 0$  and for loaded CNTRC beams  $N_{x0}$  is included.

## 5 Numerical Results

Numerical results for the natural vibrations of CNTRC beams, with various boundary conditions, are first presented to validate the viability and exactness of the present method. This is followed in a further section with calculations involving an analysis when the beams are bounded by non-classical boundary conditions while experiencing compressive loading.

### 5.1 Free Vibration Analysis of CNTRC Beams

Here, with  $N_{x0} = 0$ , after discussion of validation, key parameters which represent the characteristics of CNTRC beam vibrations, for example,  $\eta = l/h$ , the CNT volume fraction and the boundary spring stiffnesses are investigated.

For validation of the present method, the first three calculated non-dimensional frequency parameters  $\bar{\Omega} = \omega l \sqrt{\rho^p [1 - (v^p)^2] / E^p}$  for various CNT distributions and boundary conditions are compared with those published by Lin et al. [12], and, Yas and Samadi [10]. The comparisons are given in Table 1. The geometrical and material constants of the beams used here to make comparison were  $l/h = 15$ ,  $E_{11}^s = 600$  GPa,  $E_{22}^s = 10$  GPa,  $G_{12}^s = 17.2$  GPa,  $E^p = 2.5$  GPa,  $v_{12}^s = 0.19$ ,  $v^p = 0.3$ ,  $\rho^s = 1400$  kg/m<sup>3</sup>,  $\rho^p = 1190$  kg/m<sup>3</sup>. Although the results are generally lower than those of Refs. [10, 12] there is fairly good agreement.

The first three dimensionless free frequencies  $\bar{\Omega} = \omega l \sqrt{\rho^p [1 - (v^p)^2] / E^p}$  with C-S boundary conditions are shown in Table 2. The frequencies are seem to get larger in line with the volume fraction.

**Table 1** Results for the first three frequency parameters  $\bar{\Omega} = \omega l \sqrt{\rho^p [1 - (v^p)^2] / E^p}$  for various CNT distributions and different boundary conditions ( $l/h = 15$ ,  $V_s^* = 0.28$ )

Distributions	Modes	S-S			C-F		
		Ref. 12	Ref. 10	Current	Ref. 12	Ref. 10	Current
U-D beam	1	1.4348	1.4401	1.3999	0.5600	0.5612	0.5520
	2	4.1050	4.1362	4.0658	2.4449	2.4614	2.2439
	3	6.8595	6.9245	6.8345	5.2005	5.2446	5.1692
X beam	1	1.6409	1.6493	1.6342	0.6566	0.6586	0.6499
	2	4.4333	4.4752	4.3821	2.6763	2.6987	2.6712
	3	7.2258	7.3068	7.1199	5.5589	5.6150	5.5491
V beam	1	1.3975	1.4027	1.3891	0.4753	0.4761	0.4653
	2	3.8370	3.8639	3.7982	2.2543	2.2685	2.2452
	3	6.6976	6.7618	6.6259	4.9590	5.0007	4.8912

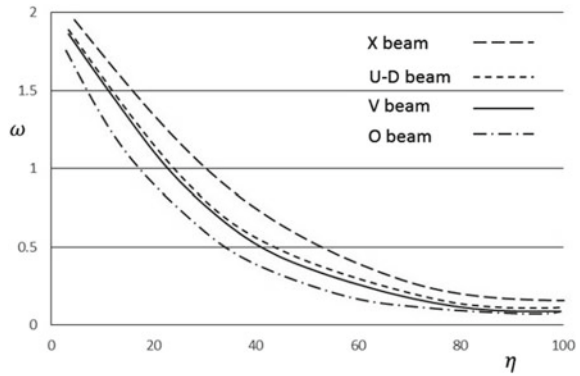
**Table 2** Variation of first three dimensionless frequencies  $\bar{\Omega} = \omega l \sqrt{\rho^p [1 - (v^p)^2] / E^p}$  with different CNT distributions and volume fractions  $(V_s^*) / (l/h = 15, (C-S))$

Distributions	C-S			$V_s^* = 0.16$			$V_s^* = 0.28$			
	$V_s^* = 0.12$	1st Mode	2nd Mode	3rd Mode	1st Mode	2nd Mode	3rd Mode	1st Mode	2nd Mode	3rd Mode
U-D beam	1.224	3.001	4.896	4.896	1.523	3.654	6.225	1.782	4.276	6.943
V beam	1.328	2.832	4.365	4.365	1.374	3.436	5.894	1.675	4.102	6.785
O beam	1.014	2.652	4.538	4.538	1.234	3.284	5.609	1.508	3.856	6.657
X beam	1.343	3.134	5.078	5.078	1.679	4.011	6.428	1.987	4.555	7.296

**Table 3** Dimensionless free frequencies of CNTCR beams with E-E boundary conditions ( $\beta = \beta_{RL} = \beta_{RR} = \beta_{TL} = \beta_{TR}$ ,  $V_s^* = 0.16$ )

$\beta$	U-D beam		O beam		V beam	
	$\eta = 5$	$\eta = 10$	$\eta = 5$	$\eta = 10$	$\eta = 5$	$\eta = 10$
$10^{-2}$	0.1389	0.1387	0.1388	0.1385	0.1387	0.1384
$10^{-1}$	0.4461	0.4259	0.4300	0.4168	0.4364	0.4243
$10^0$	1.2538	0.9917	1.1482	0.9519	1.2002	0.9901
$10^1$	1.8522	1.4999	1.5966	1.2637	1.8329	1.4821
$10^2$	2.1098	1.7561	1.9540	1.5481	2.0548	1.7084
$10^3$	2.2985	2.0365	2.2203	1.9487	2.2541	1.9568
$10^4$	2.3662	2.1161	2.2962	1.9411	2.3385	1.9978

**Fig. 2** Dimensionless fundamental frequencies with elastic-elastic boundary conditions  $\beta_{TL} = \beta_{TR} = 10$ ,  $\beta_{RL} = \beta_{RR} = 10$ . ( $V_s^* = 0.16$ )



The results for CNTRC beams with non-classical boundary conditions (E-E) are given in Table 3. The variation of the spring constants is from  $10^{-2}$  to  $10^4$  and it can be observed that the frequency increases with the value of  $\beta$  for each type of CNTRC beam.

Figure 2 shows the variation of the dimensionless fundamental frequencies for four types of CNTRC beams versus thickness ratio. E-E boundary conditions were used here. As can be observed, the beam frequencies dropped rapidly as the thickness ratio increased.

### 5.2 Analysis of Compressed CNTRC Beams

Here the vibrations with the CNTRC beam subjected to compressive loading, and with non-classical boundary conditions are studied. On Fig. 3 is shown the relationship of the dimensionless frequency as the compressive loading increases for different CNTRC beam types. It should be noted that when  $N_{x0} = 0$ , the natural



**Fig. 3** Fundamental frequency versus the compressive loading of the beams with the elastic-elastic boundary condition  $\beta_{TL} = \beta_{TR} = \beta_{RL} = \beta_{RR} = 10^2 (\eta = 15, V_s^* = 0.16)$

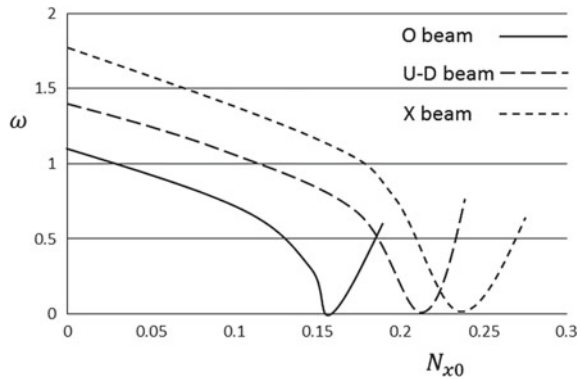
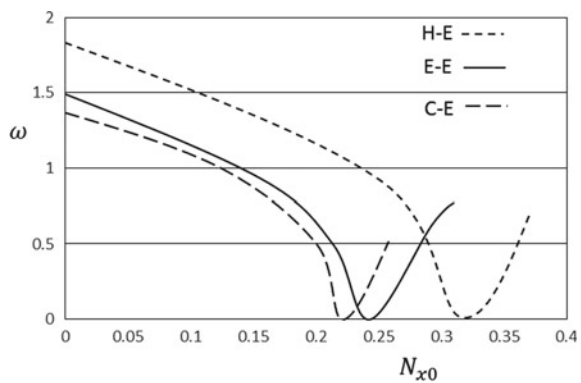


**Fig. 4** Fundamental frequency versus the compressive loading of U-D beams for different non-classical boundary conditions ( $\eta = 15, V_s^* = 0.16$ )



frequency is found. As the compression is increased a steady decline in frequency is observed until reaching zero, at which point the value of  $N_{x0}$  is the critical buckling loading.

Figure 4 also shows frequency versus compressive loading of a U-D beam. The variation for each of the non-classical boundary conditions are similar to that already shown on Fig. 3.

## 6 Conclusions

The vibration characteristics, both natural and loaded, of CNTRC beams, with both traditional and non-traditional boundary conditions, have been explored. The Chebyshev collocation method was utilized to solve the governing equations based on the Timoshenko formulation. The accuracy of the developed model and solution method was tested with results from the literature, and comparison was found to be satisfactory. For different boundary conditions and volume fractions it was found for each

that the natural frequencies which were highest were those of the X beam. Also, as the beam thickness ratio increased then the free frequencies for each of the CNTRC beam types decreased quite dramatically. Regarding the beams' vibration characteristics when under compression, it was found that the frequencies decreased greatly as the compression loading increased with the variation of the decrease noted as being dependent on the nature of elastic boundary condition used and on the nature of the CNTRC beam used.

**Acknowledgements** This work is supported by the Nazarbayev University Small Competitive Grant No. 090118FD5317. The authors declare that there is no conflict of interest and funding associated with this investigation.

## References

1. Zhu R, Pan E, Roy AK (2007) Molecular dynamics study of the stress-strain behavior of carbon-nanotube reinforced Epon 862 composite. *Mater Sci Eng* 447:51–57
2. Fox L, Parker IB (1968) Chebyshev polynomials in numerical analysis. Oxford University Press, London
3. El Barbary EME (2005) Chebyshev finite difference method for the solution of boundary-layer equations. *Appl Math Comput* 160:487–498
4. Biazar J, Ebrahimi H (2012) Chebyshev wavelets approach for nonlinear systems of Volterra integral equations. *Comput Math Appl* 63:608–616
5. Doha EH, Abd-Elhameed WM, Bassuony MA (2013) New algorithms for solving high even-order differential equations using third and fourth Chebyshev-Galerkin method. *J Comput Phys* 236:563–579
6. Zhang H, Gao C, Li H, Pang F, Zou T, Wang H, Wang N (2020) Analysis of functionally graded carbon nanotube-reinforced composite structures: a review. *Nanotechnol Rev* 9:1408–1426
7. Civalek Ö, Akbas SD, Akgöz B, Dastjerdi S (2021) Forced vibration analysis of composite beams reinforced by carbon nanotubes. *Nanomaterials* 11:571
8. Karamanli A, Vo TP (2021) Finite element model for carbon nanotube-reinforced and graphene nanoplatelet-reinforced composite beams. *Compos Struct* 264:113739
9. Ke LL, Yang J, Kitipornchai S (2010) Nonlinear free vibration of functionally graded carbon carbon nanotube-reinforced composite beams. *Compos Struct* 92:676–683
10. Yas MH, Samadi N (2012) Free vibration and buckling analysis of carbon nanotube-reinforced composite Timoshenko beams on elastic foundation. *Int J Press Vessels* 98:119–128
11. Wattanasakulpong N, Mao Q (2017) Stability and vibration analyses of carbon nanotube-reinforced composite beams with elastic boundary conditions: chebyshev collocation method. *Mech Adv Mater Struct* 24(3):260–270
12. Lin F, Xiang Y (2014) Vibration of carbon nanotube reinforced composite beams based on the first and third order beam theories. *Appl Math Model* 38:3741–3754

# Analytical, Numerical and Experimental Analysis of the Creep Behaviour of Polyethylene Polymers



A. Mostafa, D. G. S. Sanchez, N. Sirach, R. V. Padilla, and H. Alsanat

**Abstract** Polyethylene (PE) is a semi-crystalline polymer that has been used for decades in many different applications. Two commonly used forms of PE are high-density polyethylene (HDPE) and ultra-high molecular weight polyethylene (UHMWPE). Since the material is used in various industrial applications, ranging from prosthetic joints to rotational moulded tanks, the need to understand its mechanical behaviour under different loading scenarios is of high importance. Creep is a particularly important mechanical property for polymers due to their relaxation characteristics associated with prolonged loading of the polymers' chains. As such, understanding the creep behaviour of PE products is very important for its long-term performance. In the present investigation, experimental testing, analytical analysis and numerical modelling using the finite element (FE) method have been conducted on HDPE and UHMWPE samples subjected to tensile load, step-loaded creep, short-term creep, and long-term creep. Boltzmann superposition principle was utilised to predict the long-term creep behaviour using short-term creep test results. The adopted stress relaxation models, using Maxwell elements, successfully captured the experimental viscoelastic and viscoplastic response of PE. A parametric investigation was conducted using ABAQUS FE software to obtain the optimum Prony series components that can accurately simulate the creep behaviour under constant and stepped-loading scenarios. The results showed great agreement between the experimental, analytical and numerical methods. The developed FE models can be used to predict the serviceability of PE products after prolonged exposure to constant loading cases.

**Keywords** Polyethylene · High-density polyethylene (HDPE) · Ultra-high molecular weight polyethylene (UHMWPE) · Polymer · Creep · Tensile test · Modelling · Finite element analysis (FEA)

---

A. Mostafa (✉) · D. G. S. Sanchez · N. Sirach · R. V. Padilla  
Faculty of Science and Engineering, Southern Cross University, Lismore, NSW 2480, Australia  
e-mail: [ahmed.thabet@scu.edu.au](mailto:ahmed.thabet@scu.edu.au)

H. Alsanat  
School of Engineering, Al-Hussein Bin Talal University, Ma'an, Jordan

© The Author(s), under exclusive license to Springer Nature Singapore Pte Ltd. 2022  
M. Abdel Wahab (ed.), *Proceedings of the 4th International Conference on Numerical Modelling in Engineering*, Lecture Notes in Mechanical Engineering,  
[https://doi.org/10.1007/978-981-16-8806-5\\_5](https://doi.org/10.1007/978-981-16-8806-5_5)

## 1 Introduction

Polyethylene (PE) is a semi-crystalline polymer that has been used for decades in many different industries around the world. PE has had a rapid increase in consumption in the past few decades, where its production doubles every four years, making up about 31% of plastic production worldwide [1]. As production and applications of PE increase, there is a necessity for methods to determine the reliability of the material under different loading scenarios. As such, the mechanical characteristics of PE, such as tensile strength, impact strength, thermal stability, compressive strength and creep modulus, have been investigated in recent years to determine their feasibility under different applications [2]. The creep behaviour is particularly critical in engineering applications where products are under constant loads for extended periods of time. The ability for PE to withstand loading for prolonged periods has allowed it to become widely used within the manufacturing and hydraulic industries [3]. One of many applications of PE can be seen in pipe and tank systems, where high creep resistance is required due to the constant loading subjected to the pipe or tank [4]. Since PE materials' behaviour widely differs depending on the materials morphology and cross-linking density of the long/short chains, understanding the creep behaviour of a wide range of PE products is critical for its safe and efficient application in industry.

Creep testing is an important experimental method for determining many different material characteristics, including the physical aging and viscoelasticity of a non-linear material [5]. The experimental procedure for creep testing is often very time consuming and can require holding the material under a constant load for up to 10,000 h depending on the test standard [6, 7]. Due to the extensive time requirements for creep testing, this can be a very expensive and time-consuming process for manufacturers. As a result of this, various attempts have been proposed in the literature for determining the short- and long-term creep behaviour of PE analytically [5, 8, 9]. To minimise manufacturing time and costs, a simple and reliable means of determining the long-term creep behaviour of polymers from short-term experimental data is necessary to reduce costs.

Research has also been conducted to determine the inelastic deformation of polymers and predict the creep behaviour of linear low-density polyethylene using finite element analysis [10, 11]. However, to the authors' knowledge, the implementation of such an approach has yet to be presented and tested with HDPE. The limitations of existing analytical models for the creep prediction of polymers are based on one-dimensional analysis. The implementation of finite element approaches for the creep analysis of polymers will enable three-dimensional analysis, allowing for more complex structures to be modelled, such as PE rotational moulded tanks. The development of an accurate finite element model that can predict the long-term creep behaviour of HDPE and UHMWPE polymers using short-term creep data will significantly reduce manufacturing costs by eliminating costly, long-term experimental procedures.

There are currently a limited number of studies to date on the short- and long-term creep behaviour of HDPE and UHMWPE polymers. In addition, there are limited analytical and numerical studies to date that can accurately predict the creep behaviour of polymers. The reliability of modelling is still unknown across various factors and conditions such as varying dimensions, loading scenarios and polymer morphologies, limiting its application in design. This paper aims to expand the understanding of the creep response of HDPE and UHMWPE polymers by experimentally conducting creep tests on several polymers subjected to varying loading conditions. A one-dimensional analytical model is developed that utilised four Maxwell models to predict the behaviour of the experimental results. Additionally, a three-dimensional finite element model is developed to predict the long-term creep behaviour of HDPE and UHMWPE polymers based on short-term creep data.

## 2 Experimental Methods

### 2.1 Test Programme

In this study, three types of commercial grade PE samples were used, including two types of HDPE, namely HDPE 100 and HDPE 300, and one type of UHMWPE, namely Polystone 7000. These samples were tested under different loading scenarios to understand their mechanical behaviour. These loading scenarios included displacement-controlled tension tests, load-controlled tension tests, strain-rate-controlled tension tests, step-loaded creep tests, short-term creep tests, and long-term creep tests. All specimens were tested under axial tension using a 1 kN MTS universal testing machine (UTM).

Dog-bone test coupons were cut from a large sheet for each polymer type using a computer numerical control (CNC) machine. For each polymer type tested, all the test coupons were cut from the same sheet. The test coupons had a total length of 165 mm, gauge length of 50 mm, and gauge width of 13 mm, which is in accordance with ASTM D638 [12]. The nominal thickness of all three polymer sheets was 3 mm. Prior to testing, the cross-sectional dimensions of each test coupon were recorded using digital callipers with a tolerance of 0.01 mm. These recorded measurements were used for the analysis of test results.

### 2.2 Loading Schemes

Each of the three different PE types were subjected to monotonic displacement-controlled, load-controlled and strain-controlled tension. For each of these tests, the specimens were continuously loaded until fracture occurred, or until the maximum stroke of the test machine was reached. For the displacement-controlled tension tests,

the UTM was operated under a displacement-controlled setting at a constant rate of 5 mm/min. For the load-controlled tension tests, five different loading schemes were conducted at rates of 1, 5, 10, 30 and 60 N/s. For the strain-controlled tension tests, the feedback from the extensometer was used to control the loading rate of the UTM. There were three different strain-controlled loading schemes and they were 0.005, 0.01 and 0.05 mm/mm/min.

In addition to monotonic tension tests, creep tests were also conducted on each of the three different PE types. The creep tests included step-loaded creep, short-term creep and long-term creep. The creep tests were conducted with guidance from ASTM D2990 [7]. The step-loaded creep tests were conducted over nine hours, whereby the specimens were loaded to 4 MPa and held at this stress for three hours, then loaded to 6 MPa and held for three hours, then loaded to 8 MPa and held for the final three hours. Once the final stress increment had been held for three hours, the load was released, and testing was concluded. The short-term creep tests were conducted for 24 h, where the test specimen was held at a constant prescribed stress value for the entirety of the test. Six different loading schemes were used for the short-term creep tests, and these prescribed stress values were 2, 4, 6, 8, 10, and 12 MPa. The long-term creep tests were conducted for 72 h, and the specimen was held at the prescribed stress value for the entirety of the test. The different prescribed stress values for the long-term creep tests were 4, 6 and 8 MPa. A constant loading rate of 5 N/s was used for all the creep tests until the desired prescribed stress increment was achieved. After this, the UTM held the stress at this level for the required length of time by slightly adjusting the crosshead position when necessary. All the creep tests in this study were automatically executed by a real-time controlling program, where the displacement and loading readings from the MTS machine were the controlling parameters.

### ***2.3 Test Setup and Instrumentation***

The axial deformation of all the test specimens was recorded using an extensometer that was fastened to the specimen at the mid-length. The extensometer had a gauge length of 50 mm. For the specimens tested under a strain-controlled rate, the feedback from the extensometer was used to control the loading rate of the test machine. Biaxial strain gauges were also attached to the mid-length of some test coupons to measure the axial and lateral displacement at this region to determine the value of Poisson's ratio. These biaxial strain gauges had a gauge length of 5 mm, gauge resistance of 120  $\Omega$  and gauge factor of 2.08. Poisson's ratio readings for the different polymers were obtained from the biaxial strain gauge readings. A data logging system was used to measure all the load, displacement and strain values.

### 3 Analytical Analysis

#### 3.1 Linear Viscoelastic and Viscoplastic Modelling

By considering the Boltzmann superposition [13] principle of linear systems, a point in time of the materials response can be expressed as the addition of the loading responses of small intervals of the materials history. The stress, strain and relaxation time ( $\tau$ ) relationship is expressed as:

$$\sigma(t) = \int_{-\infty}^t \phi(t - \tau) \dot{\varepsilon}(\tau) d\tau \quad (1)$$

where  $\phi(t - \tau)$  is known as a transient stress relaxation function and  $\dot{\varepsilon}$  is the strain-rate. Alternatively, the strain of the material at time  $t$  can also be expressed integrally:

$$\varepsilon(t) = \int_{-\infty}^t J(t - \tau) \dot{\sigma}(\tau) d\tau \quad (2)$$

In which  $J(t - \tau)$  represents the transient creep compliance function and  $\dot{\sigma}$  is the stress-rate. Since material aging is not considered, stress and strain depend on the material's loading history. As such, Eqs. 1 and 2 can be rewritten as:

$$\sigma(t) = \int_0^t \phi(t - \tau) \dot{\varepsilon}(\tau) d\tau \quad (3)$$

$$\varepsilon(t) = \int_0^t J(t - \tau) \dot{\sigma}(\tau) d\tau \quad (4)$$

Since creep is a slow, progressive deformation under constant stress, the one-dimensional history of stress  $\sigma$  being dependent on time  $t$  can be treated as a step function initiating at time zero:

$$\sigma(t) = \sigma_0 H(t) \quad (5)$$

where  $\sigma_0$  is the constant stress and  $H(t)$  is the unit step function, considering that  $H(t) = \int_0^t \delta(\tau) d\tau$  where  $\delta$  is the Dirac delta function. By substituting Eq. (5) into (4) the creep compliance becomes:

$$J(t) = \frac{\varepsilon(t)}{\sigma_0} \quad (6)$$

In which the intercept of the creep curve on the strain axis is the instantaneous elasticity  $J_0$  from which the relaxation phase can be implemented into the Boltzmann

superposition integral. However, as a transient response is expected, an exponential is implemented within relaxation. Equation 6 can be expressed in differential form [13], thus the monotonical increment of the creep function can be written as:

$$J(t) = J_0 + \int_0^t Y(\tau) \left[1 - e^{-\frac{t}{\tau}}\right] d\tau \quad (7)$$

By considering discrete values,  $Y(\tau)$  can be further simplified:

$$Y(\tau) = \sum_{i=1}^N C_i \delta(\tau - \tau_i) \quad (8)$$

where  $\delta$  is the Dirac delta function. Therefore, by substitution:

$$J(t) = J_0 + \sum_{i=1}^N C_i \left[1 - e^{-\frac{t}{\tau_i}}\right] \quad (9)$$

Furthermore, by substituting Eq. 9 into Eq. 4 and integrating, the following is obtained:

$$\varepsilon(t) = J_0 \sigma(t) + \sigma(t) \sum_{i=1}^N C_i - \sum_{i=1}^N C_i e^{-\frac{t}{\tau_i}} \int_0^t e^{\frac{t}{\tau_i}} \dot{\sigma}(t) dt \quad (10)$$

If only one relaxation time  $\tau_1$  ( $N = 1$ ) is considered, then:

$$\varepsilon(t) = J_0 \sigma(t) + C_1 \sigma(t) - C_1 e^{-\frac{t}{\tau_1}} \int_0^t e^{-\frac{t}{\tau_1}} \dot{\sigma}(t) dt \quad (11)$$

By differentiating with respect to  $t$  and manipulating the equation, it can be expressed as:

$$(J_0 + C_1) \sigma(t) + \tau_1 J_0 \sigma'(t) = \varepsilon(t) + \tau_1 \varepsilon'(t) \quad (12)$$

where  $C_1$  is an empirical constant. Alternatively, if multiple relaxation times  $\tau_N$  ( $N > 1$ ) are considered, the differentiation formulation of linear viscoelastic modelling takes the following form:

$$\left[ p_0 + p_1 \frac{\partial}{\partial t} + p_2 \frac{\partial^2}{\partial t^2} + \dots \right] \sigma(t) = \left[ q_0 + q_1 \frac{\partial}{\partial t} + q_2 \frac{\partial^2}{\partial t^2} + \dots \right] \varepsilon(t) \quad (13)$$

where  $p_i$  and  $q_i$  are functions of  $J_0$  (i.e. instantaneous creep compliance),  $C_i$  and  $\tau_i$ .



### 3.2 Linear Viscoelastic Behaviour

Viscoelastic behaviour can be expressed in terms of a combination of springs and dampers, such as the Maxwell model. Based on Eq. 11, the following equation can be formed:

$$J(t) = J_e + J_v(t) = \frac{1}{E_0} + \sum_{i=1}^N \frac{1}{E_i} \left\{ 1 - e^{-\frac{t}{\tau_i}} \right\} \tag{14}$$

where  $E_0, E_i$  and  $N$  are the instantaneous elastic modulus, time-dependent elastic modulus and the number of Maxwell elements in the system, respectively. The instantaneous elastic compliance is  $J_e = \frac{1}{E_0}$ , and the viscoelastic time effects are represented by:

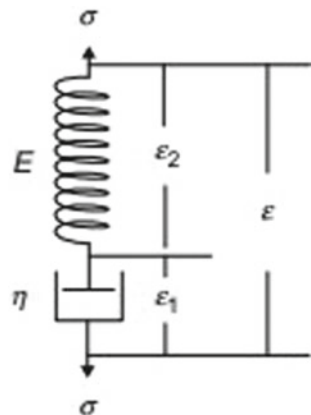
$$J_v(t) = \sum_{i=1}^n \frac{1}{E_i} \left\{ 1 - e^{-\frac{t}{\tau_i}} \right\} \tag{15}$$

where  $\tau_i = \frac{\eta_i}{E_i}$  represents the viscous moduli of the dampers ( $\eta_i$ ). However, deformation is assumed to be quasi-static, inertia is neglected, and the force or stress is the same for both the spring and dashpot, as represented in Fig. 1 [13].

By substituting Eq. 14 into Eq. 5, the governing equation of the viscoelastic model can be obtained as follows:

$$\varepsilon(t) = \int_0^t \left\{ \frac{1}{E_0} + \sum_{i=1}^N \frac{1}{E_i} \left\{ 1 - e^{-\frac{t-\tau}{\tau_i}} \right\} \right\} \sigma'(\tau) d\tau \tag{16}$$

Fig. 1 Maxwell model



### 3.3 Linear Viscoplastic Modelling

When considering viscoplastic behaviour, the creep compliance,  $J(t)$ , can be expressed by a power law:

$$J(t) = J_e + J_p(t) = \frac{1}{E_0} + C_0 t^{C_1} \quad (17)$$

where  $J_e = \frac{1}{E_0}$  is the instantaneous elastic component and  $J_p = C_0 t^{C_1}$  is the time-dependent viscoelastic component. By substituting Eq. 17 into Eq. 5:

$$\varepsilon(t) = \int_0^t \left\{ \frac{1}{E_0} + C_0(t - \tau)^{C_1} \right\} \dot{\sigma}(\tau) d\tau \quad (18)$$

where  $E_0$ ,  $C_0$  and  $C_1$  are the material constants. However, as polymers do not behave linearly due to their viscoelastic and viscoplastic properties, the Maxwell model needs to be represented in a non-linear manner.

### 3.4 Non-Linear Viscoelastic Modelling

The creep behaviour of most polymer materials showed significant dependency on both the stress level and time. As a result, linear modelling can be implemented when the stress is low. The creep compliance,  $J$ , is dependent on stress, strain and time, thus the material properties of the polymer can be correlated with stress and strain. As such, a non-linear model can be represented using the following approach:

$$J(\sigma, t) = J_e(\sigma) + J_v(\sigma, t) = \frac{1}{E_0(\sigma)} + \sum_{i=1}^n \frac{1}{E_i(\sigma)} \left\{ 1 - e^{-\frac{t}{\tau_i(\sigma)}} \right\} \quad (19)$$

where  $E_0(\sigma)$ ,  $E_i(\sigma)$  and  $\tau_i(\sigma)$  are functions of stress. By substituting Eq. 19 into Eq. 5:

$$\varepsilon(t) = \int_0^t \left\{ \frac{1}{E_0(\sigma)} + \sum_{i=1}^n \frac{1}{E_i(\sigma)} \left\{ 1 - e^{-\frac{t-\tau}{\tau_i(\sigma)}} \right\} \right\} \dot{\sigma}(\tau) d\tau \quad (20)$$

### 3.5 Non-linear Viscoplastic Modelling

For a viscoplastic model, creep compliance,  $J(\sigma, t)$ , can be written as:

$$J(\sigma, t) = J_e(\sigma) + J_p(\sigma, t) = \frac{1}{E_0(\sigma)} + C_0(\sigma)t^{C_1(\sigma)} \quad (21)$$

where  $E_0$ ,  $E_1$  and  $C_1$  are all functions of stress. The viscoplastic creep strain can be represented as follows:

$$\varepsilon(t) = \int_0^t \left\{ \frac{1}{E_0(\sigma)} + C_0(\sigma)t^{C_1(\sigma)} \right\} \dot{\sigma}(\tau) d\tau \quad (22)$$

### 3.6 Linear Interpolation of Material Parameters

Due to the non-linear creep response of HDPE and UHMWPE (distinct creep curve for each load level), curve fitting is necessary for the modelling procedure to represent the materials behaviour accurately. Since creep tests were conducted under different stress levels, particular sets of material properties will be required for each stress level. However, for stresses that were not experimentally tested, the material parameters are obtained through linear interpolation. As such, the following equation can be used to obtain the material parameters using the linear interpolation technique:

$$E_0 = E_0(\sigma_m) + \frac{\sigma - \sigma_m}{\sigma_n - \sigma_m} [E_0(\sigma_n) - E_0(\sigma_m)] \quad (23)$$

where  $E_0$  represents the instantaneous elastic modulus of the material as a function of the stress used in the experimental tests ( $\sigma_m$  and  $\sigma_n$ ). Where  $\sigma_m < \sigma < \sigma_n$ . The equation used for linear interpolation of the material parameters can be expressed as:

$$x_i(\sigma) = \frac{1}{E_i(\sigma)} = x_i(\sigma_m) + \frac{\sigma - \sigma_m}{\sigma_n - \sigma_m} [x_i(\sigma_n) - x_i(\sigma_m)] \quad (24)$$

The following equations represent linear interpolation for a viscoplastic model:

$$C_0 = C_0(\sigma_m) + \frac{\sigma - \sigma_m}{\sigma_n - \sigma_m} [C_0(\sigma_n) - C_0(\sigma_m)] \quad (25)$$

$$C_1 = C_1(\sigma_m) + \frac{\sigma - \sigma_m}{\sigma_n - \sigma_m} [C_1(\sigma_n) - C_1(\sigma_m)] \quad (26)$$

### 3.7 Least-Squares Regression

Polymers such as HDPE and UHMWPE are known to have viscoelastic properties, and as such, non-linearity within the creep response of the material is expected since its behaviour is dominated by the stress level and time. The following approach of least-square fitting can be implemented to define the Maxwell models unknown parameters and define the number of elements (N) required to represent the experimental data with minimal error. Based on the creep curves determined from Eq. 1 under constant stress, the developed strain can be expressed as:

$$\varepsilon(t) = \sigma_c \left\{ \frac{1}{E_0} + \sum_{i=1}^N \frac{1}{E_i} \left\{ 1 - e^{-\frac{t}{\tau_i}} \right\} \right\} \quad (27)$$

where  $\sigma_c$  denotes the constant engineering stress, and  $E_0$ ,  $E_i$  and  $\tau_i$  are constants defining the strain–time curve at stress  $\sigma_i$ . By assuming unknown variables such as the relaxation time and instant creep compliance, linear least-square fitting can be used with Eq. 27. This equation becomes linear with variables  $x_0 = \frac{1}{E_0}$  and  $x_i = \frac{1}{E_i}$ :

$$\varepsilon(t) = \sigma_c \left\{ x_0 + \sum_{i=1}^N \left\{ 1 - e^{-\frac{t}{\tau_i}} \right\} x_i \right\} \quad (28)$$

As a result, the least-square error fitting can be represented as:

$$f(x_i) = \sum_{j=1}^{M_k} (\varepsilon_j - \widehat{\varepsilon}_j)^2 \quad (29)$$

where  $M_k$  is the number of strain measurements,  $\widehat{\varepsilon}_j$  is the strain measurement at time  $t_i$ , and  $\varepsilon_j$  are the corresponding theoretical values. By setting  $\frac{df}{dx_i} = 0$ ,  $f(x)$  can be minimised to a set of linear simultaneous equations with respect to material parameter  $x_i$ :

$$[A]_{N*N} \{x\}_{N*1} = \{F\}_{N*1} \quad (30)$$

where,

$$A_{ij} = \sum_{p=1}^{M_k} \left\{ \sigma_c \left[ 1 - e^{-\frac{t_p}{\tau_j}} \right] \left[ 1 - e^{-\frac{t_p}{\tau_i}} \right] \right\} \quad (31)$$

$$F_i = \sum_{p=1}^{M_k} \left\{ (\widehat{\varepsilon}_p - \sigma_c x_o) \left[ 1 - e^{-\frac{t_p}{\tau_i}} \right] \right\} \quad (32)$$

As such,  $i, j = 1, \dots, N$  represents the number of Maxwell models used within the creep model. Similarly,  $\widehat{\varepsilon}_p$  represents strain measurement at time  $t = t_p$ ,  $M_k$  is the number of strain measurements considered in Eqs. 29 and 32, and  $x_o$  is evaluated

**Table 1** Tensile test results

Polymer type	Elastic modulus ( $E$ ) (MPa)	Maximum stress ( $\sigma_f$ ) (MPa)	Poisson's ratio ( $\nu$ )	Yield stress ( $\sigma_y$ ) (MPa)
HDPE 100	1238	25	0.488	25
HDPE 300	1129	23	0.459	23
UHMWPE	831	33	0.485	21

directly from the material's instantaneous response, such that:

$$x_o = \frac{1}{E_0} = \frac{\hat{\epsilon}_0}{\sigma_c} \quad (33)$$

whereby  $\hat{\epsilon}_0$  is the instantaneous strain measured at  $t = t_0 \approx 0$ .

This approach was implemented within MATLAB software to determine the number of elements needed to achieve the minimum possible fitting error. Due to the excessive number of data points obtained from experimentation, data thinning was undertaken prior to MATLAB modelling to reduce the model's computation time.

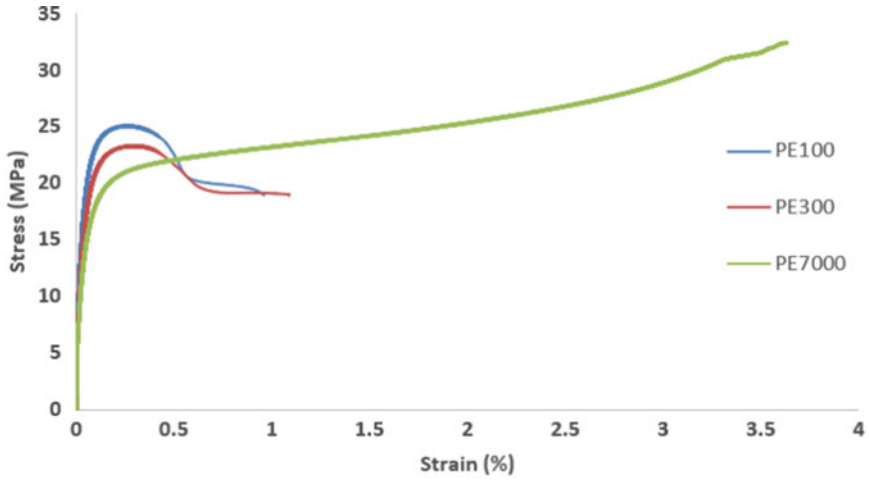
## 4 Experimental and Analytical Results

### 4.1 Displacement Rate Tensile Tests

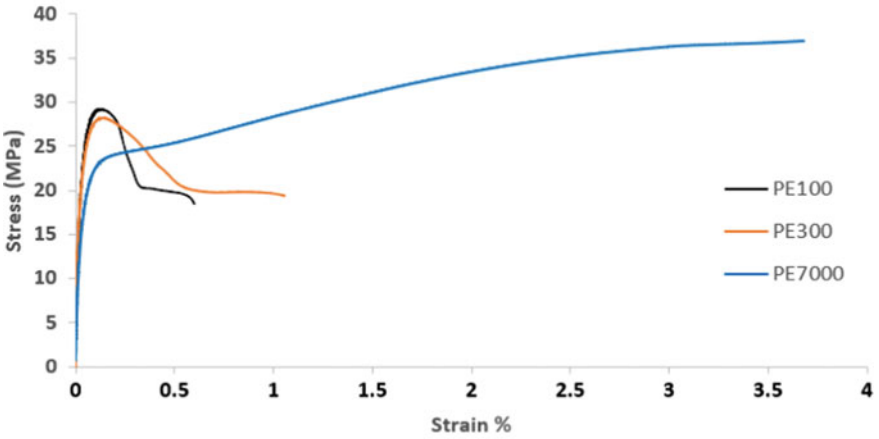
Tension tests were conducted on each of the different PE types under a displacement-controlled setting until failure. All the test samples failed by crazing rupture in the excessively stressed zone of the test coupon. The mechanical properties of the different polymer types were determined based on the average results from these tests. The test results are shown in Table 1, which include the elastic modulus ( $E$ ), the maximum stress ( $\sigma_f$ ), the yield stress ( $\sigma_y$ ), and the Poisson's ratio ( $\nu$ ).

### 4.2 Load Rate Tensile Tests

Based on the load-rate tension testing, stress versus strain was graphed for each material at five different rates, including 1, 5, 15, 30 and 60 N/s. It was found that as the loading rate increased, the viscous behaviour became less prominent as the materials elasticity allowed for greater stresses to be reached at a higher rate. Figure 2a and b show a stress-strain plot of each polymer type subjected to continuously increasing load at a rate of 1 N/s and 60 N/s, respectively. The HDPE polymers have a significantly different stress-strain response to the UHMWPE polymer as



(a)

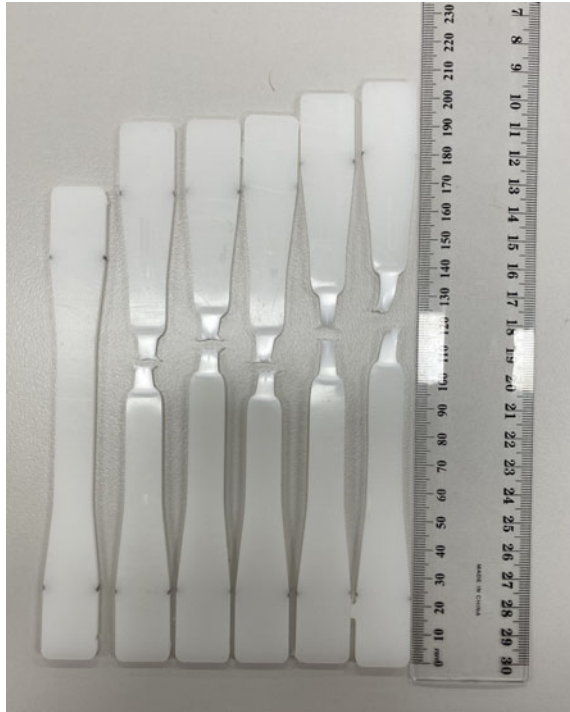


(b)

**Fig. 2** Stress–strain response **a** three different polymer types subjected to a load-rate of 1 N/s; **b** three different polymer types subjected to a load-rate of 60 N/s

seen in both figures. This difference shows the impact that the morphology and molecular structure has on polyethylene polymers. In addition, the rigidity increases as the load rate increases, since at high load rate, molecular chains are incapable of sliding as fast as the load being applied. As a result, all three materials reached yield earlier as the loading rate increased. The PE100 and PE300 reached a yield point of 25 MPa and 23 MPa, respectively, followed by strain softening as the material continued to extrude until rupture. The specimens failed soon after the yielding point since the crosshead movement of the UTM increased rapidly as it attempted to continue increasing the load. The failure modes of the PE100 samples subjected to

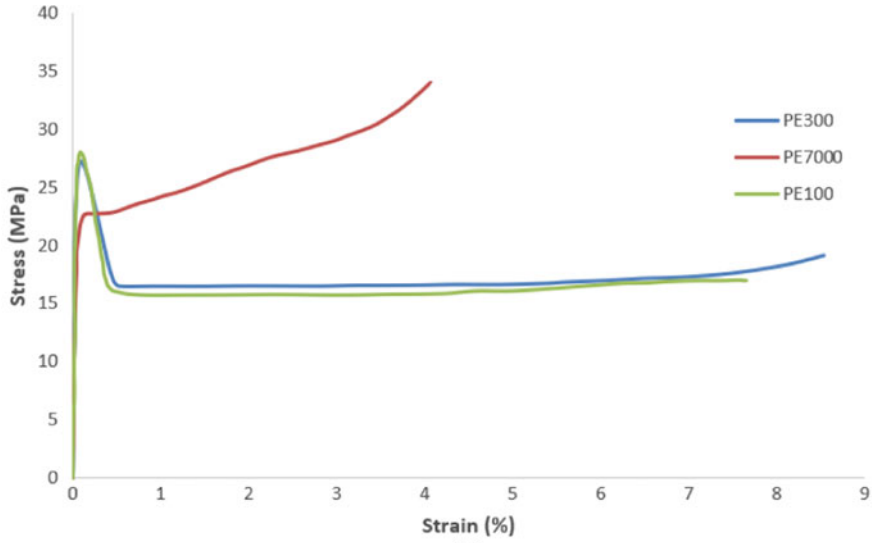
**Fig. 3** Typical failure modes of PE100 specimens subject to load-controlled tension



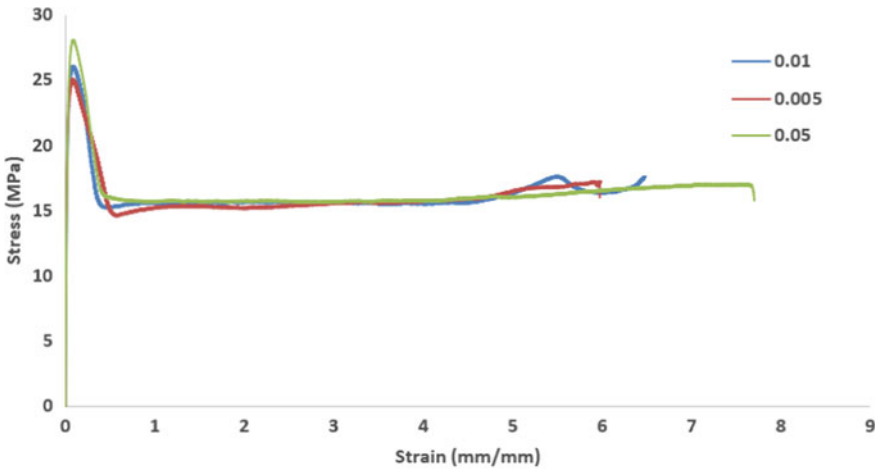
different loading rates is shown in Fig. 3, where samples with progressively slower loading rates is shown from right to left. The PE300 samples exhibited similar failure modes. The PE7000 specimens exhibited a different stress–strain response to PE100 and PE300, where the material reached a yielding point at 21 MPa, followed by strain hardening until rupture. The ultimate strength of the PE7000 samples was approximately 33 MPa, which is significantly greater than the yield stress of the material.

### 4.3 Strain Rate Tensile Tests

Similar to the response of the specimens under different load rates, increasing the strain rate resulted in a change in elastic modulus. At all three of the different strain rates (i.e. 0.005, 0.01 and 0.05), viscoelastic behaviour was prominent. This shows that when the materials were exposed to controlled increases in strain, it enabled extrusion at a more controlled rate, causing the ultimate strain to be much greater than that seen in the tensile load rate results. As seen in Fig. 4, the ultimate strain of both PE100 and PE300 greatly increased compared to the load rate tests shown in Fig. 2 due to the ability of the material to extrude viscoelastically. However, since



(a)



(b)

**Fig. 4** Stress–strain response **a** three different polymer types subjected to a strain-rate of  $0.05 \frac{1}{s}$ ; **b** PE100 three different strain-rates of  $0.05 \frac{1}{s}$ ,  $0.005 \frac{1}{s}$ , and  $0.01 \frac{1}{s}$

PE7000 has much denser chain cross-links and a different morphology than HDPE, the strain rate and load rate responses were very similar. Based on the test results, UHMWPE (PE7000) has a greater ultimate strength than HDPE, however it has a lower elastic modulus and yield stress. Figure 5 shows the damage modes of the strain-rate controlled tension tests of both PE7000 and PE300.



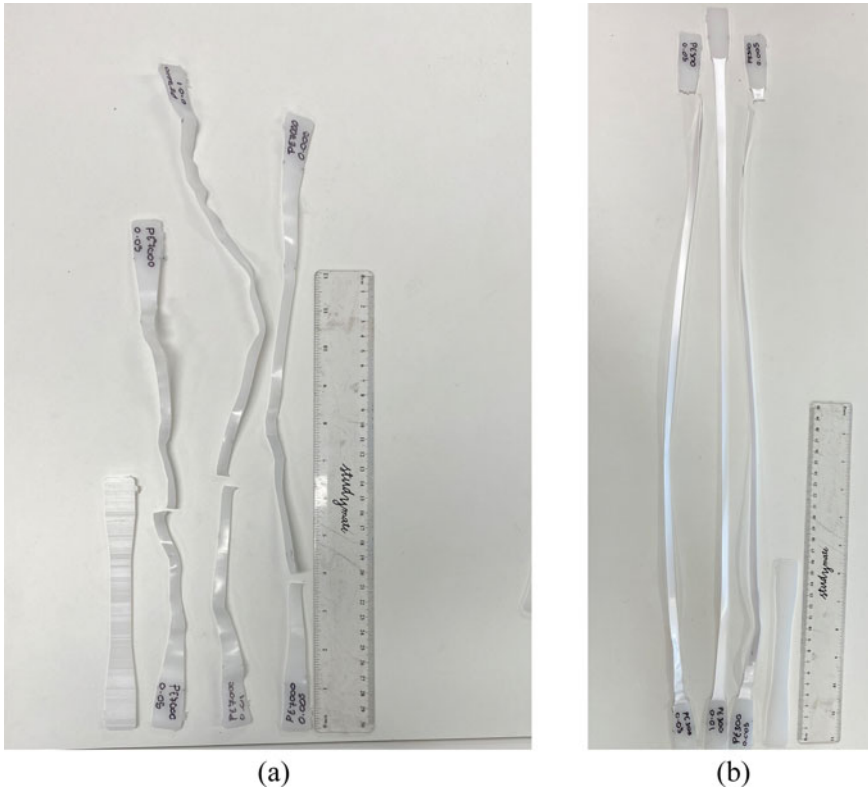


**Fig. 5** Typical failure modes of the strain-rate controlled tension tests **a** PE7000 and **b** PE300

#### **4.4 Creep Test Curve Fitting**

Based on Maxwell's model, Eq. 34 is implemented within MATLAB to predict the behaviour of the creep tests analytically. The use of non-linear least square regression was used to attain the minimum possible error. However, due to the large number of data points and the noise in the data trend obtained from the test, the overall amount of error obtained from least square regression was estimated based on the standard. A for loop was used to iterate the number of Maxwell models until the desired amount of error for the model was low enough. The results of this modelling approach were compared with various experimental tests to determine the accuracy and reliability of the model.

##### **Step-loaded creep**

Step-loaded creep was conducted to enable predictions of the PE behaviour under different loads. Further reasoning can be made as the materials loading conditions are changing, causing the material to experience a faster strain rate due to the lack

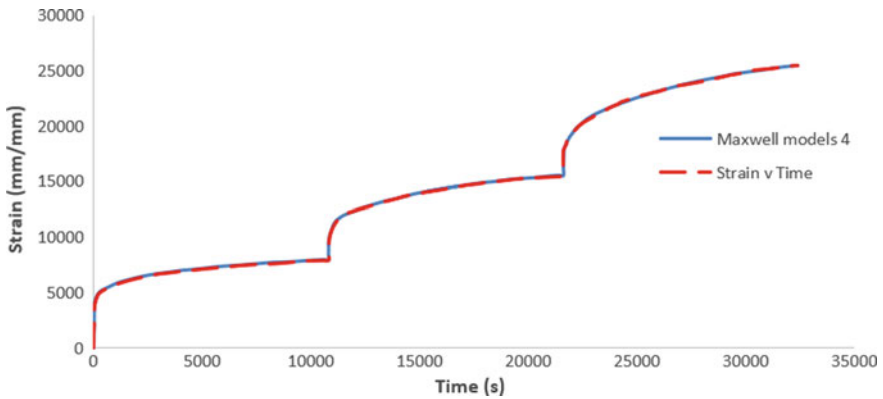


**Fig. 6** Experimental and analytical response of step-loaded creep of PE100

of relaxation the material can achieve due to the previously experienced deformation. The Maxwell model outlined earlier is tested against the experimental data to validate the reliability of the model. Figure 6 shows that using a dash pot and spring with four Maxwell elements enables the step-loaded creep PE100 experimental data to be predicted with minor deviation. This prediction is possible due to the known behaviour of a damper and a spring, where the dash pot represents the relaxation, and the elastic strain is represented by the spring. The damping behaviour is seen in Fig. 2 since the materials became more rigid at a faster rate due to the resistance to deformation triggered by the molecular structures inability to deform as fast. Inability of the PE relaxation can be seen within Fig. 4 as PE100 shows an increase in ultimate tensile strength as strain rate increases. A similar response is shown in Figs. 7 and 8 for PE300 and PE7000, respectively. However, it is evident in Fig. 8 that PE7000 experiences greater deformation than the PE100 and PE300 specimens (i.e. greater y-axis values). This outcome can be explained since the PE7000 specimen has a lower elastic modulus, and as a result, has a lower resistance to creep deformation. The difference in the responses between the materials is caused by the morphology of the material, as both HDPE and UHMWPE have different microstructures. Similar to HDPE, UHMWPE undergoes a change in material properties based on the loading condition due to its morphology changing and adapting to the stress. In addition, UHMWPE is dependent on its crystalline and amorphous phases, where any alteration to the phases can affect its mechanical behaviour [14]. However, the four element Maxwell model represented all materials at each step accurately, showing its reliability to model the step function correctly. Based on these results, the behaviour of the material can be predicted under varying loading scenarios.

The stepped behaviour can be represented by the Boltzmann's superposition principle, whereby it states that the sum of the strain outputs resulting from stress input component equates to the strain output resulting from the total stress input [16]. The Boltzmann's superposition principle is shown schematically in Fig. 9 [15]. The behaviour can be explained in further detail if a constant stress,  $\sigma_1$ , is applied over a

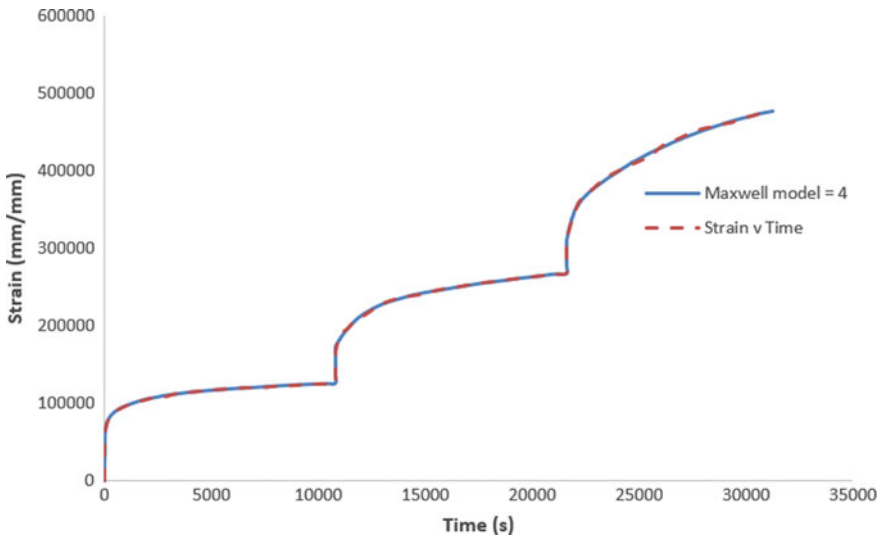


Fig. 7 Experimental and analytical response of step-loaded creep of PE300

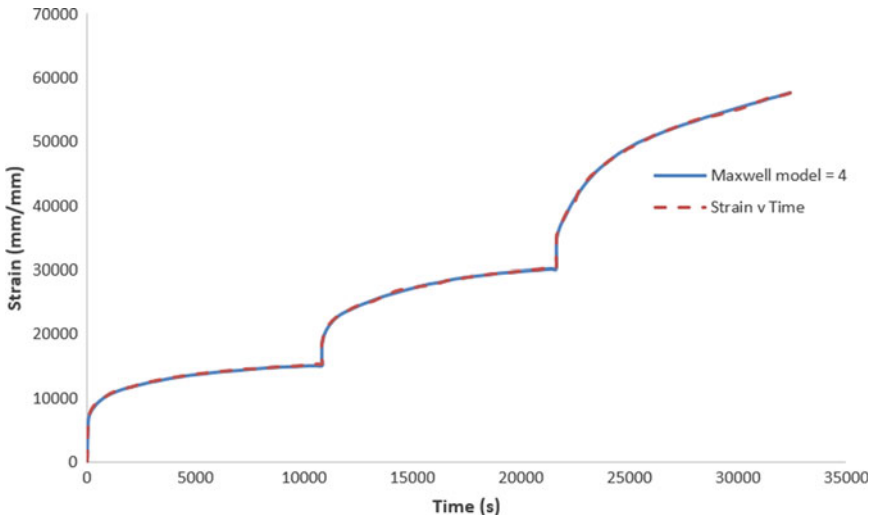


Fig. 8 Experimental and analytical response of step-loaded creep of PE7000

given time  $t = t_1$ , then:

$$\sigma(t) = \sigma_1 H(t - t_1) \tag{34}$$

which gives a creep strain equal to:

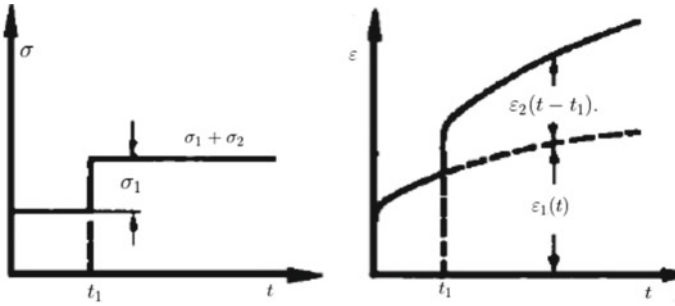


Fig. 9 Boltzmann superposition principle

$$\varepsilon(t) = \sigma_1 J(t - t_1) H(t - t_1) \tag{35}$$

**Short-term creep**

Short-term creep tests were conducted for each material at five different constant stresses. The results from these tests gave insight into the materials creep response, allowing for further validation of the Maxwell model at four elements and the determination of Prony series constants within ABAQUS. As seen in Fig. 10, PE100 was tested at five different stresses. As per the creep compliance ( $\varepsilon/\sigma$ ), strain experienced by the materials increases non-linearly due to the increase of creep acceleration

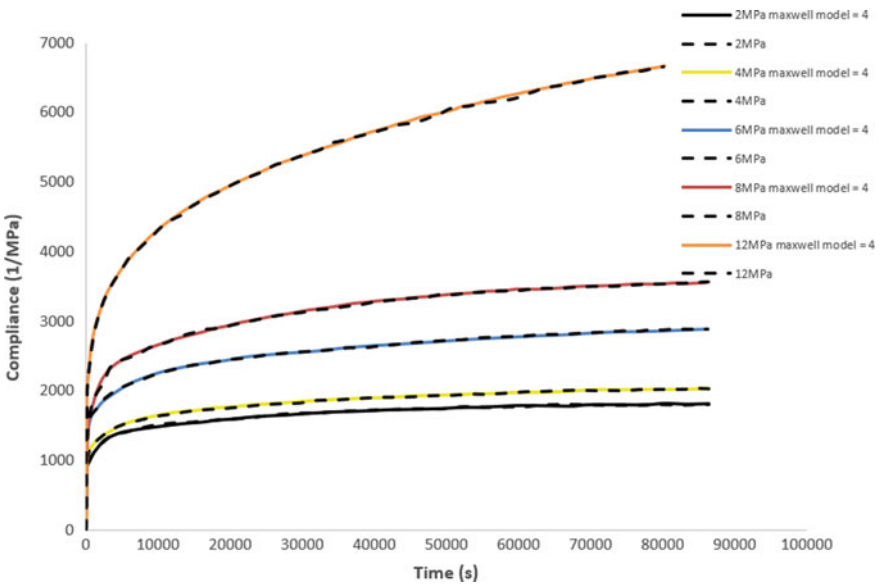


Fig. 10 Experimental and analytical curve fitting of the short-term creep response of PE100

caused by the increase of stress. Accurate curve fitting was achieved for each stress level using four Maxwell elements with an average range of error of 0.5–4%. Based on the results from experimentation, the strain increased at a consistent rate until the material reached a state of relaxation. This behaviour can also be seen in Fig. 11 for PE300, however, the strain is greater than PE100. The causes of this are expected to be due to a combination of the materials viscoelasticity being more instantaneous due to lower plastic deformation and PE300 having a lower ultimate strength. As a result, this shows that PE300 has a greater relaxation time than PE100.

Similar to PE300, PE7000 exhibits a non-linear response, with the only difference being the additional strain experienced by the material. This outcome provides insight into the materials composition, showing that the morphology of UHMWPE is more compact than that of HDPE. The morphology of PE7000 results in a lower yielding point, causing the viscoelastic behaviour to have a longer relaxation time than that of HDPE. This behaviour is evident in Fig. 12, where the material behaves similar to HDPE at lower stresses. However, once a high enough stress is experienced (i.e. 12 MPa), the materials resistance to deformation is significantly reduced due to the relaxation of the material and its varying material properties.

### Long-term creep

Long-term creep tests were conducted to understand the mechanical behaviour of the PE under constant stress, allowing for comparison with the short-term behaviour of the material. As shown in Fig. 13, the materials mechanical behaviour does not change, however irreversible plastic deformation becomes highly prominent within PE7000 due to the change in its chain cross-linking structure once stress is applied. The deformation can be explained due to the viscoelastic behaviour of the material, whereby an increase in strain rate over time yields a positive slope, even after the material reaches a state of stability. The irreversible plastic deformation increases with an increase in the constant stress. It is evident in Fig. 13 that the Maxwell model was able to curve fit the materials behaviour accurately with small deviation. An

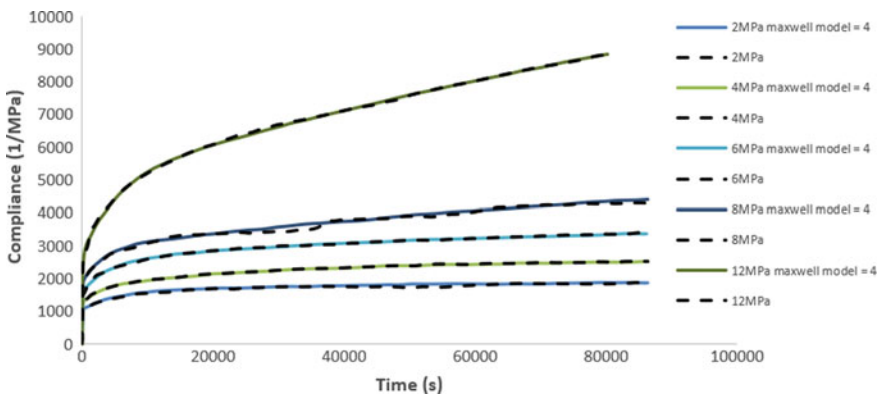


**Fig. 11** Experimental and analytical curve fitting of the short-term creep response of PE300

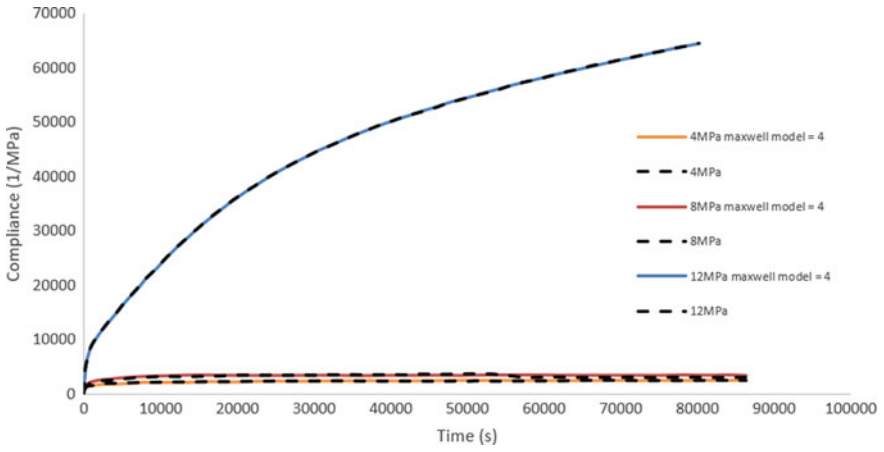


Fig. 12 Experimental and analytical curve fitting of the short-term creep response of PE7000

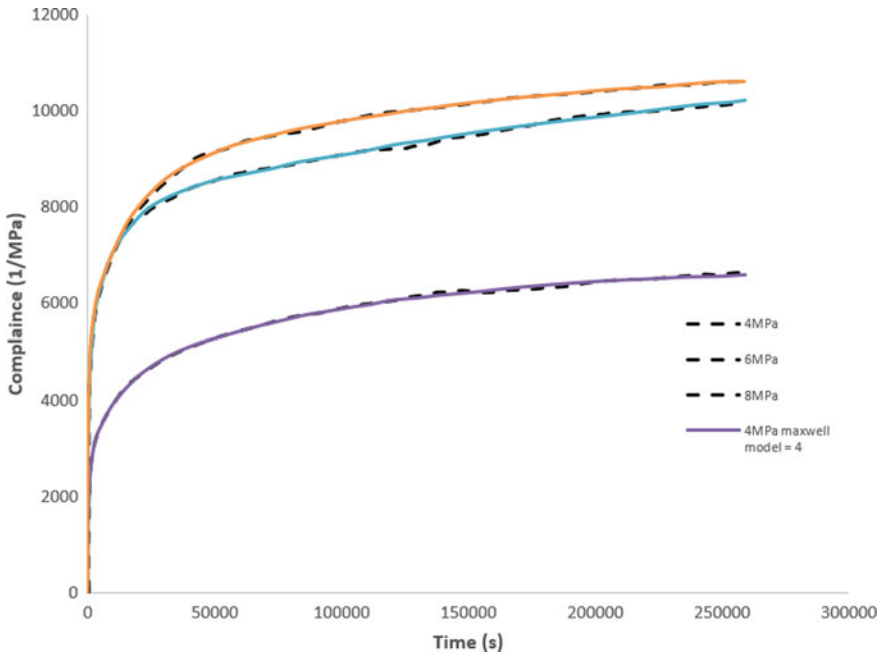
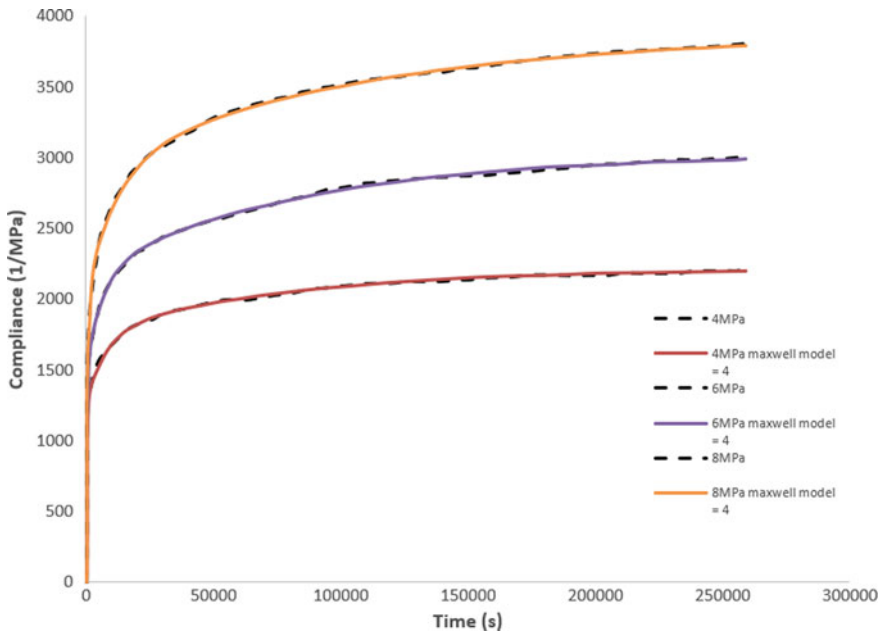


Fig. 13 Experimental and analytical curve fitting of the long-term creep response of PE7000



**Fig. 14** Experimental and analytical curve fitting of the long-term creep response of PE100

overall error of 10% within the 8 MPa curve was achieved due to the experimental data being greatly dispersed due to the amount of data points provided to the curve fit. The error is depicted in the initial behaviour of the material due to the steep curvature. The cause of error was likely due to the fluctuation in the extensometer readings, where stepped displacement readings were obtained due to sensitivity issues.

Figure 14 shows the long-term creep response of PE100 subjected to three different loading scenarios. The difference in behaviour between the PE100 and PE7000 is further highlighted as the strain of the PE7000 differs from that of the PE100 shown in Fig. 14. This can be seen in the variation in creep compliance between the two materials, where PE7000 specimens subjected to all load scenarios up to 8 MPa initially experience a compliance greater than 4000, whilst none of the PE100 specimens subjected to 8 MPa or less exhibit compliance greater than 4000 even at the highest stress. This is anticipated due to the difference in morphology between the two materials, which results in a different stiffness. In addition, the radius of the transition between the initial linear portion and the almost-horizontal portion of the response is greater for the PE7000 specimens. In contrast, the PE100 specimens have a short transition between the initial linear portion and the almost-horizontal portion of the response. Both materials experience an increase in non-linearity at greater stresses due to the differences in material properties and chains structure. It is shown in Fig. 14 that the Maxwell model made good predictions of the test results with minimal deviation and error. The model predicts unknown factors such as the relaxation time and compliance constants through curve fitting.

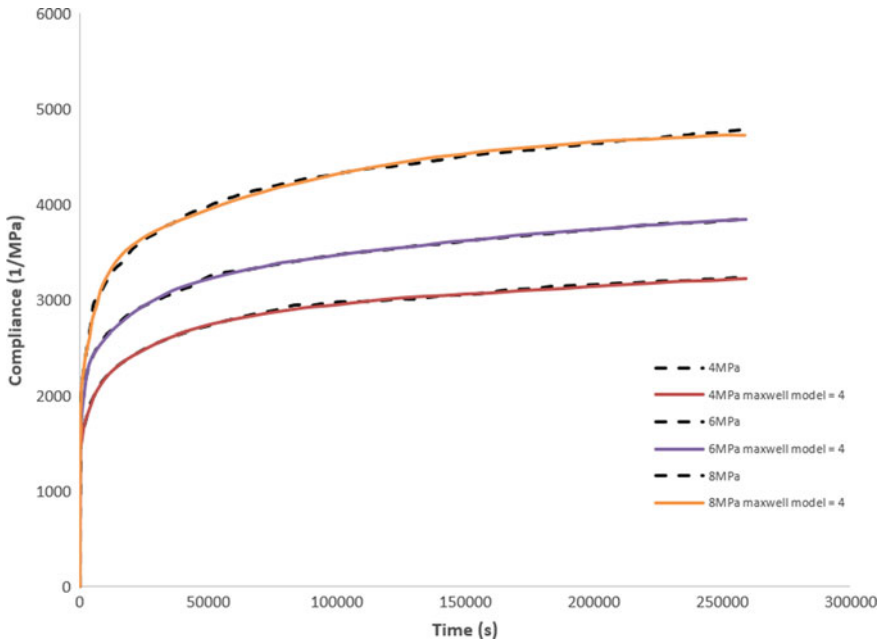


**Fig. 15** Experimental and analytical curve fitting of the long-term creep response of PE300

Figure 15 shows the long-term creep responses of the PE300 specimens, where similar to PE100, PE300 resists deformation more than PE7000. However, its resistance to plasticity is lower than that of PE100, whereby the compliance achieved by PE300 is greater than PE100. Similar to the other polymer types, the four element Maxwell model can represent the long-term creep behaviour of PE300 with low deviation and error.

## 5 Finite Element Modelling

### 5.1 Overview

The finite element software ABAQUS was used to model the step-loaded, short-term and long-term creep tests conducted in this study using Prony series. Firstly, MATLAB was used to normalise the data from the Maxwell model, allowing for input data to be evaluated within ABAQUS directly. The normalisation of data was achieved by dividing the theoretical data  $J(t)$  by  $J(0)$ , which was gathered from the curve fitting within MATLAB. From this, the Prony elements were able to be determined, which resulted in the development of a finite element model of each material. Validation of the model was achieved at a number of Maxwell elements



subjected to constant load, hence undergoing creep. As a result, a single element should output the same amount of extension and strain. However, since a single element is represented as a single homogeneous body, determining the actual strain of a coupon cannot be analysed by a single element as it is made up of numerous connected elements. As a result, convergence of the FE model is dependent on the accuracy of the Maxwell model curve fitting, as this provides an accurate representation of the materials creep behaviour once the modelled data is normalised within MATLAB, as stated previously.

## 5.2 Model Description

The use of density, elastic, and viscoelastic material properties were used to model all the polymers in this study. The density of the materials provided by the manufacturers were used for modelling ( $0.95 \text{ g/cm}^3$  for PE100 and PE7000, and  $0.96 \text{ g/cm}^3$  for PE300). For the elastic properties of each material, the elastic modulus and Poisson's ratio obtained from tension tests were used, and these values can be found in Table 1. For the viscoelastic properties, the use of the normalised data was implemented within ABAQUS, allowing for the determination of the Prony series which theoretically represents the viscoelastic properties. ABAQUS determined the Prony series based on the desired allowable average root-mean-square error. In most cases, the error was set to 0.01, or 0.001 when applicable, whilst the maximum number of terms in the Prony series was kept at four. Once the Prony values were determined, they were entered in the viscoelastic properties in ABAQUS.

Due to computational limitations, meshing the entire part with the same size elements was not practical. As a result, the coupon was partitioned to enable finer mesh in the gauge length segment, while the grip segments had a coarser mesh. This reduced the computational time while keeping the model highly accurate. Different mesh sizes were trialled at the gauge section, whereby the mesh size was progressively made smaller until the model results were no longer influenced by the mesh. The grip segments of the coupon within ABAQUS were kept at a 5 mm mesh size, whilst the gauged segment was trialled at 0.05, 0.1, 0.5, and 1 mm. It was found that at a mesh size of 0.1 mm, the results became consistent for all the ran models. As a result, 0.1 mm mesh was utilised in the gauge segment of the FE models. The meshed FE model is shown in Fig. 16.

The element type used throughout the entirety of all the models was the same. Structured meshing technique was adopted using continuum solid elements C3D20, which is a 20 node-quadratic brick element with full integration and hour-glass control. The boundary conditions of the model were setup such that they resembled the experimental procedure. One of the grip sections of the coupon was assigned ENCASTRE boundary conditions, where no translational or rotational motion would be allowed in the x, y or z directions. The other grip of the coupon was fixed for rotation in the x, y and z direction, and fixed for translation in the y and z direction. This constraint allowed for loading since translation was enabled in the x direction,

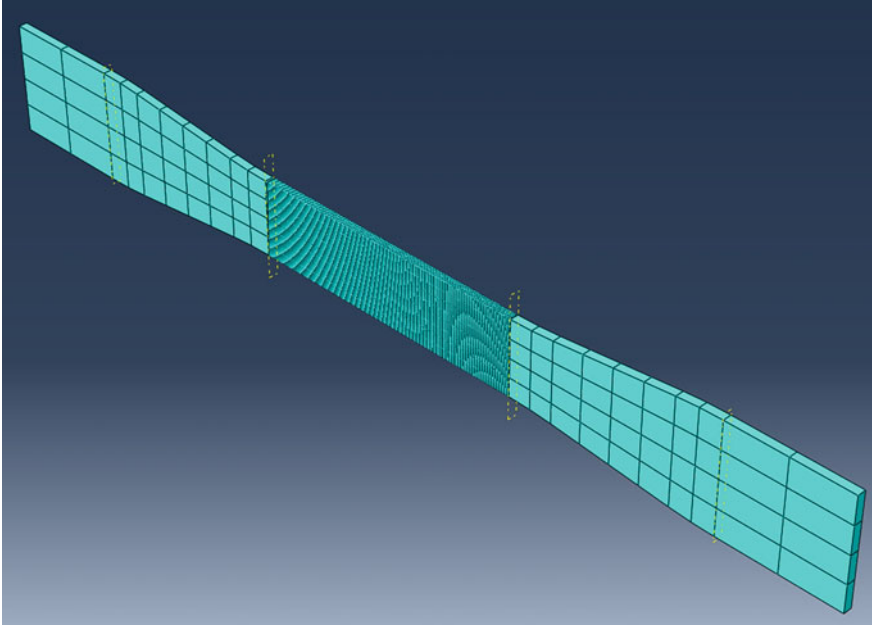


**Fig. 16** Meshing of the finite element model

allowing for movement to occur only in the lengthwise direction. The boundary conditions applied to the model are shown in Fig. 17.

### **5.3 Numerical Results**

#### **Short-term creep**

Figure 18 shows the contour plot of the FE results of a short-term creep test of PE100 under a constant loading of 12 MPa. This model was developed based on the 4 MPa short-term creep curve fitting, four Maxwell element model input in ABAQUS as four Prony series. ABAQUS does not treat the entire body as a single element, so a single element within the gauge region is selected to assess the results. As such, Fig. 19 shows the strain versus time response of the coupon. It is seen that convergence is achieved as the strain experienced by the coupon reaches approximately 0.0831, whilst the experimental outcome of the corresponding coupon was 0.0807, giving an error of 2.97%.

Determination of a Prony series was obtained based on the normalised data for PE300 at 8 MPa, which allowed for an accurate prediction of the model behaviour at higher stress levels. Figure 20 shows the short-term strain convergence using a four Prony series element under 8 MPa. Compared with the experimental results

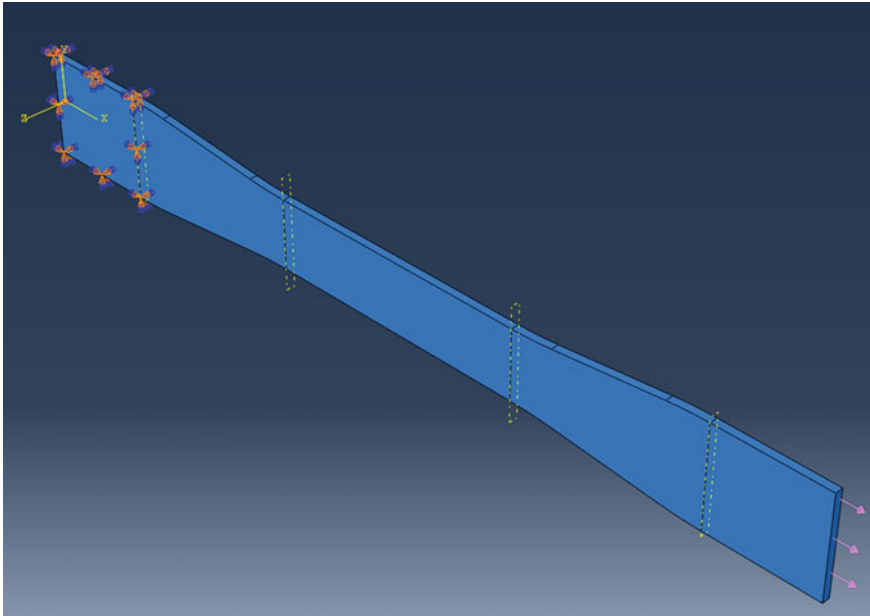


Fig. 17 Boundary conditions of the finite element model

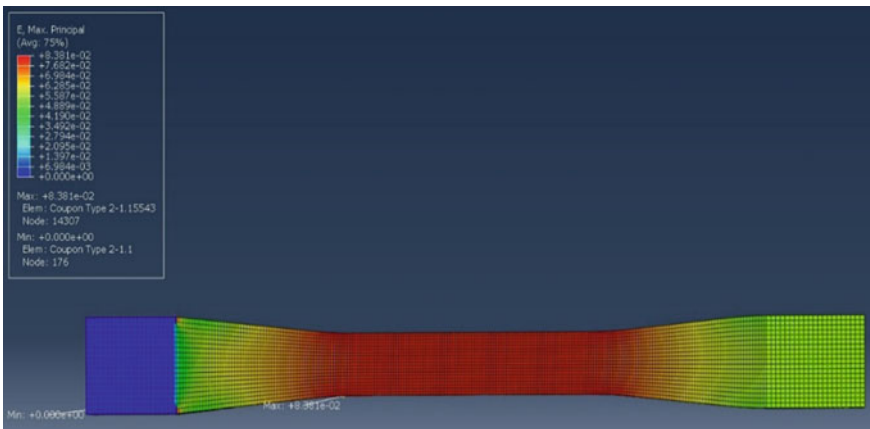
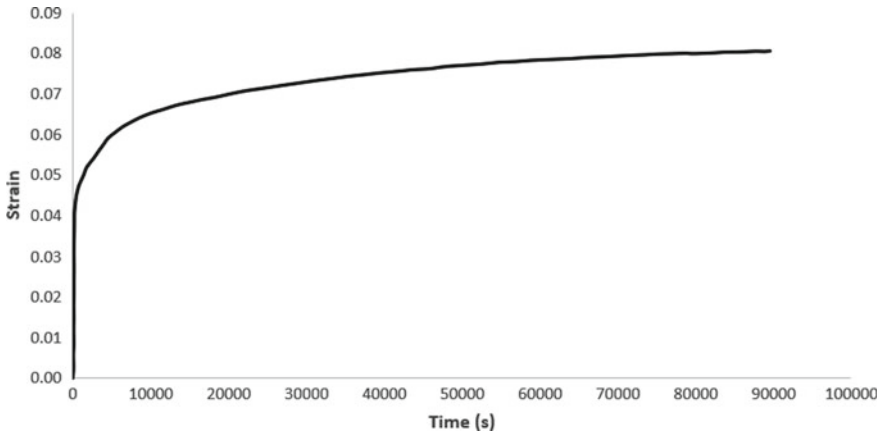
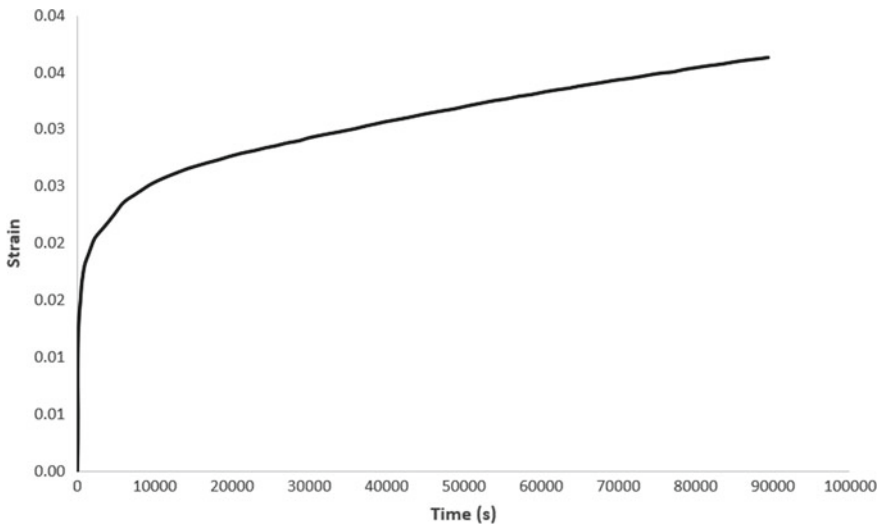


Fig. 18 Contour plot of the axial strain of PE100 subjected to short-term creep at 12 MPa

(Fig. 11), the convergence of the strain was achieved with an error margin of 7.48%. On the other hand, PE100 strain convergence using Prony series was not in good agreement with the experimental results, which may be attributed to the sensitivity of the extensometer or load cell, and the alignment of the test coupons.



**Fig. 19** Strain–time response of PE100 subjected to short-term creep at 12 MPa



**Fig. 20** Strain–time response of PE300 subjected to short-term creep at 8 MPa

The short-term numerical creep results of PE7000 are shown in Fig. 21. Compared with experimental results (Fig. 12), it is shown that convergence was also achieved with minimal error due to the curve fit deviation. Nonetheless, an error percentage of 2.31% was observed, whereby the experimental results output a strain of 0.528 and the FE model outputs a strain of 0.541. Since the model was able to represent the materials behaviour with minimal error, the material’s response was depicted accurately in terms of its viscoelastic reaction subjected to constant stress. Convergence of the

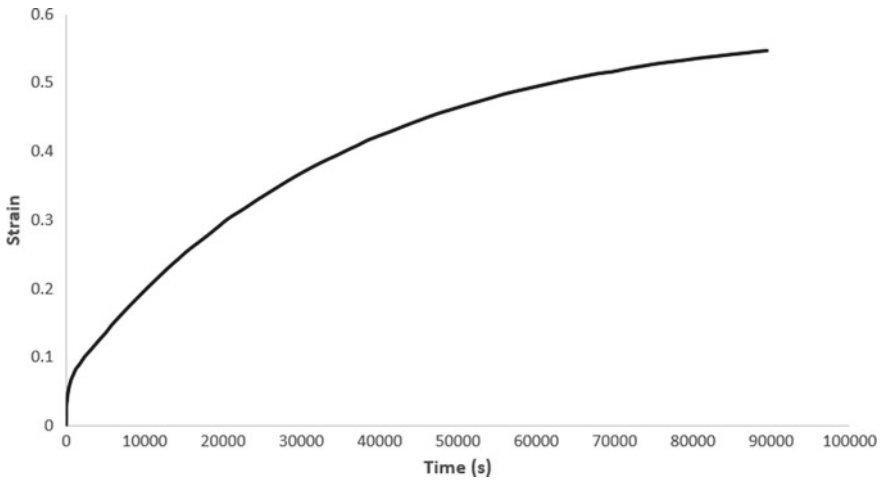


**Fig. 21** Strain–time response of PE7000 subjected to short-term creep at 12 MPa

model could also be further improved using a lower deviation when curve fitting with the Maxwell model.

### Long-term creep

The accuracy of the FE model for long-term creep was determined by comparing the FE results to the experimental results from the three-day creep tests. The normalised data allowed for the determination of the models four element Prony series. From the determination of the Prony series, the system’s reliability was able to be determined by comparing the strain output from the FE model to the experimental test. It was found that for the 4 MPa specimens, the experimental strain was 0.02035, and the FE strain was 0.02509. The strain–time curve attained from the FE model can be seen in Fig. 22. The variation in strain between the experiment (Fig. 13) and the FE model may be attributed to the uncertainties in the experimental testing as discussed in the numerical short-term creep results.

The reliability of the modelling approach can be further analysed through determination of a Prony series at each experimental load. It is understood that the Prony series of 4 MPa would have a greater error when simulating a different load, however the error will be dependent on the strain rate of the material. Since the normalised data set is based on the strain rate, the values will significantly deviate as a greater load is applied. As a result, convergence by determination of a singular Prony series is only applicable to the load from which the Prony series is determined.

Determination of the Prony series parameters depends on the accuracy of the experimental data and the curve fitting approach, whereby the time is increased to achieve an accurate curve fit since more data points are considered. In essence, the inaccuracy within the determination of the Prony series differs as the strain rate changes per unit stress, causing the PE100 FE model to have a range of error of 1

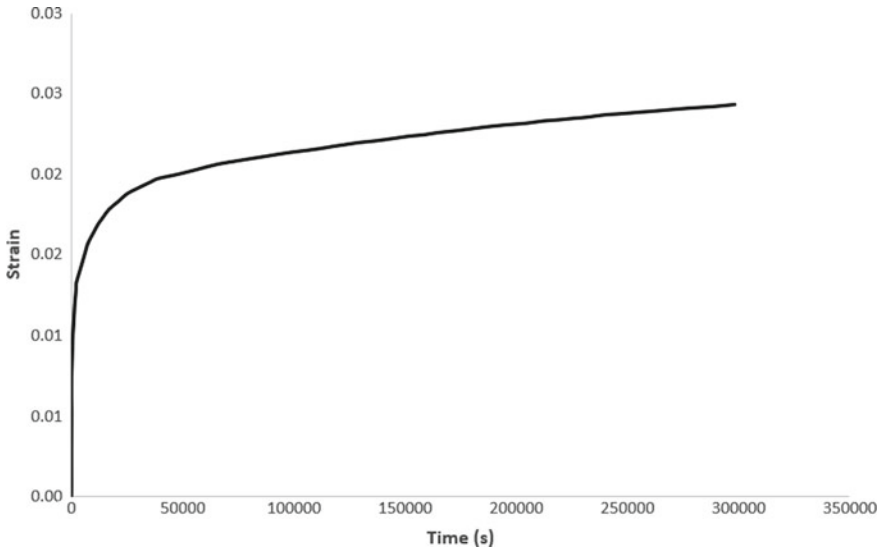


Fig. 22 Strain–time response of PE7000 subjected to long-term creep at 4 MPa

to 10%, which is similar to the short-term FE model. The contour plot of the axial strain and the FE long-term creep results of the PE100 under 4 MPa are depicted in Figs. 23 and 24, respectively. It was found that the FE model achieved a strain of 0.00816, whilst the experimental test achieved a total strain of 0.00888, resulting in a margin of error of 7.87%. As the material is represented accurately in the FE model, normalisation of the data did not allow for a curve fit lesser than  $1E-6$  mean-square error as the desired amount of Prony series elements was set at four based on the

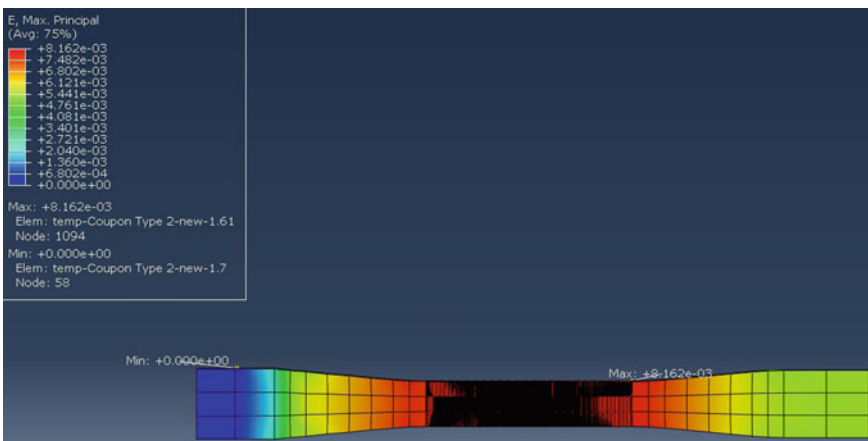


Fig. 23 Contour plot of the axial strain of PE100 subjected to long-term creep at 4 MPa

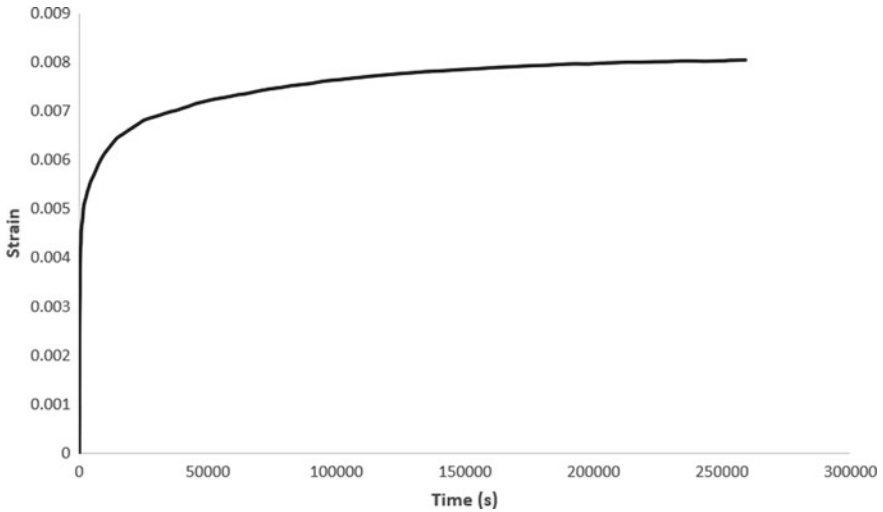


Fig. 24 Strain–time response of PE100 subjected to long-term creep at 4 MPa

optimised amount of Maxwell models. Similar outcome was achieved at stress level of 8 MPa (Fig. 25).

The accuracy of the Maxwell models is further supported by the FE results of the PE300 long-term creep response under 4 and 6 MPa as shown in Figs. 26 and 27, respectively. For the 4 MPa tests, the experimental strain was 0.0129 (Fig. 15) and the FE strain was 0.01426, giving an error of 10.54%. For the 6 MPa tests, the experimental strain was 0.0230 (Fig. 15) and the FE strain was 0.0227, giving an error of 1.39%. Summary of the experimental and FE results is shown in Table 2.

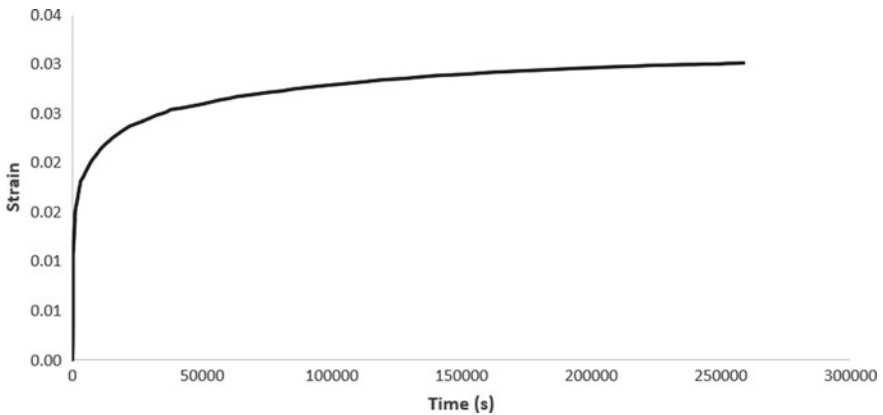
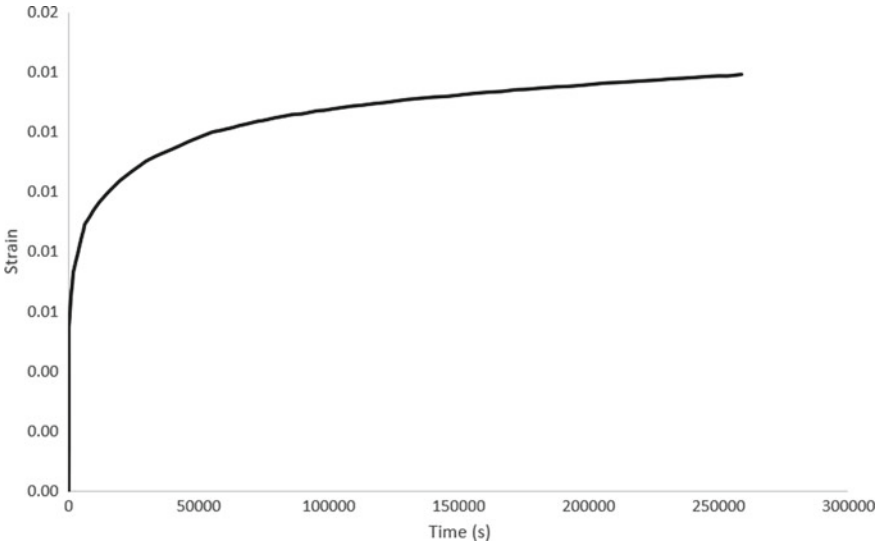
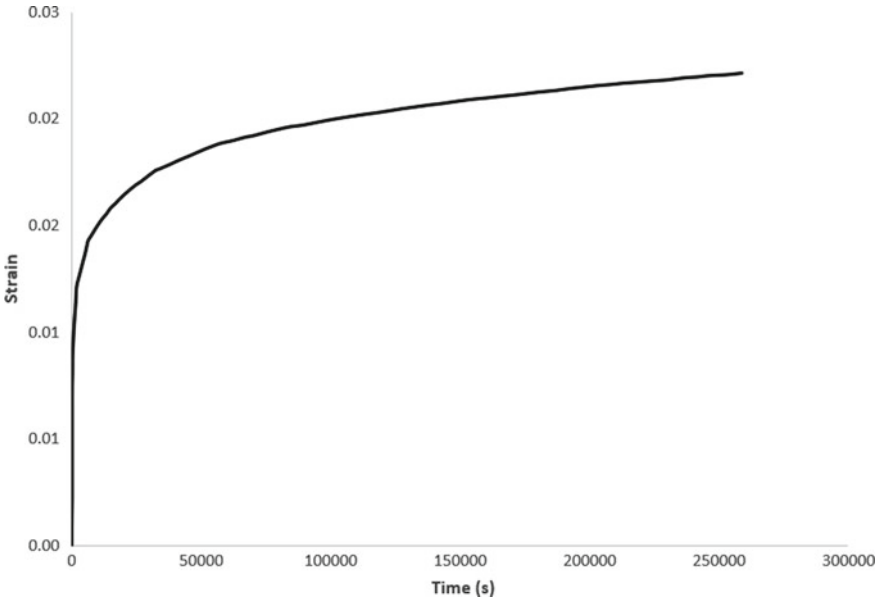


Fig. 25 Strain–time response of PE100 subjected to long-term creep at 8 MPa



**Fig. 26** Strain–time response of PE300 subjected to long-term creep at 4 MPa



**Fig. 27** Strain–time response of PE300 subjected to long-term creep at 6 MPa



**Table 2** Results from the experimental tests and finite element models

Creep test	Experimental strain	FE strain	Error (%)
HDPE 100 short-term (12 MPa)	0.08139	0.08381	2.97
HDPE 300 short-term (8 MPa)	0.03350	0.03600	7.48
UHMWPE short-term (12 MPa)	0.52878	0.54100	2.31
HDPE 100 long-term (4 MPa)	0.00888	0.008162	7.87
HDPE 300 long-term (4 MPa)	0.12700	0.12900	1.39
UHMWPE long-term (4 MPa)	0.02035	0.02509	6.77

## 6 Conclusions

The viscoelastic and viscoplastic behaviour of three different polyethylene polymers were investigated in this study, including two types of HDPE and one type of UHMWPE. The polymers were subjected to different loading conditions, including displacement-controlled tension, load-controlled tension, strain-controlled tension, step-loaded creep, short-term creep and long-term creep. An analytical model that incorporated four Maxwell elements was used to predict the experimental results. The model provided an accurate curve fit by determining unknown factors such as the relaxation time and initial creep compliance. This model was found to make predictions with a high level of accuracy. Finite element models were then developed to predict the short-term and long-term creep behaviour of the HDPE polymers using Prony Series elements. The finite element models also made good predictions of the creep behaviour of the HDPE polymers. It was found that the accuracy of the model was dependent on the accuracy of the short-term creep experimental test results. Overall, Maxwell's model enabled the creep behaviour of the two different polymer morphologies to be predicted accurately. This shows the reliability of this model for using short-term creep data to predict the long-term creep response of the material.

## References

1. Mosavian MH, Bakhtiari A, Sahebani S (2011) Tensile creep behavior of medium-density polyethylene. *J Thermoplast Compos Mater* 24(4):555–566. <https://doi.org/10.1177/0892705710393125>
2. Zhang C, Moore I (1997) Finite element modelling of inelastic deformation of ductile polymers. *Geosynth Int* 4(2):137–163. <https://doi.org/10.1680/gein.4.0091>
3. Dotson N, Galvan R, Laurence R, Tirrell M (1995) *Polymerization process modeling*. Wiley, New York, USA
4. Lai J, Bakker A (1995) Analysis of the non-linear creep of high-density polyethylene. *Polymer* 36(1):93–99. [https://doi.org/10.1016/0032-3861\(95\)90680-Z](https://doi.org/10.1016/0032-3861(95)90680-Z)
5. Zhou H, Wilkes GL (1998) Creep behaviour of high density polyethylene films having well-defined morphologies of stacked lamellae with and without an observable row-nucleated fibril structure. *Polymer* 39(16):3597–3609. [https://doi.org/10.1016/S0032-3861\(97\)10359-7](https://doi.org/10.1016/S0032-3861(97)10359-7)
6. AS/NZS 4766 (2019) *Rotationally moulded buried, partially buried and non-buried storage tanks for water and chemicals*. Standards Australia, Sydney, Australia
7. ASTM D2990–17 (2017) *Standard test methods for tensile, compressive, and flexural creep and creep-rupture of plastics*. ASTM International, West Conshohocken, PA
8. Beijer J, Spoormaker J (2000) Modelling of creep behaviour in injection-moulded HDPE. *Polymer* 41(14):5443–5449. [https://doi.org/10.1016/S0032-3861\(99\)00753-3](https://doi.org/10.1016/S0032-3861(99)00753-3)
9. Pozhil S, Menon NM, Waigaonkar SD, Chaudhari V (2020) An analytical model to predict the creep behaviour of linear low-density polyethylene (LLDPE) and polypropylene (PP) used in rotational moulding. In: 2nd international conference on recent advances in materials & manufacturing technologies. materials today: proceedings, vol 28, pp 888–892. <https://doi.org/10.1016/j.matpr.2019.12.318>
10. Torres F, Aragon C (2006) Final product testing of rotational moulded natural fibre-reinforced polyethylene. *Polym Testing* 25(4):568–577. <https://doi.org/10.1016/j.polymertesting.2006.03.010>
11. Zhang C, Moore ID (1997) Non-linear mechanical response of high density polyethylene. Part ii: uniaxial constitutive modeling. *Polym Eng Sci* 37(2):414–420. <https://doi.org/10.1002/pen.11684>
12. ASTM D638-14 (2014) *Standard test method for tensile properties of plastics*. ASTM International, West Conshohocken, PA
13. Malpass DB (2010) *Introduction to polymers of ethylene*. Wiley, New Jersey, USA
14. Pelleg J (2012) *Mechanical properties of materials*. Springer, Solid Mechanics and Its Applications. Netherlands
15. Soboyejo W (2002) *Mechanical properties of engineered materials*. Taylor & Francis, New York, USA. <https://doi.org/10.1201/9780203910399>
16. Fourie A, Bouazza A, Lupo J, Abrao P (2010) Improving the performance of mining infrastructure through the judicious use of geosynthetics. In: 9th international conference on geosynthetics. Guarujá, Brazil

# Numerical Investigation of Lithium Battery Using Heat Pipes in Electric Vehicles



Zhao Liu, Jin Zhao, Chao Wang, Yangjun Qin, and Hang Zhang

**Abstract** The battery thermal management system plays a crucial role for lithium-ion battery in electric vehicles because of its susceptible performance during fast discharging. In this study, the Newman, Tiedemann, Gu, and Kim (NTGK) electrochemical model is applied to investigate the numerical simulation on the temperature distribution within battery when discharging at various rates, which is comprehensively validated with experimental data. Following the verification, a three-dimensional heat pipe integrated system (HPIS) is designed with a novel thermal resistance model on the basis of equivalent thermal circuit method. The combination of thermal resistance between pipes and fins at the condenser section greatly predicts the temperature distribution of the system. Then the simulation model is employed to obtain the cooling efficiency of heat pipe (HP) under transient conditions. The temperature difference and maximum temperature of the battery pack under natural and forced air convection are compared. Implementation of insulating board overcomes the thermal runaway and propagation to protect the lithium-ion battery during a rapid discharging rate of adjacent cell. Simulation results reveal that the HPIS-based battery pack not only improves the heat dissipation capability, but also provides the thermal runaway protection to ensure the battery cell safety.

**Keywords** Lithium-ion battery · NTGK model · Heat pipe · Thermal resistance

## 1 Introduction

Coupled with the deepening of energy crisis and more environment pollution, new energy vehicles have been adopted worldwide due to their effective operation and lower pollutant emissions in automobile industry. Nowadays, challenge for new

---

Z. Liu · C. Wang · Y. Qin · H. Zhang  
Department of Mechanical Engineering, Guizhou University, Guiyang 550025, China

J. Zhao (✉)  
Key Laboratory of Advanced Manufacturing Technology of the Ministry of Education, Guizhou University, Guiyang 550025, China  
e-mail: [zhaoj@gzu.edu.cn](mailto:zhaoj@gzu.edu.cn)

© The Author(s), under exclusive license to Springer Nature Singapore Pte Ltd. 2022  
M. Abdel Wahab (ed.), *Proceedings of the 4th International Conference on Numerical Modelling in Engineering*, Lecture Notes in Mechanical Engineering,  
[https://doi.org/10.1007/978-981-16-8806-5\\_6](https://doi.org/10.1007/978-981-16-8806-5_6)

energy vehicles is to look for an appropriate energy storage system, which can support high mileage, fast charging and stable driving performance [1]. Lithium-ion battery possesses higher energy density, large specific power, lower self-discharging rate, longer cycle life and lighter weight than other kinds of rechargeable batteries for electric and hybrid vehicles (EV/HEV) [2].

However, lithium-ion batteries are sensitive to changes in ambient temperature, because the high temperature above 50 °C that will significantly decline the recoverable power and capacity particularly, shorten the life cycles and accelerate the degradation of battery efficiency. The optimal operating temperature range of power battery is generally from 20 to 45 °C, within which the battery will keep great balance between performance and cycle life. The maximum temperature difference of battery cell should be within 5 °C [3, 4].

Numerical research efforts have been made to study the mathematical models for different kinds of batteries to figure out the mechanism inside the cell body and connection between the electrical and chemical characteristics, as well as the thermal behavior under various working conditions [5]. Newman et al. [6] built up a lithium-ion battery model based on formula through fitting the diffusion coefficient in carbon electrode. Tiedemann et al. [7] proposed an equivalent resistance model to analyze batteries' behavior. Gu [8] used an experimentally polarization expressions to describe the losses between the positive and the negative electrodes and to predict the behavior of Zn/NiOOH batteries, such as the potential and current distribution, power, capacity and energy under instantaneous conditions. Kim et al. [9] proposed a two-dimensional thermal model of the distribution of potential and current density on the electrodes of a lithium-ion battery by means of the finite element method. Chacko and Chung [10] designed a fully coupled three-dimensional transient electrothermal model based on the finite volume method. By comparing the numerical simulation results with the experimental data, the voltage, current, temperature and state of charge (SOC) of the battery model collected under dynamic conditions were predicted more accurately.

All of the mathematical battery models designed aim to fully understand the reaction procedure of power battery. At present, due to the development of electrical technology of EV, power batteries are in eagerly demand than ever before. In order to achieve higher energy density and increase mileage, more batteries will be added to the battery pack. Therefore, for security reasons, it is urgent to enhance the battery thermal management system (BTMS) to lower the cell temperature and mitigate the temperature uniformity of the battery modules [11, 12]. Likewise, the BTMS should also meet the requirements for EV, such as: lightweight, compactness, convenient operation and maintenance, low cost and lower power consumption.

In the thermal control of the lithium-ion battery pack, plenty of strategies have been implemented to maintain high performance in batteries. Up to now, the approaches of BTMS can be performed with active and passive. The extraction of the waste heat from the integrated system by applying external energy consumption is the main mode of the active thermal management. Nevertheless, this cooling system is insufficient to provide cooling rates because of the low heat transfer coefficient. The active system principal weakness is to add equipment, like fans, pipes, fluid

circulation pumps and heat exchangers, which cost additional power [13]. The other approach, the passive BTMS, makes use of heat pipes or phase change material (PCM) to extract excess heat. There are a large amount of works using heat pipes in the EV that analyzed thermal variations in the batteries. The merits of heat pipe are high thermal conductivity, low thermal resistance, and the excellent isothermal property among the evaporator and condenser zones [14].

Wu et al. [15] validated that heat pipe with additional aluminum fins using external fans on the condenser section could greatly reduce the cell temperature. Tran et al. [16] designed a new cooling system of heat pipe with chimney ventilation to enhance the heat dissipation without any power consumption that kept the battery temperature lower than 50 °C. Zhao et al. [17] investigated a battery thermal management (BTM) combining an ultra-thin aluminum heat pipe with wet cooling by comparing with other four cooling strategies. Famouri et al. [18] predicted a transient analysis of micro flat heat pipe, in which the efficiency of heat transfer coefficient was estimated by combining experimental data. Above all, the cell temperature and uniformity of battery pack is effectively regulated within optimal range with well-designed BTM.

Numerous structural optimization methods have been applied in the heat pipe cooling system so as to enhance the thermal performance. Chen et al. [19] calculated the velocities of the cooling channels by combining a flow resistance network model and the cell temperature by analyzing a heat transfer model to optimize the configuration of the cooling system under the constant heat generation rate. Liu et al. [20] designed a “segmented” thermal resistance model to determine the thermal parameters of heat pipe and integrated that into the three-dimensional battery model for numerical simulation. Hatata et al. [21] conducted an orthogonal numerical test to obtain the sensitivity of various parameters of a battery module with cylindrical cells.

In this article, a three-dimensional electrochemical model is developed with a novel thermal resistance network, which has been used to analyze the dynamic thermal characteristics of the battery pack. The remained of this article is organized as follows: Sect. 2 validates the experimental results with the numerical data obtained by the NTGK model in ANSYS Fluent; Sect. 3 establishes a geometric HPIS-based battery pack and a novel equivalent thermal resistance circuit; Sect. 4 describes a numerical model setup and solutions. And mesh sensitivity analysis is conducted in this section; in Sect. 5, temperature distribution of the structure is testified to predict the battery thermal performance. Novel equivalent method of HP is compared with traditional one, which reveals the thermal behaviour within the battery. Improvement of the cooling effect and heat insulation efficiency of the HPIS with natural/air-forced convection under rapid discharging rates are discussed; finally, Sect. 6 concludes this article.

## 2 Measurements and Validation

### 2.1 Experimental Setup

In the experimental test, the preliminary object is to acquire the time-wise variations of the cell surface temperature and temperature distribution of batteries. Figure 1 schematically illustrates the experimental setup diagram. The integral elements of the experimental facility are (1) the battery testing system (NEWARE, EVT-100V200A) that controls the discharging rate at 1C, 2C and 3C respectively; (2) the data acquisition system for monitoring and recording temperature, voltage, and current data; (3) the computer (HP Z4 G4) to record the tested data; (4) The air conditioner which is used to maintaining a constant ambient temperature; (5) Lithium-ion battery (CATL S5E897,  $148 \times 26.5 \times 94$  mm) (6–10) thermocouples measure the temperature of battery surface. Charged and discharged though the power battery testing system, the battery is placed inside the air conditioner under at constant ambient temperature, the bottom of which insulates from the baseboard.

Before the experimental test, according to the CATL product instruction, the battery need to be calibrated preliminarily. The calibration steps are as follows: first, the battery is fully charged with a constant current 14000 mA (1/3C) up to 4.2 V in standard charging pattern. Next, the current value is reached to 2100 mA under constant voltage. Then, fast charging and discharging can be utilized. After the calibration procedure, the battery can be tested under the specified conditions.

In this experiments, three identical batteries, discharged from 4.2 to 2.75 V, are put in the conditioner and discharge on different conditions to obtain the thermal properties. Temperature and heat generation rate are monitored at the constant ambient temperature of 25 °C with three various discharge currents of 42,000, 84,000 and 126000 mA corresponding to 1C, 2C and 3C discharging rates, respectively. The

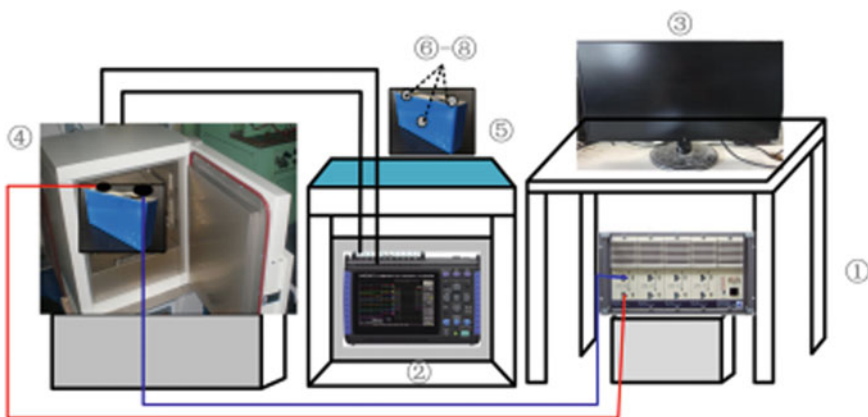


Fig. 1 Experimental setup

**Table 1** Discharge processes

Battery no	Process	Current (mA)	Shelving time (h)
1	Discharge	42,000	3
	Charge	14,000	1
2	Discharge	84,000	3
	Charge	14,000	1
3	Discharge	126,000	3
	Charge	14,000	1

procedure of experimental research for each battery cell is shown in Table 1. Shelving time is one of the most significant steps in the experiment so as to ensure the completed electrochemical reaction after test.

### 2.2 Model Description

A three-dimensional numerical model of ternary lithium-ion battery is built by Solidworks, of which the physical parameters are presented in Table 2. The positive electrode material is Al 1060 and negative electrode material is Cu. Then an electrochemical method is implemented through the NTGK model [22] approach in ANSYS Fluent. Heat generated of the cell in this model can be mainly divided into internal resistance heat and reaction heat [23]. The volumetric current transfer rate  $j_{Ech}$  of the battery is calculated as following:

$$j_{Ech} = aY[U - (\phi_+ - \phi_-)] \tag{1}$$

where  $\phi_-$  and  $\phi_+$  are the potential of negative and positive electrodes,  $a$  is the specific area of the electrode sandwich sheet in the battery, the model parameters  $Y$  and  $U$  are functions of the battery depth of discharge (DOD):

$$U = \left( \sum_{n=0}^5 a_n (DOD)^n \right) - C_2(T - T_{ref}) \tag{2}$$

**Table 2** Physical parameters of ternary lithium battery

	Material	Density (kg·m <sup>3</sup> )	Specific heat, (J·kg <sup>-1</sup> ·K <sup>-1</sup> )	Thermal conductivity (W·m <sup>-1</sup> ·K <sup>-1</sup> )
Positive electrode	Al	2680	900	234
Negative electrode	Cu	8933	385	398
Battery cell	NCM	2316	700	$k_z = 18.2;$ $k_x = k_y = 24.1$

$$Y = \left( \sum_{n=0}^5 b_n (D_o D)^n \right) \exp \left[ -C_1 \left( \frac{1}{T} - \frac{1}{T_{ref}} \right) \right] \tag{3}$$

where C1 and C2 are the NTGK model constants of battery-specific.  $a_n$  and  $b_n$  are constants tested by the experimental data. T and  $T_{ref}$  is the measuring and reference temperature.

The electrochemical reaction heat  $q_{Ech}$  is calculated as:

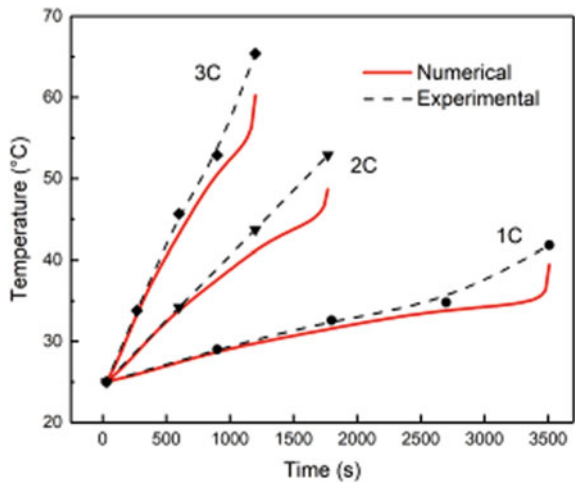
$$\dot{q}_{ECh} = j_{ECh} \left[ U - (\phi_+ - \phi_-) - T \frac{dU}{dT} \right] \tag{4}$$

The battery surface radiation effects are negligible. Energy equation is imposed and a convection heat transfer coefficient of  $10 \text{ W} \cdot \text{m}^2 \cdot \text{k}^{-1}$  is defined as boundary condition on the surfaces of the battery under a constant temperature condition of 298 K. The model is included a SIMPLE algorithm and a first-order upwind scheme to determine the energy and momentum.

### 2.3 Validation

As shown in Fig. 2, the temporal and spatial temperature are evaluated for three different discharging rates over time. The relative results indicate that the battery surface temperature raises by increasing the discharging rate. It is obvious that the average temperature in the numerical model is consistent with the experimental data. At the end of test process, the average temperature of the cell is evaluated as 37,

**Fig. 2** Experimental validation for electrochemical model





48 and 42.6 °C and the maximum deviations of the temperature are 2.9, 4.5 and 4.9% for the discharging rates of 1C, 2C and 3C, respectively. Therefore, the thermal behaviour of battery cell can be predicted by the three-dimensional electrochemical model.

### 3 Design of Heat Pipe Cooling System

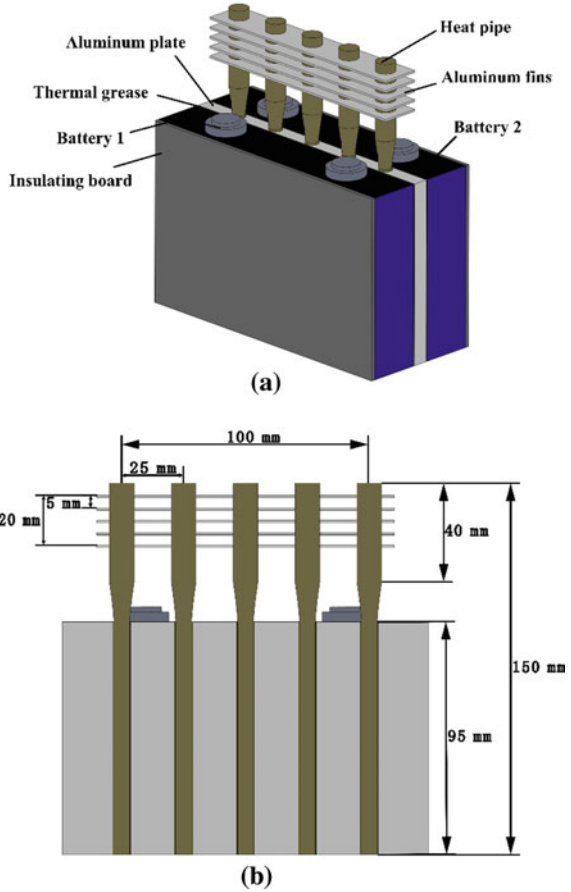
#### 3.1 Geometric Model

HP can work spontaneously without additional external power and transfer a large amount of heat in a long distance, which can be described by three processes: at first, the evaporator section absorbs heat, and then heat is transferred to adiabatic section, finally dispersed by the condenser section [24]. In addition, HP can immediately emerge phase change to transfer heat within a minor temperature difference [25]. Figure 3a presents the novel HPIS, including insulating board to prevent thermal runaway from one battery out of control, two batteries to be heat source, thermal grease to reduce the superficial thermal resistance, aluminum plate to enhance the thermal conductivity between the battery and the heat pipe, heat pipes and cooling fins to transfer heat. Each of the batteries are surrounded by the insulating board or the aluminum plate, which form a sandwiched configuration. The cylindrical HP can be inserted properly into the aluminum plate by using the thermal grease. The geometry of the HPIS is shown in Fig. 4b. The overall length of HP is 150 mm, in which the evaporator section is 95 mm with 6.5 mm radius and condenser section is 40 mm with 10 mm radius, and the space between HPs is 25 mm. The interval distance between cooling fins is 5 mm. The thermal dissipation system is coupled with natural air convection on the condenser section and passive cooling equipment fins.

#### 3.2 Equivalent Circuit Model of HPIS

In the equivalent circuit model of HPIS, the thermal behaviour of the entire cooling system is idealized by analogy with thermal resistance. The thermal equivalence is represented in Fig. 4. The specific areas express diverse components within the BTMS. For the heat pipe, heat transfer from liquid pool in the evaporator section to condenser section is ascended by the pressure difference, which is filled with working fluid in a saturated state. The vapor is generated by the outer heat source on the phase process in the evaporator section and carries heat to the condenser section, in which the liquefied liquid is brought back to the liquid pool due to the gravity force. Therefore, the phase-change process works continuously. In the equivalent model,

**Fig. 3** Heat pipe integrated system: **a** schematic of the battery cooling system; **b** geometry of the heat pipe integration



the thermal resistance circuit is principally composed of two sections: integrated thermal system and heat pipe structure.

With regard to the integrated system,  $R_f$ ,  $R_g$ ,  $R_a$ ,  $R_b$  and  $R_i$  are the thermal resistance of aluminum fin, thermal grease, aluminum plate, battery and insulating board respectively;  $R_{f,g}$ ,  $R_{h,g}$ ,  $R_{a,g}$ ,  $R_{b,g}$  and  $R_{i,b}$  are the contact thermal resistance at the surfaces of adjacent parts.

For the second section, the most significant equivalent circuit of the integrated system is the thermal resistance of heat pipe.  $R_{e,w}$ ,  $R_{c,w}$  and  $R_{w,a}$  are the thermal resistance due to the wall of condenser and evaporator, and radial direction. The thermal resistance  $R_{e,r}$  and  $R_{c,r}$  are due to the radial transfer of evaporator and condenser section.  $R_{l,v}$ ,  $R_{v,l}$  and  $R_{v,a}$  are the thermal resistance due to the gas–liquid interface and axial direction of vapor flow, which can be neglected on account of minor errors with calculation due to their extremely small order of magnitude. A segmented equivalent model of HP is more accurate to express heat transfer and thermal performance than the original one that is simply separated into liquid and gas section. In addition,

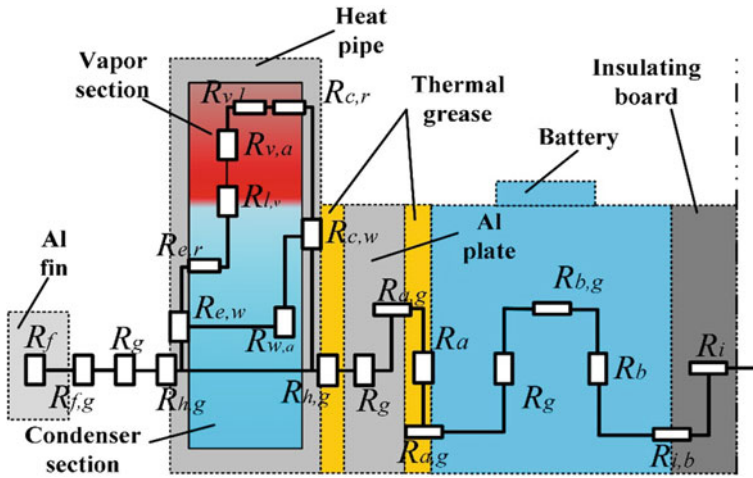


Fig. 4 Equivalent circuit model of HPIS

the equivalent circuit is applied to calculate the physical parameters and conditions for numerical simulation.

In the evaporator section, the thermal resistance  $R_e$  can be expressed as:

$$R_e = R_{h,g}^1 + R_{e,w} + R_{e,r} \text{ and } K_e = \frac{1}{R_e A_e} \tag{5}$$

$$\begin{cases} R_{h,g}^1 = \frac{1}{A_{e0} \alpha_{wall}^1} \\ R_{e,w} = \frac{\ln\left(\frac{d_o}{d_i}\right)}{2\pi L_e \lambda_w} \\ R_{e,r} = \frac{1}{A_{ei} \alpha_e} \end{cases} \tag{6}$$

where  $K_e$  is the heat transfer coefficient of liquid pool;  $A_e$ ,  $A_{e0}$  and  $A_{ei}$  are the mean, outer and inner surface area of evaporator section;  $\alpha_{wall}^1$  and  $\alpha_e$  are the heat transfer coefficient of outer wall and liquid film;  $d_o$  and  $d_i$  are the diameter of outer and inner wall;  $L_e$  is the length of evaporator section and  $\lambda_w$  is the equivalent thermal conductivity.

In the condenser section, the thermal resistance can be described as:

$$R_c = R_{h,g}^2 + R_{c,w} + R_{c,r} + R_f \text{ and } K_c = \frac{1}{R_c A_c} \tag{7}$$

$$\left\{ \begin{array}{l} R_{h,g}^2 = \frac{1}{A_{co}\alpha_{wall}^2} \\ R_{c,w} = \frac{ln\left(\frac{d_o}{d_i}\right)}{2\pi L_c \lambda_w} \\ R_{c,r} = \frac{1}{A_{ci}\alpha_c} \\ R_f = \frac{1}{\alpha_f(A_{fin1} + \eta_{fin}A_{fin2})} \end{array} \right. \quad (8)$$

where  $K_c$  is the heat transfer coefficient of vapor region;  $A_c$ ,  $A_{co}$  and  $A_{ci}$  are the mean, outer and inner surface area of condenser section;  $\alpha_{wall}^2$  and  $\alpha_c$  are the heat transfer coefficient of outer wall and radial direction;  $L_c$  is the length of cooling section;  $\eta_{fin}$  and  $\alpha_f$  are the heat transfer coefficients of fin efficiency and aluminum fin;  $A_{fin1}$  and  $A_{fin2}$  are the surface area of thermosyphon between fins and surface area of fins.

### 4 Numerical Model

Numerical survey is utilized to observe to investigate the thermal behaviour on the temperature distribution of battery system. The transient simulation is performed in the ANSYS Fluent. The numerical model considers following assumptions: (1) The radiation effects on the surface of the battery can be negligible; (2) the surface between solid and gas is no slip and the contact surface between solids is coupled; (3) heat pipe is regarded as two-section solid conductor with various thermal conductivity due to the different thermal resistance. Table 3 lists the initial specifications of the HPIS.

#### 4.1 Parameters Setup and Solution

The boundary condition parameters are significant segment for simulation process. A time-dependent solution is set up due to the battery discharge course obtained by the NTGK model, in which the battery is discharged from 4.2 to 2.75 V and the

**Table 3** Thermal properties of apparatus

	Density (kg·m <sup>3</sup> )	Specific heat, (J·kg <sup>-1</sup> ·K <sup>-1</sup> )	Thermal conductivity (W·m <sup>-1</sup> ·K <sup>-1</sup> )
Insulating board	30	1380	0.03
Thermal grease	1600	1700	4.15
Aluminum plate/fin	2719	871	202.4
Heat pipe	2702	903	2000

original depth of discharge (DoD) is set as 0. The nominal cell capacity is 42Ah. Virtual battery connection is established to connect the two cells in series. The energy equation is on. The ambient temperature is set as 25 °C and the initial temperature of the integrated system is identical with that. A convective heat transfer coefficient of 10 W·m<sup>-2</sup>·K<sup>-1</sup> is defines as boundary condition on the surfaces of solids.

The dynamic thermal behaviour of the cooling system is modeled by a transient simulation with a fixed time step of 20 s. Pressure–velocity coupling is set as simple algorithm and the objections of the momentum and energy are set as second-order upwind scheme in the stereoscopic model. In addition, under-relaxation factors are 0.7 for momentum and 1.0 for energy in solution controls.

### 4.2 Mesh Sensitivity Analysis

The HPIS is meshed with various grid sizes in order to reduce the amount of calculation and to ensure the accuracy of calculation results. The variance with different meshes of the battery maximum temperature is shown in Fig. 5. Along with the grid number increasing from 609,254 to 1,034,692, the deviation of the maximum temperature of battery is merely 0.02% that can be ignored, therefore, the mesh number of 609,254 is adopted. In addition, the skewness of mesh metric is tested to keep precise quality, of which the standard deviation maintains a stable level of 0.12 when the grid numbers can barely affect the simulation results.

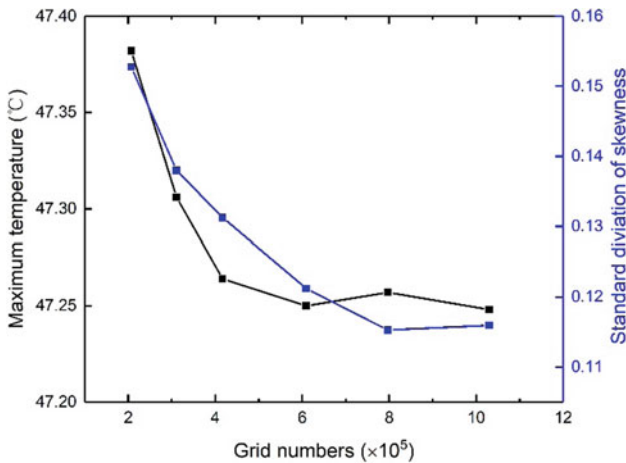


Fig. 5 Grid sensitivity test

## 5 Results and Discussion

### 5.1 Method Comparison

In order to analyze the efficiency of heat transfer of the “traditional method” and the “novel method”, the maximum temperature and temperature difference in single battery of the HPIS at 3C discharge under natural convection are presented in Fig. 6. The battery cell temperature is gradually increased with the SOC declining, which is identical to both methods. The temperature distributions of the batteries are similar between cell 1 and cell 2 due to the symmetrical structure. In novel method, the maximum temperature of the battery reaches 47.2 °C that is lower than the 48.5 °C in traditional circuit model at the end of discharge. Moreover, the temperature differences are maintained stable upward trend at initial discharging process, then increased sharply at the final stage (about SOC < 0.1). The temperature difference of one battery in latest method is reduced by 11.86% compared with original calculation when segmented heat pipe model is applied. In addition, the range of temperature is optimal to ensure the system safety, and is appropriate below 50 °C. Consequently, the precision of proposed novel thermal resistance method of heat pipe integrated into the HPIS model is higher than the traditional model.

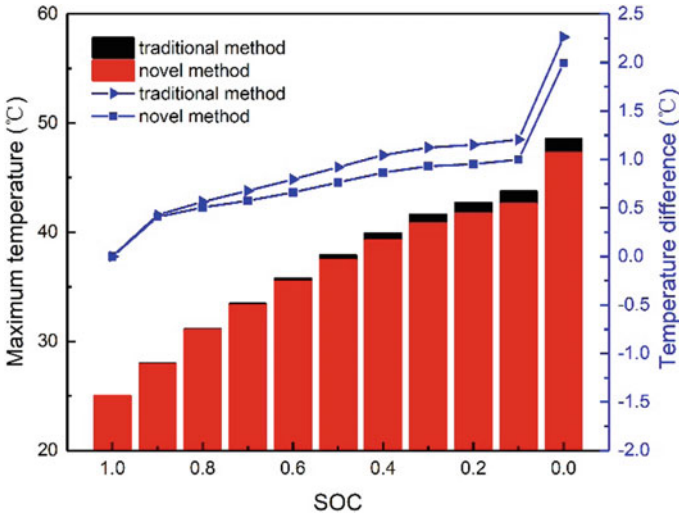


Fig. 6 Temperature variations between two methods at 3C discharging rate

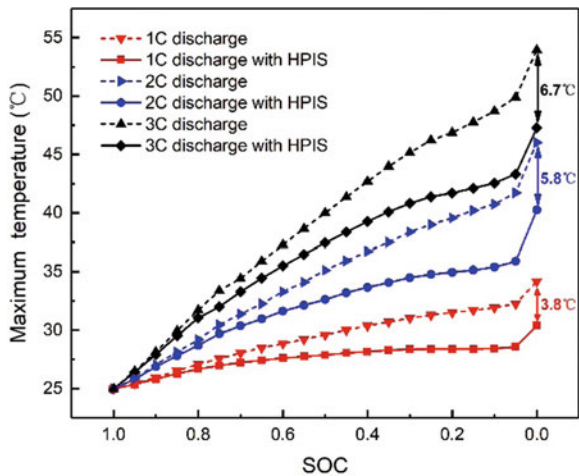
### 5.2 Temperature Distribution Analysis

The battery cycle life is greatly influenced by the maximum temperature and temperature difference of the battery pack. A notable temperature fluctuation in both battery and system can result in unexpected thermal runaway. Thus, considering the thermal performance of the HPIS with novel method under constant discharging rate in natural convection, the temperature distribution of the battery and HPIS system is analyzed at 1C, 2C and 3C discharging rate at ambient temperature of 25 °C.

Figure 7 presents the maximum temperature variation of two cases during discharging process. Due to the symmetrical structure, only one battery cell curve is shown. Without the HPs installed, the temperature of the battery pack increases dramatically. At the end of the 1C and 2C discharging rate, the maximum temperature of the battery reaches 34.2 and 46.0 °C. However, the battery temperature exceeds 50 °C that is completely out of security range under 3C discharging rate. The exterior parts of the system can easily transfer the heat to the surrounding medium through convection while the heat in the interior battery will continue to accumulate, which may avoid thermal dissipation. After the installation of HPIS, the maximum temperature of the battery decreases by 3.8 °C at the end of 1C discharge. Furthermore, the battery temperature differences between two structures extend to 5.8 and 6.7 °C under 2C and 3C discharging rate respectively, that is significantly increased by the higher discharging rate.

Moreover, the temperature differences of the pack ( $\Delta T_{pack}$ ) and of the battery cell ( $\Delta T_{cell}$ ) are presented in Fig. 8. At the end of 3C discharge,  $\Delta T_{pack}$  can up to 12.5 °C with HPIS and 15.7 °C without HPs that may slightly slow down the upward trend of temperature, between which the difference value reaches 3.2 °C. In addition, the maximum  $\Delta T_{cell}$  is 2.3 °C with HPIS, which is much higher than the initial battery pack of 1.0 °C, because the HPs contact with the single surface of the

**Fig. 7** Maximum temperature of the pack at various discharging rate



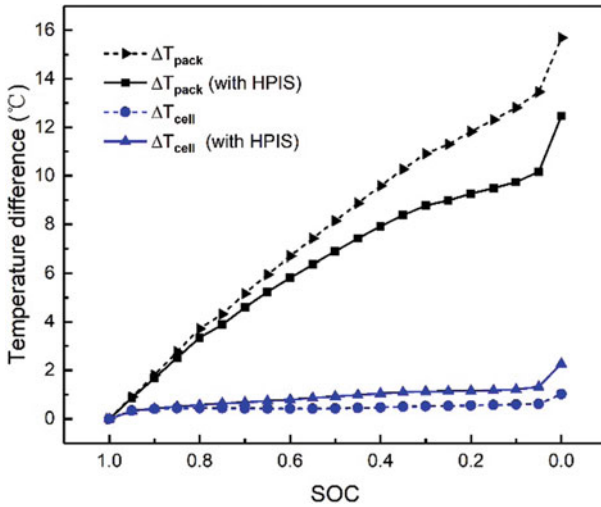
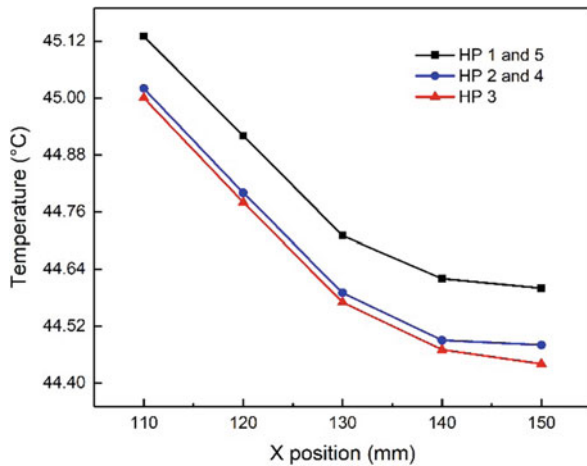


Fig. 8 Temperature difference curves at 3C discharging rate

cell with better heat dissipation performance and the opposite one is only in contact with the insulating board with lower cooling efficiency, but the temperature value is no more than 5 °C.

The temperature distribution of HPs at condenser section, confirming the number of HPs according to the x-axis direction, reveals the thermal characteristic of HPIS system. As is presented in Fig. 9, although the temperature of HP 1 and 5 is the highest value from 318.1 to 317.6 °C among HPs along the x position due to the scattered pipes distribution and insufficient effect of marginal heat transfer, the maximum

Fig. 9 Temperature distribution at HPs' condenser section along the X position





temperature difference between HPs is below 0.2 °C. Besides, the thermal distributions of HP 2, 3 and 4 become minimal, and the temperature range of HP 3 is from 318.0 to 317.4 °C possessing good heat dissipation performance at the end of condenser position, which indicates the fairly temperature uniformity of the pipes.

### 5.3 Improvement of Thermal Performance

As mentioned above, HPIS helps reduce the maximum temperature of battery conspicuously. However, under the natural convection at high discharging rate, the battery temperature cannot be maintained within the optimal operating range (<45 °C). In order to control the battery temperature under proper extent, it is necessary to implement forced air convection on the condenser section of HPs, which extremely enhances the cooling performance.

Numerical simulations using the previous model with the 148 × 10 × 47 mm gas cabin are undertaken by adopting the various air volume flow rates. As is shown in Fig. 10, The maximum temperature of batteries is predicted under 3C discharging rate. Compared to the natural convection, the air convection of 12.69m<sup>3</sup>h<sup>-1</sup> can decrease the maximum temperature by 0.36 °C. The temperature of battery can be controlled below 45 °C under the air convection higher than 25.38m<sup>3</sup>h<sup>-1</sup> at the end of 3C discharging rate. It is worth nothing that the air-cooling efficiency increases with the raising depth of discharge.

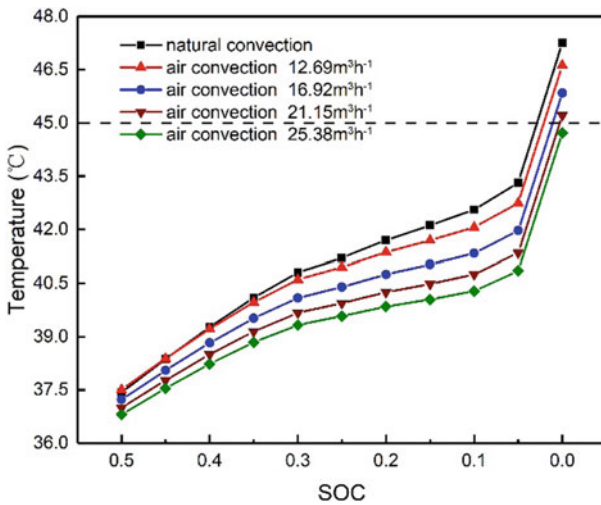


Fig. 10 Maximum temperature of battery under various convection strategies

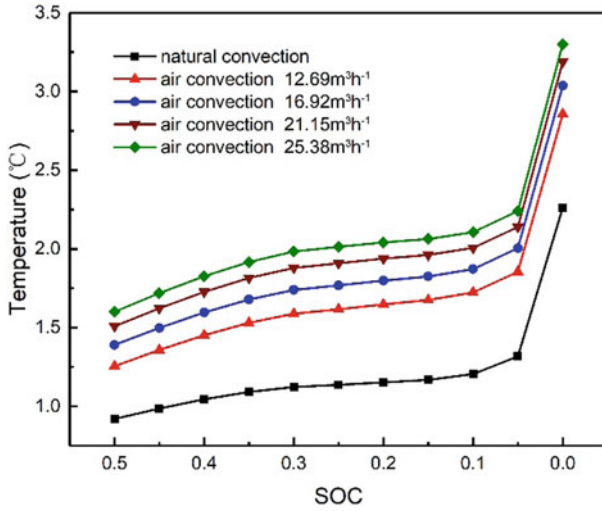


Fig. 11 Temperature difference of battery under various convection strategies

However, the uniformity of battery temperature has reduced due to the unique surface of the prismatic cell contacting with HP and excellent heat transfer characteristic. As is presented in Fig. 11, the variation of battery temperature difference is compared. For the battery with natural air convection, the temperature difference can be controlled well below 1.5 °C at first, but exceeded to 2.2 °C while the battery is fully discharged. After adding the forced air cooling, the thermal consistence of battery cell decreases sharply, of which the maximum temperature difference reaches 3.3 °C with 25.38m<sup>3</sup>h<sup>-1</sup> but is still within the optimum temperature by 5 °C. Moreover, the marginal effect of increasing air flow rate toward the gas cabin from 12.69m<sup>3</sup>h<sup>-1</sup> to 25.38m<sup>3</sup>h<sup>-1</sup> become negligible. Therefore, considering both the lower maximum temperature and less thermal uniformity, a forced air convection of 25.38m<sup>3</sup>h<sup>-1</sup> appears to prove the improvement of thermal performance of the HPIS by accelerating volume flow and enhancing heat dissipation.

### 5.4 Evaluation of Heat Insulation Efficiency

Although the HPIS has been verified to be effective in the light of cooling efficiency, the phenomenon of thermal runaway should also be attached great importance to. Considering the heat dissipation of one battery pack to the adjacent cell at the end of 3~8C discharging rate, the thermal blocking effect of insulating board should be tested. In this part, the predicted maximum temperature and trigger time (when adjacent cell temperature is above 50 °C) of the battery with the insulating board of

1 mm, 1.5 mm, 2 mm respectively compared to non-board model under natural air convection are analyzed.

The maximum temperature of the battery caused by adjacent one at high discharging rate under four schemes is presented in Fig. 12. The battery heat dissipates rapidly without insulation, in which the battery temperature exceeds 50 °C at the end of 4C discharging rate. when implementing the insulating board of various thickness, the thermal runaway situation has been effectively controlled. The highest values are 52.4 °C at 4C rate and 51.9 °C at 6C rate with 1 mm and 1.5 mm board respectively. In addition, the cell temperature can be maintained below 50 °C with 2 mm insulating board at the end of 7C rate. Although the thermal value is slightly higher than trigger value reaching 50.73 °C under 8C rate, the range of the temperature decrease is acceptable to ensure battery safety.

As can be seen from the bar in Fig. 13, the time is variable in four cases at 6, 7 and 8C discharging rate. The trigger time is slightly reduced from 300 to 160 s, taking up almost 25% and 13% of discharge time due to the high thermal conductivity between batteries. But the values increase gradually with the thickness of the insulating board. There is no trigger time under low discharging rate and 460 s of 39% discharging time at 8C rate when 2 mm board is applied, which suggests that a thicker plate is installed next to the battery is an effective method for blocking the spread of the heat.

The low thermal conductivity of the insulating board slows down the heat transfer speed of the runaway battery, providing opportunity for rapid heat transfer. In short, the present HPIS with insulating board showed a significant improvement in the level of insulation ability.

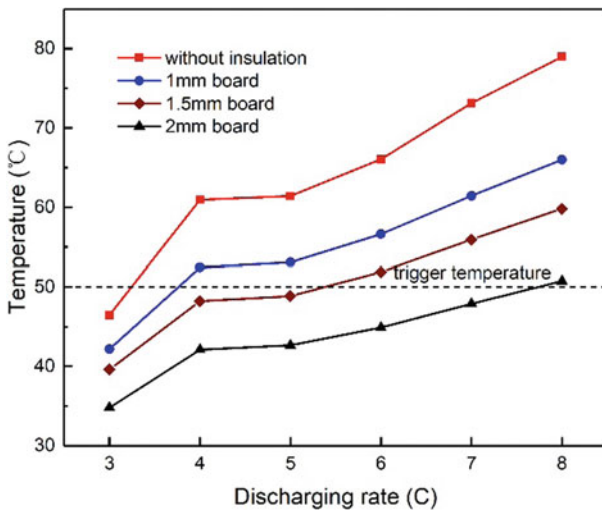
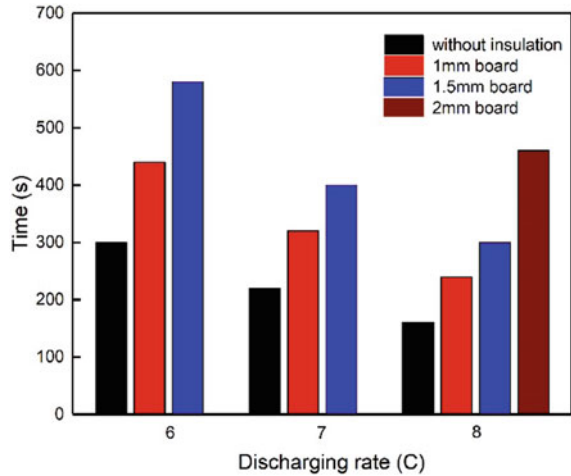


Fig. 12 Thermal performance of adjacent battery with different insulating board

**Fig. 13** Trigger time of maximum temperature at 6, 7 and 8C discharging rate



## 6 Conclusion

High operating efficiency and better thermal performance are two critical quantities that the lithium-ion battery should possess. For tackling with the thermal accumulation and runaway within the battery during fast discharging, numerous efforts are undertaken to optimize the thermal characteristic of HP to maintain the battery under damaged temperature with high uniformity. A new HPIS is introduced for efficient cooling to enhance the working performance of the battery. The novel method is calculated by equivalent thermal resistance network with forced air convection, which reveals the dynamic heat behaviour inside the cells and pipes. To prevent the propagation of thermal runaway between the adjacent batteries, an insulation strategy is proposed and testified. The numerical model is calibrated and comprehensively validated by comparing the initial predicted data with experimental results. Some conclusions are summarized as follows:

1. The NTGK model shows the considerable accuracy with the validation of experimental, which has successfully predicted the electrochemical behaviour of the battery. The average deviation coefficient of temperature between experimental data and simulation results is below 10 °C.
2. The proposed novel thermal resistance method is testified more accuracy compared with the traditional equivalent model by assessing the temperature distribution of battery pack. The maximum temperature decreases to 1.3 °C and temperature difference reduces by 11.86% when equivalent network model is applied.
3. HPIS-based battery pack displays outstanding heat transfer performance at 3C discharging rate with natural air convection, where the maximum temperature is 6.7 °C lower than the non-HPs structure. Although the temperature difference of the battery cell increases to 2.3 °C, which is still below the optimum value

- of 3 °C. The temperature distribution of HPs at condenser section presents the fairly temperature uniformity of the pipes.
4. In order to enhance the efficiency of heat transfer of the HPIS, the air-forced convection is implemented to maintain the battery operating under a much cooler condition. An air volume flow of 25.38 m<sup>3</sup>h<sup>-1</sup> can control the battery temperature below 45 °C at the end of 3C discharging rate, where the temperature difference performs with a small fluctuation.
  5. The combination of reasonable heat insulation measures can ameliorate the thermal runaway phenomenon. By varying the thickness of insulating board, the influence of the high-rate discharging battery to adjacent one can be reduced. The battery temperature is well controlled below 50 °C with 2 mm insulating board.

**Acknowledgements** The authors acknowledge the financial support received from National Nature Science Foundation of China (Grant No.51965008), Major Science and Technology projects of China of Guizhou ZNWLQC [2019]3012.

## References

1. Dunn B, Kamath H, Tarascon JM (2011) Electrical energy storage for the grid: a battery of choices. *Science* 334:928–935
2. Mohammadian SK, Zhang Y (2015) Thermal management optimization of an air-cooled Li-ion battery module using pin-fin heat sinks for hybrid electric vehicles. *J Power Sources* 273:431–439
3. Sato N (2001) Thermal behavior analysis of lithium-ion batteries for electric and hybrid vehicles. *J Power Sources* 99(1–2):70–77
4. Pesaran AA (2002) Battery thermal models for hybrid vehicle simulations. *J Power Sources* 110(2):377–382
5. Celik A, Coban H, Göcmen S et al (2019) Passive thermal management of the lithium-ion battery unit for a solar racing car. *Int J Energy Res*
6. Doyle M, Newman J, Gozdz AS et al (1996) Comparison of modeling predictions with experimental data from plastic lithium-ion cells. *J Electrochem Soc* 143(6):1890–1903
7. Tiedemann W, Newman J, Desua F (1977) *Power sources* 6. Collians DH (ed) 15
8. Gu H (1983) Mathematical analysis of a Zn/NiOOH cell. *J Electrochem Soc* 130(7):1459–1464
9. Kim US, Yi J, Shin CB, Han T, Park S (2011) Modelling the thermal behaviour of a lithium-ion battery during charge. *J Power Sources* 196(11):5115–5121
10. Chacko S, Chung YM (2012) Thermal modelling of Li-ion polymer battery for electric vehicle drive cycles. *J Power Sources* 213:296–303
11. Pesaran AA (2001) Battery thermal management in EV and HEVs: issues and solutions. *Battery Man* 43(5):34–49
12. Bandhauer TM, Garimella S, Fuller TF (2011) A critical review of thermal issues in lithium-ion batteries. *J Electrochem Soc* 158(3):R1–R25
13. Moraga NO, Xamán JP, Araya RH (2016) Cooling Li-ion batteries of racing solar car by using multiple phase change materials. *Appl Therm Eng* 108:1041–1054
14. Liang J, Gan Y, Li Y (2018) Investigation on the thermal performance of a battery thermal management system using heat pipe under different ambient temperatures. *Energy Convers Manage* 155:1–9

15. Wu MS, Liu KH, Wang YY et al (2002) Heat dissipation design for lithium-ion batteries. *J Power Sources* 109(1):160–166
16. Tran TH, Harmand S, Sahut B (2014) Experimental investigation on heat pipe cooling for hybrid electric vehicle and electric vehicle lithium-ion battery. *J Power Sources* 265:262–272
17. Zhao R, Gu J, Liu J (2015) An experimental study of heat pipe thermal management system with wet cooling method for lithium-ion batteries. *J Power Sources* 273:1089–1097
18. Famouri M, Carbajal G, Li C (2014) Transient analysis of heat transfer and fluid flow in a polymer-based micro flat heat pipe with hybrid wicks. *Int J Heat Mass Transf* 70:545–555
19. Chen K, Wang S, Song M et al (2017) Configuration optimization of battery pack in parallel air-cooled battery thermal management system using an optimization strategy. *Appl Therm Eng* 123:177–186
20. Liu F, Lan F, Chen J (2016) Dynamic thermal characteristics of heat pipe via segmented thermal resistance model for electric vehicle battery cooling. *J Power Sources* 321:57–70
21. Hatata AY, Osman G, Aladl MM (2018) An optimization method for sizing a solar/wind/battery hybrid power system based on the artificial immune system. *Sustain Energy Technol Assess* 27:83–93
22. Kwon KH, Shin CB, Kang TH et al (2006) A two-dimensional modeling of a lithium-polymer battery. *J Power Sources* 163(1):151–157
23. Rao L, Newman J (1997) Heat-generation rate and general energy balance for insertion battery systems. *J Electrochem Soc* 144(8):2697–2704
24. Huber C (2017) Phase change material in battery thermal management applications. PhD thesis. Technische Universität München
25. Kim J, Oh J, Lee H (2018) Review on battery thermal management system for electric vehicles. *Appl Therm Eng*

# Modeling the Intercooling of a Multi-stage Compression in Gas Turbines Using Absorption Chiller



Kirolos A. Amin, Mohamed ElHelw, and Osama A. Elsamni

**Abstract** The intake ambient conditions have significant influences on the performance of gas turbine plants, specifically in hot and dry locations. Cooling the compressor intake air has become one of the most common techniques for increasing the gas turbine efficiency. In the present paper, a new idea for cooling the intake air and the air at inlet to each compressor stage using a single-effect absorption chiller is proposed and modeled. The absorption chiller is driven by the heat dissipated in the inter-stage cooling. A mathematical model of the integrated gas turbine-absorption chiller is developed, validated, and assessed under different ambient conditions for two cities in Egypt, namely Alexandria (warm-humid), Aswan (hot-arid) on a daily and annual basis. The effect of ambient conditions variations on the net power production, thermal efficiency, specific fuel consumption, and CO<sub>2</sub> emission are investigated. The results show that for cities with hot-dry climates such as Aswan, especially in June, the thermal efficiency of the proposed system is better than the conventional configuration by 3.164%. Using this technique, the power output increases by 5.683%. Additionally, the emission reduction of 5.536 percent. However, in humid regions like Alexandria, due to losing the amount of condensed water in air precooling and low average ambient temperature compared to Aswan, the performance enhancement is not significant.

---

K. A. Amin (✉)

Department of Mechanical Engineering, Faculty of Engineering, Pharos University, Alexandria, Egypt  
e-mail: [kirolos.amin@pua.edu.eg](mailto:kirolos.amin@pua.edu.eg)

M. ElHelw · O. A. Elsamni

Department of Mechanical Engineering, Faculty of Engineering, Alexandria University, Alexandria 21544, Egypt

Nomenclature			
$C_p$	Specific heat at constant pressure, [kJ/kg.K]	Subscripts	
$h$	Enthalpy, [kJ/kg]	$a$	Air
$P$	Pressure, [kPa]	$g$	Gas
$T$	Temperature, [°C]	$f$	Fuel
$\rho$	Density, [kg/(m <sup>3</sup> )]	$amb$	Ambient
$x$	Solution concentration, [%]	$is$	Isentropic
$\chi$	Dryness fraction, [–]	$C\cdot C$	Cooling capacity
$RH$	Relative humidity, [%]	$p$	Pump
$LHV$	Lower heat value, [kJ/kg]	$c$	Compressor
$\dot{Q}$	Heat transfer rate, [kW]	$evap$	Evaporator
$W$	Work done, [kW]	$abs$	Absorber
$COP$	Coefficient of performance, [–]	$des$	Desorber
$r_p$	Pressure ratio, [–]	$cond$	Condenser
$SFC$	Specific fuel consumption, [kg/kWh]	$SHX$	Solution heat exchanger
$HR$	Heat rate, [kJ/kWh]	$GT$	Gas Turbine
$bwr$	Back work ratio, [–]	$PM$	Proposed Model
$\varepsilon_{CO_2}$	Carbon dioxide emissions, [kg/kWh]		
		<i>Abbreviations</i>	
<i>Greek letters</i>		$CONVBC$	Conventional Brayton Cycle
$\Delta P$	Pressure drop, [kPa]	$VARs$	Vapor absorption refrigeration system
$\gamma$	Specific heat ratio, [–]	$ISO$	International Organization for Standardization
$\omega$	Moisture content, [kg moisture/kg dry air]	$EES$	Engineering Equation Solver
$\eta$	Efficiency, [%]	$TIC$	Compressor Inlet Temperature
$\varepsilon$	Effectiveness, [–]		
$A/F$	Air to fuel ratio, [–]		



## 1 Introduction

Due to high ambient temperatures and relative humidity in Middle East region during summer, there are significant impacts on gas turbine performance. When the ambient temperature increases, the air mass flow rate decreases, leading to a reduction of the net power provided by the gas turbine plant. From this point of view, in order to improve the performance of gas turbine power plants, many researchers have investigated alternative turbine intake cooling strategies. The first innovation of a gas turbine intake air-cooling system was in 1987 in Michigan gas turbine power plant, using direct air-cooling (Gupta et al. [1]). In 1992, the off-peak ice picker was also used in the USA as a cooling system (Yingjian et al. [2]). Generally, the techniques of cooling the air at inlet to the compressors of gas turbine plants can be classified into main four techniques: high-pressure fogging, evaporative cooling, absorption chiller, and mechanical refrigeration system. This inspired many studies, summarized below.

The spraying of droplets of demineralized water into air inlet ducts is known as high-pressure fogging. This method of cooling was studied and assessed by Majdi et al. [3], Najjar et al. [4], Alhazmy et al. [5], Barakat et al. [6], Athari et al. [7], Comodi et al. [8], Ehyaei et al. [9]. According to the results and recommendations of the theoretical and practical researches, a spray cooler may increase power and enhance the efficiency of a gas turbine plant. However, in warm and dry locations, it works more efficiently, it is substantially cheaper than cooling coils, but that need huge amount water, in order to act well.

In the evaporative cooling, the latent heat of vaporization is used to reduce the ambient temperature from the dry-bulb to the wet-bulb temperature. Najjar et al. [4], Popli et al. [10], Santos et al. [11], Mohapatra and Sanjay [12], Marzouk et al. [13], White and Meacock [14] studied the potential of gas turbine power plants by suggesting the use of evaporative cooling. The findings showed that the wet-bulb influence on the inlet air temperature limits the capacity improvement, and this approach needs a considerable amount of water for optimal operation. It is especially useful in hot arid locations.

As a precooling technology, the absorption chiller recuperates the waste heat from the gas turbine exhaust gases. The impact of compressor intake air cooling using an absorption chiller was theoretically investigated by many researchers such as Majdi et al. [3], Najjar et al. [4], Popli et al. [10], Santos et al. [11], Zainali et al. [15], Mohapatra et al. [16], and Mohanty et al. [17] at different operating and climatic conditions. According to the research's findings, the absorption chiller has the advantage of being able to cool the input air to a certain temperature, increase the plant's output power, and increase the GT's efficiency. However, the heat input to the vapor absorption refrigeration system depends on the GT exhaust gasses which, in turn, reduces the heat exchangers life time and increases the maintenance costs.

To cool the ambient air entering a mechanical refrigeration system, it must pass through a chilling coil. This implies that the ambient air's wet-bulb temperature has no impact on mechanical refrigeration systems. The reduction of GT inlet air

temperature by using vapor compression refrigeration system was studied by Najjar et al. [4], Santos et al. [11], Mohapatra and Sanjay [12], Mohapatra et al. [16], Mohammed et al. [18], Al-ansary et al. [19], and Dawoud et al. [20]. There was notable deterioration in the total energy production, although the mechanical chiller enables full control over the intake conditions of the compressor. This is because the electricity needed to drive the mechanical refrigeration cycle is deducted from the gas turbine output.

It can be concluded here that the fogging system and sprays directly to the air intake of the compressor have two major drawbacks. They are; the possibility of the compressor blades damage if some water droplets penetrate the compressor, and the impracticality of the fogging system in places where the relative humidity is already high. Additionally, evaporative cooling is similar to the fogging system, except the compressor inlet does not have direct water injection. However, the performance is restricted by the site's wet-bulb temperature reading which is limited by the relative humidity of the surrounding air. Usually, the precooling using an absorption chiller utilizes waste heat from gas turbine exhaust gases which is not clean due to fouling caused by the flue gases passing over the tubes of the absorption chiller generator, resulting in a reduction in the heat exchangers lifetime. Although the mechanical refrigeration system can adjust the inlet air to any desired value, the lower the temperature it can reach, the less net power output is obtained.

In the present paper, the gas turbine performance including intake air precooling and multi-stage intercooling using absorption chiller is investigated under the ambient conditions for two cities in Egypt representative of different climatic conditions in summer, namely Alexandria (which is considered warm-humid), and Aswan (which is considered hot-arid) on a daily and annual basis. The motivations of the present study are mainly focused on the following items:

- Improving performance of gas turbines for power generation at different ambient conditions.
- lowering the compressor inlet temperature which is down to 5°C, which is much lower than the previous studies.
- Using the heat generated during the compression to be recovered and utilized in driving the absorption chiller instead of the exhaust of the gas turbine. This would keep the absorption chiller clean from the flue gases, reduce the maintenance cost, and increase heat exchangers lifetime.
- Reducing the power plant-specific fuel consumption, and CO<sub>2</sub> Emission.

## 2 Proposed Mathematical Model Analysis

The proposed model consists of a gas turbine with three stages of compression integrated with absorption chiller with regeneration, these stages are separated by two steps of intercooling techniques, as shown in Fig. 1. The gas turbine performance and the cooling capacity of the absorption chiller are developed, and assessed using Engineering Equation Solver (EES) [21]. The present paper studied the performance of

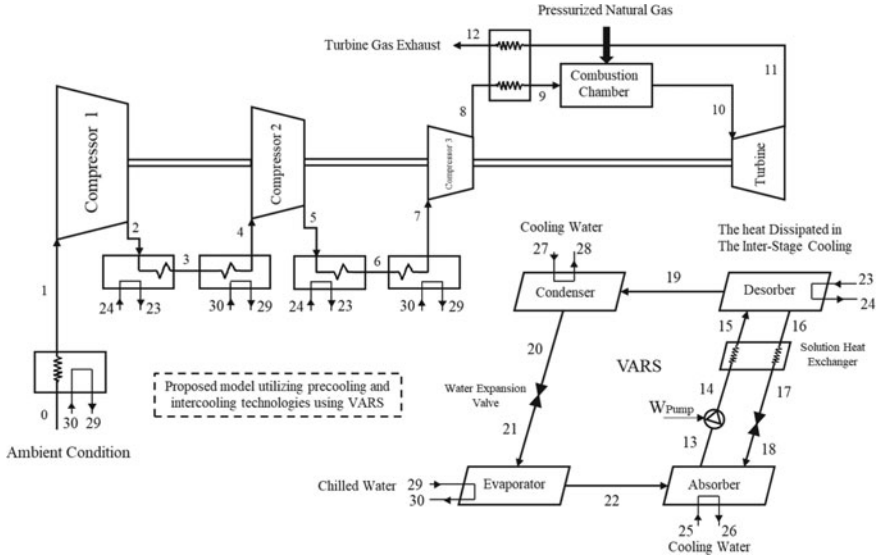


**Fig. 1** Schematic layout of the proposed model utilizing precooling and intercooling technologies using Single-Effect  $H_2O-LiBr$  absorption chillers

the proposed model, compared to the conventional Brayton cycle using perfect intercooling in which the air is cooled by cooling water as shown in Fig. 2. Comparisons include the output power, thermal efficiency, heat rate, specific fuel consumption, and environmental impact at different ambient conditions. The main input parameters are shown in Table 1.

- In the thermodynamic analysis of the integrated gas turbine and absorption chiller cycles, the following assumptions are made:
- Each VARS and gas turbine component is examined as a control volume considered to be in a steady-state, with pressure drop and heat losses to the surroundings disregarded.
- The impacts of kinetic and potential energy are insignificant.
- As a gas turbine working fluid, air is considered ideal in the Brayton cycle.
- Heat is meant to be constantly added during combustion.
- The solution and refrigerant valves are isenthalpic.

The conservation equations for the mass and energy are applied to all components and the following thermodynamics relations are presented for three identical compression stages. Note that the subscript of the variables appearing in the following equations are written according to the notations of Figs. 1 and 2. The pressure ratio of each compressor stage ( $r_p$ ) is given by:

$$r_{p1} = \frac{P_2}{P_1}, r_{p2} = \frac{P_5}{P_4}, r_{p3} = \frac{P_8}{P_7} \quad (1)$$

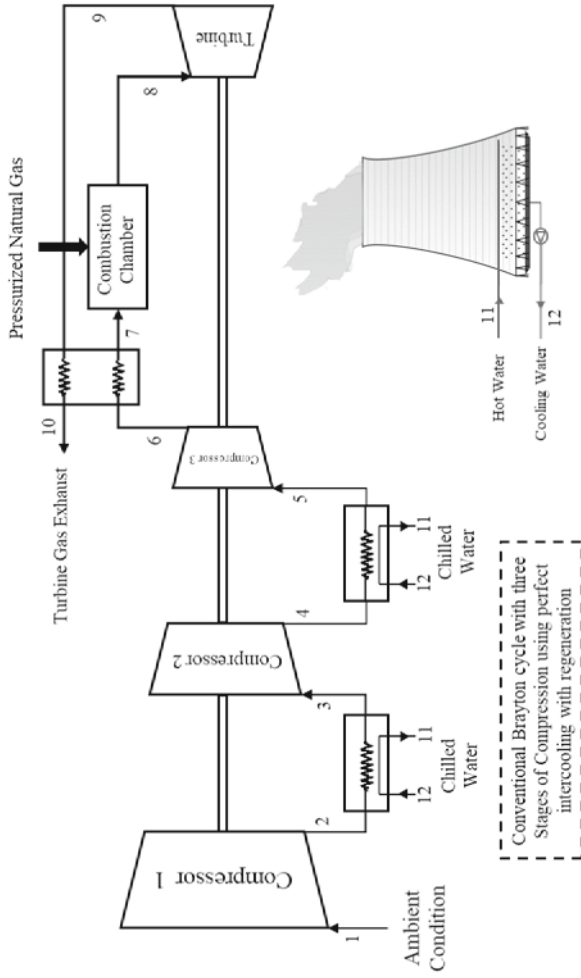


**Fig. 2** Schematic layout of conventional Brayton cycle with three Stages of Compression using perfect intercooling with regeneration

**Table 1** The proposed model input parameters [11, 22]

Item	Rate
Ambient pressure, [kPa]	101.3529
Gas lower heating value, [kJ/kg]	48,235.63
Total Compression ratio of the cycle, [-]	30
Compressor Air Inlet Temperature, [°C]	5
Compressor isentropic Efficiency, [%]	85.4
Turbine isentropic Efficiency, [%]	86.8
Combustion chamber Efficiency, [%]	99
Regeneration Effectiveness, [%]	90

where the inlet and outlet air pressures of the compressors are respectively  $P_1 = P_{\text{atm}}$ ,  $P_2$ ,  $P_4$ ,  $P_5$ ,  $P_7$  and  $P_8$ . The equation specifies the isentropic outlet temperatures that exits the compressors is determined by Eq. (2). Taking the air specific heat ratio  $\gamma_a = 1.4$ ,

$$\frac{T_{2s}}{T_1} = \left(\frac{P_2}{P_1}\right)^{\frac{\gamma_a-1}{\gamma_a}}, \quad \frac{T_{5s}}{T_4} = \left(\frac{P_5}{P_4}\right)^{\frac{\gamma_a-1}{\gamma_a}}, \quad \frac{T_{8s}}{T_7} = \left(\frac{P_8}{P_7}\right)^{\frac{\gamma_a-1}{\gamma_a}} \quad (2)$$

where the inlet and outlet air temperatures of the compressor are respectively  $T_1$ ,  $T_2$ ,  $T_4$ ,  $T_5$ ,  $T_7$  and  $T_8$ . The compressors isentropic efficiency ( $\eta_{is)C1,2,3}$ ) expressed as:

$$\eta_{is)C1} = \frac{T_2 - T_1}{T_2s - T_1}, \quad \eta_{is)C2} = \frac{T_5 - T_4}{T_5s - T_4}, \quad \eta_{is)C3} = \frac{T_8 - T_7}{T_8s - T_7} \quad (3)$$

The compressors work ( $\dot{W}_{C1,2,3}$ ) can be calculated as:

$$\dot{W}_{C1} = \dot{m}_a(h_2 - h_1), \quad \dot{W}_{C2} = \dot{m}_a(h_5 - h_4), \quad \dot{W}_{C3} = \dot{m}_a(h_8 - h_7) \quad (4)$$

The regenerator energy balance is expressed as:

$$\dot{m}_a(h_9 - h_8) = \dot{m}_g(h_{11} - h_{12}) \quad (5)$$

The regeneration efficiency ( $\eta_{\text{reg}}$ ) is considered in this study as:

$$\eta_{\text{reg}} = \frac{h_9 - h_8}{h_{11} - h_8} \quad (6)$$

The energy balance in the combustion chamber:

$$\dot{m}_a h_9 + \dot{m}_f \times LHV = \dot{m}_g h_{10} \quad (7)$$

$$\dot{m}_g = \dot{m}_a + \dot{m}_f \quad (8)$$

The heat added is also indicated as:

$$Q_{add} = \dot{m}_g h_{10} - \dot{m}_a h_8 \quad (9)$$

where the calorific value (LHV) assumed to be around 48,235.63 kJ/kg, Combustion chamber efficiency can be calculated as:

$$\eta_{C.C} = \frac{Q_{add}}{\dot{m}_f \times LHV} \quad (10)$$

This equation determines the air to fuel ratio (A/F):

$$\frac{A}{F} = \frac{\dot{m}_a}{\dot{m}_f} \quad (11)$$

The exhaust gases temperature is given by Eq. (12), Taking specific heat ratio for gases  $\gamma_g = 1.4$

$$\frac{T_{11s}}{T_{10}} = \left( \frac{P_{11}}{P_{10}} \right)^{\frac{\gamma_g - 1}{\gamma_g}} \quad (12)$$

The isentropic efficiency of a turbine allows us to calculate the actual temperature drop:

$$\eta_{(is)g.T} = \frac{T_{10} - T_{11}}{T_{10} - T_{11s}} \quad (13)$$

The compressors total work  $\dot{W}_C$  can be calculated as:

$$\dot{W}_C = \dot{W}_{C1} + \dot{W}_{C2} + \dot{W}_{C3} \quad (14)$$

The output net production of the GT ( $\dot{W}_{net}$ ) is calculated by:

$$\dot{W}_{net} = \dot{W}_{GT} - \dot{W}_C \quad (15)$$

The specific fuel consumption (SFC) is determined by:

$$SFC = \frac{3600}{AFR \times \dot{W}_{net}} \quad (16)$$

The GT efficiency ( $\eta_{th,GT}$ ) can be determined by:

$$\eta_{th,GT} = \frac{\dot{W}_{net}}{\dot{Q}_{add} \times \eta_{C.C}} \quad (17)$$

The heat rate (HR) can be expressed as:

$$HR = \frac{3600}{\eta_{th}GT} \quad (18)$$

The back work ratio (bwr) of the cycle is:

$$bwr = \frac{\dot{W}_C}{\dot{W}_{GT}} \quad (19)$$

For the current analysis, the total mass and solution balance equations for each component of the VARS Single effect are:

$$\sum \dot{m}_{in} - \sum \dot{m}_{out} = 0 \quad (20)$$

$$\sum \dot{m}_{in} x_{in} - \sum \dot{m}_{out} x_{out} = 0 \quad (21)$$

The energy balance for each component can be expressed as:

$$\left( \sum \dot{m}_{in} h_{in} - \sum \dot{m}_{out} h_{out} \right) + \sum Q_{in} - \sum Q_{out} + W = 0 \quad (22)$$

The equations of energy balance for some components of the VARS Single effect cycle are expressed as follows:

- Evaporator:

$$\dot{Q}_{evap} = \dot{m}_{22} h_{22} - \dot{m}_{21} h_{21} \quad (23)$$

- Absorber:

$$\dot{Q}_{abs} = \dot{m}_{22} h_{22} + \dot{m}_{18} h_{18} - \dot{m}_{13} h_{13} \quad (24)$$

- Condenser:

$$\dot{Q}_{cond} = \dot{m}_{19} h_{19} - \dot{m}_{20} h_{20} \quad (25)$$

- Desorber:

$$\dot{Q}_{des} = \dot{m}_{19} h_{19} + \dot{m}_{16} h_{16} - \dot{m}_{15} h_{15} \quad (26)$$

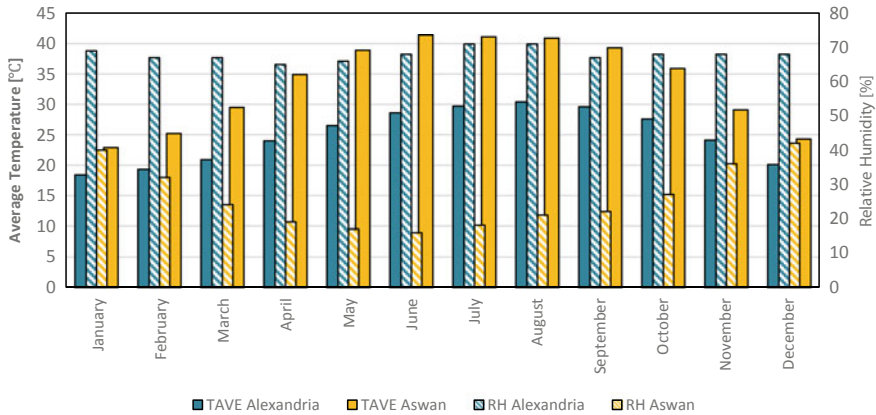


**Fig. 3** The average ambient temperatures and relative humidity throughout the year [23]

Using a coefficient of performance ( $COP_{VARS}$ ), the performance of VARS can be measured as:

$$COP_{VARS} = \dot{Q}_{evap} / \dot{Q}_{des} \quad (27)$$

### 3 Climatic Conditions in the Selected Cities in Egypt

Throughout the year, the ambient temperature of Alexandria and Aswan cities in Egypt is above the ISO requirement of 15 °C. The fluctuations in temperature and relative humidity throughout the year are seen in Fig. 3. These data are based on Atlas weather conditions [23]. The highest, average, and lowest temperatures for Alexandria, as shown in Fig. 3, are 31, 24, and 18.4 °C respectively, and are 41.4, 29.5, and 22.9 °C respectively for Aswan. It may be established that the ambient temperature and the ISO condition differ by an average of 9 and 14.5 °C for Alexandria and Aswan respectively. The highest relative humidity is 71 percent at Alexandria in July and August and 42 percent at Aswan in December, and the minimum are 65 and 16 percent for both cities respectively, as shown in Fig. 3. This means that Aswan can be classified as a hot and dry region, as contrasting to the nature of the climate in Alexandria.

### 4 Thermodynamic Modeling Results and Verification

The results are presented in three subsections. In the first subsection, the proposed model was validated using previous studies. The second subsection shows the



**Table 2** Comparison of other simulation model and predicted performance parameters

	Simulation [13]	Predicted [EES Model]	Discrepancy (%)
Fuel mass flow rate, [kg/s]	14.59	15	2.8
Heat rate, [kJ/kWh]	9435	9108	3.471
GT thermal efficiency, [%]	37	37.84	2.276
Total needed cooling capacity, [MW]	14.10	14.02	0.5492

predicted parameters of the proposed model compared to the conventional Brayton cycle at the same climatic conditions. Finally, the third subsection presents the environmental impact assessment.

#### 4.1 Verification and Error Analysis

To validate the proposed model, each component is compared with similar previous studies separately. The gas turbine and VARS models developed in Sections were validated through other published simulation, modeled by Ali Marzouk, and Abdalla Hanafi [13] to show the accuracy of the thermodynamic modeling. The error comparison results showed in Table 2, are calculated using the discrepancy which is defined by Eq. (28) were examined.

$$Discrepancy = \left( \frac{Value_{Predicted[EESModel]} - Value_{Reference}}{Value_{Reference}} \right) \times 100 \quad (28)$$

It was not possible to directly validate the expected performance features of this paper's suggested model as there was no current experimental work utilizing the same model. This is why the simulation described by Ali Marzouk, and Abdalla Hanafi is used to verify the findings of this study. It was verified under ISO standards. Table 2 presents a comparison of predicted and Simulation model [13] performance parameters for 264.344 [MW] gas turbine located at Korymat, southern Egypt using absorption chiller as a pre-cooler at ISO conditions (101.3 kPa atmospheric pressure, 15°C ambient temperature, and 60% RH). This is a positive sign of agreement because the prediction differences are within 3.4%.

#### 4.2 Results and Discussion

In EES software, the simulation and coding were achieved using both the calculation and simulation of the analyzed gas turbine and the cooling system. EES software also simulates the gas turbine cycle with pre-cooling and intercooling systems. A typical

state point results from the EES model of the VARS Single effect cycle presented in Table 3. For each state point, the predicted pressure, temperature, concentration of LiBr, enthalpy, and solution flow rate show that the single effect H<sub>2</sub>O – LiBr VARS operates between two pressure level (9.660 and 0.620 kPa). Table 4 presented the key performance parameters of the conventional Brayton cycle and the proposed model at the same input parameters and ambient conditions. In the provided comparison, the predicted performance parameters were assessed for [1 kg/s] dry air. The heat dissipated in the inter-stage cooling powered absorption chiller cools down [TIC] to 5 °C.

**Table 3** Typical state point results from EES model of the H<sub>2</sub>O – LiBr VARS Single effect cycle

State point	Temperature (°C)	Enthalpy (kJ/kg)	Pressure (kPa)	Vapor fraction (–)	Mass flow rate (kg/s)	LiBr concentration (%)
13	41.6	129.5	0.620	0.000	2.5000	61.9
14	41.6	129.5	9.660	0.000	2.5000	61.9
15	80.0	201.5	9.660	0.000	2.5000	61.9
16	101.1	253.0	9.660	0.000	2.3975	64.6
17	59.4	178.0	9.660	0.000	2.3975	64.6
18	47.8	178.0	0.620	0.007	2.3975	64.6
19	127.0	2738.4	9.660	0.000	0.1025	0.0
20	32.1	134.5	9.660	0.000	0.1025	0.0
21	0.2	134.5	0.620	0.053	0.1025	0.0
22	1.1	2502.5	0.620	1.000	0.1025	0.0

**Table 4** Comparison predicted performance parameters of the conventional Brayton cycle, and the proposed model at Alexandria and Aswan cities in Egypt in August

Variable and unit	CONVBC Alexandria	PM Alexandria	CONVBC Aswan	PM Aswan
Compressor inlet air temperature [°C]	30.4	5	40.9	5
Net power production [kW]	827.4	825.5	788.1	826.1
Thermal efficiency [%]	48.47	49.42	47.95	49.43
Heat rate [kJ/kWh]	5464	5249	5565	5248
Back work ratio [–]	0.3447	0.3164	0.3578	0.3163
Specific fuel consumption [kg/kWh]	0.1195	0.1148	0.1217	0.1148
CO <sub>2</sub> Emissions [kg/kWh]	0.3217	0.3134	0.3307	0.3134

### 4.2.1 The Influence of Weather Conditions Throughout the year on Specific Work Net

In Fig. 4, the specific net-work for the conventional Brayton cycle and the proposed model throughout the year for two cities in Egypt representative of different ambient conditions, Alexandria (warm-humid), Aswan (hot-arid) is being described. The predicted performance parameters are assessed for [1 kg/s] dry air. As shown in Fig. 4, in the conventional Brayton cycle, the lowest specific work net that happens, is clearly seen to be lower than the specific work net at the proposed model. While the proposed model, the highest specific work net can be achieved, and it also remains constant at the high ambient temperature and relative humidity, which means that the output work has been improved. In Fig. 5, the proposed model increases the specific work net

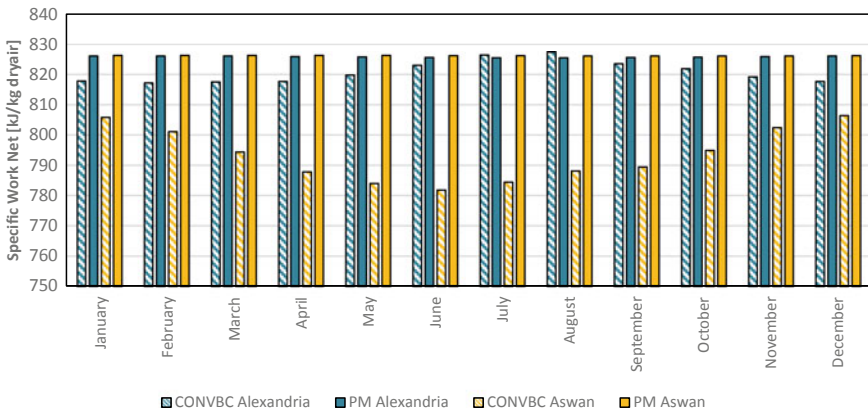


Fig. 4 Monthly average net power production per unit kilogram dry air throughout the year

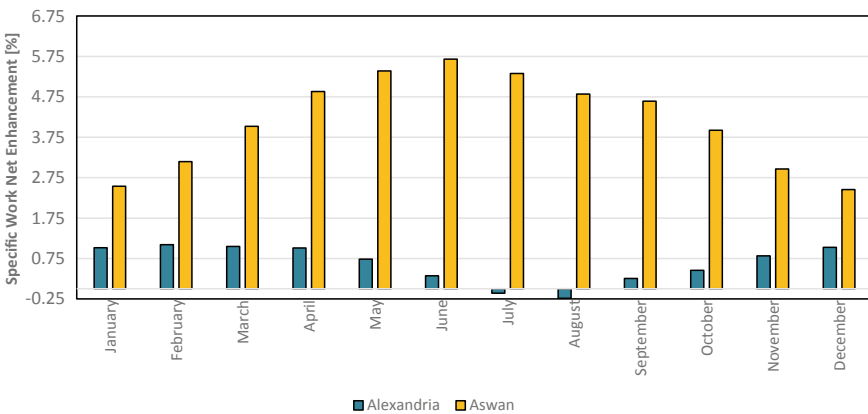
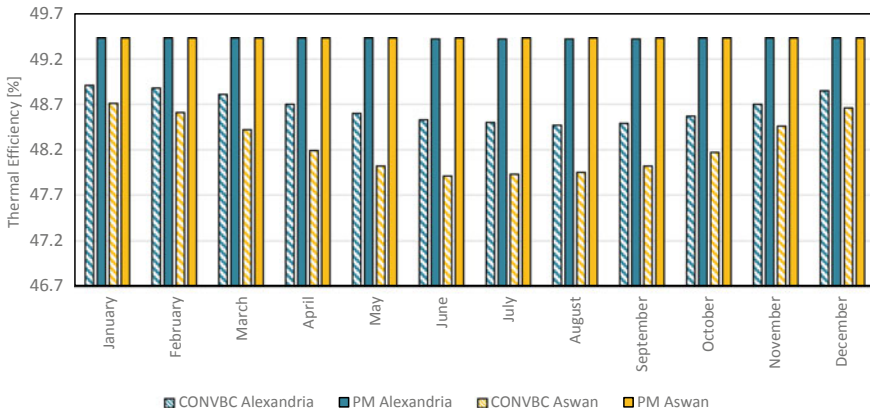


Fig. 5 Proposed model work net production enhancement throughout the year



**Fig. 6** Monthly average thermal efficiency throughout the year

at Alexandria by 0.3218 percent in June and by 1.05 percent in January and reduces by 0.2357 percent and 0.1075 percent in August and July respectively. It increases by 5.683 percent and 2.537 percent at Aswan in June and January respectively. This means the specific work net enhancement is increased significantly at the weathering conditions of high ambient temperature and low relative humidity.

**4.2.2 The Influence of Weather Conditions Throughout the Year on Thermal Efficiency**

The thermal efficiency for the conventional Brayton cycle and the proposed model throughout the year is demonstrated in Fig. 6. As the ambient air temperature and relative humidity increase, gas turbine thermal efficiency decreases significantly. The conventional Brayton cycle thermal efficiency is seen to be lower than the thermal efficiency at the proposed model and decreases even because of the rise in ambient temperature and relative humidity. While the proposed model, the highest thermal efficiency can be achieved, and it also remains constant along the year for the two selected cities. In Fig. 7, the proposed model improves thermal efficiency in August by 1.965%. It is enhanced by 1.06% percent in January at Alexandria. In Aswan, the thermal efficiency of the proposed model increases by 3.164% and 1.483% in June and January respectively.

**4.2.3 The Influence of Weather Conditions Throughout the Year on Specific Fuel Consumption**

The specific fuel consumption is demonstrated in Fig. 8. Specific fuel consumption is an indicator of how much fuel needs to be consumed to produce electricity. When

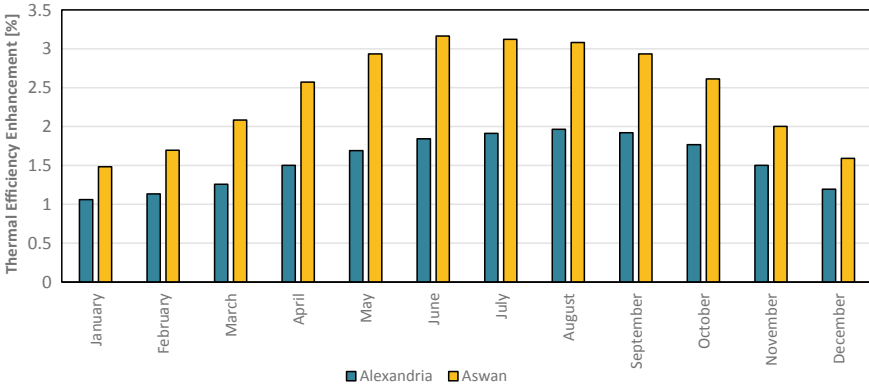


**Fig. 7** Proposed model thermal efficiency enhancement throughout the year

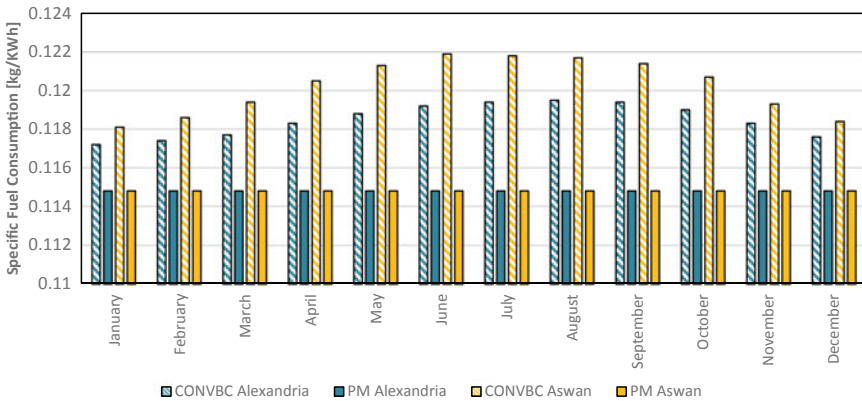


**Fig. 8** Monthly average specific fuel consumption throughout the year

the ambient temperature and relative humidity rise the gas turbine’s work increases. Hence the basic fuel consumption of the gas turbine increases significantly. Proposed model specific fuel consumption is seen to be lower than SFC at CONVBC and remains constant at different ambient conditions during the year. In Fig. 9, the specific fuel consumption decreases in August by 3.394% and by 2.091 percent in January at Alexandria. In Aswan, the SFC of the proposed model decreases by 5.797 and 2.824% in June and January respectively.

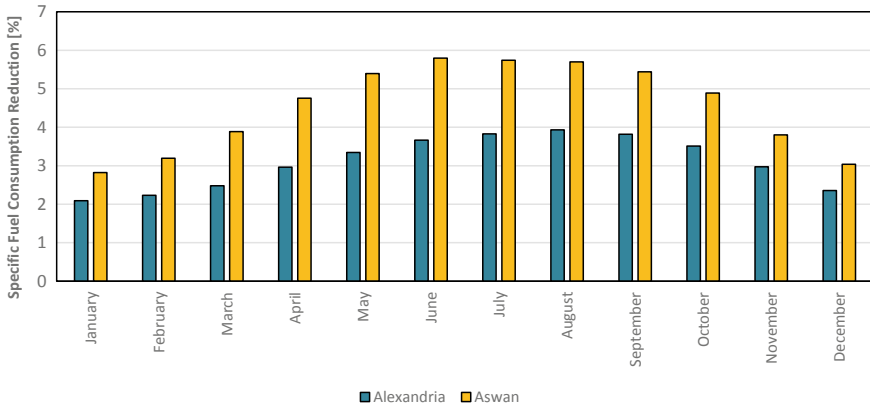


Fig. 9 Proposed model specific fuel consumption reduction throughout the year

### 4.3 Environmental Impact Assessment

The traditional supply of energy from coal, natural gas, and oil can help increase the greenhouse effect. This explains the combustion as it provides an understanding of the processes producing CO<sub>2</sub> and NO<sub>x</sub>, which are the two most critical forms of gas turbine emissions. The CO<sub>2</sub> emissions must be considered significant in all the carbon atoms in the fuel, as there is increasing public interest in greenhouse gas emissions into the atmosphere. The power plants using fossil fuels emit substantial amounts of CO<sub>2</sub>. In Fig. 10, the graph illustrates the CO<sub>2</sub> emission for the conventional Brayton cycle and the proposed model throughout the year. The proposed model CO<sub>2</sub> emission is seen to be lower than CO<sub>2</sub> emission at CONVBC and remains constant at different ambient conditions during the year. In Fig. 11, the CO<sub>2</sub> emission decreases

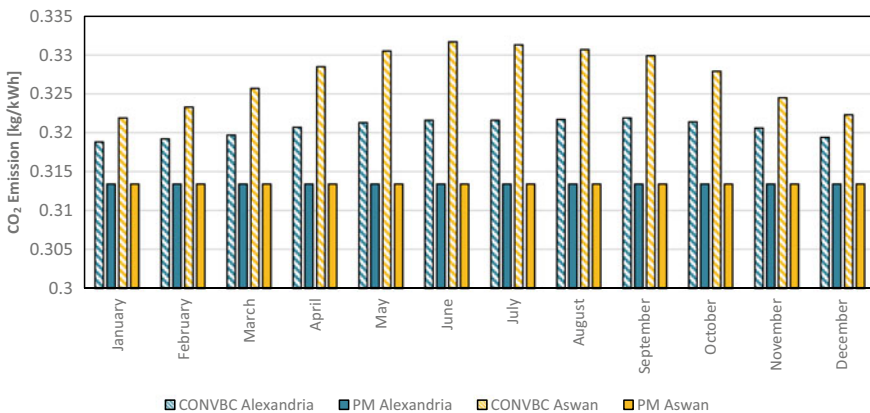
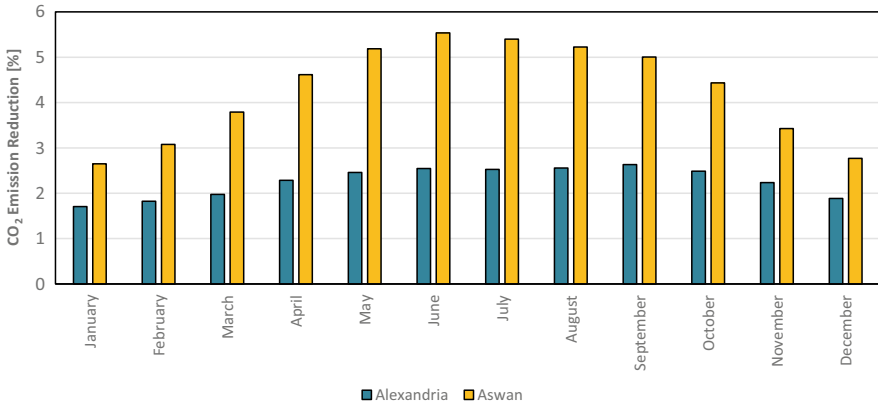


Fig. 10 Monthly average carbon dioxide emission throughout the year



**Fig. 11** Proposed model carbon dioxide emission reduction throughout the year

in August by 2.558 percent and by 1.705 percent in January at Alexandria. In Aswan, it decreases by 5.536 percent and 2.65 percent in June and January respectively.

## 5 Conclusions and Recommendations

The employment of absorption chiller in hot-arid regions, as pre-cooler and inter-cooler technique in a gas turbine plants, provides the considerable potential to enhance GT performance by recording a significant drop in temperature. Lowering the inlet air temperature of 5 °C results in an augmentation in gas turbine output capacity of 2.455 to 5.683%, enhancement in thermal efficiency of 1.483 to 3.164%, reduction in specific fuel consumption of 2.824 to 5.797%, and reduction in CO<sub>2</sub> emission of 2.65 to 5.536%. Overall, the research findings indicate that the absorption chiller system exhibits the best performance enhancement in hot and dry ambient conditions. However, in humid climates, this technique declines the gas turbine efficiency substantially with inlet air cooling since the water vapor in the air is condensed and removed. Others think the performance of some gas turbines (depending on specific processes) might improve as the humidity increases, whereas the performance of others could decrease under the same conditions since water content influences the thermodynamic properties of the input air. So, it recommended in such climates to utilize the amount of condensed water in cooling by injected it again into the air at the following stages leading to additional cooling. In fact, the selection of the suitable technique of cooling based on the location and climatic conditions of the power station. Finally, the optimal system may be modeled on the ambient conditions at each facility, according to the descriptions given above and the targets necessary, such as improving power output, lowering pollutant emissions, etc.

## References

1. Gupta KK, Rehman A, Sarviya RM (2010) Bio-fuels for the gas turbine: A review. *Renew Sustain Energy Rev* 14(9):2946–2955. <https://doi.org/10.1016/j.rser.2010.07.025>
2. Yingjian L, Abakr YA, Qi Q, Xinkui Y, Jiping Z (2016) Energy efficiency assessment of fixed asset investment projects—a case study of a Shenzhen combined-cycle power plant. *Renew Sustain Energy Rev* 59:1195–1208. <https://doi.org/10.1016/j.rser.2016.01.042>
3. Majdi Yazdi MR, Ommi F, Ehyaei MA, Rosen MA (2020) Comparison of gas turbine inlet air cooling systems for several climates in Iran using energy, exergy, economic, and environmental (4E) analyses. *Energy Conv Manag* 216:112944. <https://doi.org/10.1016/j.enconman.2020.112944>
4. Najjar YSH, Abubaker AM (2015) Indirect evaporative combined inlet air cooling with gas turbines for green power technology. *Int J Refrig* 59:235–250. <https://doi.org/10.1016/j.ijrefrig.2015.07.001>
5. Alhazmy MM, Najjar YSH (2004) Augmentation of gas turbine performance using air coolers. *Appl Therm Eng* 24(2–3):415–429. <https://doi.org/10.1016/j.applthermaleng.2003.09.006>
6. Barakat S, Ramzy A, Hamed AM, El Emam SH (2019) Augmentation of gas turbine performance using integrated EAHE and Fogging Inlet Air Cooling System. *Energy* 189:116133. <https://doi.org/10.1016/j.energy.2019.116133>
7. Athari H, Soltani S, Rosen MA, Seyed Mahmoudi SM, Morosuk T (2015) Comparative exergoeconomic analyses of gas turbine steam injection cycles with and without fogging inlet cooling. *Sustainability (Switzerland)* 7(9):12236–12257. <https://doi.org/10.3390/su70912236>
8. Comodi G, Renzi M, Caresana F, Pelagalli L (2015) Limiting the Effect of Ambient Temperature on Micro Gas Turbines (MGTs) Performance Through Inlet Air Cooling (IAC) Techniques: An Experimental Comparison between Fogging and Direct Expansion. *Energy Procedia* 75:1172–1177. <https://doi.org/10.1016/j.egypro.2015.07.561>
9. Ehyaei MA, Mozafari A, Alibiglou MH (2011) Exergy, economic & environmental (3E) analysis of inlet fogging for gas turbine power plant. *Energy* 36(12):6851–6861. <https://doi.org/10.1016/j.energy.2011.10.011>
10. Popli S, Rodgers P, Eveloy V (2013) Gas turbine efficiency enhancement using waste heat powered absorption chillers in the oil and gas industry. *Appl Therm Eng* 50(1):918–931. <https://doi.org/10.1016/j.applthermaleng.2012.06.018>
11. Santos AP, Andrade CR (2012) Analysis of gas turbine performance with inlet air cooling techniques applied to Brazilian sites. *J Aerosp Technol Manag* 4(3):341–353. <https://doi.org/10.5028/jatm.2012.04032012>
12. Mohapatra AK, Sanjay (2014) Thermodynamic assessment of impact of inlet air cooling techniques on gas turbine and combined cycle performance. *Energy* 68:191–203. <https://doi.org/10.1016/j.energy.2014.02.066>
13. Marzouk A, Hanafi A (2013) Thermo-Economic analysis of inlet air cooling in gas turbine plants. *J Power Technol* 93(2):90–99
14. White AJ, Meacock AJ (2004) An evaluation of the effects of water injection on compressor performance. *J Eng Gas Turbines Power* 126(4):748–754. <https://doi.org/10.1115/1.1765125>
15. Zainali O, Alavijeh SK (2015) Gas turbine efficiency improvement by inlet air-cooling. *Alam Cipta Journal* 8(3):18–24
16. Mohapatra AK, Sanjay (2015) Comparative analysis of inlet air cooling techniques integrated to cooled gas turbine plant. *J Energy Inst* 88(3):344–358. <https://doi.org/10.1016/j.joei.2014.07.006>
17. Mohanty B, Paloso G (1995) Enhancing gas turbine performance by intake air cooling using an absorption chiller. *Heat Recov Syst CHP* 15(1):41–50. [https://doi.org/10.1016/0890-4332\(95\)90036-5](https://doi.org/10.1016/0890-4332(95)90036-5)
18. Mohammed JS, Hamdan AM, Mohammed R (2018) Design of pre-cooler for gas turbine at Garri ( 1and2) power station by using vapor compression refrigeration system. *Int J Sci Eng Sci* 2456–7361



19. Al-ansary HA, Orfi JA, Ali ME (2013) Impact of the use of a hybrid turbine inlet air cooling system in arid climates. *Energy Convers Manage* 75:214–223. <https://doi.org/10.1016/j.enconman.2013.06.005>
20. Dawoud B, Zurigat YH, Bortmany J (2005) Thermodynamic assessment of power requirements and impact of different gas-turbine inlet air cooling techniques at two different locations in Oman. *Appl Therm Eng* 25(11–12):1579–1598. <https://doi.org/10.1016/j.applthermaleng.2004.11.007>
21. Engineering Equation Solver, EES, F-Chart software, Po Box 444042, Madison, WI 53744. <https://www.fchart.com/>
22. Nada T (2014) Performance characterization of different configurations of gas turbine engines. *Propuls Power Res* 3(3):121–132. <https://doi.org/10.1016/j.jprr.2014.07.005>
23. <https://www.weather-atlas.com/>

# On the Design and Performance Analysis of Deadlock Controller for Automated Manufacturing Systems with Unreliable Resources



Mohammad Ashraful Karim Chowdhury, M. Krid, Ahnaf Akif, and A. Mostafa

**Abstract** Deadlock problems in highly automated manufacturing system (AMS) have recently received considerable interest from both industry and academia. In most of the researches, structural analysis and reachability graph analysis have been used to develop deadlocks prevention policies for AMSs based on ordinary petri nets. These policies are considered for deadlock problems in AMS with shared and reliable resources, while AMS are timed and subjected on unreliable resources. To provide a solution for this circumstances, this research developed appropriate methods for designing controller and analyzing of AMSs with shared and unreliable resources taking into account deadlocks problems. The proposed controllers enable systems to be worked with improved performance and high resource utilization based on timed petri nets. In this research a case study is provided to demonstrate the usefulness of the deadlock-control algorithm to ensure no occurrence of deadlocks in AMS. The flexible manufacturing system has been modelled using Visual Object Net version 2.a software and the simulation is done for 26 days (8 h per day). A performance comparison between two developed policies, failures causing scrapping and process resumes subsequent to repair, is made. Moreover, some issues are recommended to select the best policy.

**Keywords** Automated manufacturing system · Deadlock control · Petri net · Simulation · Performance evaluation

---

M. A. K. Chowdhury (✉) · A. Mostafa  
Faculty of Science and Engineering, Southern Cross University, Lismore, NSW 2480, Australia  
e-mail: [mohammad.chowdhury@scu.edu.au](mailto:mohammad.chowdhury@scu.edu.au)

M. Krid  
College of Engineering, King Saud University, Riyadh, Saudi Arabia

A. Akif  
Faculty of Computer Science, Electrical Engineering and Mathematics, University of Paderborn, Paderborn, Germany

## 1 Introduction

An automated manufacturing system (AMS) comprises of interconnected different components such as robots, machine tools, fixtures, and buffers. These different product components engage in the manufacturing system at different points of time. The system generally process these components based on a stated sequential arrangement of operations and specified resource sharing. The resource sharing causes the event of deadlock states in an AMS through its operation [1–4]. Hence, there is a need for an effective deadlock-control algorithm ensuring these deadlocks do not take place in an automated manufacturing system. Petri nets are a widely used mathematical and a major graphical tool suitable for model development, analysis, and control of deadlocks in AMSs. Petri nets are utilized to define the features and behavior of an AMS, such as synchronization, conflict, and sequences. In addition, they could be used to provide behavioral properties, for example, boundedness and liveness [5]. To forbid the deadlock problem occurrences in AMS, several approaches were extracted from a Petri net tool. These approaches are categorized into three strategies: detection and recovery of deadlock, avoidance of deadlock, and prevention of deadlock [5, 6]. Three control criteria are proposed for designing and evaluating a supervisor for AMS, such as behavioral permissiveness, complexity of structure, and complexity of computation [5]. Hence, the goals of many researches are to design deadlock prevention policies with liveness-enforcing supervisors including the above mentioned criteria [5]. The deadlock control for AMS is designed for both reliable and unreliable resources. In case of AMS with reliable resources mainly two techniques analysis for deadlock prevention are available using Petri net. They are structural analysis [7, 8] and reachability graph analysis [9–11]. More often structural analysis is applied using structural objects of Petri nets, for example resource transition circuits and siphons. Here, control steps are simple and a monitor is required to be added with each empty minimal siphon to prevent itself from to be non-emptied, but the shortcomings of this method are that suboptimal result can be obtained for controlled system and the number of control places is linearly dependent on a net size [12].

The reachability graph analysis needs listing of all or a part of reachable markings. This leads to a state explosion problem. The reachability graph is divided into live zone and deadlock zone. In deadlock zone, first met bad markings are extracted and defined. In this case, Deadlock is eradicated by creating a monitor place and incorporated to prevent the first met bad markings from being reached. This process involves iterations to prevent all first met bad markings [13]. Several policies are developed to prevent the deadlock states; such as theory of region, siphon control methods, and iterative methods [8, 10, 13–18].

For unreliable resources, the existing deadlock methods were developed for class of petri net. Lawley and Sulistyono [19] investigated resource allocation in manufacturing systems using unreliable resources by developing policies of supervisory control. In this case, supervisory control allocate system buffer space which enables the system continuing to produce all part types without the failed

resource when an unreliable resource fails. Hsieh [20] developed nominal supervisory algorithms to study the proposed controlled assembly/disassembly Petri net for assembly/disassembly processes with unreliable resources. In addition, he studied the condition under which the system can still operate in case of resource failures. Wang et al. [21] proposed robust supervisory controllers for the resource allocation systems of a single-unit with unreliable resources. The first policy safeguards robust operation in case of one unreliable resource, while the second policy makes sure robust operation in case of several unreliable resources, considering that at a time maximum one resource is in a failed state. Chew et al. [22] designed two supervisors controller ensuring robust operation for systems where part types may need several unreliable resources by using a central buffer. Liu et al. [23] developed a robust deadlock prevention control system suitable for unreliable resources for a class of Petri nets focusing on divide-and-conquer deadlock control strategy. Yue et al. [24] proposed a controller for deadlock avoidance policy suitable for a class of AMS with several unreliable resources by using the modified Banker's Algorithm and residual resource capacity constraints. Yue et al. [25] also presented a robust supervisory control policy for avoiding deadlock in AMS subjected on unreliable workstations. The presented policy is developed based on two variants of Banker's Algorithm. Wang et al. [26] developed deadlock prevention controller for AMS in case of resources failure and the designed supervisor comprises of three controller to fulfil the desired properties to ensure the deadlock-free processing of AMS.

From the literature, it is evident that most researches have utilized structural analysis and reachability graph analysis to develop policies of deadlock prevention for AMSs based on ordinary Petri nets. These policies are considered for deadlock problems in AMS with reliable resources while AMS are consist of unreliable resources. However, very few researches have addressed deadlock prevention for AMS in case of unreliable resources. Therefore, there is a need for a methodology for performance analysis of AMS with unreliable resources taking into account deadlocks and suggest controllers that enable systems to be operated with improved performance and high resource utilization centered on timed as well as stochastic Petri nets.

## 2 Fundamentals of Petri Nets

A Petri net or place/transition net  $N$  is a four—tuple  $(P, T, F, W)$  where  $P$  is a finite non-empty set of places, and  $T$  is a finite non-empty set of transitions. Elements in  $P \cup T$  are called nodes with  $P \cup T = \emptyset$  and  $P \cap T = \emptyset$ ,  $P$  and  $T$  are represented by circles and bars, respectively.  $F \subseteq (P \times T) \cup (T \times P)$  is the set of directed arcs (with arrows) that join the places with transitions and vice versa.  $W : (P \times T) \cup (T \times P) \rightarrow N$  is a mapping that assigns a weight to an arc, where  $N = \{1, 2, \dots\}$ .  $N$  is called an ordinary net if  $\forall p, t \in F, W(p, t) = 1$ , denoted as  $N = (P, T, F)$ .  $N$  is called a weighted net if there exists an arc between  $p$  and  $t$ ,  $W(p, t) > 1$ . Given a net  $N = (P, T, F, W)$  and node  $a \in P \cup T$ ,  $\cdot a = \{b \in P \cup T | (b, a) \in F\}$  is called the preset of node  $a$ , while  $a \cdot = \{b \in P \cup T | (a, b) \in F\}$  is called the postset of

nodea. A marking  $M$  of  $N$  is a mapping  $M : P \rightarrow \mathbb{N}$ , where  $\mathbb{N} = \{0, 1, 2, \dots\}$ .  $(N, M_0)$  is a net system or marked net and denoted as  $PN = (P, T, F, W, M_0)$ , where  $M_0 : P \rightarrow \{0, 1, 2, \dots\}$  is an initial marking of  $PN$ . For a Petri net modeling FMS,  $M_0$  represents the different raw parts that are to be synchronously processed in the system, and the state of resources, such as machines and robots. A transition  $t \in T$  is enabled at marking  $M$  if  $\forall p \in \cdot t, M(p) \geq W(p, t)$ , which is denoted as  $M[t]$ . When a transition  $t$  fires, it removes  $W(p, t)$  tokens from each place  $p \in \cdot t$ , and deposits  $W(t, p)$  tokens in each place  $p \in t \cdot$ . Thus, it reaches a new marking  $M'$ , denoted as  $M[t]M'$ , where  $M'(p) = M(p) - W(p, t) + W(t, p)$ . A net is self-loop free or pure if for all  $a, b \in P \cup T, W(a, b) > 0$  and  $W(b, a) = 0$ . Incidence matrix  $[N]$  in a net  $N$  is an integer matrix that consists of  $|P|$  rows and  $|T|$  columns with  $[N](p, t) = W(t, p) - W(p, t)$ .

Let  $(N, M_0)$  be a Petri net with  $N = (P, T, F, W)$ . A transition  $t \in T$  is live if for all  $M \in R(N, M_0), \exists M' \in R(N, M)$ , there is a firing sequence  $M'[t]$  holds. A transition is dead at  $M_0$  if  $\nexists t \in T, M_0[t]$  holds.  $M'$  is said to be reachable from  $M$  if there exist a firable finite transition sequence  $\delta = \{t_1, t_2, t_3, \dots, t_n\}$ , and markings  $M_1, M_2, M_3, \dots, \text{ and } M_{n-1}$  such that  $M[t_1]M_1[t_2]M_2[t_3]M_3 \dots M_{n-1}[t_n]M'$ , which is denoted as  $M[\delta]M'$ , satisfying the state equation  $M' = M + [N]\vec{\delta}$ , where  $\delta \rightarrow: T \rightarrow \mathbb{N}$  is a mapping  $t$  in  $T$  to the number of occurrences of  $t$  in  $\delta$ , and called a Parikh vector or a firing count vector. The set of markings reachable from  $M$  in  $N$  is called the reachability set of Petri net  $(N, M)$  and represented as  $R(N, M_0)$ . A net  $N$  with initial marking  $M_0$  is said to be  $k$ -bounded if for all  $M \in R(N, M_0), M(p) \leq k (k = \{1, 2, 3, \dots\})$ . A net is said safe if all its places are safe, the number of tokens in each place  $p$  does not exceeds one.

$P$ -vector (place vector) and  $T$ -vector (transition vector) are column vectors. The former  $I : P \rightarrow \mathbb{Z}$  catalogued by  $P$ , and called a  $P$ -invariant or place invariant if  $I \neq 0$  and  $I^T \cdot [N] = 0^T$ . The latter  $J : T \rightarrow \mathbb{Z}$  catalogued by  $T$ , and called a  $T$ -invariant or transition invariant if  $J \neq 0$  and  $[N] \cdot J = 0$  where  $\mathbb{Z}$  is the integers set. If each element of  $I$  is non-negative the  $P$ -invariant  $I$  is called a  $P$ -semiflow or place semiflow. Suppose  $I$  be a place invariant of a Petri net with  $(N, M_0)$  and  $M$  is a reachable marking from the initial marking  $M_0$ . Then,  $I^T M = I^T M_0$ . Let  $\|I\| = \{p | I(p) \neq 0\}$  be a support of place invariant  $I$  and can be classified into three parts. Firstly,  $\|I\|^+$  is a positive support of place invariant  $I$ , and  $\|I\|^+ = \{p | I(p) > 0\}$ . Secondly,  $\|I\|^-$  is a negative support of place invariant  $I$ , and  $\|I\|^- = \{p | I(p) < 0\}$ . Finally,  $I$  is a minimal place invariant if  $\|I\|$  is not a superset of the support of any other one and its components are mutually prime. Let  $l_i$ 's be the coefficients of Place invariant  $I$  if for all  $p_i \in P, l_i = I(p_i)$ . Because an ordinary and weighted Petri nets do not deal with sensors and actuators, an extended Petri nets has been developed to deal with both sensors and actuators, it called automation Petri net (APN). APN is an eight-tuple  $(P, T, F, In, En, X, Q, M_0)$  where  $P, T, F$ , and  $M_0$  are explained above.  $In$  is an inhibitor arc that denoted by an arc with small circle (not arrow), an inhibitor arc connects an input place  $p$  to a transition  $t$ , transition  $t$  is enabled if the input place  $p$  have tokens less than the inhibitor arc weight  $In(p, t)$ .  $En$  is an enabling arc that represented by an arc with empty arrow, an enabling arc connects

an input place  $p$  to a transition  $t$ , transition  $t$  is enabled if the input place  $p$  have tokens at least equal the enabling arc weight  $En(p, t)$ .  $X = \{x_1, x_2, \dots, x_m\}$  is a set of firing conditions associated with the transitions, which can be recognized as external events such as sensor readings.  $Q = \{q_1, q_2, \dots, q_n\}$  is set of actions that can be assigned to the places,  $Q$  may be more than one action in any place. In the APN, the movement of tokens between their places represents the behavioural of the APN and is achieved by the firing of the enabled transitions.

### 3 Methodology

Like any other research study; it is very important to select the appropriate methodology for deadlock controller design for AMSs using unreliable resource and analyzing the performance for developed method. Figure 1 illustrates the steps of the proposed methodology, which are described as follows:

#### 3.1 Deadlock Prevention Method

This section describes a method that is inspired by Li et al. [15] and called an elementary siphons control method. The strict minimal siphons (SMS) in a Petri net are categorized into elementary and dependent. In the sequel,  $\Pi$  is defined to represent the set of strict minimal siphons, where  $\Pi_E$  is the sets of elementary one and  $\Pi_D$  is the sets of and dependent (redundant) one. Unless specified otherwise, while we mention a siphon, we refer to a strict minimal one.

**Definition** (Li et al. [8]) Let  $S \subseteq P$  be a siphon of  $N$ .  $P$ -vector  $\lambda_S$  is called the characteristic  $P$ -vector of  $S$  if  $\forall p \in S, \lambda_S(p) = 1$ , otherwise  $\lambda_S(p) = 0$ .

**Definition** (Li et al. [8]) Let  $N = (P, T, F)$  be a net with  $|P| = m, |T| = n$  and we assume  $N$  has  $k$  SMS,  $S_1, S_2, \dots, S_k, m, n, k \in \mathbb{N}$ . Let  $\lambda_{S_i}(\eta_{S_i})$  be the characteristic  $P(T)$ -vector of siphon  $S_i, i \in 1, 2, \dots, n$ . We define  $[\lambda]_{k \times m} = [\lambda_{S_1}, \lambda_{S_2}, \dots, \lambda_{S_k}]^T$  and  $[\eta]_{k \times n} = [\lambda]_{k \times m} \cdot [N]_{m \times n}$  is called the characteristic  $P(T)$ -vector matrix of the siphons of  $N$ , where  $[N]_{m \times n}$  is an incidence matrix.

Finding elementary siphons is relatively easy in a Petri net system  $(N, M_O)$  given all siphons. For doing this, firstly, matrix  $[\lambda]$  is created and then  $[\eta]$ , the number of elementary siphons in  $N$  is the rank of  $[\eta]$ . Afterwards, linearly independent vectors can be come across in  $[\eta]$ . Last of all, the siphons corresponding to these linearly independent vectors are the elementary siphons in the net system  $(N, M_O)$ .

**Theorem** (Li and Zhou [27]) Let  $N$  be an ordinary Petri net and  $S_1-S_n$  be the siphons in  $N$  with respect to elementary siphons. Control place  $V_S$  is added to  $N$ , the new net system is denoted as  $(N1, M1)$  and the initial token of place control  $V_S$  is computed

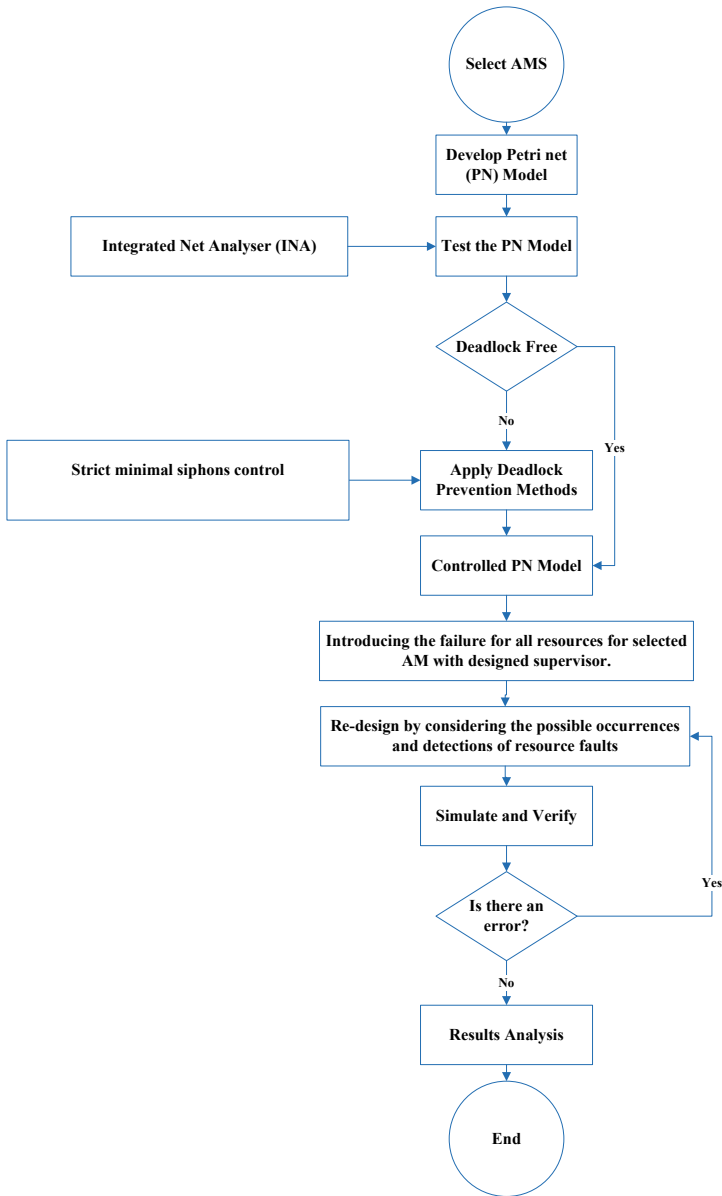


Fig. 1 Proposed methodology

as  $M(V_S) = M_O(S) - \xi_S, 1 \leq \xi_S \leq M_O(S) - 1$ , where  $\xi_S$  is denoted as the control depth variable of siphon  $S$ , which implies the minimum number of tokens that siphon can hold. Then  $S$  is invariant-controlled.

**Theorem** (Li and Zhou [15]) Let  $(N, M_O)$  be a net system and  $S_0$  be a strictly dependent siphon with respect to elementary siphons,  $S_1, S_2, \dots$ , and  $S_n$ . If  $S_1, S_2, \dots$ , and  $S_n$  are invariant controlled by adding control places  $V_{S_1}, V_{S_2}, \dots$ , and  $V_{S_n}$ , and  $M_0(S_0) > \sum_{i=1}^n a_i \cdot M_0(S_i) - \sum_{i=1}^n a_i \cdot \xi_{S_i}$  holds; then  $S_0$  is controlled, where  $a_i$  is a constant.

Based on the elementary siphons concept, the applied deadlock prevention algorithm presented by Li and Zhou [27] is stated below:

---

Policy for elementary siphons

---

Input: A model based on Petri net  $(N, M_0)$

Output: A Petri net system that is controlled  $(N_1, M_1)$ .

**Step 1:** Pinpoint all the strict minimal siphons of Petri net model  $N$  using INA software.

**Step 2:** The SMS  $T$ -vector matrix[7].

**Step 3:** Find all the elementary siphons with regard to  $N$ . All other remaining are the dependent siphons.

**Step 4:** Add a control place  $V_S$  for each elementary siphon  $S$  as such that:

- The input and output arcs (all weights are ones) of  $V_S$  are linked to the source transitions that have routes directing to the sink transitions and connected from the taking places of  $S$  correspondingly.

- Calculate the initial place control token  $VSM(MV_S) = M_0(S) - \xi_S, 1 \leq \xi_S \leq M_0(S) - 1$ .

**Step 5:** Reiterate Step 4 till all elementary siphons are taken into account.

**Step 6:** Adjust  $\xi_i$  in a way that all dependent siphons are controlled.

---

To demonstrate the above algorithm, the Petri net model illustrated in Fig. 2 is considered. The model comprises of a single robot  $R$  that processes a part at a time, one machine  $M$  that holds a part at a time, one loading buffer ( $I1$ ), and an unloading buffer ( $O1$ ). One part type is processed in the manufacturing system (PA). The robot

**Fig. 2** Petri net model constructed for an AMS

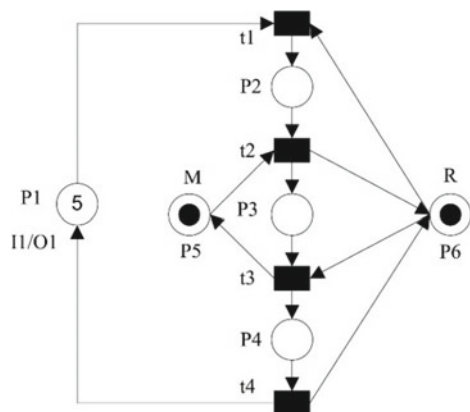
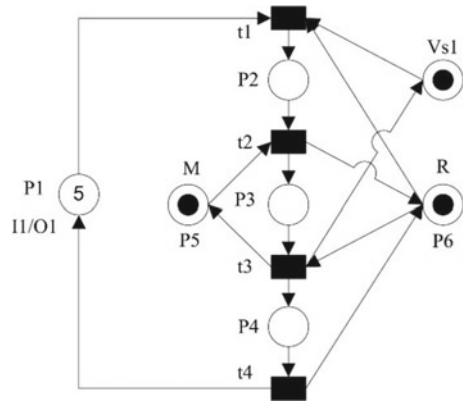




**Fig. 3** Controlled Petri net model



reaches the loading buffer, grips, and loads PA to the M. If M finishes its operation, the robot reaches the machine, grips, and unloads the part to the unloading buffer. The Petri net model comprises of four transitions and six places. The places can be defined as the following set partition:  $P^0 = \{p_1\}$ ,  $P_R = \{p_5, p_6\}$ , and  $P_A = \{p_2, p_3, p_4\}$ , where  $P^0$ ,  $P_R$ , and  $P_A$  are the input, resources, and operation places, respectively. The model has five reachable markings along with four minimal siphons. At least one of siphon is a strict minimal siphon. Its augmented siphon is  $S = \{p_4, p_5, p_6\}$  (Fig. 3).

### 3.2 Failures Handling Policies

In a manufacturing system, the states of a machine comprises of idle, busy, failure, starvation and blocking. Failure causes idleness and randomness in manufacturing system and consequently failures influence the performance of manufacturing system. The process of failure is characterized by using either of the two calculation: the process that counts the number of failures within a given period of time or the statistical properties of the time between consecutive failures. The process completion time is referred to the time a job spends on the processor which includes the up time for processing and the down time in case of failures. The down time due to failures is the span from the failure occurring to the repair activity completing. The performance of the failure handling policies is very crucial for automated manufacturing system and it is measured by the factors such as failure reacting time, the repair waiting time and the repairman utilization. Failure occurrence and failure detection are different. Sophisticated programmed machinery can fail irrespective of the machine status. If failure occur at idle, the failure can be detected immediately and this is called operation-independent failure detection. Generally failures take place while the machines are processing jobs in a manufacturing environment. The failures that are occurred at any time span either idle or running, however

detected during the operations of the machine, is called operation-dependent failure detection. In operation-independent failure detection, repair activity is carried out through the idle processes and there is no effect on the process completion time. When the failure of machine occur, repairman receives signal to repair it. Otherwise, it waits until any of repairman are available. Usually, the failed resources are taken into consideration in service according to the FIFO rule. For a case of failure, the unit being processed on the machine may resume being processed or take new processing time, may be discarded or may take the same process for the beginning. Two interrupted-job-handling policies will be considered in this study as followed:

(1) Failures Resulting Scrapping

Sometimes, particularly in high-speed automated manufacturing systems, the unit being processed needs to be scrapped in case of a failure. The completion time in this cases is the time a unit spends on the machine until its process is completed before a failure occurs. Upon failure, the machine goes to repair before starting the process new unit. In this case, down time does not include into the process completion time.

(2) Process Resumes Subsequent to Repair

In this policy, after repairing the resource the interrupted unit starts along with a new processing time. Then, the unit leaves the process after its processing time is completed. In this case, the process completion time is calculated by summing up the following: processing time on machine until the failure occurs, down time as a result of failures and processing time without stoppages.

Based on the failures resulting scrapping concept, the proposed policy is stated as follows:

---

Policy one (Failures Resulting Scrapping)

---

Input: Model of Petri net  $(N, M_0)$  of an AMS, where  $N = (P^0 \cup P_A \cup P_R, T, F, W)$ .

Step 1: Compute all elementary siphons for the Petri net  $(N, M_0)$ .

Step 2: For each siphon elementary siphon, add a monitor  $V_s$

Step 3: Determine all resources of system, for each one:

- Design transitions to represent breakdown resource, state of resource at failure, and repair operation.
- Design places to represent failure, state of resource at failure, and repair operation.
- Add test arcs from “failure” place to state of resource at failure transitions.
- Add inhibitor arcs from “failure” place to start and end transitions of failed resource.

Step 4: Output  $(N_1, M_1)$ .

Step 5: End.

---

To demonstrate the above policy one, the manufacturing process model subject to failures is considered based on Petri nets for the perspective of taking repair immediately. The manufacturing process model of a single station comprises of the following components: a stochastic failure process and repair process, a machine, a buffer with a suitable job arrival process and a buffer for output. The assumption for the model is that failures may take place at any time. The transition representing

‘break down’ simulates the failures of machine that can have different distribution implying the failure rate.

Figure 4 shows failures causing scrapping, in the right block, the inhibitor arcs from “failure” place to “t1”, “t2”, “t3” and “t4” transitions denoting the failure is detected during the idle or operating states, and the job on the failed robot is interrupted before the time delay  $\mu$  finished. Moreover, a new job or finished job from the input buffer or machine, respectively cannot start its processing in case of the robot breakdowns. When a robot is repaired, it instantaneously processes the next job or finished job from the machine. Transitions “t13”, “t14” and “t15” represent the idle, loading, and unloading states of robot at failure, respectively. The test arc from “failure” place to “t13”, “t14” and “t15” transitions denotes that if the failure is detected the transitions enable to fire. Place (R state at failure) indicates the robot state at failure. “t10” represent the breakdown occurrence for robot, “t11” represent detect of failure, starting repairing, and deposit a token to Place (scrap) that denotes that the part is scrapped. Place (Repair) indicates the repairing operation. “t12” represents represent the repair end and the robot is ready to start processing.

The same manner for machine in left block shown in Fig. 4, a new job or finished job from the input buffer or robot, respectively cannot proceed its processing in case the machine is broken down. When the machine is repaired, it instantaneously starts processing the following job that coming from robot. Transitions “t8” and “t9” represent the idle and busy states of machine at failure, respectively. The test arc from “failure” place to “t8” and “t9” transitions denotes that if the failure is detected the transitions enable to fire. Place (M state at failure) indicates the machine state at

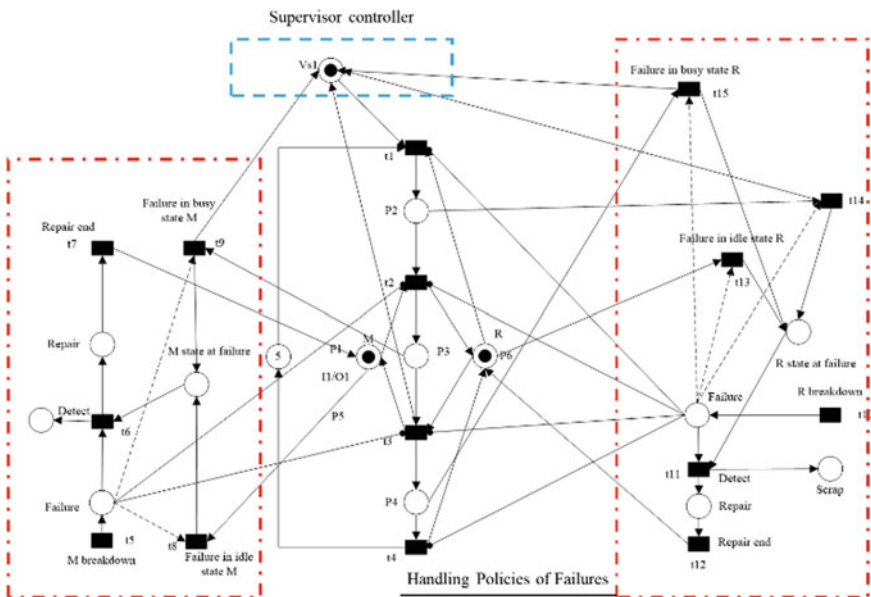


Fig. 4 Policy one (Failures Resulting Scrapping)

failure. “t5” represent the breakdown occurrence for machine, “t6” represent detect of failure, starting repairing, and deposit a token to Place (scrap) that denotes that the part is scrapped. Place (Repair) indicates the repairing operation. “t7” represents the repair end and the machine is set to start processing.

The policy two is modified policy of policy one, the proposed policy is stated as follows:

---

Policy two (Process Resumes Subsequent to Repair)

---

Input: Model of Petri net  $(N, M_0)$  of an AMS, where  $N = (P^0 \cup P_A \cup P_R, T, F, W)$ .

Step 1: Compute all elementary siphons for a given Petri net  $(N, M_0)$ .

Step 2: Add a monitor  $V_s$  for each siphon elementary siphon in such a way that:

Step 3: Determine all resources of system, for each one:

- Design transitions to represent breakdown resource, state of resource at failure, repair operation, and restart operation.
- Design places to represent failure, state of resource at failure, repair operation, restart operation.
- Add test arcs from “failure” place to state of resource at failure transitions.
- Add inhibitor arcs from “failure” place to start and end transitions of failed resource.
- Add inhibitor arcs from “, restart” places to restart idle transition.

Step 4: Output  $(N_1, M_1)$ .

Step 5: End.

---

To demonstrate the above policy two, Fig. 5 is the modified model of Fig. 5, which in right block the inhibitor arcs from “restart” places to restart idle transition

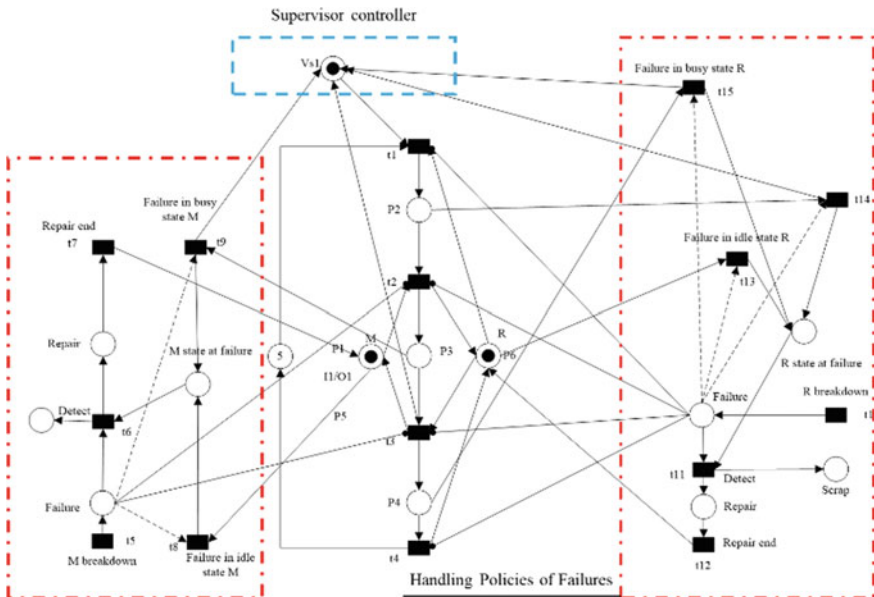


Fig. 5 Policy two (Process Resumes Subsequent to Repair)

denote that the restart idle will be fired if there is no failure occurred at busy state of robot. Transitions “t16”, “t17” and “t18” represent the restart operation in case of idle, unloading, and loading states of robot at failure, respectively. If “t16” fires the robot will be operated in idle place, if “t17” fires the robot will be operated in unloading place, and if “t18” fires the robot will be operated in loading place.

The same manner for machine in left block as illustrated in Fig. 5 the inhibitor arc from “restart” place to restart idle transition denotes that the restart idle will be fired if there is no failure occurred at busy state of machine. Transitions “t7”, and “t8” represent the restart operation in case of idle and busy states of machine at failure, respectively. If “t7” fires the machine will be operated in idle place, and if “t8” fires the machine will be operated in busy place.

### 4 Case Study

The section describes a case study along with the application of the proposed methodology. The production sequence of the case study is presented in Fig. 6a and several studies have been consulted in this case study (Uzam [13], Chen et al. [25, 28], and Nasr et al. [29]). The components of the system are: two robots (R1 and R2; each robot can hold a part at a time), four machines (M1, M2, M3, and M4; each machine can process one part at a time), two loading buffers (I1 and I2), and two unloading buffers (O1 and O2). PA and PB are contemplated in the system configuration. The developed Petri net model for case study is presented in Fig. 6b. The parameters of selected case study are shown in Table 1. They are number of places, number of transitions, set partition, SMS, dependent siphons, elementary siphons, reachable markings. Using the adopted elementary siphons algorithm the required monitor calculation is stated as follows. The rank of  $[\eta]$  is 3 since the first row

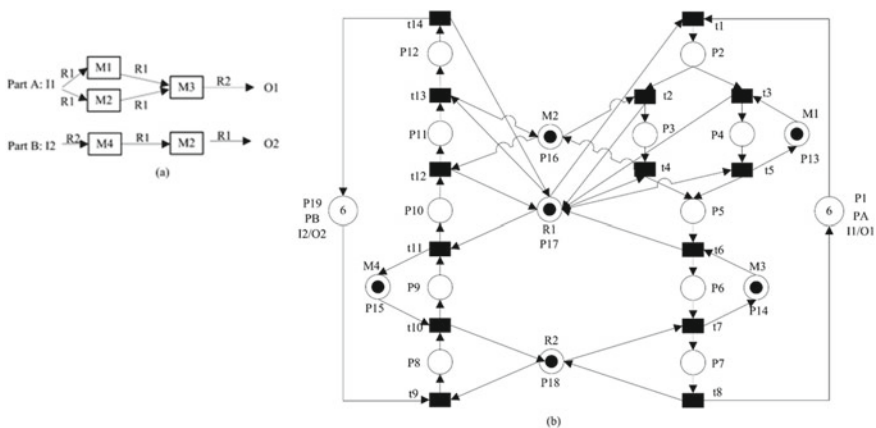


Fig. 6 a Production sequence of the case study and b Petri net model for the case study

**Table 1** Main parameters of case study

Parameter	Value
No. of places	19
No. of transitions	14
Set partition	$P^0 = \{p_1, p_{19}\}$ $P_R = \{p_{13}, \dots, p_{18}\}$ $P_A = \{p_2, \dots, p_{12}\}$
SMS	5
Dependent siphons	2
Elementary siphons	3
Reachable markings	282

$\eta_{S_1}$  can be linearly represented by the second and fourth rows, and first row  $\eta_{S_3}$  can be linearly represented by the fourth and fifth rows. Therefore,  $S_1$  and  $S_3$  are dependent siphons and  $S_2, S_4$  and  $S_5$  are elementary siphons. For elementary siphon  $S_2, S_4$  and  $S_5$ , due to Theorem 3.1, we add a monitors  $V_{S_2}, V_{S_4}$  and  $V_{S_5}$  for them.  $V_{S_2}$  has preset  $V_{S_2} = \{t_4, t_5, t_{13}\}$ , postset  $V_{S_2} = \{t_4, t_5, t_{13}\}, V_{S_2} = \{t_1, t_{11}\}, M(V_{S_2}) = 2$ , and  $\xi_{S_2} = 1$ .  $V_{S_4}$  has preset  $V_{S_4} = \{t_7, t_{11}\}$ , postset  $V_{S_4} = \{t_1, t_9\}, M(V_{S_4}) = 3$ , and  $\xi_{S_4} = 1$ .  $V_{S_5}$  has preset  $V_{S_5} = \{t_4, t_{13}\}$ , postset  $V_{S_5} = \{t_2, t_{11}\}, M(V_{S_5}) = 3$ , and  $\xi_{S_5} = 1$ . Figure 7 shows the controlled system of the Petri net model in Fig. 6a Production sequence of the case study and Fig. 6b Petri net model for the case study after adding monitors using the applied algorithm. The results of the algorithm that is applied for case study with regard to the numbers of monitors, arcs, and reachable states are presented in Table 2.

After applying the proposed method, the model is working now without deadlock state. So, this model will be extended to timed petri net and unreliable resource. Two policies for unreliable resources are proposed in Sect. 3.3 and applied to evaluate the performance of these policies in FMSs Fig. 7 illustrate the developed Petri net model with Failures Causing Scrapping policy. Moreover, second policy that is Process Resumes after Repair was applied on the developed Petri net model, as illustrated in Fig. 8.

Required monitor calculation:

N =	-1	1	0	0	0	0	0	0	0	0	0	0	0	0	0	0	0	-1	0	0	
	0	-1	1	0	0	0	0	0	0	0	0	0	0	0	0	0	0	-1	1	0	0
	0	-1	0	1	0	0	0	0	0	0	0	0	-1	0	0	0	0	1	0	0	0
	0	0	-1	0	1	0	0	0	0	0	0	0	0	0	0	1	-1	0	0	0	0
	0	0	0	-1	1	0	0	0	0	0	0	0	1	0	0	0	-1	0	0	0	0
	0	0	0	0	-1	1	0	0	0	0	0	0	0	-1	0	0	1	0	0	0	0
	1	0	0	0	0	0	-1	0	0	0	0	0	0	0	0	0	0	0	0	1	0
	0	0	0	0	0	0	0	1	0	0	0	0	0	0	0	0	0	0	0	-1	-1

(continued)

(continued)

	0	0	0	0	0	0	0	-1	1	0	0	0	0	0	-1	0	0	1	0
	0	0	0	0	0	0	0	0	-1	1	0	0	0	0	1	0	-1	0	0
	0	0	0	0	0	0	0	0	0	-1	1	0	0	0	0	-1	1	0	0
	0	0	0	0	0	0	0	0	0	0	-1	1	0	0	0	1	-1	0	0
	0	0	0	0	0	0	0	0	0	0	0	-1	0	0	0	0	1	0	1
$\lambda =$	0	0	0	0	0	0	1	0	0	0	0	1	1	1	1	1	1	1	0
	0	0	0	0	1	0	0	0	0	0	0	1	1	0	0	1	1	0	0
	0	1	0	0	0	0	1	0	0	0	0	1	0	1	1	1	1	1	0
	0	1	0	0	0	0	1	0	0	1	0	1	0	1	1	0	1	1	0
	0	1	0	0	1	0	0	0	0	0	0	1	0	0	0	1	1	0	0
$\eta =$	-1	0	0	0	0	0	1	0	-1	0	0	0	1	0					
	1								1										
	-1	0	0	1	1	0	0	0	0	0	-1	0	1	0					
	1										1								
	0	-1	0	0	-1	0	1	0	-1	0	0	0	1	0					
		1			1				1										
	0	0	0	-1	-1	0	1	0	-1	0	1	0	0	0					
				1	1				1										
	0	-1	0	1	0	0	0	0	0	0	-1	0	1	0					
		1									1								

### 5 Computational Results and Analysis

The purpose in analysis of flexible manufacturing system is to evaluate the proposed policies and their performance. In this case study, as the above mentioned four machines, two robot and two buffer for input and output. Time for machines, robots, MTTF and uptime were assigned. The FMS has modeled using Visual Object Net version 2.a Software. The simulation is run for 8 h per day, 26 days. The results of Visual Object Net simulation in terms of the throughput, utilization resources, percentage of repair time and idle time percentage can be summarized as follows.

Figure 9 through 12 show throughput, utilization resources, percentage of repair time and idle time percentage, respectively. For the throughput, in Fig. 9, reliable system model attains greater produced number of part A and part B compared to proposed policies. Moreover, policy one provides greater produced number of part A and part B than policy two. From the Fig. 10, it can be found that reliable model obtains utilization better than proposed policies at M1, M2, M3, R1 and R2, and attains same utilization at M4 and R2. In addition, policy one obtains utilization better than policy two at M1, M3, M5, R1 and R2. The Fig. 11 indicates that, both proposed policies have the same percentage of repair time for all resources. Finally, From the Fig. 12, it can be found that reliable model obtains idle time percentage better than proposed policies at M1, M2, and M3, and approximately the same percentage at R1

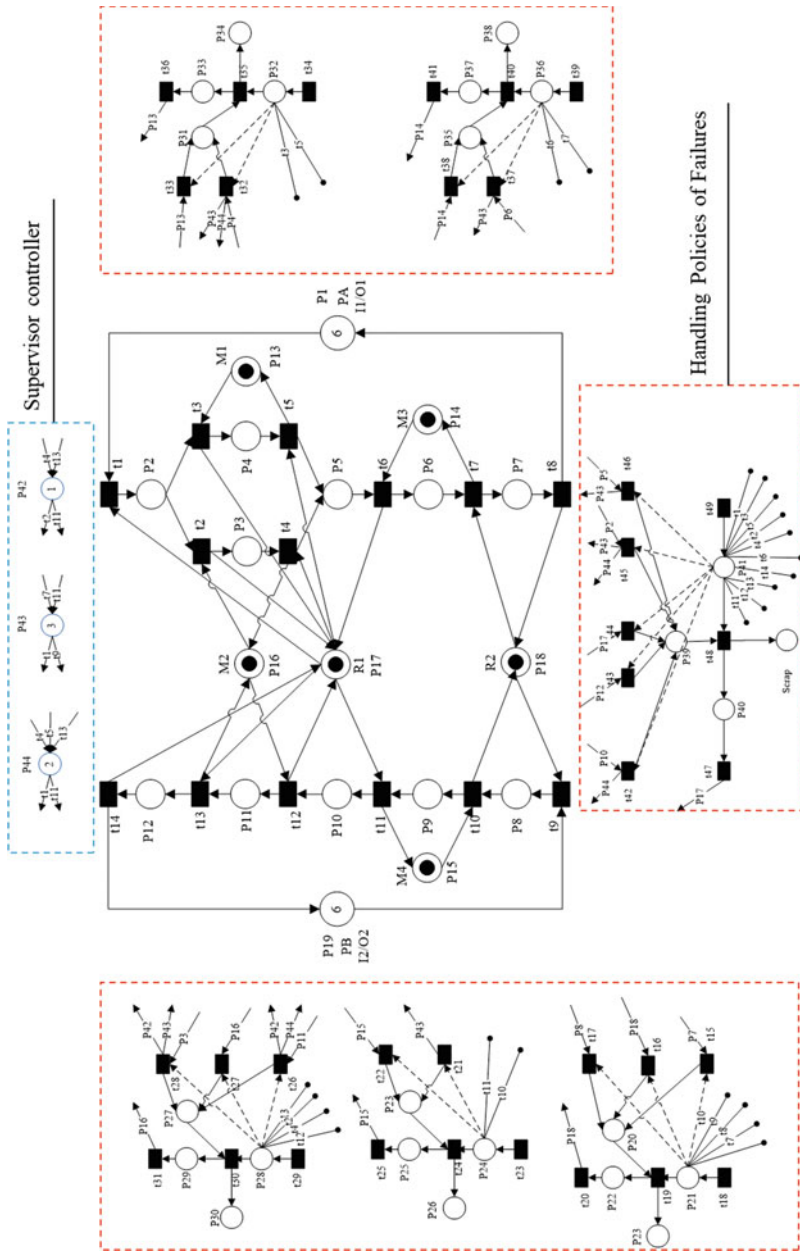


Fig. 7 Petri net model of policy one for case study



**Table 2** Supervisor performance analysis of applied algorithm for case study

Parameter	SMS	ES
Monitors number	5	3
Arcs number	21	13
Reachable states number	182	205

and R2. In addition, policy one obtains idle time percentage better than policy two at M1, and M3, while policy two obtains idle time percentage better than policy one at M2, and M4, and approximately the same percentage at R1 and R2.

## 6 Conclusion

Research works have been dedicated on the development of deadlock prevention controller based on Petri nets for AMS having properly worked resources. Nevertheless, in reality AMS come across unpredicted resource failures. To address this issue, a robust deadlock prevention controller for an AMS with unreliable resources has been proposed in this research. The developed robust controller ensures the liveness of the controlled system in the existence of resource failure. In this paper, a methodology has been illustrated systematically in the context of an automated manufacturing system. At the first step, a supervisor is designed to prevent the deadlock using the elementary siphons control method. Later, two policies, Policy one: Failures Resulting Scrapping and Policy two: Process Resumes Subsequent to Repair, are proposed to handle the failures occurrence in the resources. Finally, the models are simulated using Visual Object Net (Version 2.a) to investigate and evaluate the performance analysis of proposed policies such as utilization of resources and throughput. When it is required, normal and inhibitor arcs are utilized to connect controllers with system model. In this instance, the developed supervisor can ensure no deadlock occurrence in case of resource failure. The results shown that the proposed policies are qualified with robustness and liveness for unreliable systems. Furthermore, by using the proposed policies it is realized that the resource utilization and productivity are different for the case study due to conflict situation in placers. Performance analysis of selected case study showed that the variation in utilization and throughput for system under the reliable and unreliable resources. Moreover, the proposed Failures Resulting Scrapping policy provides greater produced number of parts than Process Resumes Subsequent to Repair policy compared with reliable system. Therefore, the applying Process Resumes Subsequent to Repair policy lead to the increase in total completion time for the parts and selecting this policy depend on the cost and manufacturer policy. The proposed methodology is useful to develop supervisory controller for automated manufacturing systems with unreliable resources and to analyze the system to evaluate the effectiveness of the developed model.

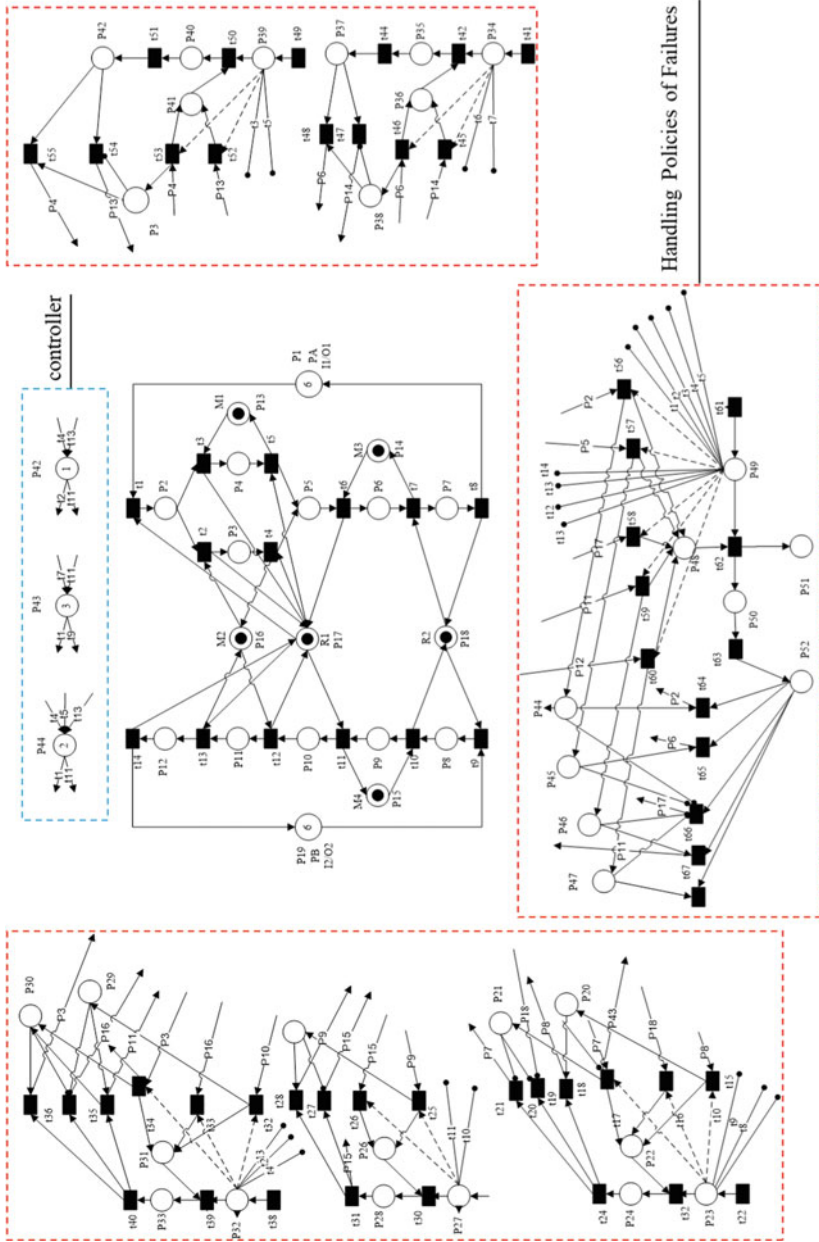
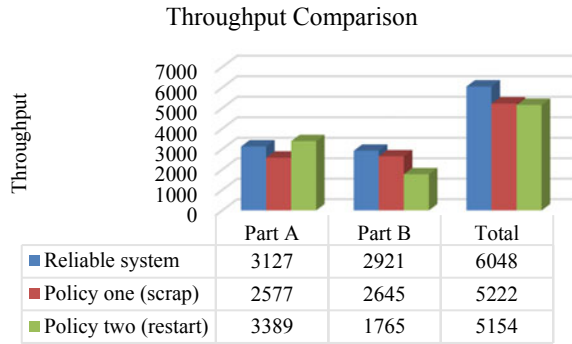
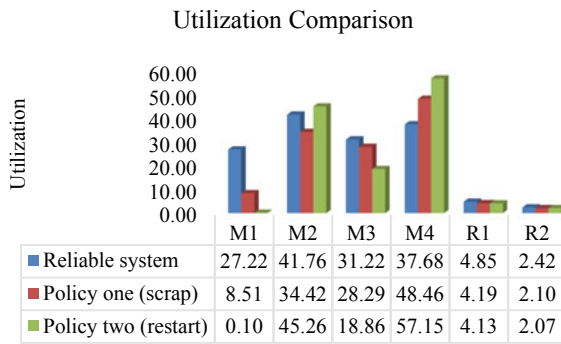


Fig. 8 Petri net model of policy two for case study

**Fig. 9** System throughput for the Petri net model



**Fig. 10** System utilization for the Petri net model



**Fig. 11** Percentage of repair time of the system for the Petri net model

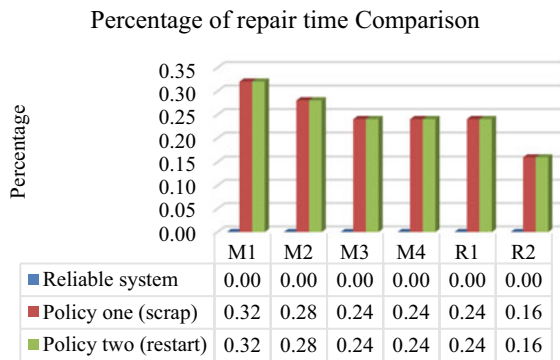
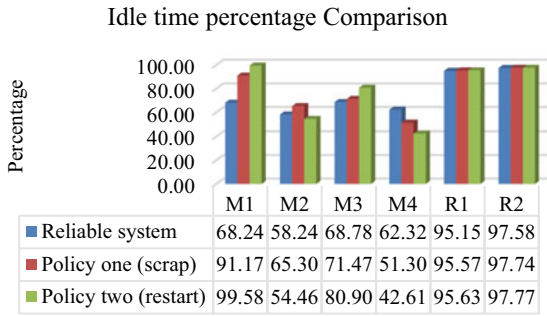


**Fig. 12** System idle time for the Petri net model



## References

- Li Z, Zhou M, Wu N (2008) A survey and comparison of Petri net-based deadlock prevention policies for flexible manufacturing systems. *IEEE Trans Syst Man Cybern Part C: Appl Rev* 38(2):173–188
- Li Z, Wu N, Zhou M (2012) Deadlock control of automated manufacturing systems based on Petri nets—a literature review. *IEEE Trans Syst Man Cybern Part C: Appl Rev* 42(4):437–462
- Abdulaziz M, Nasr EA, Al-Ahmari A, Kaid H, Li Z (2015) Evaluation of deadlock control designs in automated manufacturing systems, international conference on industrial engineering and operations management
- Chen Y, Li Z, Barkaoui K, Giua A (2015) On the enforcement of a class of nonlinear constraints on Petri nets, *Automatica*, 55, pp 116–124
- Chen Y, Li Z, Khalgui M, Mosbahi O (2011) Design of a maximally permissive liveness-enforcing Petri net supervisor for flexible manufacturing systems. *IEEE Trans Autom Sci Eng* 8(2):374–393
- Wysk RA, Yang N-S, Joshi S (1991) Detection of deadlocks in flexible manufacturing cells. *IEEE Trans Robot Autom* 7(6):853–859
- Chao DY (2009) Direct minimal empty siphon computation using MIP. *Int J Adv Manuf Technol* 45(3–4):397–405
- Chao DY (2011) Improvement of suboptimal siphon-and FBM-based control model of a well-known. *IEEE Trans Autom Sci Eng* 8(2):404–411
- Ghaffari A, Rezg N, Xie X (2003) Design of a live and maximally permissive Petri net controller using the theory of regions. *IEEE Trans Robot Autom* 19(1):137–141
- Uzam M, Zhou M (2004) Iterative synthesis of Petri net based deadlock prevention policy for flexible manufacturing systems. *IEEE Int Conf Syst Man Cybern* 5:4260–4265
- Uzam M (2004) The use of the Petri net reduction approach for an optimal deadlock prevention policy for flexible manufacturing systems. *Int J Adv Manuf Technol* 23(3–4):204–219
- Lautenbach K (1987) Linear algebraic calculation of deadlocks and traps. In: *Concurrency and Nets*, First ed. Springer, US, pp 315–336
- Uzam M (2002) An optimal deadlock prevention policy for flexible manufacturing systems using Petri net models with resources and the theory of regions. *Int J Adv Manuf Technol* 19(3):192–208
- Chao DY (2010) Fewer monitors and more efficient controllability for deadlock control in S3PGR2 (systems of simple sequential processes with general resource requirements). *Comput J* 53(10):1783–1798
- Li Z, Zhou M (2004) Elementary siphons of Petri nets and their application to deadlock prevention in flexible manufacturing systems. *IEEE Trans Syst Man Cybern Part A: Syst Hum* 34(1):38–51

16. Pan Y-L, Tseng C-Y, Row T-C (2017) Design of improved optimal and suboptimal deadlock prevention for flexible manufacturing systems based on place invariant and reachability graph analysis methods. *J Alg Comput Technol* 1748301817710922
17. Zhao M, Uzam M (2017) A suboptimal deadlock control policy for designing non-blocking supervisors in flexible manufacturing systems. *Inf Sci* 388:135–153
18. Cong X, Gu C, Uzam M, Chen Y, Al-Ahmari AM, Wu N, Zhou M, Li Z (2018) Design of optimal petri net supervisors for flexible manufacturing systems via weighted inhibitor arcs. *Asian J Control*
19. Lawley MA, Sulistyono W (2002) Robust supervisory control policies for manufacturing systems with unreliable resources. *IEEE Trans Robot Autom* 18(3):346–359
20. Hsieh F-S (2006) Robustness analysis of Petri nets for assembly/disassembly processes with unreliable resources. *Automatica* 42(7):1159–1166
21. Wang S, Chew SF, Lawley MA (2008) Using shared-resource capacity for robust control of failure-prone manufacturing systems. *IEEE Trans Syst Man Cybern-Part A: Syst Hum* 38(3):605–627
22. Chew SF, Wang S, Lawley MA (2009) Robust supervisory control for product routings with multiple unreliable resources. *IEEE Trans Autom Sci Eng* 6(1):195–200
23. Liu G, Li Z, Barkaoui K, Al-Ahmari AM (2013) Robustness of deadlock control for a class of Petri nets with unreliable resources. *Inf Sci* 235:259–279
24. Yue H, Xing K, Hu Z (2014) Robust supervisory control policy for avoiding deadlock in automated manufacturing systems with unreliable resources. *Int J Prod Res* 52(6):1573–1591
25. Yue H, Xing K, Hu H, Wu W, Su H (2015) Robust supervision using shared-buffers in automated manufacturing systems with unreliable resources. *Comput Ind Eng* 83:139–150
26. Wang F, Xing K-Y, Zhou M-C, Xu X-P, Han L-B (2016) A robust deadlock prevention control for automated manufacturing systems with unreliable resources. *Inf Sci* 345:243–256
27. Li Z, Zhou M (2005) Comparison of two deadlock prevention methods for different-size flexible manufacturing systems. *Int J Intell Control Syst* 10(3):235–243
28. Chen Y, Li Z, Zhou M (2012) Behaviorally optimal and structurally simple liveness-enforcing supervisors of flexible manufacturing systems. *IEEE Trans Syst Man Cybern Part A: Syst Hum* 42(3):615–629
29. Nasr EA, El-Tamimi AM, Al-Ahmari A, Kaid H (2015) Comparison and evaluation of deadlock prevention methods for different size automated manufacturing systems. *Math Probl Eng* 501:537893

# The Device to Simulate Movement of Teeth Jaw



Ho Thi Thuy Duong, Tran Nam Cuong, Nguyen Thu Khoa,  
Nguyen Tran Kim Hoang, and Nguyen Tuong Long

**Abstract** This paper presents equipment to simulate the motion of the lower jaw when chewing. The device is designed with a jaw attached to the denture. The lower jaw will be held and moved like the environment in the mouth. The main principle of the device is based on the new ideas of the marginal motion of incisors on the vertical plane (Posselt diagram) and the trajectory of the jaw on the horizontal plane (Gothic arc). The horizontal and vertical motions of the lower jaw transform into two linear translational motion and rotation motion around the fixed axis. The structure of device is designed to simulate the mean chewing force in a range of 7–15 kg (70–150 N). Translational motion using belt transmission mechanism and movement around the fixed axis using the gears transmission mechanism is applied in order to achieve the requirement of design. This paper uses the finite element method to calculate and optimize components of the device by ANSYS software, then the implementation of model will be carried out. The main load-bearing component calculated are: the durability of the lower jaw attachment having a yield stress of 0.5643 MPa. The yield stress value of the components is less than the yield stress of plastic PLA material 70 MPa, the components will meet the durable operation of the device. The part of device is manufactured by 3D printing technology with PLA material. Stepper motor will be used to provide movement for the whole system and controlled by Arduino. A loadcell is used to collect data of acting force on the upper jaw. The model was built with three basic testing phases (opening, closing, and occlusion) and a graphic user interface which makes the device more friendly to users. The device is successfully built with many mechanisms of the lower jaw that allows the movements corresponding the mean chewing force, which helps doctors having multiple options to examine dentures. In the future, we will improve software and frequently update user requirements to build more complex motion trajectory as well as improve the precision of the device.

---

H. T. T. Duong (✉) · T. N. Cuong · N. T. Khoa · N. T. Long  
Centre of Computational Mechanics, HCMC University of Technology, Ho Chi Minh City,  
Vietnam

N. T. K. Hoang  
Quoc An Dental Clinic, Ho Chi Minh City, Vietnam

**Keywords** Mechanics · Simulate movement · Posselt · The lower jaw

## 1 Introduction

The dental problems are one of the issues that are being concerned. It is not only related to beauty but also related to health problems. Currently, the most common dental problems are tooth decay and tooth loss, and teeth are an important part of the body. Teeth have a huge role in creating balance on the face, determining the ability to pronounce and starting point of the process of digesting food and absorbing nutrients. Methods protect the structure of teeth to limit damage and have timely orthodontic interventions. Regarding the problem of tooth loss, it can be restored by implanting dentures. Since this method is the most common, the quality of the denture should be taken into care. In this research, we propose device as a reasonable foundation that can support denture quality control devices and ensure medical quality. The quality of dentures must be ensured, otherwise it can easily lead to the risk of infection, pulpitis, gingivitis, bleeding gums, impaired chewing function and jaw deformation.

At the same time the problem of researching this dental device is more and more popular. Many research are strongly developed such as simulating the chewing process for the purpose of testing dental materials and implants and for the purpose of analyzing food samples [1] and a design of mastication robot for texture analysis of foods in similar environment of human masticatory process respect [2–4]. The research method of motion simulation device is carried out according to the following procedure: Firstly, the pathology of tooth loss is increasingly popular. Secondly, building a computational model based on the orbital data of the mandibular teeth is obtained from the experiment. Thirdly, performing calculations based on experimental parameters. Finally, creating pilot device.

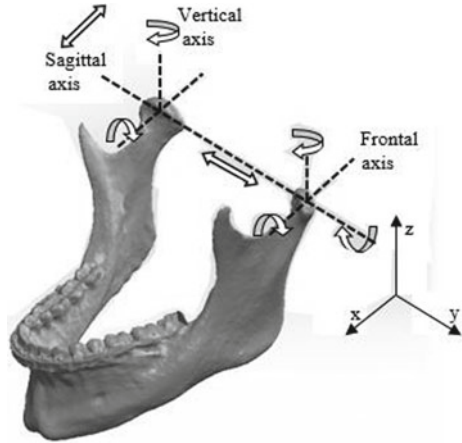
Being aimed at the problems of existing literatures and the demand for force detection in the process of denture replacement, a device to simulation movement of teeth jaw (BK-DD) is proposed, designed, fabricated and tested. The BK-DD can simulate the real masticatory movement of human to the largest extent and obtain the mean chewing force of a lower jaw effectively in a range of 7–15 kg (70–150 N) [8]. At the same time, the BK-DD can provide denture performance tests for the individual dental patient.

## 2 Actuation Lower Jaw Movement Analysis

### 2.1 Degrees of Freedom of Lower Jaw Analysis

Human stomatognathic system is mainly composed of the teeth, the jaws and the masticatory muscles. Human teeth can be divided into incisors, canines and molars, which have a laterally zygomorphic and transversely zygomorphic distribution [5].

**Fig. 1** Degrees of freedom of lower jaw analysis



When lower jaw performs biting function, crushing and chewing, the biomechanical system of the lower jaw will move with six degree of freedom (DOF) according to the trajectory recorded by the midpoint located on lower jaw Fig. 1. These movements are rotational and translational movements at the temporomandibular position. A translational motion moves the lower jaw to the side (left and right), a translational motion moves the lower jaw forward—backward and at each convex condyle in the temporomandibular perform two rotations. With the flexible movement of the lower jaw is easy to bite, tear, chew, and crush food. Besides, it helps a lot for the salivary system to soften food before it goes to the stomach, which helps protect the digestive system.

Because of flexibility of the musculature, it is difficult to model the design of a device with a movable joint that meets the needs for the degrees of freedom of the lower jaw. Through the kinematic analysis of human mandible, it is found that the mandible movement only needs three main degrees of freedom.

## 2.2 Degrees of Freedom of BK-DD Analysis

The main principle of the device is design bases on the new ideas of the marginal motion of incisors on the vertical plane (Posselt diagram) and the trajectory of the jaw on the horizontal plane (Gothic arc) Fig. 2 [2, 8]. Maximum dimension drawn on 2D plane Table 1 [2, 3]. The horizontal and vertical motion of the lower jaw transforms into two linear translational motion and rotation motion around the fixed axis. Movements are the translational degrees of freedom in X and Y directions, and the rotational degrees of freedom in X.

If a point is marked located on lower jaw performs marginal movement in all directions, the point will draw a shape in space [8]. It is the borderline for the mandibular range of motion. Marginal movements of the mandible are the maximum



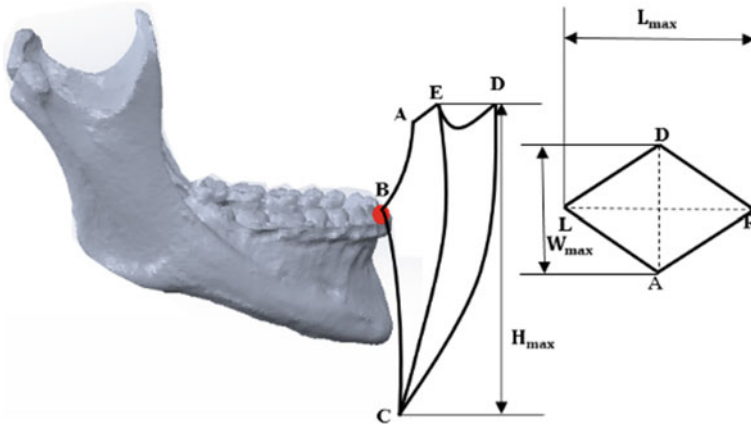


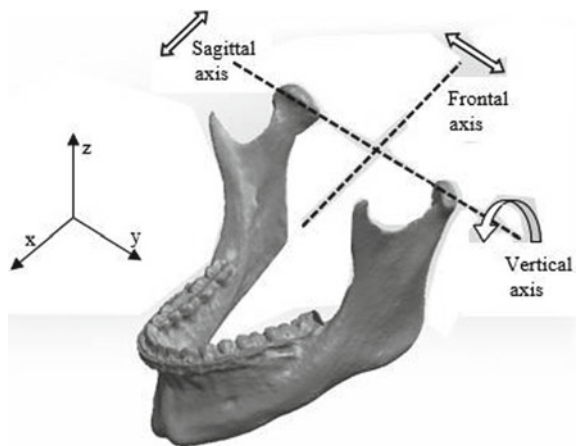
**Fig. 2** The border movement at the incisor point

**Table 1** Maximum dimension drawn on 2D plane [3]

Stages	Symbol	Dimension (m)
The mouth opens widest	$H_{max}$	0,05
The lower jaw forward and backward	$L_{max}$	0,012
The lower jaw to the side (left and right)	$W_{max}$	0,015

positions that the point can be reached. The horizontal and vertical motion of the lower jaw transforms into two linear translational motion and rotation motion around the fixed axis Fig. 3.

**Fig. 3** BK-DD Degrees of freedom analysis



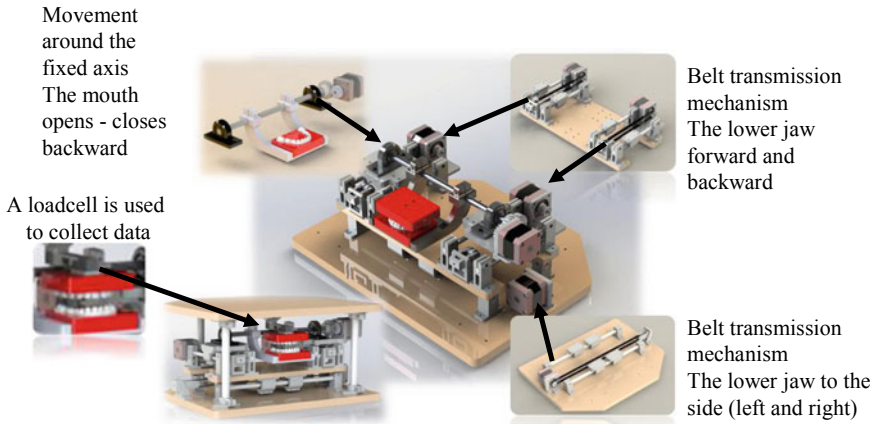


Fig. 4 Schematic diagram of the BK-DD

### 3 BK-DD Design

#### 3.1 BK-DD Platform

Translational motion using belt transmission mechanism and movement around the fixed axis using the gears transmission mechanism in order to archive requirement of design. When the lower jaw performs the movement of opening and closing the mouth, the lower jaw performs the hinge movement. Movement around the fixed axis is using the gears transmission mechanism. When the stepper motor starts the torque transmission causes the gear transmission to drive the shaft. At the bearing position is responsible keeping the shaft from moving along the axis (Fig. 4).

#### 3.2 Simulation and Examination of and Estimate Durability of the Lower Jaw Attachment

Due to the simple problem so it is possible to use the program default mesh size that has been computed for the object size. In addition, since we used the convergence history tool, the meshes in the important areas were smooth again based on the results so the initial mesh size is acceptable. Mesh statistics: 156,131 nodes và 90,319 elements.

The value of torque is calculated according to the maximum torque of the motor in the model, reaching a value of 2,8 N.m [6]. The chosen material is PLA plastic listed material. The mesh has been optimized via the Convergence tool in the results section of the von Mises stress so that the results will be converged on stress and the related results will correlate with the stress results. Because the object is fixed at

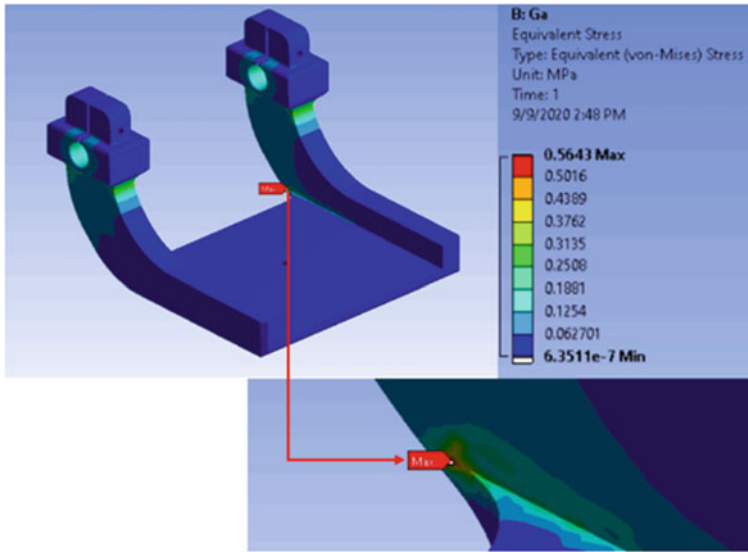


**Fig. 5** The jaw attachment stress result

**Table 2** The lower jaw attachment and PLA plastic material stress

	Stress (MPa)	Preferences
The jaw attachment simulation result	0.5643	–
PLA plastic material	70	[7]

the jaw attachment side and the moment at the shaft hole, the material will be pulled and compressed more at the shaft hole and the region with special geometry, which is the jaw frame curve, so the stress will be concentrated at the shaft hole and the transition between the two aforementioned regions, the maximum stress at one point is 0,5643 MPa and less than the yield stress, which is 70 MPa [7]. But that point is geometrically degenerated, therefore its value does not need to be considered (Fig. 5 and Table 2).

### 3.3 Practical Model

The BK-DD is manufactured and located in the Centre of Computational Mechanics. Firstly, the manufacture is the machining of mechanical parts. Secondly, the parts of device are manufactured by 3D printing technology at Centre of Computational Mechanics. Finally, the control circuit of BK-DD is designed (Fig. 6).

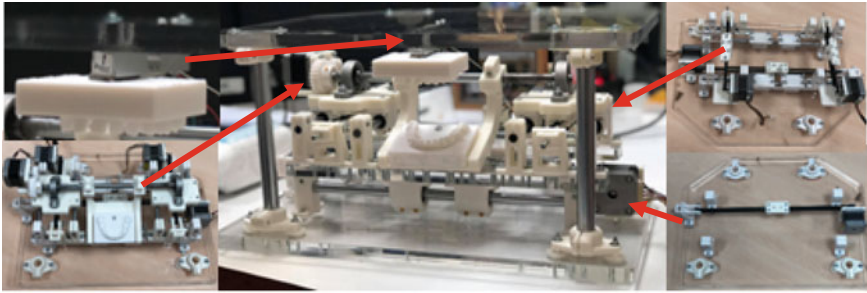


**Fig. 6** The device to simulate movement of teeth jaw (BK-DD)

### 3.4 Data Collection Method and Control System

The research has two goals. Firstly, survey the functional orbital in fact to build a method functional orbital program. Secondly, build the actuator, exploit the newly established trajectory function, simulate this trajectory on the model. The study will conduct experiments on humans, in order to get the orbit of the lower jaw and collect coordinate data when performing chewing movements using image processing method.

The method of obtaining orbital data will be done by attaching a fixture marked with a red dot determined in a fixed way, followed by the volunteer who performs the chewing process and is simultaneously recorded in Fig. 7 in two vertical planes with front view and left view, respectively.

Through processing algorithms in python programming language, the study obtained a set of coordinates on three coordinate axis. Then, interpolating from this data set, the research obtained a trajectory function Fig. 8. Based on the mechanical analyze, the motions of the whole system have been modeled into three basic movements: translation in the x-axis, translation in the y-axis, and rotation around the x-axis.

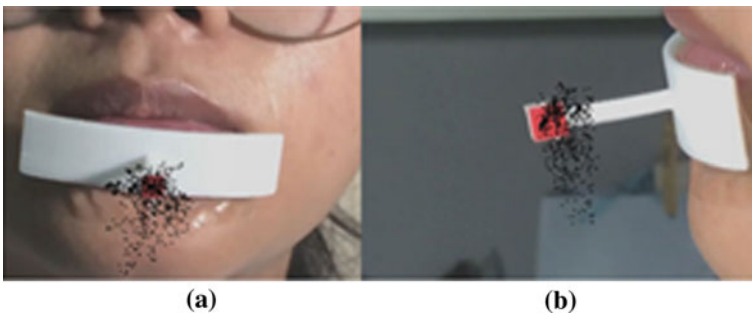


**Fig. 7** Data collection method; **a** Front view; **b** Left view

**Fig. 8** Data visualization

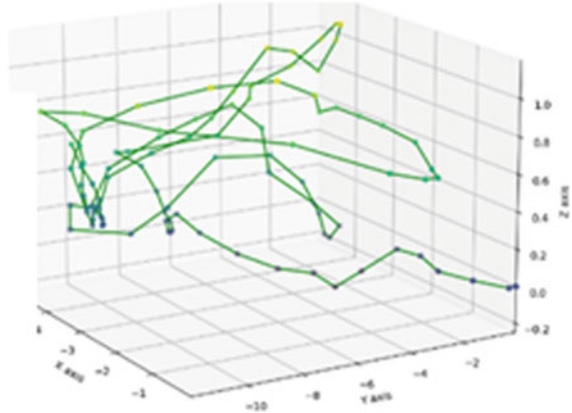


**Table 3** Step motor parameters [6]

Parameters	Value
Step	1,8° (200 step/round)
Holding moment	0,4 N.m
Torque	0,022 N.m
Rotor inertia	$5,4 \cdot 10^{-6} \text{ kg} \cdot \text{m}^2$
Step error	$\pm 5\%$
Motor size	$0,042 \times 0,042 \times 0,04 \text{ m}$
Shaft diameter	0,005 m

The design control diagram for NEMA 17 stepper motor [6] is open loop control system. Central controller using Kit Arduino BLE SoC ESP 32 WeMos D1 R32, microprocessor Espressif ESP32 dual core Tensilica LX6 processor for 240 MHz processing speed and 328 KB RAM (Table 3).

The operating principle of the system is presented as follows: Based on the existing derivative orbital equation, we discretized the equation into multiple coordinate points equidistant along the trajectory. The central microcontroller will calculate the number of steps (of the motor) to make the move between two adjacent points, then convert into control pulses, then sent to the motor through the DRV8255 driver. The motor group perform simultaneously to simulate the trajectory.

## 4 Conclusion

The BK-DD is proposed, designed, simulated, fabricated and tested that consists of power system, control and driving system, and a loadcell is used to collect data and suporting system. Durability of the lower jaw attachment maximum stress is 0.5643 MPa, which is less than the yield stress of PLA material [7]. The BK-DD

can provide a trust mean chewing force in a range of 7–15 kg (70–150 N) [8]. The interface is designed to be user-friendly, material expert or doctor operate easily the device according to the intended use. The lower jaw movement according to trajectory is performed base on the human sampling experiment, then building the movement trajectory of the lower jaw from the experiment. The horizontal and vertical motion of the lower jaw transforms into two linear translational motion and rotation motion around the fixed axis.

The trajectory comparison indicates that this new device is qualified to get a high accuracy mandible movement. The future work will focus on the application in the long-time performance of the denture quality test device and the application in device design for denture quality. It will build foundation and premise for future applications in the field of biomechanics.

## References

1. Xu W, Lewis D, Bronlund J, Morgensern M (2007) Mechanism, design and motion control of a linkage chewing simulator for food evaluation. *J Food Eng* 82(2):189–198
2. Ren L, Yang J, Tan Y, Hu J, Liu D, Zhu J An intelligent dental robot. ISSN: 0169–1864 (Print) 1568–5535 (Online). 11 June 2018
3. Wen H, Xu W, Cong M (2015) Senior Member, IEEE, Kinematic model and analysis of an actuation redundant parallel robot with higher kinematic pairs for jaw movement. *IEEE Trans Ind Electron* 62(3)
4. Lee SJ, Kim BK, Chun YG, Park DJ (2018) Design of mastication robot with life-sized linear actuator of human muscle and load cells for measuring force distribution on teeth. Dr. Haliyo S (ed), pp 127–136. 28 Mar 2018
5. Sarig R, Slon V, Abbas J et al (2013) Malocclusion in early anatomically modern human: a reflection on the etiology of modern dental misalignment. *Plos One* 8(11):e80771
6. Laurb9 (2020). <https://github.com/laurb9/StepperDriver>
7. Torres J, Coteló J, Karl J, Gordon AP Me-chanical property optimization of FDM PLA in shear with multiple objectives. 2015 the minerals, metals & materials
8. Hung Hoang Tu (2004) *Can Khop Hoc*. Medical Publisher, Ho Chí Minh City

# The Plane Problem of Poroelasticity for a Semi-plane



Natalya Vaysfeld and Zinaida Zhuravlova

**Abstract** Poroelastic materials are widely used in many engineering applications. However, the problems of poroelasticity are usually complicated, and their analytical solutions are not often found. In this paper the semi-plane of poroelastic material is considered for the case when the boundary is loaded by mechanical load, and it is fully drained. The problem is formulated in a plane statement regarding two displacements of the solid skeleton and the pore pressure. The initial problem is reduced to a one-dimensional problem with the help of an infinite Fourier transform. The one-dimensional problem is formulated as a vector boundary-valued problem. The general solution of the vector homogeneous equation is constructed with the help of matrix differential calculation. According to it, the corresponding matrix equation is considered, and its fundamental solutions were derived. The vector of unknown constants is found for two subcases (when the integral transform parameter is greater than zero and when it is less than zero) from the boundary conditions. So, the analytical solution of the initial problem is derived. The displacements, stress and pressure inside the semi-plane are investigated. The cases of distributed and concentrated load are considered.

**Keywords** Semi-plane · Poroelasticity · Integral transform

## 1 Introduction

The mathematical modelling of poroelastic materials is a relevant problem in many areas of science and engineering, such as development of oil and gas fields and others. The theory of poroelasticity was developed by Terzaghi [1] for the one-dimensional case. The three-dimensional case and the generalization of the poroelasticity theory was done by Biot [2]. In [3] a formulation of Biot's linear theory suitable for problems

---

N. Vaysfeld · Z. Zhuravlova (✉)  
Odessa I.I. Mechnikov National University, Odessa 65082, Ukraine  
e-mail: [z.zhuravlova@onu.edu.ua](mailto:z.zhuravlova@onu.edu.ua)

of soil mechanics was proposed. The equations of consolidation were reformulated in terms of undrained coefficients in [4].

The static contact problem about a rigid punch on the free surface of a linear porous elastic half-plane was solved with the use of a Fourier transform and a singular integral equation in [5]. The dynamic response of a poroelastic half-plane soil medium subjected to moving loads was studied analytically/numerically under conditions of plane strain in [6]. The loading function was presented there by a Fourier series expansion.

It is well known that the apparatus of mathematical physics' boundary problems allows successful modeling of many complex dynamic problems of elasticity and destruction [7–9]. Authors of the present investigation set as their goal the application of the apparatus of generalized integral transforms and discontinuous problems to the solving of poroelasticity problems. With this aim the solving of the known model problem is proposed. It is derived by analytical transforms, and the exact formulae for the displacements, stress and pore pressure are found.

## 2 Statement of the Problem

The poroelastic semi-infinite plane  $y > 0$  is considered. It's boundary  $y = 0$  is loaded by the load  $l(x)$ , and perfect drainage conditions are fulfilled [10]:

$$\sigma_y|_{y=0} = -l(x), \tau_{xy}|_{y=0} = 0, p|_{y=0} = 0 \quad (1)$$

Here  $p(x, y)$  is pore pressure,  $\sigma_y(x, y)$ ,  $\tau_{xy}(x, y)$  are normal and shear effective stresses.

The system of equilibrium and storage equations has the following form [11]

$$\begin{cases} \frac{\partial^2 u}{\partial x^2} + \frac{\kappa-1}{\kappa+1} \frac{\partial^2 u}{\partial y^2} + \frac{2}{\kappa+1} \frac{\partial^2 v}{\partial x \partial y} - \frac{\alpha}{G} \frac{\kappa-1}{\kappa+1} \frac{\partial p}{\partial x} = 0, \\ \frac{\partial^2 v}{\partial x^2} + \frac{\kappa+1}{\kappa-1} \frac{\partial^2 v}{\partial y^2} - \frac{2}{\kappa-1} \frac{\partial^2 u}{\partial x \partial y} - \frac{\alpha}{G} \frac{\partial p}{\partial y} = 0, \\ \frac{\partial^2 p}{\partial x^2} + \frac{\partial^2 p}{\partial y^2} - \frac{\alpha}{k} \left( \frac{\partial u}{\partial x} + \frac{\partial v}{\partial y} \right) - \frac{S_p}{k} p = 0 \end{cases} \quad (2)$$

where  $u(x, y) = u_x(x, y)$ ,  $v(x, y) = u_y(x, y)$  are displacements of the solid skeleton,  $\kappa = 3 - 4\mu$  is Muskhelishvili's constant,  $\mu$  is Poisson ratio,  $G$  is shear modulus,  $\alpha$  is Biot's coefficient,  $S_p$  is storativity of the pore space,  $k$  is permeability.

The stress state of the semi-plane, which satisfy (1)–(2) should be found.



### 3 One-Dimensional Problem

The initial problem (1)–(2) is reduced to the one-dimensional problem with the help of infinite Fourier transform applied with regard to variable  $x$ :

$$\begin{bmatrix} u_\gamma(y) \\ v_\gamma(y) \\ p_\gamma(y) \end{bmatrix} = \int_{-\infty}^{\infty} \begin{bmatrix} u(x, y) \\ v(x, y) \\ p(x, y) \end{bmatrix} e^{i\gamma x} dx$$

The one-dimensional problem in the transform space is formulated in vector form

$$\begin{cases} L_2 \mathbf{y}_\gamma(y) = 0, \\ (1 - \mu)v'_\gamma(0) - i\gamma\mu u_\gamma(0) = \frac{1-2\mu}{2G} l_\gamma, \\ u'_\gamma(0) - i\gamma v_\gamma(0) = 0, \\ p_\gamma(0) = 0 \end{cases} \tag{3}$$

Here  $L_2 \mathbf{y}_\gamma(y) = I \mathbf{y}_\gamma'' - R \mathbf{y}_\gamma' + P \mathbf{y}_\gamma$ ,  $\mathbf{y}_\gamma = \begin{pmatrix} u_\gamma(y) \\ v_\gamma(y) \\ p_\gamma(y) \end{pmatrix}$ ,  $I$  is identity matrix,  $R =$

$$\begin{pmatrix} 0 & \frac{2i\gamma}{\kappa-1} & 0 \\ \frac{2i\gamma}{\kappa+1} & 0 & \frac{\alpha}{G} \frac{\kappa-1}{\kappa+1} \\ 0 & \frac{\alpha}{k} & 0 \end{pmatrix}, P = \begin{pmatrix} -\gamma^2 \frac{\kappa+1}{\kappa-1} & 0 & \frac{\alpha i \gamma}{G} \\ 0 & -\gamma^2 \frac{\kappa-1}{\kappa+1} & 0 \\ \frac{\alpha i \gamma}{k} & 0 & -\gamma^2 - \frac{S_p}{k} \end{pmatrix}. \text{ The general solution of}$$

the homogeneous equation in (3) is constructed with the help of matrix differential calculation [12]. Accordingly to it the corresponding matrix equation is considered  $L_2 Y_\gamma = 0$ . The matrix  $Y_\gamma$  is chosen in the form  $Y_\gamma = e^{\eta y} I$  and substituted into the matrix equation. So, the equality  $L_2 e^{\eta y} I = M(\eta) e^{\eta y}$  is derived, where  $M(\eta) = I \eta^2 - R \eta + P$ .

The solution of the matrix homogeneous equation is constructed in the form [13]

$$Y(y) = \frac{1}{2\pi i} \oint e^{\eta y} M^{-1}(\eta) d\eta,$$

here  $M^{-1}(\eta)$  is the inverse matrix to  $M(\eta)$ .

The determinant of the matrix  $M(\eta)$  has four different roots  $\eta_{1,2} = \pm\gamma$ ,  $\eta_{3,4} = \pm\sqrt{\gamma^2 + \frac{S_p}{k} + \frac{\alpha^2(\kappa-1)}{GK(\kappa+1)}}$ , so there are derived four fundamental matrix solutions  $Y_i(y), i = \overline{1, 4}$ . The matrix solution  $Y_3(y)$  corresponding to the root  $\sqrt{\gamma^2 + \frac{S_p}{k} + \frac{\alpha^2(\kappa-1)}{GK(\kappa+1)}}$  is not considered, because the components of the matrix are increasing when  $y > 0$ .

The general solution of the problem (3) has the following form

$$\mathbf{y}_\gamma(y) = Y^-(y) \begin{pmatrix} c_1 \\ c_2 \\ c_3 \end{pmatrix} \tag{4}$$

Here  $Y^-(y) = \begin{cases} Y_1(y) + Y_4(y), \gamma < 0, \\ Y_2(y) + Y_4(y), \gamma > 0, \end{cases}$   $c_i, i = 1, 2, 3$  are constants which are found for each form of  $Y^-(y)$  from boundary conditions in (3).

## 4 Analytical Solution

After inversion of the expression (4) the analytical solution of the initial problem (2) has the following form

$$\mathbf{y}(x, y) = \frac{1}{2\pi} \left[ \int_{-\infty}^0 (Y_1(y) + Y_4(y)) \begin{pmatrix} c_{1,1} \\ c_{1,2} \\ c_{1,3} \end{pmatrix} e^{-i\gamma x} d\gamma + \int_0^{\infty} (Y_2(y) + Y_4(y)) \begin{pmatrix} c_{2,1} \\ c_{2,2} \\ c_{2,3} \end{pmatrix} e^{-i\gamma x} d\gamma \right] \quad (5)$$

Here  $c_{i,j}, i = 1, 2, j = 1, 2, 3$  are constants found from boundary conditions in (3), index  $i = 1$  corresponds to the case when  $\gamma < 0$ , and index  $i = 2$  corresponds to the case when  $\gamma > 0$ .

## 5 Graphical Results and Discussion

The calculations were done for Ruhr sandstone [10], where  $G = 1.33 \cdot 10^{10}$  N/m<sup>2</sup>,  $\mu = 0.12$ ,  $\alpha = 0.637$ ,  $k = 2 \cdot 10^{-13}$  m<sup>4</sup>/N · s,  $S_p = 3.9215 \cdot 10^{-11}$  m<sup>2</sup>/N.

The case with concentrated load  $l(x) = \delta(X)$  is considered, and the results are presented on Figs. 1 and 2. As the load is symmetric, pore pressure and normal effective stress are symmetric. The biggest absolute values for these functions are reached when  $x = 0$ .

At the line  $y = 1$  pore pressure (Fig. 1) is positive, decreasing to zero some way away from the point  $x = 0$ . This is caused by the drainage, which starts at the boundary of the semi-plane  $y = 0$ , and which produce a tendency for shrinkage of the semi-plane's boundary. The effective stress  $\sigma_y(x, 1)$  (Fig. 2) is negative, which is agreed with the compressive concentrated load. Stress's  $\sigma_y(x, 1)$  peak is at the point  $x = 0$ ,

where the load is applied. The case with distributed load  $l(x) = \begin{cases} 1, -1 < x < 1 \\ 0, x \notin [-1, 1] \end{cases}$

is considered. The results are shown in Figs. 3 and 4. The load is symmetric, so pore pressure and normal effective stress are symmetric. The biggest absolute values for these functions are reached when  $x = 0$ .

The pore pressure (Fig. 3) is positive at the line  $y = 1$ , decreasing to zero some way away from the point  $x = 0$ . The values of  $p(x, 1)$  for this load are bigger than for the case with the concentrated load. The values of effective stress  $\sigma_y(x, 1)$  (Fig. 4) for this load are also bigger by absolute value than for the case with the concentrated load.

Fig. 1 Pore pressure

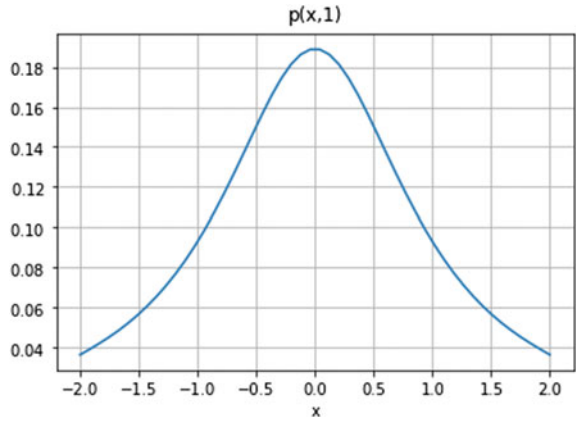


Fig. 2 Effective stress

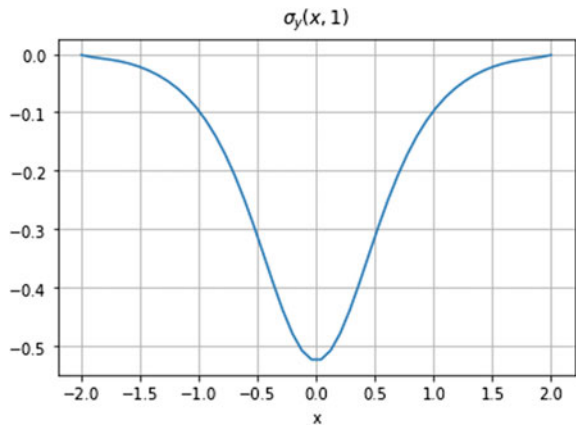
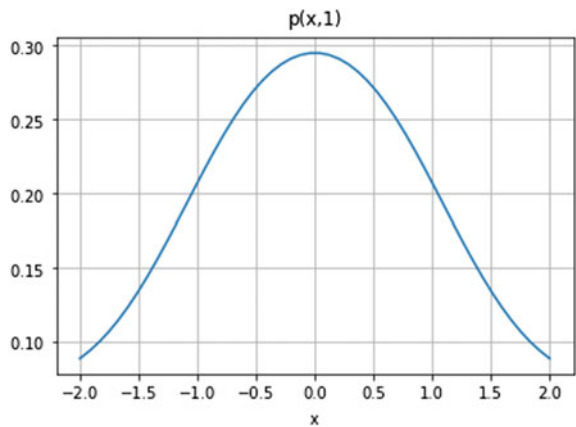
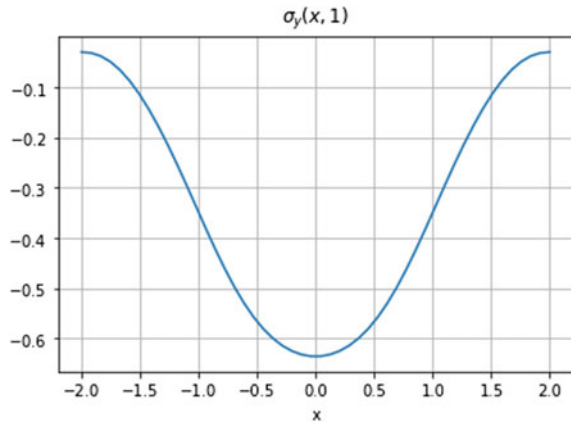


Fig. 3 Pore pressure



**Fig. 4** Effective stress

## 6 Conclusions

1. The analytical solution for poroelastic semi-plane is constructed with the help of the integral transform method and apparatus of matrix differential calculation.

2. Normal and shear effective stress, and pore pressure are investigated for different mechanical loads.

3. The comparison of the given problem results was done for the case when parameter  $\alpha = 0$  with the given known solution for elastic half-space.

4. The proposed approach can be used for a more complicated shape of domains weakened by defects.

## References

1. Terzaghi K (1925) *Erdbaumechanik auf bodenphysikalischer Grundlage*. Deuticke, Wien
2. Biot MA (1941) General theory of three-dimensional consolidation. *J Appl Phys* 12:155–164
3. Verruijt A (1969) Elastic storage of aquifers. In: R.D. Wiest (ed) *Flow through porous media* (1969)
4. Rice J, Cleary M (1976) Some basic stress diffusion solutions for fluid-saturated elastic porous media with compressible constituents. *Rev Geophys Space Phys* 14(2)
5. Scalia A, Sumbatyan MA (2000) Contact problem for porous elastic half-plane. *J Elast* 60:91–102
6. Theodorakopolous DD (2003) Dynamic analysis of a poroelastic half-plane soil medium under moving loads. *Soil Dyn Earthq Eng* 23:521–533
7. Kaplunov J, Prikazchikov DA, Rogerson GA (2005) On three-dimensional edge waves in semi-infinite isotropic plates subject to mixed face boundary conditions. *J Acoust Soc Am* 118(5). <https://doi.org/10.1121/1.2062487>
8. Zhubadynskiy Y, Mykhas'kiv VV (2018) Acoustic filtering properties of 3D elastic metamaterials structured by crack-like inclusions. In: 2018 XXIIIrd international seminar/workshop on direct and inverse problems of electromagnetic and acoustic wave theory (DIPED), pp 145–148. <https://doi.org/10.1109/DIPED.2018.8543137>

9. Hakobyan VN, Grigoryan AH (2021) Plane stress state of a uniformly piece-wise homogeneous plane with a periodic system of semi-infinite interphase cracks. *Vestnik Samarskogo Gosudarstvennogo Tekhnicheskogo Universiteta, Seriya Fiziko-Matematicheskie Nauki* 25(1):67–82
10. Cheng AH-D (2016) *Poroelasticity. Theory and applications of transport in porous media*, vol 27. Springer
11. Verruijt A (2010) *An introduction to soil dynamics. Theory and applications of transport in porous media*, vol 24. Springer (2010)
12. Vaysfel'd ND, Zhuravlova ZYu (2015) On one new approach to the solving of an elasticity mixed plane problem for the semi-strip. *Acta Mech* 226(12):4159–4172. <https://doi.org/10.1007/s00707-015-1452-x>
13. Popov GYa (2013) *Exact solutions of some boundary problems of deformable solid mechanic (in Russian)*. Astroprint, Odessa

# Crack Propagations in Functionally Graded Material Using a Phase-Field NURBS-Based Finite Element Approach



Khuong D. Nguyen, H. Nguyen-Xuan, and Magd Abdel Wahab

**Abstract** This study presents a hybrid phase-field formulation combining isogeometric analysis with a local refinement multipatch algorithm (VUKIMS algorithm) to predict damage in functionally graded material structures. The power-law index of the Mori–Tanaka mixture rule will impact the critical force point. We have confirmed that this approach is an effective computational tool for functionally graded materials. As a result, the effective size of cubic NURBS elements is half of a length-scale parameter for balancing the achieved accuracy and computational cost in most examples.

**Keywords** NURBS-based finite elements · Phase-field model · Functionally graded material · Local refinement mesh

## 1 Introduction

Recently, functionally graded materials (FGMs) [1], which are an advanced material in a family of composite materials, have become the most attractive for researchers. The FGM is a functional composition of two different materials, for instance, metal-ceramic and ceramic-ceramic. The mixture of rules, including exponential, sigmoid, and power laws, allows FGM to possess a smooth and continuous gradation in the domain. FGM prevails over a laminated composite material in structures working in high-temperature gradients, including the nuclear, aerospace industry, because it can

---

K. D. Nguyen (✉)

Department of Electrical Energy, Metals, Mechanical Constructions & Systems, Faculty of Engineering and Architecture, Ghent University, 9000 Ghent, Belgium  
e-mail: [duykhuong.nguyen@ugent.be](mailto:duykhuong.nguyen@ugent.be)

H. Nguyen-Xuan

CIRTech Institute, Ho Chi Minh City University of Technology (HUTECH), 70000 Ho Chi Minh City, Vietnam

M. Abdel Wahab

Soete Laboratory, Faculty of Engineering and Architecture, Ghent University, 9000 Ghent, Belgium

reduce the phenomena of residual stress components, de-bonding, and delamination. Besides, relying on technology innovation based on 3D printing [2, 3], promising to produce the functionally graded (FG) structures more efficiently. Through this technology, FGM can become more prevalent in practical engineering by its benefits. Therefore, the FGM failure must be exploited theoretically before manufacturing.

Additionally, the vital task of the solid mechanics field is initial and growth crack prediction in a solid. This task can be solved by the fracture mechanics field concentrating on studying the failure modes of the structures under multiple loading types. Numerous methods have been introduced by many previous works [4–6] for a prediction of fracture failure mechanisms correctly. Using the stress intensity, the stress intensity factor (SIF) concept was proposed to evaluate the energy of the crack tip zone. Two categories, discrete and smeared approaches, were implemented to study damage behaviors under a discontinuous zone. An enriched displacement variable formulation within enriched elements, using a partition of unity method (PUM), is proposed as a primary idea for such enriched formulation family [7–10], which plays an outstanding role in the discrete approaches. However, crack merging and branching challenges, tracking the crack pattern topology, and even crack initiation still exists, particularly in three-dimensional fracture problems.

On the contrary, Miehe [11] firstly proposed a phase-field approach, as a smeared method, to deal with the above issues. Without any criterion, the phase-field approach effectively predicts a complex failure, including crack branching, kinking, and nucleation [12–14]. It recently became the most attractive method for researchers because it works well in multiple cracks, cracks merging [15]. A scalar auxiliary variable is investigated for the phase-field approach in implementing discontinuous zones. Typically, the phase-field approach is considered as a coupled-field problem that contains both displacement and phase-field variables.

Recently, the phase-field model was proved to be a promising method for investigating the damage mechanisms of composite materials, such as laminated composite materials [16–18], fiber-reinforced composite materials [19, 20]. Some research uses the phase-field model to compute the damage on FGM structures [21, 22]. However, their limitation is on a family of  $C^0$ -continuity elements limited, for instance, a finite element approach, which was shown less accuracy than higher-order approaches.

Regarding a higher-order approximated method, isogeometric analysis (IGA) [23] uses a NURBS function as a basis function for the finite element approach. It was built on higher-order continuity elements, which help to increase the accuracy of the solution. A VUKIMS algorithm [24] was used to build a local refinement mesh to reduce the unnecessary elements for the computation. Our previous study successfully applied IGA with the VUKIMS algorithm to compute crack propagation in a homogeneous brittle material [25]. It helps the IGA approach to overcome the computational cost to display accurately crack pattern topology. It requires tiny elements used for the damaged areas. Besides, IGA has been a useful computational tool for the FGM structures under static and dynamic analysis [26]. IGA can provide an ultra-accurate solution with a coarse mesh level for the FGM structures by using higher-order NURBS basis functions.

This paper aims to extend this phase-field formulation success by combining IGA with the VUKIMS algorithm, as a locally refined algorithm, from the homogenous material to the functionally graded material. A tension single notched edge plate is considered to demonstrate the accuracy and efficiency of current solutions compared with the previous work.

## 2 A NURBS-Based Formulation for a Phase-Field Model

### 2.1 NURBS Basis Functions

A NURBS geometry (or NURBS surface)  $(\mathbf{S}(\xi, \eta))$ , which was built by bivariate NURBS basis functions  $(R_{i,j}^{p,q}(\xi, \eta))$  on parametric space  $\xi$  and  $\eta$ , can be expressed in [27] more detailed formulations

$$\mathbf{S}_{\xi,\eta} = \sum_{i=1}^n \sum_{j=1}^m R_{i,j}^{p,q}(\xi, \eta) \mathbf{P}_{i,j} \quad (1)$$

where  $\mathbf{P}_{i,j}$  stands for the  $n \times m$  control points. The bivariate NURBS basis functions are determined on  $\Xi$  and  $\mathbf{H}$  knot vectors corresponding to  $\xi$ - and  $\eta$ -coordination, as given as

$$R_{i,j}^{p,q}(\xi, \eta) = \frac{w_{i,j} N_{i,p}(\xi) M_{j,q}(\eta)}{\sum_{i=1}^n \sum_{j=1}^m w_{i,j} N_{i,p}(\xi) M_{j,q}(\eta)} \quad (2)$$

where  $w_{i,j}$  is the weight parameter of control points  $\mathbf{P}_{i,j}$  while  $N_{i,p}$ , and  $M_{j,q}$  are B-spline basis functions on each parametric coordination. For instance, the B-spline basis function is built from a non-decrease, open and non-uniform knot vector  $\Xi = \{\xi_1, \xi_2, \dots, \xi_{n+p+1}\}$ ,  $n$  control points, and  $p$  basis function order, as depicted by the Cox-de Boor formulation as.

In the case of zero-order,  $p = 0$ ,

$$N_{i,0}(\xi) = \begin{cases} 1 & \text{if } \xi_i \leq \xi < \xi_{i+1} \\ 0 & \text{otherwise} \end{cases} \quad (3)$$

and

$$N_{i,p}(\xi) = \frac{\xi - \xi_i}{\xi_{i+p} - \xi_i} N_{i,p-1}(\xi) + \frac{\xi_{i+p+1} - \xi}{\xi_{i+p+1} - \xi_{i+1}} N_{i+1,p-1}(\xi) \quad (4)$$



where,  $1 \leq i \leq n + p$ ,  $p \geq 1$ , and  $\frac{0}{0}$  is an assumption of zero number.

Typically, the displacement and phase-field variables are used to simulate a crack propagation problem by using IGA and phase-field approach, as expressed as

$$\mathbf{u}(\xi, \eta) \approx \hat{\mathbf{u}}(\xi, \eta) = \sum_{i=1}^n \sum_{j=1}^m R_{i,j}^{p,q}(\xi, \eta) \cdot \mathbf{u}_{i,j} \quad (5)$$

$$\phi(\xi, \eta) \approx \hat{\phi}(\xi, \eta) = \sum_{i=1}^n \sum_{j=1}^m R_{i,j}^{p,q}(\xi, \eta) \cdot \phi_{i,j} \quad (6)$$

where  $R_{i,j}^{p,q}(\xi, \eta)$  is a NURBS basis function,  $\mathbf{u}_{i,j}$  and  $\phi_{i,j}$  are phase-field and displacement variables corresponding to control point  $\mathbf{P}_{i,j}$ , respectively.

## 2.2 Phase-field Formulation

With the phase-field approach, governing balance equations, as described as a strong form, can be expressed for a coupled-field problem of the displacement and phase-field variables as follows:

$$\nabla \cdot \boldsymbol{\sigma} + \mathbf{b} = 0 \text{ on } \Omega \quad (7)$$

$$\mathcal{G}_C(\mathbf{x}) \left[ \frac{\phi}{l_0} - l_0 \Delta \phi \right] - 2(1 - \phi) \mathcal{H}(\boldsymbol{\varepsilon}, \mathbf{x}) = 0 \text{ on } \Omega \quad (8)$$

with the Neumann-type boundary conditions:

$$\boldsymbol{\sigma} \cdot \mathbf{n} = \mathbf{t} \text{ on } \partial\Omega_t \text{ and } \nabla \phi \cdot \mathbf{n} = 0 \text{ on } \partial\Omega \quad (9)$$

where  $\mathbf{t}$  is the traction force on the boundary  $\partial\Omega_t$  and  $\mathbf{b}$  is the body force. A history-field parameter of  $\mathcal{H} := \max \psi_e(\boldsymbol{\varepsilon}, \mathbf{x})$  defined as a maximum value of strain energy. For loading and unloading conditions, this parameter must satisfy the Karush–Kuhn–Tucker conditions [28], as follows:

$$\psi_e - \mathcal{H} \leq 0, \dot{\mathcal{H}} \geq 0, \dot{\mathcal{H}}(\psi_e - \mathcal{H}) = 0 \quad (10)$$

where the strain energy  $\psi_e$  is computed by

$$\psi_e(\boldsymbol{\varepsilon}, \mathbf{x}) = \frac{\lambda(\mathbf{x})}{2} (\text{tr}(\boldsymbol{\varepsilon}))^2 + \mu(\mathbf{x})(\boldsymbol{\varepsilon} : \boldsymbol{\varepsilon}) \quad (11)$$

In this study, an isotropic phase-field formulation is used. This work defined the stress tensor, which is given as

$$\boldsymbol{\sigma} = g(\phi) \frac{\partial \psi_{e0}}{\partial \boldsymbol{\varepsilon}} = g(\phi) \mathbf{D} : \boldsymbol{\varepsilon} \quad (12)$$

where a quadratic degradation function is defined  $g(\phi) = (1 - \phi)^2$ . Typically,  $\phi$  is set equal to 1 to describe a fully broken domain.  $\mathbf{D}$  is a tangent linear elastic tensor of the material. The strain tensor  $\boldsymbol{\varepsilon}$  is assumed as an infinitesimal strain tensor, as defined as  $\boldsymbol{\varepsilon} = \text{symm}[\nabla \mathbf{u}]$ .

From the strong form equations in Eqs. (7)–(9), the weak form equations can be expressed by applying variational principles, as given as

$$\int_{\Omega} \boldsymbol{\sigma} \delta \boldsymbol{\varepsilon} d\Omega = \int_{\partial\Omega_i} \mathbf{t} \cdot \delta \mathbf{u} d\Gamma + \int_{\Omega} \mathbf{b} \cdot \delta \mathbf{u} d\Omega \quad (13)$$

$$\int_{\Omega} \left\{ \mathcal{G}_C \left[ \frac{1}{l_0} \phi \delta \phi + l_0 \nabla \phi \cdot \nabla \delta \phi \right] - 2(1 - \phi) \mathcal{H} \delta \phi \right\} d\Omega = 0 \quad (14)$$

The approximations of the displacement  $\mathbf{u}$  and the phase-field  $\phi$  variables are given as

$$\mathbf{u} = \sum_{i=1}^m R_i^{\mathbf{u}} \mathbf{u}_i, \quad \phi = \sum_{i=1}^m R_i \phi_i \quad (15)$$

where  $m$  stands for the control point number on each element. Using the IGA approach,  $R_i$  is defined as a NURBS basis function, as given in Eq. (2), corresponding to control point  $i$ th on the NURBS surface. The shape function matrix is expressed as follows:

$$R_i^{\mathbf{u}} = \begin{bmatrix} R_i & 0 \\ 0 & R_i \end{bmatrix} \quad (16)$$

The derivative of the displacement and phase-field variables are given as

$$\boldsymbol{\varepsilon} = \sum_{i=1}^m \mathbf{B}_i^{\mathbf{u}} \mathbf{u}_i \quad \text{and} \quad \nabla \phi = \sum_{i=1}^m \mathbf{B}_i^{\phi} \phi_i \quad (17)$$

where derivative matrices are depicted as

$$\mathbf{B}_i^{\mathbf{u}} = \begin{bmatrix} R_{i,x} & 0 & R_{i,y} \\ 0 & R_{i,y} & R_{i,x} \end{bmatrix}^T, \quad \mathbf{B}_i^{\phi} = [R_{i,x} \ R_{i,y}]^T \quad (18)$$

The virtual of both fields and their gradient tensor in Eqs. (13) and (14) can be computed as

$$\begin{aligned}\delta \mathbf{u} &= \sum_{i=1}^m R_i^{\mathbf{u}} \delta \mathbf{u}_i \text{ and } \delta \phi = \sum_{i=1}^m R_i \delta \phi_i \\ \delta &= \sum_{i=1}^m \mathbf{B}_i^{\mathbf{u}} \delta \mathbf{u}_i \text{ and } \nabla \delta \phi = \sum_{i=1}^m \mathbf{B}_i^{\phi} \delta \phi_i\end{aligned}\quad (19)$$

The variational equilibrium equation of the external and internal work increments for crack propagation using phase-field formulation is given for a quasi-static problem as

$$\delta W_{int} - \delta W_{ext} = 0 \quad (20)$$

where  $\delta W_{int}$  and  $\delta W_{ext}$  which are under the variational form of internal and external energies can be expressed as

$$\begin{aligned}\delta W_{int} &= \int_{\Omega} \frac{\mathcal{G}_C}{l_0} \phi \delta \phi d\Omega + \int_{\Omega} \mathcal{G}_C l_0 \nabla \phi \cdot \nabla \delta \phi d\Omega \\ &\quad + \int_{\Omega} -2(1-\phi) \mathcal{H} \delta \phi d\Omega + \int_{\Omega} \boldsymbol{\sigma} \delta \boldsymbol{\varepsilon} d\Omega\end{aligned}\quad (21)$$

$$\delta W_{ext} = \int_{\Omega} \mathbf{b} \cdot \delta \mathbf{u} d\Omega + \int_{\partial \Omega_t} \mathbf{t} \cdot \delta \mathbf{u} d\Gamma \quad (22)$$

The variational equilibrium equation in Eq. (20) is derived as

$$\begin{aligned}&\int_{\Omega} \frac{\mathcal{G}_C}{l_0} \phi \delta \phi d\Omega + \int_{\Omega} \mathcal{G}_C l_0 \nabla \phi \cdot \nabla \delta \phi d\Omega + \int_{\Omega} \boldsymbol{\sigma} \delta \boldsymbol{\varepsilon} d\Omega \\ &= \int_{\Omega} \mathbf{b} \cdot \delta \mathbf{u} d\Omega + \int_{\partial \Omega_t} \mathbf{t} \cdot \delta \mathbf{u} d\Gamma + 2 \int_{\Omega} (1-\phi) \psi_e \delta \phi d\Omega\end{aligned}\quad (23)$$

In this study, a staggered scheme is used to solve the nonlinear problem was first investigated by Miehe [29]. A displacement control Newton–Raphson scheme is proposed to minimize the internal potential energy.

The linear algebraic equation system can be computed as follows:

$$\begin{bmatrix} \mathbf{K}_{ij}^{\mathbf{u}\mathbf{u}} & 0 \\ 0 & \mathbf{K}^{\phi\phi} \end{bmatrix} \begin{Bmatrix} \Delta \mathbf{u} \\ \Delta \phi \end{Bmatrix} = \begin{Bmatrix} -\mathbf{r}_i^{\mathbf{u}} \\ -\mathbf{r}_i^{\phi} \end{Bmatrix} \quad (24)$$

The tangent stiffness matrices and the residual vectors of the displacement and phase-field variables are given as

$$\mathbf{K}_{ij}^{\phi\phi} = \frac{\partial r_i^\phi}{\partial \phi_j} = \int_{\Omega} \left\{ \mathcal{G}_C l_0 (\mathbf{B}_i^\phi)^T \mathbf{B}_j^\phi + \left[ 2\mathcal{H} + \frac{\mathcal{G}_C}{l_0} \right] N_i N_j \right\} d\Omega \quad (25)$$

$$\mathbf{K}_{ij}^{\mathbf{u}\mathbf{u}} = \frac{\partial \mathbf{r}_i^{\mathbf{u}}}{\partial \mathbf{u}_j} = \int_{\Omega} (\mathbf{B}_i^{\mathbf{u}})^T (1 - \phi)^2 \mathbf{D} \mathbf{B}_j^{\mathbf{u}} d\Omega \quad (26)$$

$$r_i^\phi = \int_{\Omega} \left\{ \mathcal{G}_C \left[ \frac{1}{l_0} N_i \phi + l_0 (\mathbf{B}_i^\phi)^T \nabla \phi \right] - 2(1 - \phi) \mathcal{H} N_i \right\} d\Omega \quad (27)$$

$$\mathbf{r}_i^{\mathbf{u}} = \int_{\Omega} (\mathbf{B}_i^{\mathbf{u}})^T \boldsymbol{\sigma} d\Omega - \int_{\Omega} (\mathbf{N}_i^{\mathbf{u}})^T \mathbf{b} d\Omega - \int_{\partial\Omega_t} (\mathbf{N}_i^{\mathbf{u}})^T \mathbf{t} d\partial\Omega_t \quad (28)$$

An elasticity material tensor  $\mathbf{D}$  depends on point material location  $\mathbf{x}$ , as given as:

$$\mathbf{D}(\mathbf{x}) = \frac{E(\mathbf{x})}{(1 + \nu(\mathbf{x}))(1 - 2\nu(\mathbf{x}))} \begin{bmatrix} 1 - \nu(\mathbf{x}) & \nu(\mathbf{x}) & 0 \\ \nu(\mathbf{x}) & 1 - \nu(\mathbf{x}) & 0 \\ 0 & 0 & \frac{1 - 2\nu(\mathbf{x})}{2} \end{bmatrix} \quad (29)$$

### 2.3 Functionally Graded Materials

Generally, in a functionally graded material (FGM), the material property distributions are graded by changing volume fraction functions. Typically, the FGM is a composition of two distinct materials. It changes from 100% of the first compound volume fraction to the second. It has the ability of smooth and continuous distribution concerning spatial directions by using a mixture rule. For instance, the volume fractions of the first and the second materials with the material gradation along with the  $y$ -axis corresponding to the top and the bottom edge,  $V_t$  and  $V_b$ , respectively, as shown in Fig. 1, are given as

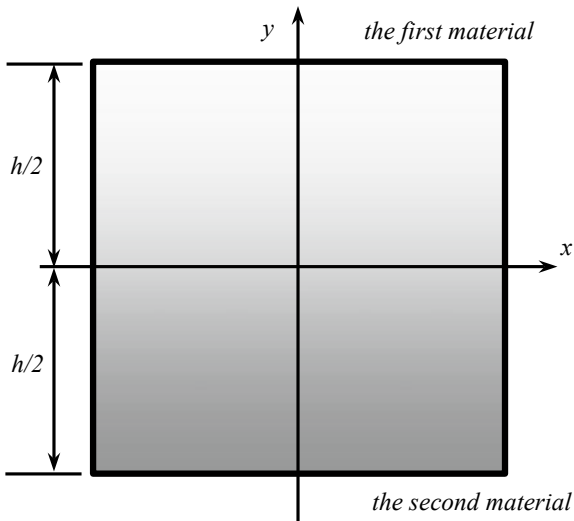
$$V_t = \left( \frac{1}{2} + \frac{y}{h} \right)^n, \quad V_b = 1 - V_t \quad (30)$$

where  $n$  is a power parameter,  $h$  is the vertical edge length of the plate.

Mori and Tanaka have proposed a model in order to define graded functions that satisfy continuous matrix and randomly particulate phase distribution, namely the Mori–Tanaka scheme. The effective parameters of bulk modulus ( $K$ ) and shear modulus ( $\mu$ ) are expressed as

$$\frac{K - K_b}{K_t - K_b} = \frac{V_t}{1 + V_b \frac{K_t - K_b}{K_b + 4/3\mu_b}}, \quad \frac{\mu - \mu_b}{\mu_t - \mu_b} = \frac{V_t}{1 + V_b \frac{\mu_t - \mu_b}{\mu_b + f_1}} \quad (31)$$

**Fig. 1** A distributed material property of FGM along a y-axis



where  $f_1 = \frac{\mu_b(9K_b+8\mu_b)}{6(K_b+2\mu_b)}$ ,  $K_t$  and  $K_b$  are bulk modulus, and  $\mu_t$  and  $\mu_b$  are shear modulus of the first and the second materials, which correspond to the top and bottom edges. Hence, the remaining parameters, including Young’s modulus ( $E$ ), Poisson’s ratio ( $\nu$ ), and Lamé’s first parameter ( $\lambda$ ), are defined as

$$E = \frac{9K\mu}{3K + \mu}, \nu = \frac{3K - 2\mu}{2(3K + \mu)}, \text{ and } \lambda = K - \frac{2\mu}{3} \tag{32}$$

In terms of the criterion for fracture, a critical energy release rate  $\mathcal{G}_C$  is computed from the fracture toughness,  $K_{IC}$  by

$$\mathcal{G}_C = \frac{K_{IC}^2}{E'} \tag{33}$$

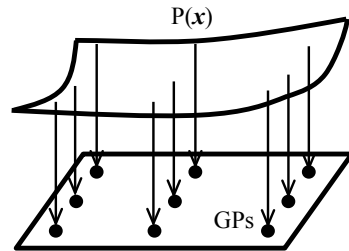
where  $E' = E/(1 - \nu^2)$  is used for plane strain problem while  $E' = E$  is used for plane stress problem. In FGM,  $\mathcal{G}_C$  variation is assumed as a graded function by using rule mixture function depicted as

$$\mathcal{G}_C = \mathcal{G}_{Ct}V_t + \mathcal{G}_{Cb}V_b \tag{34}$$

where  $\mathcal{G}_{Ct}$  and  $\mathcal{G}_{Cb}$  are computed for the first and the second material on the top and bottom edge, respectively.

In order to implement the material gradation in the structure, graded elements are used by storing the material properties and fracture parameters on the Gauss points of the elements, as described in Fig. 2. In this study, a full of  $(p + 1) \times (q + 1)$  Gauss–Legendre quadrature, located on each element, is used to evaluate an integral

**Fig. 2** Graded elements for FGM



approximation on an element. Here the polynomial orders,  $p$  and  $q$ , of basis functions correspond to bidirectional NURBS surface.

### 3 Numerical Results

#### 3.1 Verification Test of Tension Single Edge Notched Plate

This section demonstrates the accuracy of the current method by considering an alumina  $\text{Al}_2\text{O}_3$  / zirconia  $\text{ZrO}_2$  functionally graded square plate. The plate has a side length of 1 mm. The plate is assumed as plane strain conditions. On the left side of the plate, it has a single edge notched plate with a length of 0.5 mm and is applied a tensile loading, as illustrated in Fig. 3. The rule of mixtures for this problem uses the Mori–Tanaka scheme described in Eq. (31). Table 1 describes the elastic and fracture parameters that are chosen the same as Hadraba [30]. Besides, a length-scale number of  $l_0 = 0.003$  mm was chosen for this section.

In order to prove the advantages of non-conforming mesh multipatches IGA or local mesh compared with traditional FEM, the first test, which is the material gradation along the  $y$ -axis with 100% of  $\text{Al}_2\text{O}_3$  at the bottom and 100% of  $\text{ZrO}_2$  at the top of the plate, is considered with the power-law exponent parameter of  $n = 1$ . The top edge is applied an incremental monotonic displacement vertically was  $\Delta u = 10$  nm for the first 130 loading steps, and  $\Delta u = 0.1$  nm for the subsequent loading steps to split the broken plate completely.

Firstly, both global and local refinement mesh of linear B-spline elements is validated in the present solution by Hirshikesh [21], who used the FE approach with triangular elements (T3), as shown in Fig. 5. The coarsest mesh and their global and local refinement mesh, using 12 patches to model this problem, are illustrated in Fig. 4a with a length-scale number of 0.0075 mm. To implement the horizontally pre-existing crack, two pairs of patches (2–3 and 6–7) are disconnected from their variables on the interfaces. Because the predicted crack will propagate horizontally, the patch numbers of 6, 7, 10, and 11 chosen to refine in order to build a local mesh with a size of an element of  $h = l_0$  are shown in Fig. 4c, while Fig. 4b depicts a global mesh that has all elements have the same effective size  $h = l_0$ . There is a two-level

**Fig. 3** A description of the geometry and boundary conditions

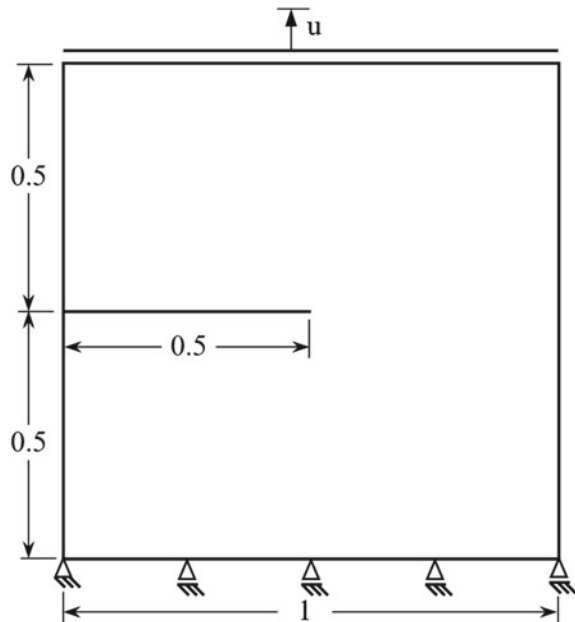


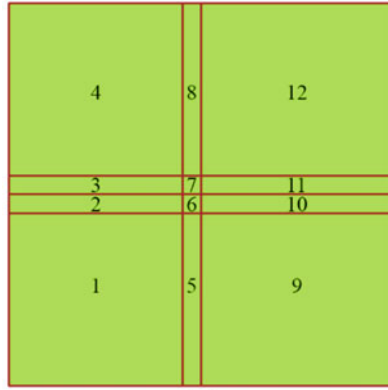
**Table 1** Material properties of alumina  $\text{Al}_2\text{O}_3$  and zirconia  $\text{ZrO}_2$

	$\text{Al}_2\text{O}_3$	$\text{ZrO}_2$
$E(\text{GPa})$	380	210
$\nu$	0.26	0.31
$K_{\text{IC}} (\text{MPa}\cdot\text{m}^{1/2})$	5.2	9.6

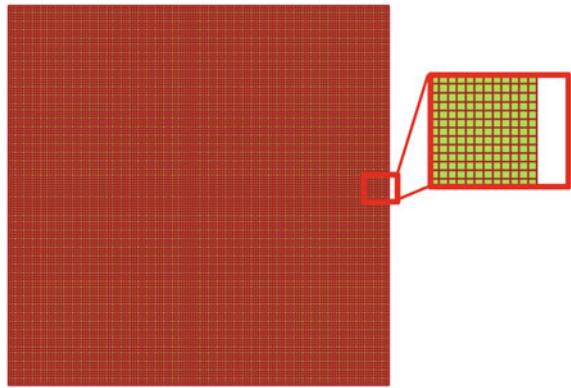
mesh of the effective element size of  $h = l_0$  and  $h = l_0/2$  considered in this step. It should be noted that the linear B-spline element is a particular case of a Q4 element in FEM which shows more accuracy than the triangular one in the case of the same numbers of elements.

In this first test, the linear B-spline element of four cases of the mesh with different effective sizes and types of mesh are used to verify the present solution with Hirshikesh [21] in the case of the power-law exponent parameter  $n = 1$ . The computational time and the numbers of a degree of freedoms shown in Table 2 are much different, although Fig. 5a shows minor deviations in both global and local mesh cases. Significantly, computational time and the numbers of the degree of freedoms of the local refinement mesh are much less than the global one. In particular, the computational time of local refinement mesh can speed up is over 12 times and 16 times with the effective size of  $h = l_0$  and  $h = l_0/2$ , respectively. In addition, the required memory of the computer can be reduced due to the DOF numbers being reduced over ten times and 14 times corresponding to two of the effective size level. Hence, the obtained result can reduce the computational cost while maintaining the solution's accuracy thanks to the local refinement mesh. The time computing

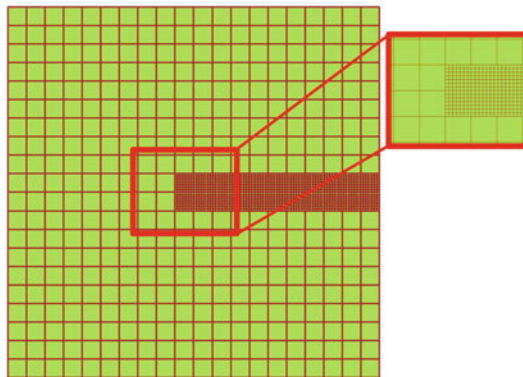
**Fig. 4** The multipatch mesh of the square plate: **a** the coarsest mesh, **b** global, and **c** local refinement mesh with the effective size of  $h = l_0$  with length-scale  $l_0 = 0.0075$  mm



(a)

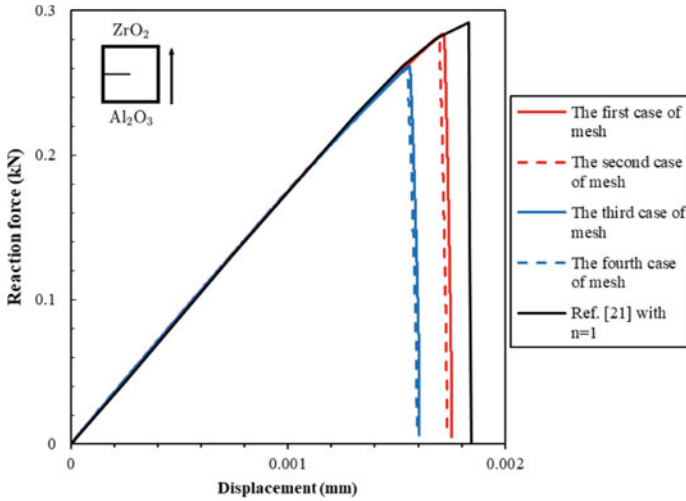


(b)

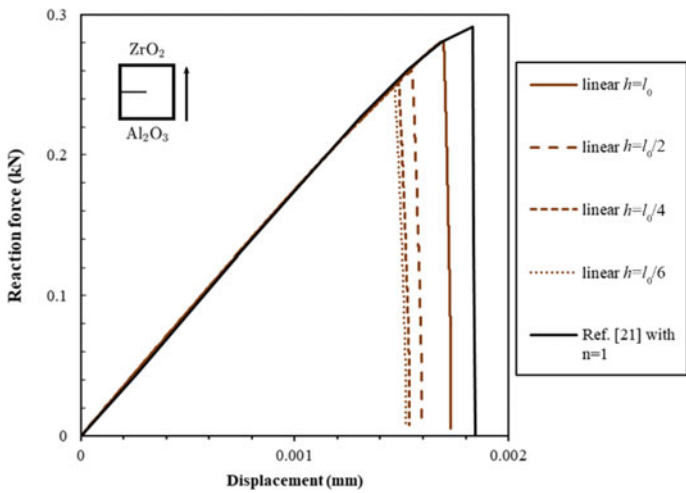


(c)





(a) four cases of the mesh



(b) different effective sizes of local refinement mesh

**Fig. 5** Reaction force versus displacement for linear B-spline elements

**Table 2** DOF numbers and time consumption in the several cases of linear B-spline elements

Case of mesh	Type of refinement mesh	Effective element size	DOF numbers	Time consumption (min)
1	global	$h = l_0$	55,488	1317
2	local	$h = l_0$	5148	106
3	global	$h = l_0/2$	218,700	3967
4	local	$h = l_0/2$	15,000	236

**Table 3** DOF numbers and time consumption in the several cases of higher-order B-spline elements with local refinement mesh

Case of mesh	Order approach	Effective element size	DOF numbers	Time consumption (min)
5	linear	$h = l_0/4$	51,228	690
6	linear	$h = l_0/6$	110,232	1446
7	cubic	$h = l_0$	7176	420
8	cubic	$h = l_0/2$	18,084	1164
9	cubic	$h = l_0/4$	56,376	3934
10	quartic	$h = l_0$	8298	901
11	quartic	$h = l_0/2$	19,734	2550

values of all results are evaluated in the same computer using AMD Ryzen 7 2700X processor until the crack separates the plate.

It should be noted that the obtained results of the first and the second cases of the mesh with the effective size of  $h = l_0$  are in good agreement with Hirshikesh [21]. However, the critical force point decreases when the effective size is set to half of  $l_0$ , including the third and fourth mesh (please see Fig. 5a). A convergence test is considered by using four different sizes of the linear B-spline elements, including  $h = l_0, l_0/2, l_0/4,$  and  $l_0/6$  (please see Fig. 5b). Hence, we assume that when using the effective size  $h = l_0/6$ , the solution is a converged result. It is easy to see that the used number of DOFs of this solution is high, approximately 110,232-DOFs, causing a large memory consuming and costly computational time. Therefore, a higher-order B-spline element can be used to gain a higher accuracy for the solutions than the linear one.

Next, the higher orders of B-spline element, using local refinement mesh with finer mesh, are considered to obtain more exact solutions. The DOF numbers and the time consumption of different meshes are shown in Table 3, while Fig. 6 shows the critical force points of these meshes. As a result, to balance the solutions' accuracy and computational cost, the cubic B-spline element is suitable for FGM structures in the following analyses with effective size  $h = l_0/2$ .

### 3.2 A Functionally Graded Material Square Plate

This section shows the effects of a power-law exponential parameter  $n$  in Eq. (30) on critical force points of the FGM plate. The distributed material properties are shown in Fig. 7. The cubic B-spline element is used to obtain the solutions for all analyses with an effective size  $h = l_0/2$ .

Curves of reaction force versus displacement result are illustrated in Fig. 8. The results have been confirmed by Hirshikesh's solutions [21]. However, the current predictions of critical force points are lower than those in Ref. [21]. The differences

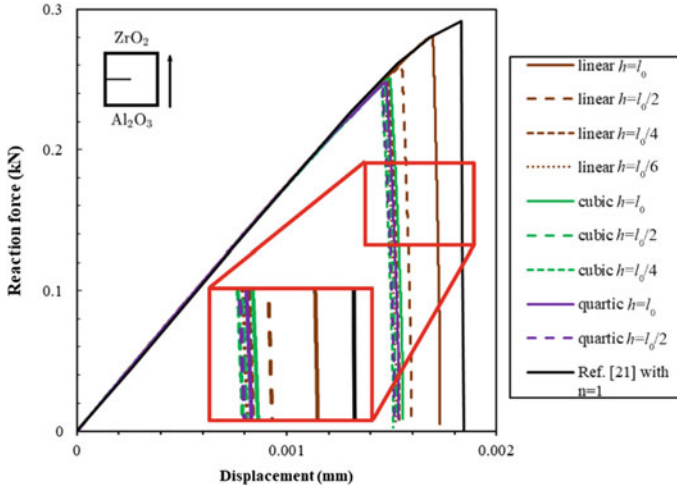


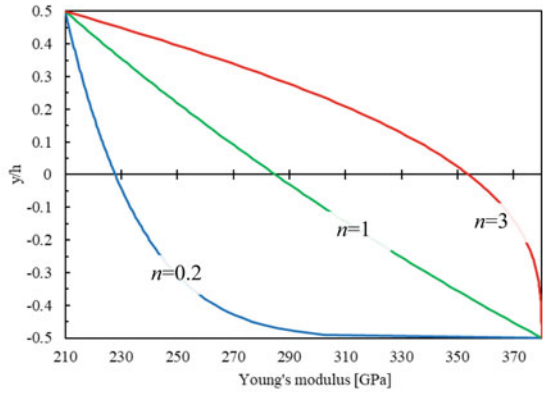
**Fig. 6** Curves of reaction force versus displacement for different mesh

occur because Hirshikesh's approach uses T3 elements shown to be less accurate than cubic B-spline elements for the current approach. However, the trends in most cases of the different power-law exponent parameters are the same with Hirshikesh [21]. Besides, the predicted crack path is illustrated in Fig. 9 with local refinement mesh of the cubic B-spline elements with the power-law exponent parameter  $n = 1$  and the effective size  $h = l_0/2$ . As a result, using the length-scale parameter  $l_0 = 0.003$  mm, the crack topology is guaranteed as a highly accurate solution.

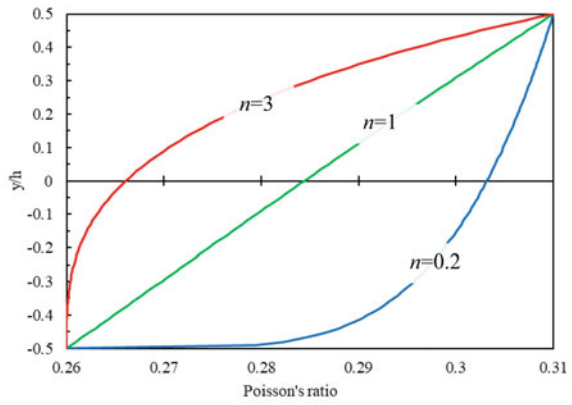
## 4 Conclusion

This study demonstrated the phase-field model as a practical computational tool to solve the damage problem for an FGM plate. The proposed approach is a combination of IGA and VUKIMS algorithms to build a locally refined mesh. This algorithm helps the proposed approach to overcome the computational cost caused by phase-field approximation. Moreover, the convergence rate of the numerical solutions can be increased significantly by using higher-order B-spline elements. As a result, we demonstrated that the cubic B-spline element is good for balancing the achieved accuracy and the computational cost with the effective size  $h = l_0/2$ . The previous study confirmed the current numerical result accurately. Therefore, the phase-field approach is promising to analyze crack propagation for the complex behavior of advanced materials and complicated geometry domain in engineering practice.

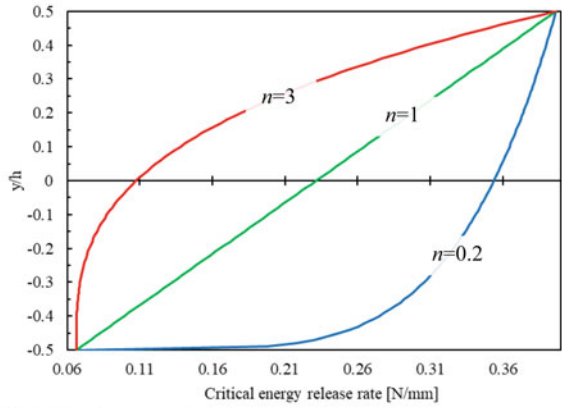
**Fig. 7** The distributed material properties



(a) Young's modulus



(b) Poisson's ratio



(c) Critical energy release rate

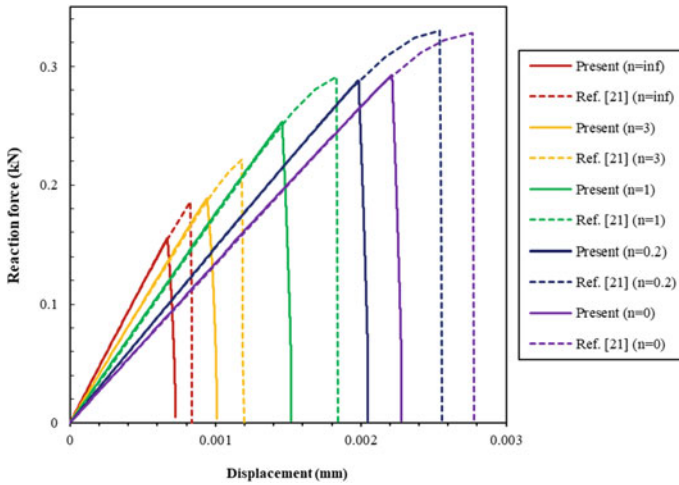
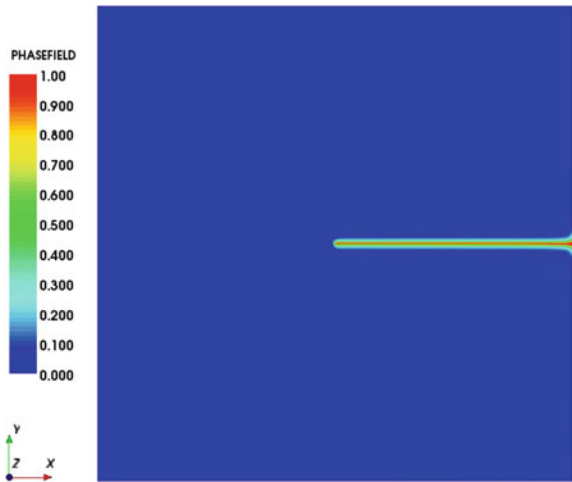


Fig. 8 Reaction force versus displacement for various power-law indexes

Fig. 9 The predicted crack path of the tension plate with the power-law exponent parameter  $n = 1$



**Acknowledgements** The authors acknowledge VLIR-UOS TEAM Project’s financial support, VN2017TEA454A103, “An innovative solution to protect Vietnamese coastal riverbanks from floods and erosion”, funded by the Flemish Government.

## References

1. Koizumi M (1997) FGM activities in Japan. *Compos Part B-Eng* 28:1–4
2. Craveiro F, Nazarian S, Bartolo H, Bartolo PJ, Pinto Duarte J (2020) An automated system for 3D printing functionally graded concrete-based materials. *Additive Manuf* 33. <https://doi.org/10.1016/j.addma.2020.101146>
3. Shang C, Wang C, Li C, Yang G, Xu G, You J (2020) Eliminating the crack of laser 3D printed functionally graded material from TA15 to Inconel718 by base preheating. *Opt Laser Technol* 126. <https://doi.org/10.1016/j.optlastec.2020.106100>
4. Griffith AA (1921) VI. The phenomena of rupture and flow in solids. *Philosophical transactions of the royal society of London. Ser Contain Papers Math Phys Char* 221:163–198
5. Francfort GA, Marigo J-J (1998) Revisiting brittle fracture as an energy minimization problem. *J Mech Phys Solids* 46:1319–1342. [https://doi.org/10.1016/S0022-5096\(98\)00034-9](https://doi.org/10.1016/S0022-5096(98)00034-9)
6. Bourdin B, Francfort GA, Marigo J-JJOE (2008) The variational approach to fracture 91:5–148
7. Moes N, Dolbow J, Belytschko T (1999) A finite element method for crack growth without remeshing. *J Numer Methods Eng* 46:131–150
8. Nguyen NT, Bui TQ, Zhang C, Truong TT (2014) Crack growth modeling in elastic solids by the extended meshfree Galerkin radial point interpolation method. *Eng Anal Boundary Elem* 44:87–97
9. Yadav A, Godara R, Bhardwaj G (2020) A review on XIGA method for computational fracture mechanics applications. *Eng Fract Mech* 107001
10. Peake MJ, Trevelyan J, Coates G (2013) Extended isogeometric boundary element method (XIBEM) for two-dimensional Helmholtz problems. *Comput Methods Appl Mech Eng* 259:93–102. <https://doi.org/10.1016/j.cma.2013.03.016>
11. Miehe C, Welschinger F, Hofacker M (2010) Thermodynamically consistent phase-field models of fracture: Variational principles and multi-field FE implementations. *Int J Numer Meth Eng* 83:1273–1311. <https://doi.org/10.1002/nme.2861>
12. Schlüter A, Willenbücher A, Kuhn C, Müller R (2014) Phase field approximation of dynamic brittle fracture. *Comput Mech* 54:1141–1161. <https://doi.org/10.1007/s00466-014-1045-x>
13. Borden MJ, Verhoosel CV, Scott MA, Hughes TJR, Landis CM (2012) A phase-field description of dynamic brittle fracture. *Comput Methods Appl Mech Eng* 217–220:77–95. <https://doi.org/10.1016/j.cma.2012.01.008>
14. Ren HL, Zhuang XY, Anitescu C, Rabczuk T (2019) An explicit phase field method for brittle dynamic fracture. *Comput Struct* 217:45–56. <https://doi.org/10.1016/j.compstruc.2019.03.005>
15. Deoekar S, Vemaganti K (2017) A computational study of the dynamic propagation of two offset cracks using the phase field method. *Eng Fract Mech* 182:303–321. <https://doi.org/10.1016/j.engfracmech.2017.08.003>
16. Patil RU, Mishra BK, Singh IV, Bui TQ (2018) A new multiscale phase field method to simulate failure in composites. *Adv Eng Softw* 126:9–33. <https://doi.org/10.1016/j.advengsoft.2018.08.010>
17. Alessi R, Freddi F (2017) Phase-field modelling of failure in hybrid laminates. *Compos Struct* 181:9–25
18. Zhang P, Feng Y, Bui TQ, Hu X, Yao W (2020) Modelling distinct failure mechanisms in composite materials by a combined phase field method. *Compos Struct* 232:111551
19. Yin BB, Zhang LW (2019) Phase field method for simulating the brittle fracture of fiber reinforced composites. *Eng Fract Mech* 211:321–340. <https://doi.org/10.1016/j.engfracmech.2019.02.033>
20. Zhang P, Hu X, Bui TQ, Yao W (2019) Phase field modeling of fracture in fiber reinforced composite laminate. *Int J Mech Sci* 161:105008
21. Hirshikesh, Natarajan S, Annabattula RK, Martínez-Pañeda E (2019) Phase field modelling of crack propagation in functionally graded materials. *Compos Part B: Eng* 169:239–248. <https://doi.org/10.1016/j.compositesb.2019.04.003>
22. Torabi J, Ansari R (2020) Crack propagation in functionally graded 2D structures: A finite element phase-field study. *Thin-Walled Struct* 151. <https://doi.org/10.1016/j.tws.2020.106734>

23. Hughes TJR, Cottrell JA, Bazilevs Y (2005) Isogeometric analysis: CAD, finite elements, NURBS, exact geometry and mesh refinement. *Comput Methods Appl Mech Eng* 194:4135–4195. <https://doi.org/10.1016/j.cma.2004.10.008>
24. Coox L, Greco F, Atak O, Vandepitte D, Desmet W (2017) A robust patch coupling method for NURBS-based isogeometric analysis of non-conforming multipatch surfaces. *Comput Methods Appl Mech Eng* 316:235–260. <https://doi.org/10.1016/j.cma.2016.06.022>
25. Nguyen KD, E.Augarde C, Coombs WM, Nguyen-Xuan H, Abdel-Wahab M (2020) Non-conforming multipatches for NURBS-based finite element analysis of higher-order phase-field models for brittle fracture. *Eng Fract Mech* 235. <https://doi.org/10.1016/j.engfractmech.2020.107133>
26. Nguyen KD, Nguyen-Xuan H (2015) An isogeometric finite element approach for three-dimensional static and dynamic analysis of functionally graded material plate structures. *Compos Struct* 132:423–439. <https://doi.org/10.1016/j.compstruct.2015.04.063>
27. Piegel L, Tiller W (2012) *The NURBS book*. Springer Science & Business Media
28. Singh N, Verhoosel CV, de Borst R, van Brummelen EH (2016) A fracture-controlled path-following technique for phase-field modeling of brittle fracture. *Finite Elem Anal Des* 113:14–29. <https://doi.org/10.1016/j.finel.2015.12.005>
29. Miehe C, Hofacker M, Welschinger F (2010) A phase field model for rate-independent crack propagation: robust algorithmic implementation based on operator splits. *Comput Methods Appl Mech Eng* 199:2765–2778. <https://doi.org/10.1016/j.cma.2010.04.011>
30. Hadraba H, Maca K, Cihlar J (2004) Electrophoretic deposition of alumina and zirconia. *Ceram Int* 30:853–863. <https://doi.org/10.1016/j.ceramint.2003.09.020>

# Superfluid Core Cooling Influence in the Braking Index of Young Pulsars



Carlos Frajuca  and and Fabio da Silva Bortoli 

**Abstract** A young pulsar is a neutron star that rotates and, as it has a high magnetic field that provokes emission of electromagnetic radiation on its magnetic poles, pulsates if the emission direction is aligned with Earth. The frequencies of these electromagnetic pulses decrease with time. This decrease of frequency is quantified by a quantity called braking index which symbol is  $n$ . There is a canonical model to describe this process, in this model considers the pulsar magnetic a rotating dipole. In this case  $n$  is equal to 3 in theory. In general observational data from pulsars shows that the braking index is always lower than 3. This work sets a new piece for this model, based on a small modification from the canonical one. This model incorporates the influence of the cooling of the neutron star superfluid core as its density increases as the pulsar cools down. This happens because of the increasing of superfluid core density, causing the star to decrease its size as the temperature also decreases, changing the inertia moment of the neutron star to a lower value furthermore causing the rotation to accelerate or to decrease less. The result shows that the influence of this process is important only when the star is very young.

**Keywords** Superfluid core · Pulsars · Braking index · Transient cooling

## 1 Introduction

Graviton Group is a research group in Brazil which studies gravity, the work is mainly done in Gravitational Waves (GWs) related topics. As a neutron star is a natural candidate for GW sources, the Graviton group also studies this kind of star.

Gravitational waves were finally detected after a long set of trials planned in 2010 [1] but started many years before. Finally the first detection was made in 2015 [2, 3]. Before that, gravitational waves emission reached very significant evidence with

---

C. Frajuca (✉)

Rio Grande Federal University, Rio Grande, RS 96201-900, Brazil

F. da Silva Bortoli

Federal Institute of Sao Paulo, Sao Paulo, SP 01109010, Brazil



the decrease of orbit period of the binary pulsar **PSR B1913 + 16**, which is a binary pulsar system. This was the first binary system ever discovered and, its orbital period is decreasing in function of time, there were calculations that this decrease is due to the emission of GWs [4]. The earliest experiments for GW detection happened in the early sixty decade [5] with the detectors that are called resonant mass GW detectors [6–9], but were not successful because they operated in the wrong frequency range domain.

The Graviton group efforts for the detection of GW are done in a resonant mass gravitational wave detector called Schenberg. Schenberg detector is a spherical mass that vibrates as gravitational waves pass through, as it vibrates, six microwave parametric sensors on the sphere surface in a half dodecahedron distribution [10, 11] mechanically amplifies and measures this vibration which is proportional to the GW strength. The direction of these GWs can be calculated from the output signal of these 6 sensors.

The microwave parametric sensors are resonant transducers coupled to a microwave resonant cavity which needs a very pure microwave signal with a very low phase noise. The efforts of the Brazilian group are presented in [12–27] references. Many of the articles presented in these references are made using Finite Element Modeling (FEM) [28, 29].

## 2 Pulsars

Pulsars are modeled as stars made of neutrons with very high magnetic fields. These stars form from the explosion and collapse of an original star that exploded as a supernova [30]. This star emits electromagnetic radiation due to its very high magnetic field that accelerates electrons in its magnetic poles, as the star rotates in a different axis, an observer in a direction that crosses these electromagnetic beams will see a pulsate electromagnetic signal, this object is called a pulsar. These pulses are emitted in very regular and well defined intervals, and are used to characterize the pulsar. As the pulsar rotates it emits electromagnetic waves in the radio band and loses energy by such emission.

This process can be modelled by a spherical magnetized dipole which rotates its magnetic field axis misaligned with in relation to the rotation axis, this model is called canonical because it is the more common one used to model a pulsar.

Observational data show that the pulses frequency of the pulsar is decreasing in function of time, then the rotation of the star is also decreasing or the stars are spinning down, according to the canonical model it happens because the star is losing energy by emission of electromagnetic waves [31]. This decay can be, in the canonical model, quantified using a dimensionless parameter called: the braking index, and represented by the letter  $n$ , and can be written by the product of the angular rotational velocity of the star by the second derivative in time of the angular rotational velocity divided by the derivative in time of the angular rotational velocity of the star squared. In the canonical model  $n$  should always be equal to three (3) for all pulsars.

However, observations of many pulsars show that the real braking index is always smaller than 3, implying that this canonical model should be modified [32]. In this work the authors suggest that the cooling process of young neutron stars could make the braking index smaller than 3.

### 3 The Neutron Star Cooling Down Process

Neutron stars are created by the remains of a Supernova explosion. Then the original neutron star is very hot and very dense. The processes of cooling down a neutron star are the so-called URCA processes.

The Direct ‘‘Urca’’ process (DURCA) is made by direct neutrino-emission, being the simplest one. It can be described by:

$$b_1 \rightarrow b_2 + l + \nu_1^*,$$

$$b_2 + l \rightarrow b_1 + \nu_1,$$

noting that  $l$  is a lepton,  $b_1$  and  $b_2$  are protons or neutrons and  $\nu_1^*$  are antineutrinos and  $\nu_1$  neutrinos of the lepton.

The modified URCA process (MURCA) is a slight modification from the DURCA process and works at much lower densities and temperatures, it can also cool down the neutron star but at a different rate, rates as low as 7 orders of magnitude less emissivity. It can be described by:

$$n + N \rightarrow p + N + l + \nu_1^*, \quad (1)$$

$$p + N + l \rightarrow n + N + \nu_1 \quad (2)$$

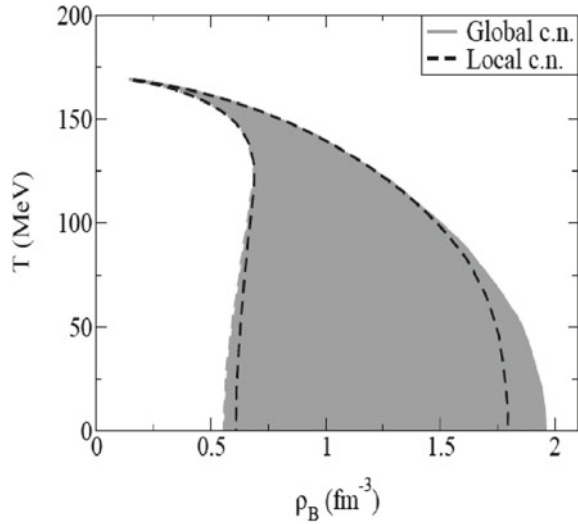
noting that  $N$  is a proton or a neutron (a nucleon),  $n$  is a neutron,  $p$  is a proton and  $\nu_1^*$  is the antineutrino and  $\nu_1$  is the neutrino of the correspondent lepton.

As a result, DURCA is the dominant process in the cooling down of neutron star superfluid cores in young pulsars.

### 4 The Density of Neutron Star Increases as It Cools Down

The DURCA process happens due to the emission of neutrinos, the temperature of the pulsar superfluid core decreases and, as a result, its density increases as shown in Fig. 1 [34]. As the density increases, the radius of the star decreases making the neutron star smaller. Using the angular momentum conservation the angular

**Fig. 1** Baryon density versus temperature for neutron star core density assuming neutrality in global and local charge. Source [33]



velocity of the neutron star should increase. That will be the case if there is only it happening, but the neutron star is also losing angular momentum by the emission of electromagnetic waves.

The cooling down of the neutron star should make the angular velocity decaying less proniciate. Let's now try to quantify the process.

## 5 The Superfluid Core Cooling Down

Neutron star superfluid core cooling is a very complex process. In a period from one hundred to one hundred thousand years, a double logarithmic scale graphic presents a cooling in a straight line as can be seen on Fig. 2 [35].

## 6 The Potential for Neutron Matter

The potential of neutron matter in the neutron star superfluid core can be approximated to the potential of a neutron inside a nucleus. This potential is shown in Fig. 3, where a straight line tangent to the curve in the potential energy equal to zero is plotted, this line represents a temperature of  $10^9$  K, which represents a thermal energy for the neutron of around 0.1 MeV. This slope of such a line in that position is about 0.001 fm/MeV. The question now is what happens to the curve if the temperature decays to  $10^8$ ? The potential will shift to the left multiplying the change in energy by the slope of the line. Then the neutrons will dislocate closer to one another by 0.0001 fm.

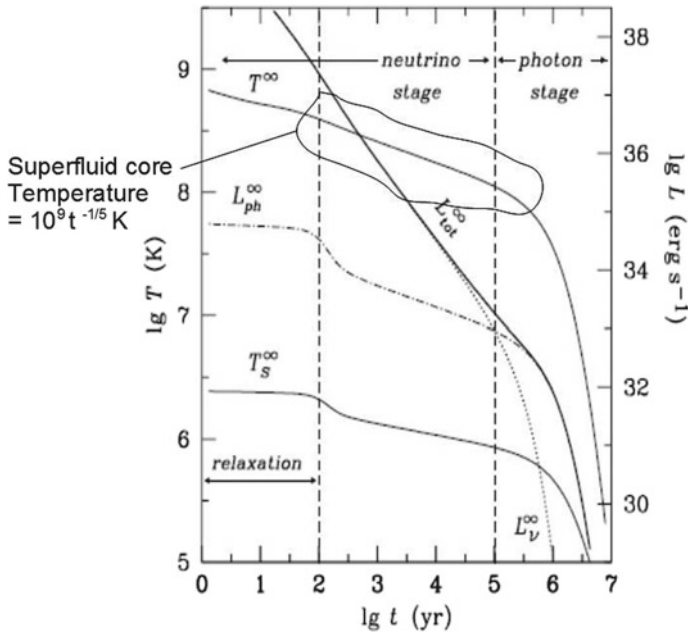
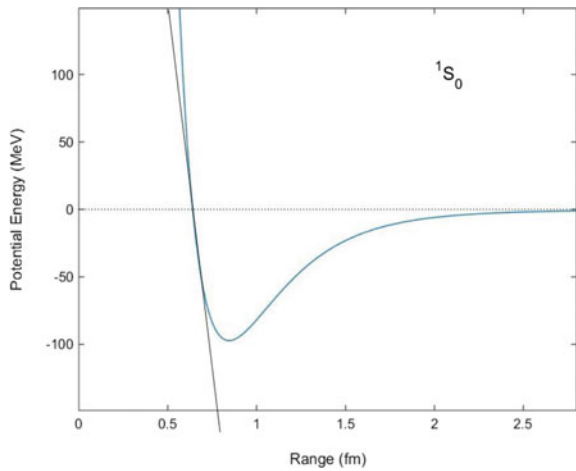


**Fig. 2** The circled region on the  $T^\infty$  curve shows the period where the star cools down as a straight line. This also shows an expression for temperature in function of time for the period between 100 and 100,000 years when the dominant process is the DURCA. Source [34]

**Fig. 3** The neutron potential is plotted versus the distance from another neutron inside the neutron matter



## 7 Conclusions

As the distance between neutrons in the neutron matter decreases due to decrease in temperature, the neutrons will dislocate closer to one another by a part in 10,000. Neutron star has a radius of the order of 10,000 m, then the pulsar star will decrease its size by about one meter in diameter as the age of the star changes from 100 to 100,000 years.

This results corroborates that young pulsars shrink as they cool down, making the pulsars to have a braking index lower than 3 as the star decelerates less than without the cooling. Nevertheless the result presented here represents a very small variation to be measured in real pulsars, as this decrease in temperature and size occurs in a very long time.

**Acknowledgements** CF acknowledge FAPESP: grant #2013/26258/4 and grant #2006/56041/3.

## References

1. The Gravitational Waves International Committee Roadmap (GWIC) (2010) A global plan. University of Glasgow Department of Physics and Astronomy - Kelvin Building (G12 8QQ), Glasgow, pp 117
2. Taylor JH, Hulse RA, Fowler LA, Gullahorn GE, Rankin JM (1976) Further observations of the binary pulsar PSR 1913+16. *Astrophys J* 206:L53
3. Weber J (1960) Detection and generation of Gravitational Waves. *Phys Rev* 117:306
4. Thorne KS (1987) 300 years of gravitation. Cambridge University Press, Cambridge, p 330
5. Blair DG (1991) The detection of Gravitational Waves. Cambridge University Press, Cambridge
6. Richard JP (1984) Wide-band bar detectors of gravitational radiation. *Phys Rev Lett* 167:165
7. Richard JP (1982) In: Ruffini R (ed) Proceedings of the Second Marcel Grossmann meeting on general relativity. North-Holland, Amsterdam
8. Frajuca C et al (2004) *Class Quantum Grav* 21:1107
9. Frossati G (1997) In: Velloso Jr WF, Aguiar OD, Magalhaes NS (eds) Proceedings of the first international workshop for an omnidirectional gravitational radiation observatory. World Scientific, Singapore
10. Merkowitz SM, Johnson WW (1997) Techniques for detecting gravitational waves with a spherical antenna. *Phys Rev D* 56:7513
11. Merkowitz SM, Johnson WW (1993) Truncated icosahedral gravitational wave antenna. *Phys Rev Lett* 70:2367
12. Frajuca C (1996) Otimização de transdutores de dois modos mecânicos para detectores de ondas gravitacionais. Phd Dissertation—Universidade de São Paulo, São Paulo, 97 p
13. Frajuca C et al (1999) Perspectives on transducers for Spherical Gravitational Wave Detectors. In: Proceedings 3rd Edoardo amaldi conference on gravitational waves (Pasadena, USA, July 1999). AIP conference proceedings 523 (New York, AIP), p 417
14. Bortoli FS et al (2016) On the massive antenna suspension system in the Brazilian Gravitational Wave Detector Schenberg. *Brazilian J Phys* 46:308
15. Aguiar OD et al (2005) The Brazilian gravitational wave detector Mario Schenberg: progress and plans. *Class Quantum Grav* 22:209
16. Frajuca et al (2002) Transducers for the Brazilian gravitational wave detector Mario Schenberg. *Class Quantum Grav* 19:1961

17. Magalhaes NS et al (1997) A geometric method for location of gravitational wave sources. *Astrophys J* 475:462
18. Magalhaes NS et al (1995) Determination of astrophysical parameters from the spherical gravitational wave detector data. *MNRAS* 274:670
19. Frajuca C, Bortoli FS, Magalhães NS (2005) Resonant transducers for spherical gravitational wave detectors. *Braz J Phys* 35:1201
20. Aguiar OD et al (2006) The Brazilian gravitational wave detector Mario Schenberg: status report. *Class Quantum Grav* 23:239
21. Frajuca C, Bortoli FS, Magalhaes NS (2006) Studying a new shape for mechanical impedance matchers in Mario Schenberg transducers. *J Phys: Conf Ser* 32:319
22. Frajuca C, Bortoli FS, Magalhães NS (2006) Planning to improve the mechanical quality factor in the transducer impedance matchers for Mario Schenberg detector. *J Phys: Conf Ser* 32:315
23. Aguiar OD et al (2004) The Brazilian spherical detector: progress and plans. *Class Quantum Grav* 21:459
24. Frajuca C, Magalhaes NS, Horiguti AM (2008) Study of six mechanical impedance matchers on a spherical gravitational wave detector. *J Phys: Conf Ser* 122:012029
25. Bortoli FS et al (2010) A physical criterion for validating the method used to design mechanical impedance matchers for Mario Schenberg's transducers. *J Phys: Conf Ser* 228:012011
26. Ribeiro KL et al (2004) Tests with superconducting re-entrant cavities for transducer applications in gravitational wave detectors. *Class Quantum Grav* 21:1225
27. Andrade LA et al (2004) Ultra-low phase noise 10 GHz oscillator to pump the parametric transducers of the Mario Schenberg gravitational wave detector. *Class Quantum Grav* 21:1215
28. Bathe K-J (1996) *Finite element procedures*. Prentice Hall, NJ
29. Filho AA (2000) *Elementos Finitos*. Erica, Sao Paulo
30. Wu F, Xu RX, Gil J (2003) The braking indices in pulsar emission models. *Astron Astrophys* 409:641
31. Chukwude AE, Baiden AA, Onuchukwu CC (2010) Measurements of radio pulsar braking indices astron. *Astrophys* 515:A21
32. Chen WC, Li XD (2010) Why the braking indices of young pulsars are less than 3? *Astron Astrophys* 450:L1
33. Ho WCG, Anderson N (2015) Rotational evolution of young pulsars due to superfluid decoupling. *Nature Phys* 8:787
34. Yakolev DG. et al (2004) Neutron star cooling. [arXiv:0409751v1](https://arxiv.org/abs/0409751v1)
35. Dexheimer V, Negreiros R, Schramm S, Hempel M (2012) Deconfinement to quark matter in neutron stars—the influence of strong magnetic fields. [arXiv:1208.1320v1](https://arxiv.org/abs/1208.1320v1)

# Simulation of a 2D Large Transformation Elastoplasticity Problem Using the ANM



Chafik El Kihal, Omar Askour, Youssef Belaasilia, Abdellah Hamdaoui, Bouazza Braikat, Nouredine Damil, and Michel Potier-Ferry

**Abstract** In this paper, a high-order algorithm, based on the Asymptotic Numerical Method (ANM) is proposed, for the numerical solution of large-transformation elastoplasticity problems in a 2D case. The ANM algorithm combines three techniques: a Taylor series representation, a discretization technique and a continuation procedure. In order to use the Taylor series representation, we show in particular how to regularize the behavior law in the case of large elastoplastic transformations. The objective is to define a behavior law that takes into account the two unilateral conditions: the elastic-plastic transition and the elastic discharge. In this framework, the 2D problem is formulated using the Lagrangian formulation and discretized using the Finite Element Method (FEM). A comparison between the results obtained by the proposed approach and those obtained by the Abaqus code is presented. This comparison has shown that the proposed modeling is efficient to solve this type of problem.

**Keywords** Asymptotic Numerical Method (ANM) · Plasticity · Finite deformations · Regularization · Finite Element Method (FEM)

## 1 Introduction

In this work, we extend, as in [1], the algorithm based on the ANM developed for the resolution of the elasto-plastic structures problems in small deformations [1–3], to the resolution of elasto-plastic problems in finite transformation and we discuss the influence of the path parameter by introducing new parametrization. We also discuss the influence of the regularization parameters. The ANM, is an alternative to the classical methods to solve nonlinear problems [4, 5], it is based on the representation

---

C. El Kihal (✉) · O. Askour · Y. Belaasilia · A. Hamdaoui · B. Braikat · N. Damil  
Laboratoire d'Ingénierie et Matériaux LIMAT, Faculté des Sciences Ben M'Sik, Hassan II  
University of Casablanca, B.P 7955 Sidi Othman, Casablanca, Morocco

M. Potier-Ferry  
LEM3, CNRS, Arts et Métiers ParisTech, Université de Lorraine, F-57000 Metz, France

of the solution “branch” by “branch” [6]. Each “branch” is represented by using Taylor series with respect to a path parameter. The ANM has been applied with success to solve several problems in non-linear elasticity, in fluid mechanics and in bifurcation problems [6]. Thanks to the regularization technique, it is possible to solve with ANM strongly nonlinear problems with unilateral conditions encountered, for example, in plasticity or in contact problems [6]. The plastic behavior induces two unilateral conditions relating to the passage from the elastic state to the plastic state and vice versa (discharge). To take these two conditions into account in finite elasto-plasticity, we introduce as in the case of small deformation [2, 3] and in large deformation [1], two regularization functions into the behavior equations involving both the stress and its derivative. These regularizations allow us to apply the Taylor series representation, and after the finite element method and a continuation method to acquire the entire solution “branch” by “branch”. The formalism remains general and applicable to any type of structures. Applications on elasto-plastic structures are presented in the context of two-dimensional finite elements in plane stress. The results obtained by the proposed approach are satisfactory in comparison with those of Abaqus [7]. We will discuss on the numerical example the choice of the different regularization parameters introduced to replace the initial problem into a regularized one. We will also discuss the influence of a new parameterization.

## 2 Formulation of the Regularized Problem in Large Deformation

We consider an elastoplastic solid occupying a domain  $\Omega_0$  and subjected to a loading  $C(t) \{F_{ext}\}$  on the boundary  $\partial\Omega_0$ ; where  $\{F_{ext}\}$  is a given vector and  $C(t)$  is a time-dependent load parameter. The equilibrium in the Lagrange configuration is written in the matrix form:

$$\int_{\Omega_0} \langle \delta L \rangle^t [A(f)] \{\tau\} d\Omega_0 = C(t) \int_{\partial\Omega_0} \langle \delta v \rangle \{F_{ext}\} dS_0 \quad (1)$$

where  $\{\tau\}$  is the Kirchhoff stress tensor,  $\{L\}$  is the velocity gradient vector with respect to the Lagrange variable  $X$ ,  $f$  is the inverse of the deformation gradient tensor  $F$ , and  $v$  is the velocity vector. Where  $[A(f)]$  is the matrix representation of gradient deformation inverse in the 2D case. We use the hypotheses of the additive decomposition of the total strain rate  $\{D\}$ , into two parts, a plastic strain  $\{D^p\}$  and an elastic strain  $\{D^e\}$ :  $\{D\} = \{D^p\} + \{D^e\}$ . The elastic behavior law part, can be derived from the stress and elastic strain rate vectors relation in the following matrix form:

$$\{\tau^J\} = [C^{elas}] (\{D\} - \{D^p\}) \quad (2)$$

where  $\{\tau^J\}$  is the Jaumann stress tensor,  $[C^{elas}]$  is the matrix representing of the fourth order tensor of elastic constants. The Jaumann stress tensor is used to fulfill



the objectivity of the behavior law and it can be express as the difference between the Kirchhoff stress tensor and the rotations associated to the structure movement that are represented by the non-symmetric part of the velocity gradient tensor. The plastic behavior part is given by the normality condition:

$$\{D^p\} = \dot{\lambda} \left\{ \frac{\partial f_y}{\partial \tau} \right\} = \dot{\lambda} \{n\} \quad (3)$$

where  $\dot{\lambda}$  is the time derivative of the plastic multiplier,  $\{n\}$  is the flow direction vector and  $f_y$  is the yield function:

$$f_y = \frac{q - \tau_e}{\tau_e}; \quad \tau_e = \tau_y + h\epsilon^p; \quad \epsilon^p = \int \sqrt{\frac{3}{2} D^p : D^p} dt = \int \dot{\lambda}; \quad q^2 = \frac{3}{2} \tau^d : \tau^d \quad (4)$$

where  $q$  is the equivalent stress,  $\tau_e$  is the effective stress,  $\tau_y$  is the yield stress,  $h$  is the plastic modulus,  $\epsilon^p$  is the equivalent plastic strain and  $\tau^d$  is the deviator of the Kirchhoff stress tensor. In this case, the normal vector  $\{n\}$  is given by  $\frac{3}{2}$ . To express the plastic strain rate, one must take into consideration the unilateral condition between the plastic multiplier and the yield function, which can be reformulated in the form of the Kuhn–Tucker's condition:

$$\dot{\lambda} \geq 0, \quad f_y \leq 0, \quad \dot{\lambda} f_y = 0 \quad (5)$$

By combining these equations. We get:

$$\dot{\lambda} = g(f_y) \langle n : D \rangle \quad (6)$$

The non-analytical functions  $g(f_y)$  and  $\langle \cdot \rangle$  are expressed as:

$$\begin{cases} g(f_y) = 0 & \text{if } f_y < 0 \\ g(f_y = 0) = \frac{2\mu}{2\mu+h} \end{cases} \quad \begin{cases} \langle n : D \rangle = 0 & \text{if } n : D < 0 \\ \langle n : D \rangle = n : D & \text{else} \end{cases} \quad (7)$$

$\mu$  is the shear modulus. The non-regular character of the elasto-plastic law in finite transformation is due to the fact that the two functions  $g(\cdot)$  and  $\langle \cdot \rangle$  in (6) are not analytical. In order to use a Taylor representation in the ANM, the equations in (7) have to be regularized. Following the same idea as in [1–3], we replace the Eq. (7) by the following equation:

$$\dot{\lambda} = G(f_y) H(D) \quad (8)$$

The function  $G$  regularizes the elastic-plastic transition and the function  $H$  regularizes the elastic discharge:

$$G(f_y) = \frac{\eta_\beta}{\frac{f_y^2}{2\mu} \tau_e + \eta_\beta \left( \frac{3}{2} + \frac{h}{2\mu} (1 + f_y) \right)}; \quad H(H - \xi) = \eta_2^2 \xi^2; \quad \xi = n : D \quad (9)$$

We have introduced two small given regularization parameters  $\eta_2$  and  $\eta_3$  and a typical given value of the strain rate  $\dot{\tau}_c^2$ . The von-Mises equivalent stress has also to be regularized:  $q^2 = \frac{3}{2}\tau^d : \tau^d + \tau_y^2\eta_1$ ; where  $\eta_1$  is a small regularization parameter. As a means to assess the capability of the proposed approach in a standard process (elastic, plastic, elastic unloading), we impose a time-dependent load parameter  $C(t)$  given by the following relation:

$$\left(C - C_m \frac{t}{T_m}\right) \left(C - C_m \left(2 - \frac{t}{T_m}\right)\right) = \eta_4^2 C_m^2 \quad (10)$$

where  $C_m$  and  $T_m$  are given parameters and  $\eta_4$  is a fourth non-dimensional regularization parameter in the problem. In order to clarify the computation of the use of the ANM algorithm, we introduce the following quadratic equations:

$$\widehat{F} = f_y^2, \quad Den = \frac{\widehat{F}}{2\mu}\tau_e + \eta_3 \left(\frac{3}{2} + \frac{h}{2\mu}(1 + f_y)\right), \quad GDen = \eta_3 \quad (11)$$

This regularized problem of elastoplasticity in finite transformation can be written in the following compact form:

$$R(U(t), C(t)) = 0 \quad (12)$$

where  $R$  is the residual vector,  $U(t)$  is the unknown vector which has the following components:  $(v, \tau, \tau^j, D, D^p, G, H, \omega, f, F, L, l, R, q, n, \xi, Den, f_y, \widehat{F}, \tau_e, \dot{\lambda})$  and  $C(t)$  is a time-dependent scalar loading parameter.

### 3 Resolution Strategy Using the ANM

In the ANM, the unknown  $U$  and the loading  $C$  are represented in the form of a truncated power series truncated at an order  $N$  as follow:

$$\begin{cases} U(a) = U^j + \sum_{i=1}^N a^i U_i \\ C(a) = C^j + \sum_{i=1}^N a^i C_i \end{cases} \quad a \in [0, a_{max}] \quad (13)$$

where  $(U^j, C^j)$  is a known and given regular solution corresponding to  $a_{max}$  is an approximation of the validity range of the representation (13). In this paper, we propose to use a new parameterization equation in the form:

$$a = \alpha_1 (t - t^j) t_1 + \alpha_2 (C - C^j) C_1 + \alpha_3 (u - u^j) u_1 \quad (14)$$

In (14),  $t$  and  $C$  are respectively the time and the load and  $u$  represents the displacement which can be related to the velocity as follow:

$$v = \frac{du}{dt}, \quad v = \frac{du}{dt} = \frac{du}{da} \times \frac{da}{dt} \quad (15)$$

The coefficients  $\alpha_i$ , for  $i = 1, 3$  are equals to 0 or 1. In this paper, we shall discuss the influence of the choice of these parameters. By injecting the Taylor series representations (13) of the unknown  $U$  and the loading parameter  $C$  into the nonlinear problem to be solved (12) we obtain, after term-by-term identification, the linear problems verified by each term of the series (13):

$$\text{order } 1 : \quad \int_{\Omega_0} \langle \delta L \rangle ( {}^t [A(f_0)] \{ \tau_1 \} + {}^t [A(f_1)] \{ \tau_0 \} ) d\Omega_0 = C_1(t) \{ F_{ext}(\delta v) \} \quad (16)$$

$$\text{order } k \geq 2 : \quad \int_{\Omega_0} \langle \delta L \rangle ( {}^t [A(f_0)] \{ \tau_k \} + {}^t [A(f_k)] \{ \tau_0 \} ) d\Omega_0 = C_k(t) \{ F_{ext}(\delta v) \} + \{ P_k^{nl} \} \quad (17)$$

with ( $2 \leq k \leq N$ ), and where  $\{ \tau_k \}$  and  $\{ f_k \}$  are deduced from the series representation of the behavior law for  $k = 1 : N$ :

$$\{ \tau_k \} = \mathcal{L}(v_k) + \{ \tau_k^{nl} \} \quad (18)$$

$$\{ f_k \} = \mathcal{L}(v_k) + \{ f_k^{nl} \} \quad (19)$$

The terms  $\{ P_k^{nl} \}$ ,  $\{ \tau_k^{nl} \}$ ,  $\{ f_k^{nl} \}$  depend on the previous orders. We use a classical FEM to solve these linear problems in velocity. The discretized velocity vectors  $\{ v_k \}$  at order  $k$  are solution of linear problems having the same tangent matrix:

$$\begin{aligned} [K_t] \{ v_0 \} &= C_1 \{ F^{ext} \} \quad \text{for } k = 1 \\ [K_t] \{ v_{k-1} \} &= C_k \{ F^{ext} \} + \{ P_k^{nl} \} \quad \text{for } k \geq 2 \end{aligned} \quad (20)$$

where  $[K_t]$  denotes the classical tangent stiffness matrix,  $\{ P_k^{nl} \}$  is a vector that depends on the previous orders.

The whole solution to the nonlinear problem (12) is obtained branch-by-branch using a continuation path-following method [6]. The evaluation of the solution at the end of each branch becomes the new starting point of the next branch. The validity range  $a_{\max}$  of the parameter  $a$  can be estimated by the following relation ( $\epsilon$  is a given tolerance parameter):

$$a_{\max}(\{U\}^{(i)}) = \left( \epsilon \frac{\| \{U_1^{(i)}\} \|}{\| \{U_N^{(i)}\} \|} \right)^{\left(\frac{1}{N-1}\right)} \quad (21)$$

where  $U^{(i)}$  is a component of the vector  $\{U\}$ . In this work within plasticity, as in [2], we define the validity range  $a_{\max}$  as the smaller one corresponding to each component of the vector  $U^{(i)}$ :

$$a_{\max} = \inf(a_{\max}(\{U^{(i)}\})) \quad (22)$$

Once  $a_{\max}$  calculated, the starting solution ( $\{U^{(i)}\}, C^j$ ) in (19) to the next branch is evaluated by  $U^j = U((a_{\max}))$  and  $C^j = C((a_{\max}))$ .

## 4 Numerical Application in 2D Case

The numerical application concerns a 2D plate with a circular hole in the middle, of a length  $L = 100$  mm and a width  $l = 40$  mm. The mechanical characteristics of the structure are: the Young modulus  $E = 200000$  MPa, the Poisson ratio  $\nu = 0.3$ , the initial yield stress  $\tau_y = 240$  MPa, and a hardening modulus  $h = 2000$  MPa. The circular hole is of radius  $r = 7.6$  mm in the center of the plate. The plate is subjected to a traction force. The test involves applying a loading  $C(t)P$  on the right and the left edges (see Fig. 1). We reproduce a typical process: elastic, plastic, and elastic unloading. In (14) we choose the parameters  $C_m = 33$  and  $T_m = 33$  for the evolution of  $C(t)$ . According to symmetry, we consider only the quarter of the plate. For the discretization of the structure, we choose four nodes iso-parametric finite elements for the velocity. The structure is then discretized with  $18 \times 18$  nodes.

The parameters of regularization have been chosen as:  $\eta_1 = 10^{-2}$ ,  $\eta_2 = 10^{-4}$ ,  $\eta_3 = 9 \cdot 10^{-5}$  and  $\eta_4 = 5 \cdot 10^{-3}$ . This choice of such parametrization, is the result of several conducted numerical studies to choose the optimum parameters for obtaining the convergence of the solution branch with the minimum steps. We haven't reported this numerical study in this paper. In Fig. 2, we represent the solution obtained by the proposed algorithm where we have represented the equivalent von-Mises stress according to the equivalent plastic strain at the highlighted point (see Fig. 1). This figure shows that the proposed algorithm is able to reproduce an elastoplastic loading and unloading process in large deformation. In Fig. 2, we represent the obtained solution in the case of a truncation order  $N = 15$ , a tolerance parameter  $\epsilon = 10^{-3}$  and a parametrization Eq. (14), defined by the coefficients  $\alpha_1 = 1$ ,  $\alpha_2 = 1$  and  $\alpha_3 = 0$ . The curves obtained with the proposed algorithm are in good agreement with those found by the code Abaqus in the three zones: elastic loading, plastic loading and elastic discharge. The curve obtained by the ANM algorithm has required, in this case, 125 "branch", which correspond to 125 inversions of the tangent stiffness matrix. The same solution by Abaqus has required 98 increment and 128 iterations, which correspond to 226 tangent stiffness matrix inversions.

In order to discuss the influence of parameterization, we define six strategies (a combination of time parameter (T), load parameter (C) and displacement (or velocity) parameter (V) by giving the values 1 and / or 0 to each of the coefficients  $\alpha_i$  ( $i = 1, 2, 3$ ) in the parameterization Eq. (14) in the following form:

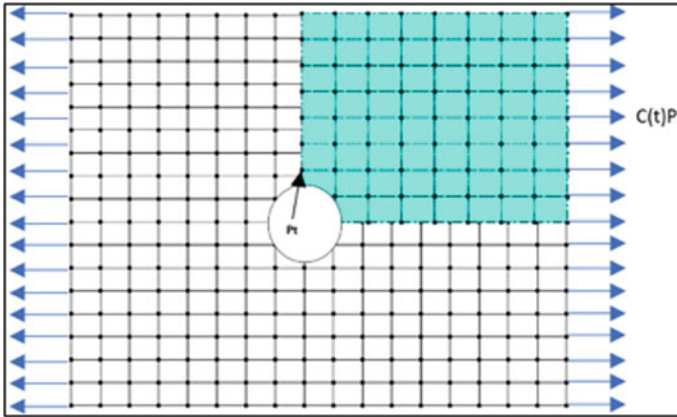
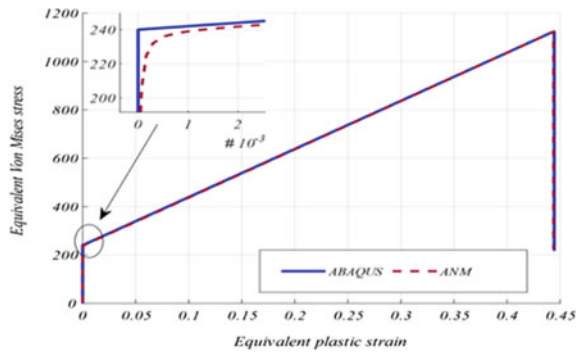


**Fig. 1** Tensile test for a 2D holey plate

**Fig. 2** Response curve equivalent stress versus equivalent plastic strain. The parameters of the algorithm are  $N = 15$ ,  $\epsilon = 10^{-3}$ . Comparison with results of the industrial code ABAQUS



- PT:  $\alpha_1 = 1, \alpha_2 = 0, \alpha_3 = 0$
- PCT:  $\alpha_1 = 1, \alpha_2 = 1, \alpha_3 = 0$
- PTV:  $\alpha_1 = 1, \alpha_2 = 0, \alpha_3 = 1$
- PCV:  $\alpha_1 = 0, \alpha_2 = 1, \alpha_3 = 1$
- PV:  $\alpha_1 = 0, \alpha_2 = 0, \alpha_3 = 1$
- PCTV:  $\alpha_1 = 1, \alpha_2 = 1, \alpha_3 = 1$

with the notations: PT: Parameterization based on the time; PCT: Parameterization based on load parameter and time; PTV: Parameterization based on time and displacement Velocity); PCV: Parameterization based on load and displacement (Velocity); PV: Parameterization based on displacement (Velocity); PCTV: Parameterization based on load parameter, time and displacement (Velocity).

From Table 1, it can be observed that for this large deformation elasto-plasticity problem, and for each parametrization that by increasing the truncation order the number of branches needed to draw the whole curve in Fig. 2 decreases as has been classically observed in previous work of ANM. For all these tests, we can notice that

**Table 1** Influence of the truncation order  $N = 10, N = 15, N = 20, N = 30$  and the parametrization parameters on the number of ANM steps. Comparison with Abaqus

	Order 10	Order 15	Order 20	Order 30
PT	165	126	112	104
PCT	166	125	111	103
PCTV	188	140	124	113
PTV	239	141	129	114
PCV	192	142	128	115
PV	191	187	171	168
Abaqus	226			

the number of inverted matrices in the proposed algorithm and for all the parameterizations used, is always lower than the number of inverted matrices in Abaqus. We can also observe from these numerical tests that the first two parameterizations, the parameterization based on the time (PT) and the parameterization based on load parameter and time (PCT) use the least number of matrix inversions, almost half compared to Abaqus for order 20. The number of matrix inversions increases when using a velocity-based parameterization.

## 5 Conclusion

In this work we proposed an algorithm based on the Asymptotic Numerical Method ANM to solve elasto-plastic problems in finite transformations. In the framework of the ANM, the elasto-plastic behavior law has to be replaced by regular ones in order to represent the solution in the form of a Taylor series. A study of the influence of the parameterization has been done numerically. The comparison between the results obtained by the proposed algorithm and those obtained by the Abaqus code showed that this numerical modeling is effective for solving elasto-plastic problems in finite transformations.

## References

1. Assidi M (2007) Méthode asymptotique numérique pour la plasticité. Université Paul Verlaine de Metz, France, Thèse de Doctorat
2. Assidi M, Zahrouni H, Damil N, Potier-Ferry M (2009) Regularization and perturbation technique to solve plasticity problems. *Int J Mater Form* 2(1):1–14
3. Hamdaoui A, Braikat B, Damil N (2016) Solving elastoplasticity problems by the asymptotic numerical method: influence of the parameterizations. *Finite Elem Anal Des* 115:33–42
4. Ypma TJ (1995) Historical development of the Newton-Raphson method. *SIAM Rev* 37(4):531–551

5. Crisfield MA (1979) A faster modified Newton-Raphson iteration. *Comput Methods Appl Mech Eng* 20(3):267–278
6. Cochelin B, Damil N, Potier-Ferry M (2007) *Méthode asymptotique numérique*. Hermes Lavoissier
7. Abaqus (2014) Version. 6.14 Documentation. Dassault Systemes Simulia Corporation, vol 651, p 6.2

# Modeling the Interface Between User Skin and Wearable Equipment, a Case Study



M. Filomena Teodoro

**Abstract** For an adequate building of wearable equipment, it is determinant to consider comfort issues. The estimation of the contact between equipment and skin is an important process to guarantee comfort. To estimate the contact, an approach using nonlinear regression was used to get empirical models. Eighty participants were subjected to compression and decompression tests, applying different indenters in each participant. All collected data contributed to estimate empirical models.

**Keywords** Wearable equipment · Compression test · Soft tissue deformation · Comfort · Nonlinear estimation · Statistical modeling · ANOVA

## 1 Introduction

Rehabilitation equipment has a high rate of rejection/discontinuation of use (greater than 30% [1]). A solution to overcome this problem is the use of simulation of the contact between skin and equipment to develop rehabilitation equipments suitable for the intended function, but which also take into account the comfort of the user [2]. For this it is essential that the contact between the user and the equipment be quantified. However, in order to numerically simulate the contact between equipment and the skin, it is necessary to have equations that satisfactorily can reproduce the mechanical behavior of the skin, as well as the need to know the limits of load application for the user's safety and comfort [3]. Taking into account the variability of the mechanical behavior of the skin, it is desirable that the determination of the coefficients of those equations and the load application limits be based on experimental results. The mechanical behavior of the skin depends on the place where the contact occurs,

---

M. F. Teodoro (✉)

CINAV, Center of Naval Research, Naval Academy, Portuguese Navy, 2810-001 Almada, Portugal

e-mail: [maria.alves.teodoro@marinha.pt](mailto:maria.alves.teodoro@marinha.pt); [maria.teodoro@tecnico.ulisboa.pt](mailto:maria.teodoro@tecnico.ulisboa.pt)

CEMAT, Center for Computational and Stochastic Mathematics, Instituto Superior Técnico, Lisbon University, 1048-001 Lisboa, Portugal



the gender and age of the individual, among other factors, as well as the used test parameters. So, depending on so many factors, it is difficult to obtain such coefficients and limits [4, 5].

The purpose of the study is to determine whether the mechanical behavior of the skin can be modeled by performing a nonlinear regression [6] of experimental data, if the results are consistent for a group of individuals and also to verify if, for this group of participants, the load limits for safety and comfort remain stable. The data was collected using compression and decompression tests in each participant, applying distinct indenter diameters. To simulate the contact, empirical models were developed using nonlinear fitting.

This article is divided in seven sections. An introduction starts the manuscript; in Sect. 2 are presented some motivations and references; follows Sect. 3 with a brief description of the used methodology; in Sect. 4 is performed the empirical application; in Sects. 5 and 6 are detailed the results and is done the discussion; by last the article ends with the conclusions.

## 2 Preliminaries

The aim for this research is as follows: discomfort is one of the main reasons for stopping the use of rehabilitation devices. Pressure forces arising at the interface between the person and the device causes discomfort. Mathematical models are required to simulate skin-to-wear contact such an orthosis [4]. Considering the motivation, the proper development of wearable equipment implies to take into account the comfort, simulating skin contact with the equipment. Empirical models developed by nonlinear fitting, described in Sects. 5 and 6, are a convenient tool for assessing comfort. A sample of 80 young people was selected. Data were collected by compression and decompression tests, taking into account the application of different indenter diameters in each participant.

## 3 Methodology

### 3.1 Analysis of Variance

#### 3.1.1 Experimental Design One Factor

The purpose of these methods is to compare  $k$  treatments ( $k \geq 2$ ) [7, 8]. Imagine a random selection of  $k$  groups of individuals, each with size  $n_i$ ,  $i = 1, \dots, k$ . Each group  $i$  supported the treatment  $i$ ,  $i = 1, \dots, k$ . If each group has the same size, the design is considered as balanced. If only two independent random samples are studied ( $k = 2$ ),  $t$ -tests are useful to compare the means of each group. The  $t$ -tests

are adequate to compare two independent samples, but when there exist  $k > 2$  independent samples, it is usual to use the analysis of variance technique. The data of  $k$  samples is usually written as  $y_{ij}$ , with  $Y$  the value of the variable under study, for individual  $j$  in sample  $i$ ,  $j = 1, \dots, n_i, i = 1, \dots, k$ . To compare simultaneously the means of  $k$  groups it is usual to compare simultaneously all groups, for example the parametric methods Scheffé [9] or Tukey are the most used. For a nonparametric approach we can use Jonckheere–Terpstra test [10, 11] or even Kruskal Wallis test [12, 13]. In [14] the author describes a wide number of nonparametric techniques.

### 3.1.2 Theoretical Model

Formal inference to compare means of different treatments implies the definition of probabilistic models. It is supposed that the variable under study  $Y_i$  associated to the  $i$ th treatment is Gaussian with mean  $\mu_i$  and variance  $\sigma^2$ . If  $Y_{ij}$  is a random variable (rv) associated to the observed value  $y_{ij}$  the probabilistic model is given by (1)

$$Y_{ij} = \mu_i + \varepsilon_{ij}, (j = 1, \dots, n_i, i = 1, \dots, k), \tag{1}$$

with  $\varepsilon_{ij}$  rv's independents and Gaussian

$$\varepsilon_{ij} \cap N(0, \sigma^2). \tag{2}$$

The model can be rewritten as (3)

$$Y_{ij} = \mu + \alpha_i + \varepsilon_{ij}, (i = 1, \dots, k, j = 1, \dots, n_i). \tag{3}$$

We are able to obtain confidence intervals at  $(1 - \alpha) \times 100\%$  for each  $\mu_i$ . Since  $\widehat{\mu}_i = \bar{y}_i$  and from (1) and (2) we can conclude

$$\bar{y}_i \cap N(\mu_i, \sigma^2) \tag{4}$$

following

$$\frac{\bar{y}_i - \mu_i}{\sigma/\sqrt{n_i}} \cap N(0, 1) \tag{5}$$

or, if  $\sigma$  is unknown,

$$\frac{\bar{y}_i - \mu_i}{S/\sqrt{n_i}} \cap t_{[N-k]}. \tag{6}$$

The confidence intervals (CI) considering a confidence level  $(1 - \alpha) \times 100\%$  for each  $\mu_i$  are given by (7)

$$\bar{y}_i - t_{[N-k; 1-\alpha/2]} \frac{s}{\sqrt{n_i}} \leq \mu_i \leq \bar{y}_i + t_{[N-k; 1-\alpha/2]} \frac{s}{\sqrt{n_i}}. \tag{7}$$

To investigate whether the treatments have identical means or not can be tested the the hypothesis (8) using as statistical test the formula (6)

$$H_0 : \mu_1 = \dots = \mu_k \text{ versus } H_1 : \text{ some } \mu_i \text{ are not equal.} \quad (8)$$

A rejection of  $H_0$  means that there is experiential evidence that treatments differ from each other. In terms of the effect of treatment  $\alpha_i$ , the above hypothesis can be described as

$$H_0 : \alpha_1 = \dots = \alpha_k = 0 \text{ versus } H_1 : \text{ some } \alpha_i \text{ are not null.} \quad (9)$$

To perform the test defined by (9) it is necessary to calculate the total variability of  $\hat{\mu}_i = \bar{y}_i$  around  $\hat{\mu} = \bar{y}$  given by the sum of squares of treatment deviations (10)

$$SS_{TREAT} = \sum_{i=1}^k n_i (\bar{y}_i - \bar{y})^2. \quad (10)$$

A large  $SS_{TREAT}$  suggests that the treatments are distinct. It is necessary to take its average value, dividing by the degrees of freedom (11)

$$MS_{TREAT} = \frac{\sum_{i=1}^k n_i (\bar{y}_i - \bar{y})^2}{k - 1} \quad (11)$$

and compare with the variability of each observation within the sample, i.e., with the mean sum of squared errors defined as (12)

$$MSE = s^2 = \frac{\sum_{i=1}^k \sum_{j=1}^{n_i} (y_{ij} - \bar{y}_i)^2}{N - k} = \frac{SSE}{N - k}. \quad (12)$$

The  $F$  test statistic associated to test hypothesis (9) is given by (14)

$$F = \frac{\text{average sum of squares due to treatments}}{\text{mean sum of squares of residuals}} \quad (13)$$

$$= \frac{MS_{TREAT}}{MSE} \cap F(k - 1, n - k). \quad (14)$$

The critical region of test (9), for significance level  $\alpha$  is given by (15)

$$F|_{H_0} > F_{(k-1, n-k, 1-\alpha)}. \quad (15)$$

The total variability  $SST$  (16) is measured by the squared mean of the deviations of each observation from the overall mean

$$SST = \sum_{i=1}^k \sum_{j=1}^{n_i} (y_{ij} - \bar{y})^2 \quad (16)$$

and can be decomposed by the sum of two terms: the inter-group variability given by  $SS_{TREAT}$  and a variability within each group  $SSE$ , given by (17)

$$SST = SS_{TREAT} + SSE. \quad (17)$$

## 4 Empirical Application

### 4.1 The Individuals

In order to achieve the proposed objectives, indentation tests were performed at a specific point on the leg considering eighty healthy individuals, aged between 20 and 28 years, 40 women and 40 men. Some details can be found in Table 1.

### 4.2 Experimental Methods

Forces perpendicular to the lower limb surface are applied at a velocity of 1 mm/s [2] until unbearable pain<sup>1</sup> is perceived by the participant (see Fig. 1).

There are considered different spherical stainless steel indenters. They were applied by increasing order of diameters: (see Fig. 2). The tests are performed with each indenter considering increasing diameters for each location (5, 10, 15 and 20 mm). Maximum force and deformation are measured in a specific location (see Fig. 3), corresponding to a particular point of contact between lower limb and orthosis AFO.

**Table 1** Sample mean and sample standard deviation of mass and height for each group of participants (Males and Females)

Group	Mass (Kg)	Height (m)
Female	59,6±10,9	1,63±0,07
Male	77,4±12,3	1,76±0,06

<sup>1</sup> Perception of Pain: “Unpleasant emotional and sensory experience associated with tissue damage” [15].

**Fig. 1** Forces perpendicular to the lower limb surface are applied at a velocity of 1 mm/s until unbearable pain is perceived by the participant

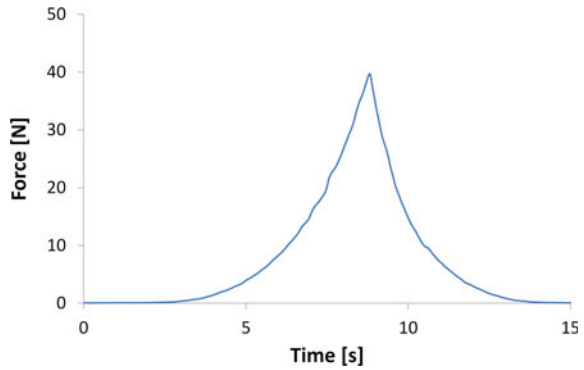
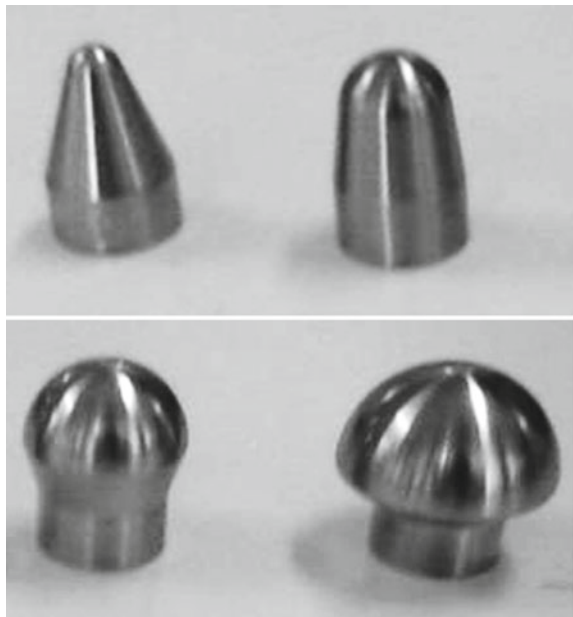


**Fig. 2** Different spherical stainless steel indenters: 5, 10, 15 and 20 mm of diameter



The force is measured by the soft tissues test equipment with a force transducer (0–250 N) placed in the indenter; a potentiometer transducer (0–50 mm) registers the deformation (see Fig. 4, on left).

The results are collected at a sampling frequency of 40 Hz. The indenter is positioned perpendicularly to the anatomic test point, approaching the skin and starting the indentation at a constant speed. When the individual feels the maximum pain limit, a controller acts and the indenter turns to its initial position, at the same speed. In Fig. 4 (on right) we illustrate a test applied to a participant (22 years old, female with a BMI of 22.8) with the leg supported during the tests, specifically the left anterior part of the leg.



Fig. 3 Participant test point

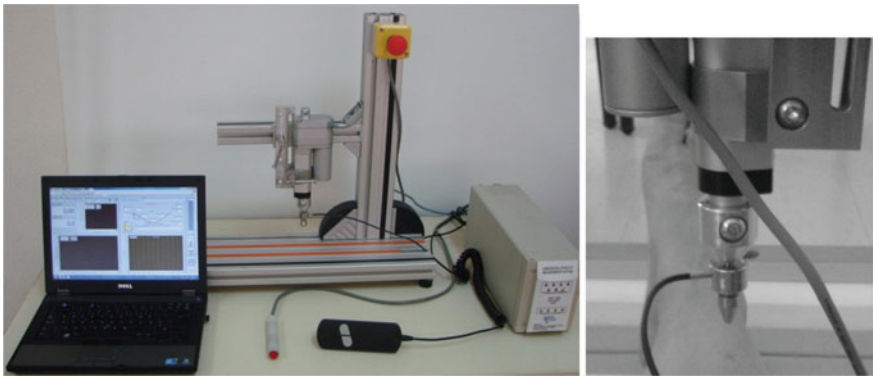
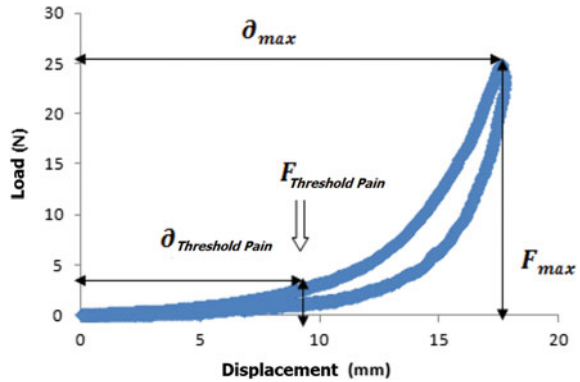


Fig. 4 Test Equipment (on left). Example how a test is applied. The leg is supported (on right)

Each test consisted by the compression of the test point until the individual felt the maximum pain, allowing to register the maximum force  $F_{Max}$  and the deformation values  $\delta$ . During the test, each individual verbalized the onset of pain, allowing to obtain deformation and strength for the pain threshold. Each participant performed five tests. A compression-decompression curve was obtained for each test (Fig. 5).

**Fig. 5** Representation of typical compression and decompression curves



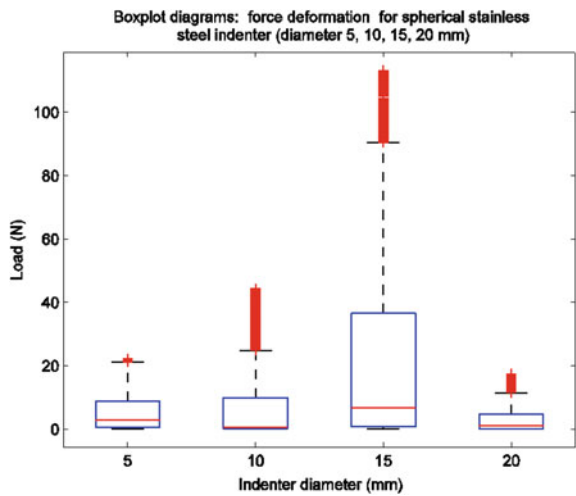
Notice that Fig. 5 presents two separate parts: the compression curve (top) and decompression curve (bottom).

### 5 Results

As expected, the maximum forces increased as the indenter diameter increased. Results may be affected by previous local skin damage. We can confirm this fact observing Fig. 6. The damage is evidenced when the indenter diameter is 20 mm.

The test described in expression (8) was performed. Using formula (15) we obtained a significant test ( $p - value < 0.005$ ). There is statistical evidence that the maximum force is strongly related on diameter of indenter. Also were compared

**Fig. 6** Box-plot diagrams for the maximum force per indenter diameter. Diameter: 5, 10, 15 and 20 mm



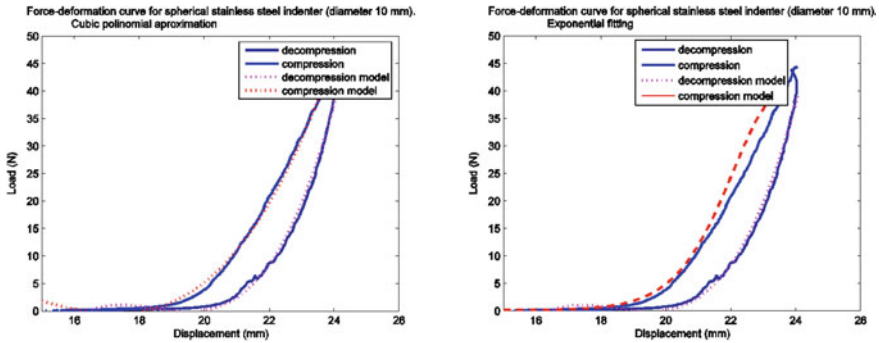


**Fig. 7** Force—deformation models using Cubic Polynomial Regression (left) and exponential regression (right). Indenter diameter = 10 mm. In red—estimated values, in blue—observed values

the results obtained per each pair of two distinct diameters. (à priori *t*-test and à posteriori Scheffé simultaneous Confidence Intervals). When we consider the larger diameter (20 mm) the data is clearly distinct from the other cases. The maximum force is different when compared with the remaining cases (*p* – value < 0.0001). It is compatible with with the existence of damage when the indenter diameter is 20 mm.

To model the force versus deformation, an approach considering nonlinear regression was performed. Several models were obtained applying the logarithmic, the exponential, the polinomial and the power regression. Considering the behavior of the force versus deformation curve, only the regression with adjustment of the exponential function,  $y = ae^{bx}$  and the regression with adjustment of the polinomial function, in particular when  $y = ax^b$ , are advisable, the determination coefficient  $R^2$  is above 0.90. Variables *x* and *y* are commonly named explanatory (or independent) and explained (or dependent) variables, respectively. These two approaches were applied to all the cases: the models that relate applied force and skin deformation were estimated considering the four distinct diameters for the stainless steel indenters.

As example of our actual work, the cases when diameters 10 and 20mm are illustrated. In Fig. 7 we present the application of cubic polynomial regression (on left) and exponential (on right) when diameter is 10 mm.

When is considered the case diameter = 10 mm, the exponential regression model is less robust. The model has a lower capacity of explanation. The best model is obtained by a cubic polynomial model, with a higher determination coefficient (relatively to exponential fitting) and in accordance with [16].

When diameter = 20 mm, both approaches are similar, with a good capacity of explanation (Fig. 8).

Table 2 shows the results obtained for the exponential regression,  $y = ae^{bx}$ . The the coefficient of determination,  $R^2$ , is very close to 1 ( $R^2 = 0.9176$ ). In particular,



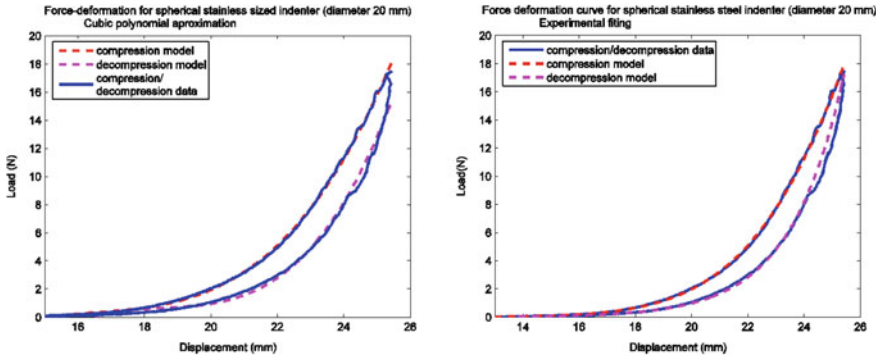


**Fig. 8** Force—deformation models using Cubic Polynomial Regression (left) and exponential regression (right). Indenter diameter = 20 mm. In red—estimated values, in blue—observed values

**Table 2** Estimates of the model coefficients using nonlinear regression. Exponential regression case, diameter = 20 mm

Exponential Regression	a	b	R <sup>2</sup>
Parameter estimate	0,4313	0,2421	0,91765
Variance	0,0351	0,0010	

the estimate of parameter *b* indicates the relative variation  $\Delta y/y$  of the variable *y* (force), when the variable *x* (deformation) varies by one absolute unit ( $\Delta x = 1$  mm).

Instead a polynomial of third order, we considered a monomial of third order  $y = ax^3$  as the author of [16]. To confirm the third order of the monomial, it was used a power function  $y = ax^b$ , expecting that the estimate of parameter *b* be close to three. The coefficients estimates are shown in Table 3. The coefficient of determination, is close to 1,  $R^2 = 0.9792$ , greater than the  $R^2$  from exponential fitting case (see Table 2). This fact indicates that the power function is a better model of regression. The estimate of parameter *b* is close to 3, the estimated model is close to a monomial of third degree, confirming the author of [16]. Also, we notice that the estimate of *b* represents the relative variation  $\frac{\Delta y}{y}$  of the variable *y* (force) when the variable *x* (deformation) varies by one relative unit ( $\frac{\Delta x}{x} = 1$ ).

All described models were validated and residual analysis was successfully completed.

Force and displacement values were recorded for pain threshold and maximum supported pain. The maximum load limit to apply will always be the maximum pain, which would indicate danger of injury. The pain threshold will be the recommended loading for the equipment to be comfortable. These data was statistically treated in two different groups, male and female. The results will be published in a future paper,

**Table 3** Estimates of the model coefficients using nonlinear regression. Power regression case, diameter = 20 mm

Power Regression	a	b	R <sup>2</sup>
Parameter estimate	0,0401	2,9329	0,9792
Variance	0,0055	0,2300	

detailing the results, but, shortly, we can illustrate that both the maximum strength and the strength at the pain threshold are, in general, higher in the male group and also present a higher dispersion. The 1st and 3rd quartiles are also higher in the male group than in the female group. However, the ratio between applied force at the pain threshold (maximum pain) has a smaller dispersion for the male group.

## 6 Discussion

In rehabilitation equipment projects, it is important to simulate the contact between them and the user. For this it is necessary to know equations representing the mechanical behavior of the skin and the load application limits in order to guarantee the user's safety. Indentation tests were performed at a specific point on the leg in eighty healthy individuals, 40 women and 40 men. Force and deformation were recorded in each test, namely the pair of values for pain threshold and for maximum pain. It appears that both the exponential regression and the power regression show an adequate fit to the experimental data, but the exponential regression shows worst approximation to the experimental data. It is also observed that all pain threshold strength values are greater than 1 N, which makes it possible to use the range of forces greater than 1 N in the used regressions (e.g. logarithmic regression). Different behaviors between genders were found regarding strength and deformation supported in the pain threshold and in the maximum pain. The median for the male gender for all values is higher, the force presents a greater dispersion in relation to the female gender; the deformation presents a smaller dispersion for the female group. The difference found between genders can be justified bearing in mind that the anatomical location of the point under test is an area where muscle tone is important. It is also verified that the range of values for both strength and deformation in the pain threshold are similar for both groups. This does not happen for maximum pain. Summarizing, we can establish that:

- The maximum forces increased with the increasing diameters of the indenter, however results may be affected by previous local skin damage;
- All the curves show similar shapes with good data fitting, even though they correspond to different indenters and different levels of applied load;

- The results for deformation and forces show some variations. The compression curve is always above the decompression one;
- The deformation is in conformity with the expected maximum from the literature;
- The force is related with the displacement with models obtained by non linear estimation;
- For 10 and 20 mm diameter indenter cases, are presented cubic polynomial models (approximately) and exponential models;
- These non-linear models were the best adjustment to the data. Validation of models and residual analysis were successfully completed.

## 7 Conclusions

In order to verify if it is possible to reproduce the mechanical behavior of the skin by performing the regression of the experimental data, if the results are consistent for a group of individuals and to verify if the load application limits in safety and comfort remain stable for this group of individuals, leg point indentation tests were performed on 80 participants. The results show that:

- The estimated models, using polynomial fitting are consistent with the literature;
- Power regression shows a good fit to the experimental curves.
- The empirical models, using exponential fitting have in general good performance for a specific range of indenter diameter;
- At the pain threshold, force and deformation values are in the same range for both genders.
- The exponential models can also provide a simpler equation with few parameters to adjust and an easier physical interpretation of the relation between load and deformation of the tissues.

This work shows that the use of either power regression or exponential regression is feasible but that their coefficient values can have a significant variation. These results show the need for continuity of tests, for other test parameters and for other types of location in order to confirm the results obtained. New models are being tested with more data using a wide range of individuals and new information about physical and psychological conditions; As future work, an extended effort is needed to characterize both the soft tissues properties and the level of tolerance for applied pressure, deformation and force and hence the ability to design for comfort. Further tests are needed with a larger sample and more indenter diameters and anatomic locations.

**Acknowledgements** This work was supported by Portuguese funds through the *Center of Naval Research (CINAV)*, Portuguese Naval Academy, Portugal and *The Portuguese Foundation for Science and Technology (FCT)*, through the *Center for Computational and Stochastic Mathematics (CEMAT)*, University of Lisbon, Portugal, project UID/Multi/04621/2019. The author also acknowledges her colleagues P. Silva and C. Pina by their availability and ideas discussion.

## References

1. Mann W (2005) Smart technology for aging, disability and independence: the state of the science. Wiley, New York
2. Rodrigues M, et al (2013) Influência da velocidade de penetração no limiar da dor à compressão. In: Proceedings of the 5<sup>o</sup> Congresso Nacional de Biomecânica, Espinho, Portugal
3. Sanders J, Goldstein B, Leotta D (1995) Skin response to mechanical stress: adaptation rather than breakdown - a literature review. *J Rehabil Res Dev* 32:214–226
4. Silva P (2011) Computational modelling of a wearable ankle-foot orthosis for locomotion analysis and comfort evaluation. PhD thesis, Instituto Superior Técnico
5. Silva P, et al (2012) Measuring discomfort: from pressure pain threshold to soft tissues deformation. *J Biomech* 45(S1 S576)
6. Seber G, Child D, Wild C (2017) Nonlinear regression. Wiley, Blackwell
7. Morgado L, Teodoro F, Perdicoulis T (2010) Métodos Estatísticos em Ciências Biomédicas. Universidade de Trás-os-Montes e Alto Douro (UTAD), Vila-Real, Portugal
8. Tamhane A, Dunlop D (2001) Statistics and data analysis: from elementary to intermediate. Prentice Hall, New Jersey
9. Scheffé H (1959) The analysis of variance. Wiley, New York
10. Jonckheere A (1954) A distribution-free k-sample test against ordered alternatives. *Biometrika* 41:133–145
11. Terpstra T (1952) The asymptotic normality and consistency of kendall's test against trend, when ties are present in one ranking. *Indagationes Mathematicae* 14(3):327–333
12. Bewick V, Cheek L, Ball J (2004) Statistics review 9: analysis of variance. *Crit Care* 7:451–459
13. Bewick V, Cheek L, Ball J (2004) Statistics review 10: further nonparametric method. *Crit Care* 8(3):196–199
14. Sprent P, Smeeton NRE (2001) Applied nonparametric statistical methods. Chapman & Hall/CRC, London
15. Vitor A, et al (2008) The psychology of pain: a literature review. *RECIIS - Electron J Commun Inf Innov Health* 2(1):85–94
16. Pons J (2008) Wearable robots: biomechatronic exoskeletons. Wiley, Blackwell

# Reinforcement Learning to Refine FEM Meshes for Acoustic Problems



Mathieu Gaborit, Gwénaél Gabard, and Olivier Dazel

**Abstract** Numerical methods are central to modern engineering and the Finite Element Method (FEM) specifically is used in a variety of domains and for countless applications. One of the main challenges of using FEM lies in the choice of parameters to generate the mesh. This is particularly the case in acoustics. Indeed, for the phenomena to be correctly modelled, the mesh parameters must be chosen in concordance with the frequency range of interest. So far, the choices regarding the mesh are mostly guided by past experience or widely accepted guidelines (for instance 7–10 points per wavelength when using quadratic elements). In this contribution, we explore the use of reinforcement learning to construct and refine a FEM mesh. This technique implies that the machine is learning how to complete a given task based solely on the so-called state of the environment (including a measure of the error on the result). The key aspect of this research is to challenge the traditional guidelines used for acoustic problems by letting a machine explore and converge without human intervention. The overall strategy will be introduced and demonstrated on simple problems, the results compared with pre-existing recommendations and the challenges ahead will be briefly presented.

**Keywords** FEM · Reinforcement learning · Acoustics · Machine learning

---

M. Gaborit (✉)

ECO2 Centre for Vehicle Design, KTH Royal Institute of Technology, SE 10044 Stockholm, Sweden

Marcus Wallenberg Laboratory, KTH Royal Institute of Technology, SE 10044 Stockholm, Sweden

e-mail: [gaborit@kth.se](mailto:gaborit@kth.se)

G. Gabard · O. Dazel

LAUM UMR CNRS 6613, Le Mans Université, FR 72100 CEDEX Le Mans, France

© The Author(s), under exclusive license to Springer Nature Singapore Pte Ltd. 2022  
M. Abdel Wahab (ed.), *Proceedings of the 4th International Conference on Numerical Modelling in Engineering*, Lecture Notes in Mechanical Engineering,  
[https://doi.org/10.1007/978-981-16-8806-5\\_15](https://doi.org/10.1007/978-981-16-8806-5_15)

209

## 1 Introduction

Numerical methods are a cornerstone of modern engineering and the Finite Element Method (FEM) particularly is employed in many, if not all, fields of engineering sciences. Its versatility and ease of use make it ideal to obtain both quick estimates or much refined final results. Hundreds of reports and papers every year reference or extend FEM, thus contributing to its widespread recognition.

With modern software packages, obtaining a FEM prediction for a given problem is just a few clicks away. However tuning the parameters to reach a satisfying result with confidence still requires experience. In the case of acoustic problems, various published works provide differing recommendations concerning the numbers of elements per wavelength or the critical features that should be finely meshed in order to obtain a good approximation of the true solution. These heuristics depend on the complexity of the domain, on the order and kind of interpolation chosen and on the physical phenomena to be captured. A number of conditions have to be met for the model to be accurate and fine-tuning the numerical parameters often relies on trial and error.

The present contribution is a work in progress aiming to let a computer *learn* how to adjust the meshing parameters of a FEM model. To this end, a simple Reinforcement Learning (RL, [2]) stack is implemented with a number of FEM-based environments to be explored by the software. This attempt at using the adaptivity of RL to infer a refinement strategy for a FEM problem is merely a first step that we think could help better understand how an observable learning agent refines a FEM mesh in a reproducible way.

## 2 Protocol Description

This section briefly describes the test problem and the key aspects of the RL stack. As a general note, RL is a class of machine learning techniques based on (software) agents interacting with a given environment in order to obtain a reward [2, 3]. The training process helps agents refine their decision to maximise the cumulative reward. Many types of agents and reward schemes exist and will not be covered in detail here.

### 2.1 Environment

The environments in RL consist of a context represented by a set of states and a reward function. In the present application, the context is a simple one-dimensional FEM problem with two domains. It can be parametrized so that the agent can alter the mesh refinement. The associated set of states can be represented by a 9-tuple

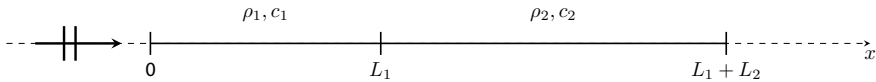


**Fig. 1** Depiction of the computational domain and its parameters

**Table 1** Description of the reward rules

Type	Definition	Reward
Bounds	More than 400 steps $N_i > N_{\max}$ , $i = 1, 2$ $N_i < 1$ , $i = 1, 2$	-10000
Success	$\epsilon < 10^{-4}$	10000
Step	Step	-1

containing the immutable set of parameters for each FEM domain, the number of elements in each domain and the latest relative error.

The FEM problem to be solved, and shown in Fig. 1, consists of a 1D finite space separated into two fluid domains, each having different parameters. The acoustic pressure in this domain is governed by the Helmholtz equation and discretized by linear elements. The left boundary condition induces an incoming plane wave with a unit pressure. The right boundary is rigid (null pressure gradient). The relative numerical error  $\epsilon$  is computed by comparing the reflection coefficient obtained using FEM and using a semi-analytical resolution based on Ref. [1] (similar to transfer matrices).

For clarity, the density, speed of sound and number of elements in the domain  $i$  are denoted by  $\rho_i$ ,  $c_i$  and  $N_i$ .

The proposed reward function is simple and described in Table 1. Basically, failure to comply with set bounds concerning the number of elements in each domain or the maximum number of steps leads to a large negative reward. Success, i.e. the error dropping below a given threshold, leads to an equally large positive one. In addition to these rules, each step taken leads to a small negative reward as an incentive for the agent to solve the problem in a minimum number of steps.

The environment used in this contribution proposes a set of actions of the form:

$$N_i \leftarrow N_i + \Delta_i, \quad (1)$$

where  $i = 1, 2$  and  $\Delta_i \in \{-10, -1, 0, 1, 10\}$ . The left arrow denotes the assignment of a new value (right-hand side) to the symbol on the left-hand side. Depending on the current state, only legal actions are proposed to the agent at each step, i.e. actions that break none of the constraints on  $N_i$  exposed in Table 1.

## 2.2 Agents

The RL agents used in the present contribution are based on *q-learning* which relies on querying and updating a table  $Q$  matching possible (state, action) pairs to their expected reward. At each step, the agent receives the current state of the environment and a list of possible actions. It picks an action following a so-called  $\varepsilon$ -greedy policy [3]:

$$\begin{cases} \text{optimal action, if } x < \varepsilon \\ \text{random action, otherwise} \end{cases} \quad (2)$$

with  $x$  a realisation of a uniform random variable on  $[0, 1]$  and  $\varepsilon$  is a hyperparameter controlling the trade-off between exploration and exploitation of the existing knowledge. The optimal action is defined as the one that maximises the expected *return*, i.e. the overall reward.

The agent have a number of hyperparameters standard for *q-learning*: the exploration/exploitation trade-off parameter  $\varepsilon$ , the learning rate  $\alpha$  that controls how fast the agent corrects the errors and the discount rate  $\gamma$  that controls how the previously earned rewards are discounted at each step. The tuning of these hyperparameters is a subject in itself and described in the literature relevant to RL [2]. For the record, all the results proposed hereafter are generated using

$$\varepsilon = 0.6, \quad \alpha = 0.4, \quad \gamma = 0.98 . \quad (3)$$

## 2.3 Training and Success Assessment

The training and validation process are based on solving many of these two-domain problems. First, we define a target application range and bounds for the parameters (frequency  $f$  and domain variables  $\rho_i$  and  $c_i$ ):

$$\begin{aligned} 15 &\leq f \leq 1000, \\ L &= L_1 + L_2 = 1, & 0.4L &\leq L_1 \leq 0.6L, \\ \rho_1 &= 1.2, & 0.5\rho_1 &\leq \rho_2 \leq 2\rho_1, \\ c_1 &= 343, & 0.5c_1 &\leq c_2 \leq 2c_1. \end{aligned} \quad (4)$$

Sets of parameters are then drawn in these ranges using Latin Hypercube Sampling to ensure optimal coverage of the ranges. The training dataset consists of  $N_{train} = 270$  examples and the test set of  $N_{test} = 30$  cases. The training is performed for a number of epochs as presented in Algorithm 1 which leads to matrices  $E$  and  $T$  containing the final error and number of required steps for each test examples at each epoch.



**Algorithm 1:** Training process

---

**Result:** the errors  $E$  and number of steps  $T$  on the test set  
 populate  $Q$  with 0 for all (state,action) pair;  
 initialize matrices  $T$  and  $E$  of size  $N_{epochs} \times N_{test}$ ;  
**for each epoch in**  $1 \dots N_{epoch}$  **do**  
   **for each training case do**  
     initialise environment with the case's parameters;  
     initialize agent with local  $Q_a = Q$ ;  
      $t \leftarrow 0$ ;  
      $\epsilon \leftarrow 1$ ;  
     **while**  $\epsilon > 10^{-4}$  and  $t \leq 400$  **do**  
        $t \leftarrow t + 1$ ;  
       state,  $\epsilon \leftarrow$  agent interacts with environment;  
       update  $Q_a$ ;  
     **end**  
      $Q \leftarrow Q_a$ ;  
   **end**  
   **for each test case do**  
     initialise environment with the case's parameters;  
     initialize agent with local  $Q_a = Q$ ;  
      $t \leftarrow 0$ ;  
      $\epsilon \leftarrow 1$ ;  
     **while**  $\epsilon > 10^{-4}$  and  $t \leq 400$  **do**  
        $t \leftarrow t + 1$ ;  
       state,  $\epsilon \leftarrow$  agent interacts with environment;  
       update  $Q_a$ ;  
     **end**  
      $E(epoch, case) \leftarrow \epsilon$ ;  
      $T(epoch, case) \leftarrow t$ ;  
   **end**  
**end**

---

### 3 Results

Figure 2 presents the evolution of the mean relative error on the training and test datasets with respect to the epoch. In Fig. 2, it is clear that the mean numerical error is decreasing as the epochs pass, both on the training datasets and on the test dataset. More interestingly, one can note in Fig. 3 that the number of steps required to solve the test problems decrease with the epochs. This is a sign that the system as a whole is learning how to solve the refinement problem better by looking at previous examples. Overall, the reward obtained by the agents on the test datasets increases as the training goes (see Fig. 4).

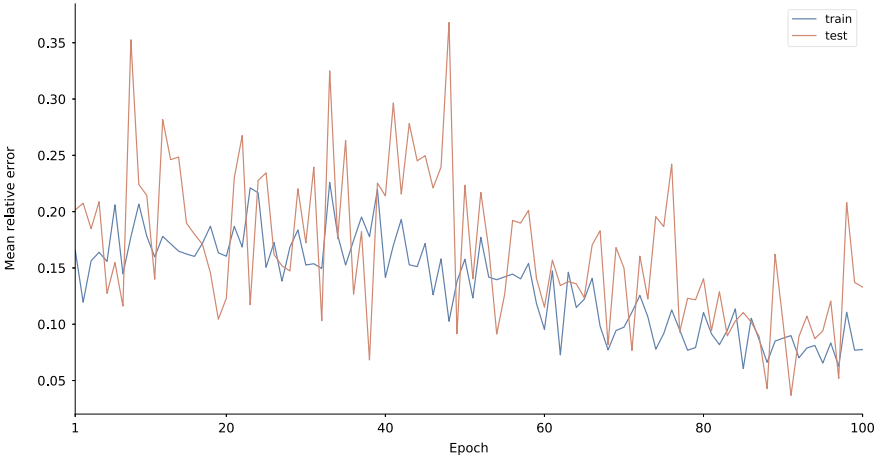


**Fig. 2** Evolution of the mean error with respect to the training epoch on the training and test datasets

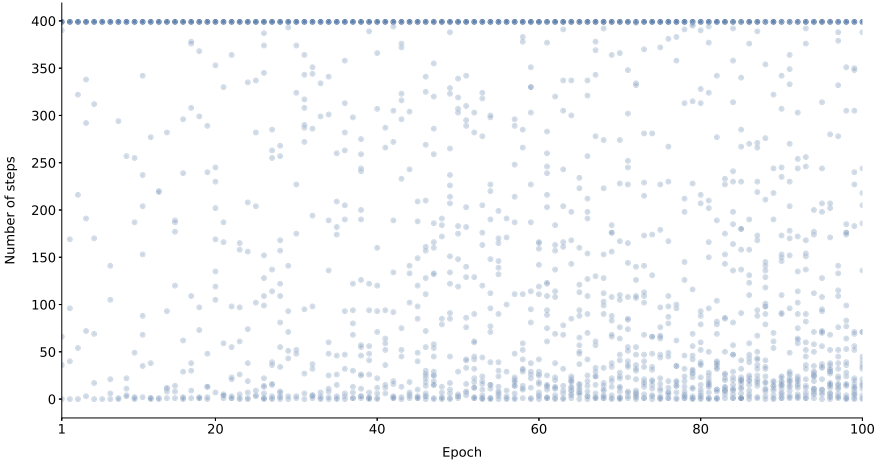


**Fig. 3** Evolution of the number of steps require to solve the test problems with respect to the training epoch

## 4 Perspectives

In this contribution we present the first steps taken to implement a RL solution to a mesh refinement task for an acoustic problem. The current setup is simplistic and work is under way to extend the approach to 2D domains and more complex problems. Overall, our objective is less to improve the refinement task itself than to investigate how the agents approach the problem and tune the parameters.

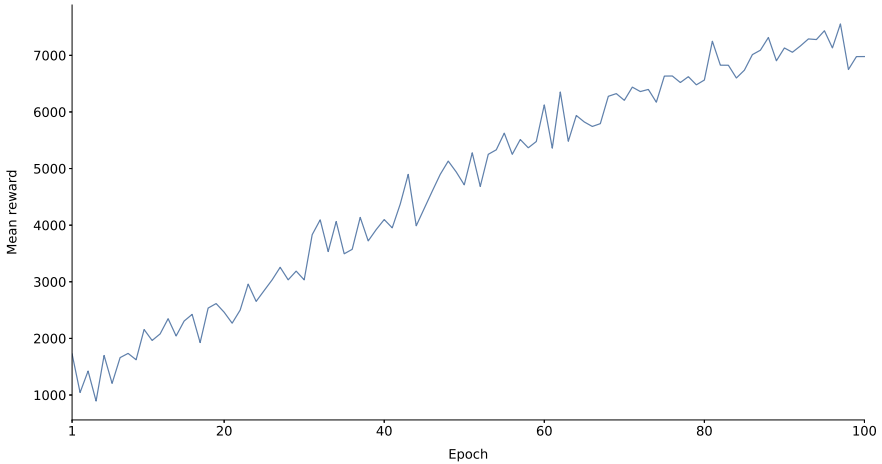


**Fig. 4** Mean reward obtained by the agents with respect to the epoch

Different extensions regarding the agent behaviour or the environment can be considered and among them, we intend to replace the continuous state-space mostly controlled by the error by a discrete one. This will allow to reduce the number of states to be stored in  $Q$  and overall help transfer training between different cases.

## References

1. Dazel O, et al (2013) A stable method to model the acoustic response of multilayered structures. *J Appl Phys* 113(8):083506. ISSN: 00218979. <https://doi.org/10.1063/1.4790629>
2. Sutton RS, Barto AG (2018) Reinforcement learning: an introduction, 2nd edn. Adaptive computation and machine learning series. The MIT Press, Cambridge, 526 p. ISBN: 978-0-262-03924-6
3. Watkins CJCH (1989) Learning from delayed rewards. PhD thesis, King's College, Cambridge